Data Reduction Techniques for Very Long Baseline Interferometric Spectropolarimetry

A thesis submitted in fulfilment
of the requirements for the degree of
Doctor of Philosophy
of Rhodes University

by

ATHOL JAMES KEMBALL

December 1992

ABSTRACT

This thesis reports the results of an investigation into techniques for the calibration and imaging of spectral line polarization observations in Very Long Baseline Interferometry (VLBI). A review is given of the instrumental and propagation effects which need to be removed in the course of calibrating such obervations, with particular reference to their polarization dependence. The removal of amplitude and phase errors and the determination of the instrumental feed response is described. The polarization imaging of such data is discussed with particular reference to the case of poorly sampled cross-polarization data. The software implementation of the algorithms within the Astronomical Image Processing System (AIPS) is discussed and the specific case of spectral line polarization reduction for data observed using the MK3 VLBI system is considered in detail.

VLBI observations at two separate epochs of the 1612 MHz OH masers towards the source IRC+10420 are reduced as part of this work. Spectral line polarization maps of the source structure are presented, including a discussion of source morphology and variability. The source is significantly circularly polarized at VLBI resolution, but does not display appreciable linear polarization. A proper motion study of the circumstellar envelope is presented, which supports an ellipsoidal kinematic model with anisotropic radial outflow. Kinematic modelling of the measured proper motions suggests a distance to the source of $\sim$ 3 kpc. The cirumstellar magnetic field strength in the masing regions is determined as 1-3 mG, assuming Zeeman splitting as the polarization mechanism.

ACKNOWLEDGEMENTS

I would like to thank the National Radio Astronomy Observatory in Charlottesville, Virginia, for their support in the form of a pre-doctoral fellowship, and their hospitality throughout my stay. This work was made possible through the efforts of Dr Phil Diamond, who provided encouragement and assistance throughout the project. I thank Professor Eddie Baart for his support and assistance. Dr Bill Cotton provided advice on many aspects of polarization VLBI data reduction. I acknowledge the financial support of the Foundation for Research Development while at Rhodes University.

This work would not have been possible without the patience and encouragement of my wife and family.

TABLE OF CONTENTS

LIST OF FIGURES

LIST OF TABLES

CHAPTER 1: INTRODUCTION

1.1 Basic Theory of Very Long Baseline Interferometry (VLBI)

The technique of VLBI has found wide use in modern radio astronomy in both astronomical and geodetic applications (Reid and Moran 1988). This has included the fine-scale mapping of radio sources with sub-milliarcsecond resolution and the determination of earth orientation and rotation parameters to high accuracy. It is distinguished from connected-element interferometry by the use of independent time and frequency standards at each antenna. Comprehensive reviews exist of the technique and unnecessary detail will be avoided here (Rogers 1976; Thompson, Moran and Swenson 1986, hereafter TMS).

High resolution interferometric mapping of radio source structure exploits the Fourier transform relation between the source brightness distribution $B(\eta,\zeta,\omega)$ and the mutual coherence of the radiation in the far field $\Gamma(u,v,\tau)$,

$$\Gamma(u,v,\tau) = \int\int B(\eta,\zeta,\omega)e^{-j2\pi(\eta u+\zeta v)}d\eta d\zeta\ e^{-j\omega\tau}\,d\omega \qquad 1.1$$

where (η,ζ) are angular coordinates on the sky, $\omega = 2\pi\nu$ is the angular frequency of the radiation, τ is a time lag and (u,v) are measured in the spatial frequency plane orthogonal to the source direction $\mathbf{s}_0, (\eta = 0, \zeta = 0)$. This relation holds in the limit of a spatially incoherent radiation field of limited angular extent (Clark 1986; TMS p.57 ff.).

In the case of VLBI, the radiation is detected at a number of widely-spaced antennas where the signals are recorded on high density magnetic tape using independent local oscillators and time standards. The VLBI signal path is shown schematically in Fig. 1.1. The complex cross-correlation function of the independently-recorded signals $S(\mathbf{r}_i,t)$ is subsequently formed as,

$$r(u,v,\tau) =< S(\mathbf{r}_1,t)S^*(\mathbf{r}_2,t-\tau) >$$

The (u,v) coordinates in this approximation are the projection of the antenna-separation vector $(\mathbf{r}_1 - \mathbf{r}_2)$ in the plane normal to $\mathbf{s}_0$, and $r(u,v,\tau)$ is consequently a measure of the spatial coherence of the field. The brackets <> denote the ensemble average of the enclosed quantity and an asterisk is used to indicate complex conjugation. The signals recorded at each antenna are assumed to be stationary, ergodic noise processes which allows ensemble averages to be replaced by time averages. The mutual coherence of the field $\Gamma(u,v,\tau)$ is determined from the cross-correlation function $r(u,v,\tau)$ by the calibration and removal of propagation, instrumental and geometric effects.

Earth rotation varies (u,v) and if $r(u,v,\tau)$ is sufficiently well-sampled, equation (1.1) can be inverted to yield $B(\eta,\zeta,\omega)$ by the use of indirect imaging techniques (Roberts 1984).

1.2 Spectral Line Polarization VLBI

This simple formulation so far neglects the polarization properties of the source brightness distribution or any detailed discussion of instrumental effects. In general, instrumental contamination ensures that VLBI data reduction is not straightforward, but the determination of the full polarization structure of the source distribution by VLBI techniques presents special difficulties. This requires the independent recording of two orthogonal polarizations at each antenna and a good understanding of all instrumental and propagation effects for each recorded signal in each sense of polarization.

Polarization VLBI observations of continuum sources were first successfully performed by Cotton *et al.* (1984). Data reduction techniques for these types of

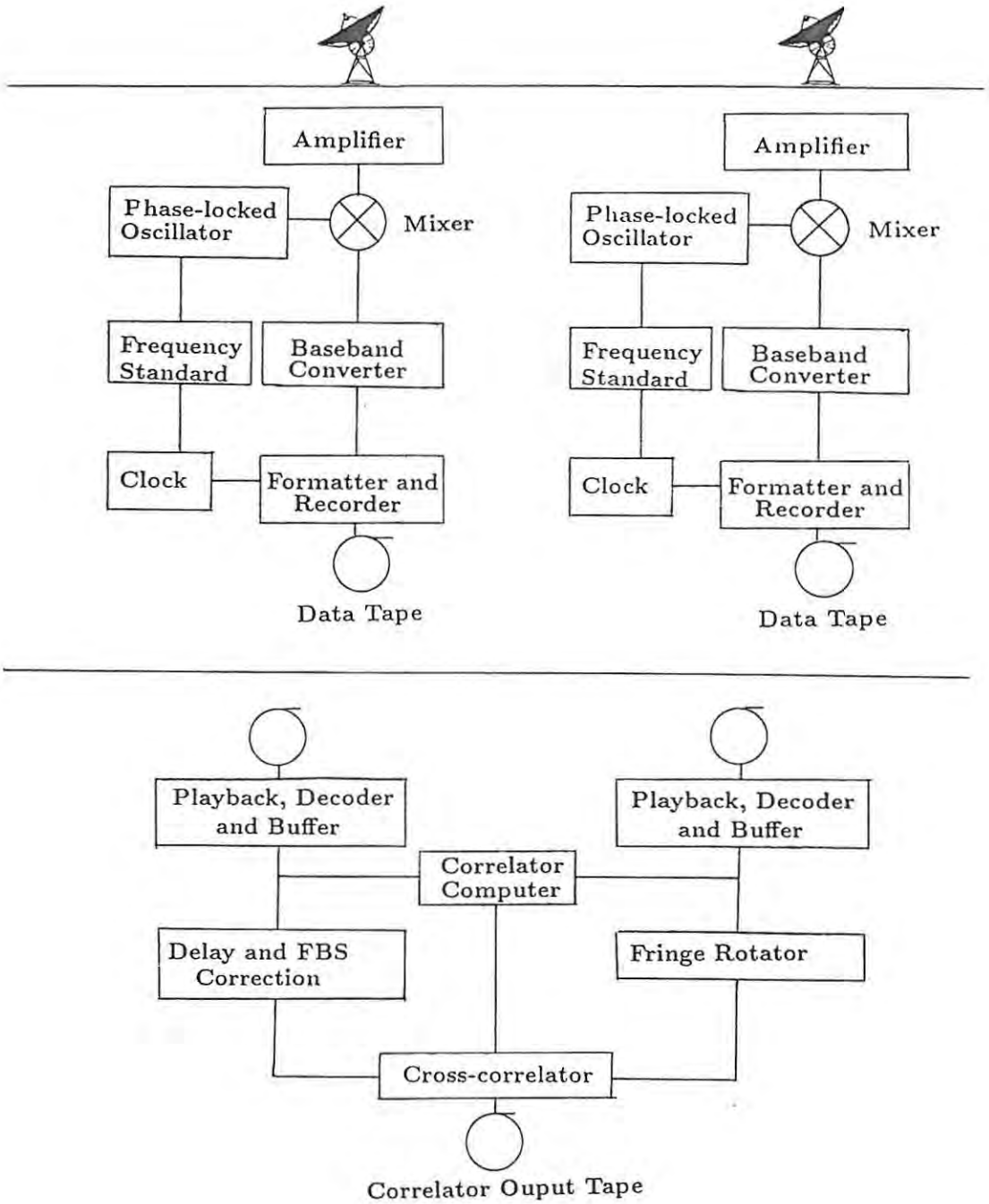

Fig. 1.1. A schematic diagram of the VLBI signal path during recording and subsequent cross-correlation (after TMS p.252). Specific VLBI recording systems may differ in the exact details of fringe rotation, delay correction and cross-correlation.

observations are discussed by Cotton (1989) and Roberts *et al.* (1991). Polarization calibration for connected-element interferometry is discussed by Morris, Radhakrishnan and Seielstad (1964) and Conway and Kronberg (1969). In continuum VLBI the angular frequency dependence of the source brightness distribution is not of interest over the recorded bandwidth. In spectral line observations the source structure may vary significantly as a function of the observed angular frequency. The difficulties in calibrating spectral line polarization VLBI have limited work in this field. Garcia-Barreto *et al.* (1988) have reported results for such observations where a partial polarization calibration was performed.

The scientific potential of polarization VLBI is considerable (Roberts *et al.* 1991) in both continuum and spectral line mode. Continuum polarization observations have provided important insights into the polarization and magnetic field structure in extragalactic sources (Gabuzda, Wardle and Roberts 1989). The field of spectral line polarization observations holds the promise of providing information on the polarization structure of maser sources and the magnetic field distribution in both circumstellar and star-forming regions.

1.3 Polarization in OH/IR stars at 1612 MHz

Early observations of 1612 MHz hydroxyl maser emission towards OH/IR stars, characterised by their OH and infra-red (IR) emission, revealed little polarization, in contrast to the interstellar OH masers where high polarization is frequently found. Notable exceptions are the supergiant OH sources where some polarization is observed and the long-period variable stars W Hya and U Ori, in which some highly circularly polarized features have been found (Cimerman 1979; Reid *et al.* 1979). Polarized components may, however, be more prevalent in OH/IR sources than previously indicated. Narrow, circularly polarized features have been found in single antenna OH/IR spectra observed with high velocity resolution (Cohen *et al.* 1987). If this is interpreted as due to the Zeeman effect then

a magnetic field in the masing regions of several mG is indicated. Such a field may be an important dynamical influence on the outflowing gas and consequently the envelope geometry (Chapman and Cohen 1986).

1.4 Thesis Objectives

The difficulties in calibrating and imaging polarization VLBI data have restricted the scientific potential of this technique, and there is much to be gained from a systematic evaluation of data reduction techniques for these types of observations using currently available computing resources and image processing software.

The present work is concerned with the implementation and evaluation of data reduction techniques for VLBI spectropolarimetry within the Astronomical Image Processing System (AIPS), maintained by the National Radio Astronomy Observatory. An antenna-based approach to calibration has been adopted throughout this work.

Spectral line polarization data taken on the European VLBI Network of the 1612 MHz OH maser emission towards the OH/IR star IRC+10420 have been reduced as part of this investigation. This has provided information on the envelope geometry at VLBI resolution and the detailed structure of the circumstellar maser polarization for this source. The data were recorded using the MK3 VLBI system and the capacity to process such data within AIPS has been further developed. An earlier epoch MK2 observation in left-circular polarization is also analysed as part of this work. The source is widely held to be a proto-planetary nebula or post-AGB object and the OH maser emission is unusual for its polarization properties.

The basic theory of spectral line polarization VLBI is outlined in Chapter 2 and a review of data reduction techniques is given in Chapter 3. The analysis of

the MK2 data is described in Chapter 4. The calibration and imaging of the MK3 observations is discussed in Chapter 5. These are believed to be the first spectral line polarization VLBI observations where a full polarization calibration has been performed, including instrumental feed calibration, and the first polarization VLBI imaging of circumstellar 1612 MHz maser emission. These are also the first such observations using the MK3 VLBI system with all post-correlation reduction performed within AIPS.

A review of the source properties of IRC+10420 is given in Chapter 6 and the kinematic and polarization structure of the source is discussed in Chapter 7 including a proper motion analysis. Appendix A contains detailed information regarding the correlation of MK3 spectral line data and the importing of such data into AIPS.

The aim of this work has been to implement and evaluate data reduction techniques for VLBI spectropolarimetry to further the development of polarization VLBI.

CHAPTER 2: SPECTRAL LINE POLARIZATION VLBI

Introduction

This chapter concerns the instrumental and propagation effects that need to be removed in the course of calibrating spectral line polarization VLBI observations. Particular reference is made to the polarization dependence of these corrections.

2.1 Instrumental and Propagation Effects

This section traces the path for each of the two recorded signals in each polarization, which are here assumed to be oppositely circularly polarized.

2.1.1 Preliminary Definitions

The incident electric field from the direction $\mathbf{s}(\eta, \zeta)$ can be decomposed into right- and left-circularly polarized components as,

$$\mathbf{E}^R(\eta,\zeta,t) = \frac{1}{\sqrt{2}} E^R(\eta,\zeta,\omega)(\mathbf{e}_\delta - j\mathbf{e}_\alpha)e^{j\omega t}$$
$$\mathbf{E}^L(\eta,\zeta,t) = \frac{1}{\sqrt{2}} E^L(\eta,\zeta,\omega)(\mathbf{e}_\delta + j\mathbf{e}_\alpha)e^{j\omega t}$$

where $(\mathbf{e}_\delta, \mathbf{e}_\alpha)$ are unit vectors on the plane of the sky in the direction of increasing declination (north) and right ascension (east) respectively. This complies with the IEEE definition of the sense of polarization as adopted by the International Astronomical Union (IAU 1973; TMS p.97 ff.). The components E^R and E^L are complex and define the polarization state of the radiation (Jackson 1962). Propagation through the ionosphere, troposphere and receiving electronics at each antenna introduces an excess phase $\Delta\phi(\omega, t)$ which is polarization dependent. The effects of interstellar propagation are not considered here. The excess group delay

$\mathcal{L}_g$ and excess phase-delay $\mathcal{L}_p$ are defined in the standard manner as $\mathcal{L}_g = \frac{\partial \triangle \phi(\omega,t)}{\partial \omega}$ and $\mathcal{L}_p = \frac{\triangle \phi(\omega,t)}{\omega}$. Propagation through a medium of refractive index n introduces an excess phase-delay $\mathcal{L}_p = \frac{1}{c}\int (n-1)ds$ (TMS, p.407), where ds is an element of path-length, and an excess group delay $\mathcal{L}_g = \frac{1}{c}\int (n + \omega\frac{\partial n}{\partial \omega} - 1)ds$ (Davies 1965).

2.1.2 The Ionosphere

The right- and left-circularly polarized components propagate through the ionosphere with differing phase velocity, thus rotating the plane of polarization of an incident linearly polarized wave. This Faraday rotation needs to be removed as part of the polarization calibration. In the quasi-longitudinal approximation for the Earth's magnetic field the index of refraction for the regular ionosphere, as a function of frequency ν, can be written as (TMS, p.443),

$$n \sim 1 - \frac{1}{2}\frac{\nu_p^2}{\nu^2} \mp \frac{1}{2}\frac{\nu_p^2 \nu_B \cos\theta}{\nu^3} + O(\nu^{-4})$$

where ν_p is the plasma frequency and ν_B is the gyrofrequency. These are defined as $\nu_p = \frac{e}{2\pi}\sqrt{\frac{N_e}{\epsilon_0 m}}$ and $\nu_B = \frac{eB}{2\pi m}$, where e is the electron charge magnitude, m is the electron mass, ϵ_0 the permittivity of free space and N_e the electron density. The component of the magnetic field along the direction of propagation is $B\cos\theta$. The upper and lower signs refer to the propagation of left- and right-circularly polarized components respectively.

The excess differential phase-delay between the right- and left-circularly polarized components in the regular ionosphere is therefore,

$$\mathcal{L}_p^{R-L} = \frac{1}{c\nu^3}\int \nu_p^2 \nu_B \cos\theta ds + O(\nu^{-4})$$

where $O(\nu^n)$ denotes the order of the residual terms in the expression. Note that in this approximation $\mathcal{L}_g^{R-L} \sim -2\mathcal{L}_p^{R-L} + O(\nu^{-4})$ and $\mathcal{L}_p \sim -\mathcal{L}_g + O(\nu^{-3})$.

Extrapolating the result of Evans and Hagfors (1968) at 100 MHz yields an estimated zenith Faraday rotation of $\sim 15(\frac{\nu}{100 MHz})^{-3}$ ns by night and ten times this value by day. Large changes may occur over short time intervals at sunrise or sunset. The excess phase $\triangle\phi$ due to propagation through the ionosphere will be denoted by $\gamma = \omega\mathcal{L}_p$.

Ionospheric absorption and propagation effects in the irregular ionosphere caused by phenomena such as spread-F and travelling ionospheric disturbances (TID's) are considered by Hagfors (1976). The effects of ionospheric irregularities on radio-interferometric data are reviewed by Gwinn (1984).

2.1.3 The Troposphere

The troposphere, or neutral atmosphere, is non-dispersive and is usually considered to consist of a water vapour component and a dry component. The excess dry path length in the zenith direction is well determined by the surface barometric pressure at the antenna site and is typically ~ 2.3 m under standard conditions (Davies 1965). The wet component delay can be estimated from the surface relative humidity or more sophisticated techniques such as water vapour radiometry (Elgered 1982).

The total atmospheric delay under standard conditions can be modelled by a modified cosecant law (Chao 1970; Robertson 1975),

$$\mathcal{L}_p = \mathcal{L}_g = \rho_m \left[\sin\theta_m + \frac{0.00143}{\tan\theta_m + 0.0445}\right]^{-1}$$

where $\theta_m(t)$ is the elevation of the source from station m at time t, and ρ_m is the zenith delay at station m (typically ~ 7 ns as discussed above). The excess phase due to propagation through the troposphere will be denoted by $\epsilon = \omega\mathcal{L}_p$.

A discussion of atmospheric propagation effects in both the ionosphere and troposphere and their effect on VLBI observables is given by Bartel (1990). The

effects of absorption and phase fluctuations in the neutral atmosphere are discussed by Moran (1989).

2.1.4 Feeds

The circularly polarized feeds at each antenna typically admit some fraction of the orthogonal component of polarization due to imperfect polarization splitters and reflections between the sub-reflector and the antenna and the receiver (Napier 1989). The actual feed response in each sense of polarization $(\mathbf{G}^{R'}, \mathbf{G}^{L'})$ can be modelled as the superposition of purely circular modes $\mathbf{G}^R$ and $\mathbf{G}^L$ as (Conway and Kronberg 1969),

$$\begin{aligned} \mathbf{G}^{R'} &= \frac{1}{\sqrt{1 + D^{R*} D^R}} (\mathbf{G}^R + D^R \mathbf{G}^L) \\ \mathbf{G}^{L'} &= \frac{1}{\sqrt{1 + D^{L*} D^L}} (\mathbf{G}^L + D^L \mathbf{G}^R) \end{aligned} \tag{2.1}$$

The terms (D^R, D^L) are complex and reflect the degree of instrumental contamination from the orthogonal polarization. This formalism is an equivalent parametrization of elliptically-polarized feeds in each nominal sense of recorded polarization. The feeds deviate from the desired ellipticity $(\chi^R = -\frac{\pi}{4}, \chi^L = \frac{\pi}{4})$ by $\triangle\theta = \arctan|D|$ and have orientation $\psi = \frac{1}{2}\arg(D)$. The axial ratio of the semi-major to semi-minor axis of the polarization ellipse is $\frac{1+|D|}{1-|D|}$ (Conway and Kronberg 1969).

The purely circular modes $\mathbf{G}^R$ and $\mathbf{G}^L$ in this coordinate system take the form,

$$\begin{aligned} \mathbf{G}^R &= \frac{1}{\sqrt{2}} (\mathbf{e}_\delta + j\mathbf{e}_\alpha) e^{-j\alpha(t)} \\ \mathbf{G}^L &= \frac{1}{\sqrt{2}} (\mathbf{e}_\delta - j\mathbf{e}_\alpha) e^{j\alpha(t)} \end{aligned}$$

where $\alpha(t)$ is the parallactic angle of the antenna with respect to the source direction. The parallactic angle is the angle between the local source meridian and elevation great circle of the antenna and is given by (Hjellming 1983),

$$\alpha(t) = \arctan[\frac{\cos\lambda_{lat}\sin H}{\sin\lambda_{lat}\cos\delta - \cos\lambda_{lat}\sin\delta\cos H}] \tag{2.2}$$

where λ_{lat} is the antenna latitude and (H, δ) are the apparent hour angle and declination of the source at the antenna. The parallactic angle is zero for equatorially mounted antennas but non-zero for altitude-azimuth antennas which rotate with respect to a given source direction as a function of time.

The detected voltage at frequency ω in polarization p is $(\mathbf{G}^p.\mathbf{E})$ where,

$$\begin{aligned}(\mathbf{G}^p.\mathbf{E}) &= \frac{1}{\sqrt{1+D^{p*}D^p}}S^p e^{j(\omega t+\epsilon+\gamma^p)} \\ S^R &= E^R e^{-j\alpha(t)} + D^R E^L e^{j(\alpha(t)+\gamma^{L-R})} \\ S^L &= E^L e^{+j\alpha(t)} + D^L E^R e^{-j(\alpha(t)+\gamma^{R-L})}\end{aligned} \tag{2.3}$$

where ϵ and γ^p are the excess phase terms after propagation through the neutral atmosphere and ionosphere respectively, and $\gamma^{R-L} = \gamma^R - \gamma^L$.

The instrumental terms (D^L, D^R) are usually assumed constant in time and independent of frequency or direction. The latter condition can be justified in VLBI as the field of interest is typically much smaller than the primary antenna beam solid angle. The $D-$ terms, also known as cross-talk terms, are usually small i.e. $D \leq 0.1$.

2.1.5 Receivers, Electronics and Geometry

A considerably simplified model is adopted in this section to illustrate the basic response of the receiving system. Individual antennas in typical VLBI experiments differ widely in their specific electronics and receiving system components.

All however have in common the frequency conversion of the RF signal to an intermediate frequency using a phase-stable local oscillator system. Net upper sideband frequency conversion is assumed here. The resulting baseband signal is recorded on high-density magnetic tape over a suitable video bandwidth. The frequency and time stability is provided by hydrogen masers or rubidium atomic standards.

The recorded signal $S'(t)$ at frequency ω from direction $\mathbf{s}$ can be represented after Moran (1973) as,

$$S^{R'}(t) = S^R(t)g^R(t)B^R(\omega)e^{j[(\omega-\omega_0)t-\omega\tau_g+\theta_{LO}(t)+\theta_0^R+(\omega-\omega_0)\tau_i^R+\psi_i+\epsilon+\gamma^R]}$$
$$S^{L'}(t) = S^L(t)g^L(t)B^L(\omega)e^{j[(\omega-\omega_0)t-\omega\tau_g+\theta_{LO}(t)+\theta_0^L+(\omega-\omega_0)\tau_i^L+\psi_i+\epsilon+\gamma^L]} \quad (2.4)$$

where g is the antenna amplitude gain in the specific sense of polarization, incorporating the factor $\frac{1}{\sqrt{1+D^p \cdot D^p}} \sim 1$ in equation (2.1) and all atmospheric, elevation , receiver and antenna directivity effects, and $B(\omega)$ is the composite complex passband response which is assumed time-independent. The local oscillator phase is modelled as $\theta_{LO} = \omega_0 t + \theta_{LO}(t) + \theta_0$, and ψ_i is the residual instrumental phase. The composite group delays (τ_i^R, τ_i^L) include the clock offset and the differential instrumental delays for each polarization. First order phase slopes in $B(\omega)$ are incorporated in these group delays. The recorded signals in (2.4) have an additive instrumental noise component associated with the detection and amplification of the signal. This term is assumed implicit in what follows in the interests of clarity.

The phase stability $\theta_{LO}(t)$ of the atomic frequency standards is discussed by Vessot (1976). This dictates the integration time that can be used in averaging the correlated signals before coherence losses become significant. For hydrogen masers coherence times of the order of several minutes are possible for observations at centimetre wavelengths.

The phase term $\omega(t - \tau_g)$ references the recorded signals to the Earth-centre arrival time of the wavefront and places each antenna in the same Lorentzian geocentric coordinate system. The geometric delay τ_{mg} at antenna m with respect to the direction $\mathbf{s}$ is,

$$\tau_{mg} = \mathbf{r}_m . \mathbf{s}$$

where $\mathbf{r}_m$ is the antenna vector in the geocentric coordinate system. The time-variable geometric delay implies a Doppler frequency offset $\nu_{dop} = \frac{\omega}{2\pi}\frac{\partial \tau_g}{\partial t}$ at each antenna.

2.1.6 Phase Ambiguity, Noise and Recorder Effects

The MK2 and MK3 recording systems are currently used in VLBI observations (Clark 1973; Whitney *et al.* 1976). The VLBA system (Kellermann and Thompson 1985) is expected to be in full operation in late 1992. The MK2 system is restricted to a maximum bandwidth of 2 MHz while the MK3 system offers increased total bandwidth and the flexibility of simultaneously recording multiple independent baseband signals. The latter property allows full spectral line polarization VLBI observations. Such observations can only be achieved in the MK2 system using polarization switching or the use of a network of mixed antenna polarizations (Garcia-Barreto *et al.* 1988) with the attendant logistical difficulties and reduced (u, v) coverage. Both recording systems use 1-bit sampling of the recorded baseband signal thus losing all total power information. The quantization scheme also affects the relation between the observed and actual cross-correlation and the sensitivity of the correlation measurement (TMS p.217).

The MK2 recorders have a fixed sampling rate of 4 MHz and use pre-averaging at the correlator to process smaller bandwidths. The MK3 system records at the Nyquist rate of $2\Delta\nu$ with a fixed 4 MHz playback rate at the correlator. The

correlator load is thus increased by a factor $\frac{2}{\Delta\nu_{MHz}}$ over the 4 MHz rate for a bandwidth $\Delta\nu < 2$ MHz. The increased correlator load causes difficulties for spectral line observations over smaller bandwidths.

The phase of the recorded signal is only known modulo 2π and the absolute residual phase resulting from propagation and instrumental effects at each VLBI antenna is also undetermined. The absence of total phase information introduces an ambiguity in the absolute source position unless the total phase can be reconstructed in post-processing (Alef 1989) which is only possible in specialised cases (Marcaide and Shapiro 1983). The phase uncertainty does not prevent the determination of source structure relative to an arbitrary position through the use of closure phase self-calibration techniques (Pearson and Readhead 1984).

Propagation and instrumental effects introduce noise in the amplitude and phase of the cross-correlations formed from the recorded signals. These quantities have a non-Gaussian distribution (TMS p.166) but in the strong signal case $\sigma_\phi \sim \frac{1}{SNR}$, where SNR is the amplitude signal to noise ratio of the correlated data.

2.2 Correlation

The correlator forms the complex cross-correlation function for each antenna pair after a correction $\Delta\tau$ for the expected differential geometric, atmospheric and clock delay offsets between the two stations. The complex cross-correlation function can be represented for each antenna pair (m, n) as,

$$r^{pq}_{mn}(u, v, \tau) = < S'^{p}_{m}(t) S'^{q*}_{n}(t + \Delta\tau - \tau) >$$

where $p, q \in [RCP, LCP]$ denotes the polarization state of the signal and (u, v) are defined in section 1.1. The reference station used in computing the differential delay defines the reference frequency and phase of the cross-correlation

function. The recorded time of the cross-correlation is the wavefront transit time at the reference station.

A residual term $\omega_0 \triangle\tau$ which arises from performing the delay correction at the intermediate frequency $(\omega - \omega_0)$ is removed by a process known as fringe rotation (Moran 1973). As the signals are infinitely clipped the delay correction is rounded to the nearest bit, thus introducing a time-variable fractional bit delay error. This and other corrections resulting from digital correlation are removed in part in the correlator and in part in the immediate post-processing as discussed for the MK3 system in Appendix A. The data are assumed corrected for these effects in what follows.

The Fourier transform of the cross-correlation function to angular frequency yields the cross-power spectrum,

$$r(u,v,\omega) = \int r(u,v,\tau) e^{-jw\tau}\, d\tau$$

The radio signal is to a good approximation spatially incoherent and stationary, satisfying the relation,

$$< E^p(\mathbf{s}_1,\omega_1) E^{q*}(\mathbf{s}_2,\omega_2) >= \delta(\mathbf{s}_1 - \mathbf{s}_2)\delta(\omega_1 - \omega_2) < E^p(\mathbf{s},\omega) E^{q*}(\mathbf{s},\omega) >$$

Integrating over the field of interest Ω at each antenna and exploiting the incoherence of the field, the residual terms in r^{pq}_{mn} for frequency ω can be factorised as,

$$r^{pq}_{mn}(u,v,\omega) = G^p_m\, G^{q*}_n \int\int_\Omega < S^p_m(\omega) S^{q*}_n(\omega) > e^{j\omega[\triangle\tau_g(\mathbf{s}) - \triangle\tau_g(\mathbf{s}_0)]}\, d\eta d\zeta$$

where $\triangle\tau_g(\mathrm{s}) = \tau_{mg}(\mathrm{s}) - \tau_{ng}(\mathrm{s})$ and $G_m^p = g_m^p B^p(\omega) e^{j\phi_m^p}$ is the complex instrumental gain for antenna m in polarization p, incorporating the residual differential terms from (2.4) remaining after correlation. For a field of limited angular extent a Fourier transform relation (TMS p.61) is recovered between $< S_m^p(\omega) S_n^{q*}(\omega) >$ and the cross-correlation function as,

$$r_{mn}^{pq}(u,v,\omega) = G_m^p G_n^{*q} \int\int_{\Omega} < S_m^p(\omega) S_n^{q*}(\omega) > e^{-j2\pi(\eta u + \zeta v)} \, d\eta d\zeta$$

The Stokes parameters of the incident radiation $(I,Q,U,V)(\eta,\zeta,\omega)$ in the circularly polarized basis (E^R, E^L) take the form (Conway and Kronberg 1969),

$$\begin{aligned}
< E^L E^{L*} > (\eta,\zeta,\omega) &= LL(\eta,\zeta,\omega) = I(\eta,\zeta,\omega) + V(\eta,\zeta,\omega) \\
< E^R E^{R*} > (\eta,\zeta,\omega) &= RR(\eta,\zeta,\omega) = I(\eta,\zeta,\omega) - V(\eta,\zeta,\omega) \\
< E^R E^{L*} > (\eta,\zeta,\omega) &= RL(\eta,\zeta,\omega) = Q(\eta,\zeta,\omega) + jU(\eta,\zeta,\omega) \\
< E^L E^{R*} > (\eta,\zeta,\omega) &= LR(\eta,\zeta,\omega) = Q(\eta,\zeta,\omega) - jU(\eta,\zeta,\omega)
\end{aligned}$$

The counterparts of the Stokes parameters in the visibility plane are,

$$\begin{aligned}
I(\eta,\zeta,\omega) \quad \mathcal{F} \quad \mathcal{I}(u,v,\omega) &= \frac{1}{2}[\mathcal{RR}(u,v,\omega) + \mathcal{LL}(u,v,\omega)] \\
V(\eta,\zeta,\omega) \quad \mathcal{F} \quad \mathcal{V}(u,v,\omega) &= \frac{1}{2}[\mathcal{RR}(u,v,\omega) - \mathcal{LL}(u,v,\omega)] \\
Q(\eta,\zeta,\omega) \quad \mathcal{F} \quad \mathcal{Q}(u,v,\omega) &= \frac{1}{2}[\mathcal{RL}(u,v,\omega) + \mathcal{LR}(u,v,\omega)] \\
U(\eta,\zeta,\omega) \quad \mathcal{F} \quad \mathcal{U}(u,v,\omega) &= \frac{1}{2}j[\mathcal{LR}(u,v,\omega) - \mathcal{RL}(u,v,\omega)]
\end{aligned} \tag{2.5}$$

where $\mathcal{F}$ denotes Fourier transformation and the Fourier or visibility counterparts of $\{RR, LL, RL, LR\}(\eta,\zeta,\omega)$ are denoted by $\{\mathcal{RR}, \mathcal{LL}, \mathcal{RL}, \mathcal{LR}\}(u,v,\omega)$. Expanding $< S_m^p(\omega) S_n^{q*}(\omega) >$ using the relation (2.3) yields,

$$
\begin{aligned}
r^{RR}_{mn}(u,v,\omega) &= (G^R_m\, G^{R*}_n)[(\mathcal{RR})e^{-j(\alpha_m-\alpha_n)} + (\mathcal{RL})D^{R*}_n\, e^{-j(\alpha_m+\alpha_n)}e^{j\gamma^{R-L}_n} \\
&\quad + (\mathcal{LR})D^R_m\, e^{j(\alpha_m+\alpha_n)}e^{j\gamma^{L-R}_m} + (\mathcal{LL})D^R_m\, D^{R*}_n\, e^{j(\alpha_m-\alpha_n)}e^{j(\gamma^{L-R}_m-\gamma^{L-R}_n)}] \\
r^{LL}_{mn}(u,v,\omega) &= (G^L_m\, G^{L*}_n)[(\mathcal{LL})e^{j(\alpha_m-\alpha_n)} + (\mathcal{LR})D^{L*}_n\, e^{j(\alpha_m+\alpha_n)}e^{j\gamma^{L-R}_n} \\
&\quad + (\mathcal{RL})D^L_m\, e^{-j(\alpha_m+\alpha_n)}e^{j\gamma^{R-L}_m} + (\mathcal{RR})D^L_m\, D^{L*}_n\, e^{-j(\alpha_m-\alpha_n)}e^{j(\gamma^{R-L}_m-\gamma^{R-L}_n)}] \\
r^{RL}_{mn}(u,v,\omega) &= (G^R_m\, G^{L*}_n)[(\mathcal{RL})e^{-j(\alpha_m+\alpha_n)} + (\mathcal{RR})D^{L*}_n\, e^{-j(\alpha_m-\alpha_n)}e^{j\gamma^{L-R}_n} \\
&\quad + (\mathcal{LL})D^R_m\, e^{j(\alpha_m-\alpha_n)}e^{j\gamma^{L-R}_m} + (\mathcal{LR})D^R_m\, D^{L*}_n\, e^{j(\alpha_m+\alpha_n)}e^{j(\gamma^{L-R}_m-\gamma^{R-L}_n)}] \\
r^{LR}_{mn}(u,v,\omega) &= (G^L_m\, G^{R*}_n)[(\mathcal{LR})e^{j(\alpha_m+\alpha_n)} + (\mathcal{LL})D^{R*}_n\, e^{j(\alpha_m-\alpha_n)}e^{j\gamma^{R-L}_n} \\
&\quad + (\mathcal{RR})D^L_m\, e^{-j(\alpha_m-\alpha_n)}e^{j\gamma^{R-L}_m} + (\mathcal{RL})D^L_m\, D^{R*}_n\, e^{-j(\alpha_m+\alpha_n)}e^{j(\gamma^{R-L}_m-\gamma^{L-R}_n)}]
\end{aligned}
\tag{2.6}
$$

2.3 Imaging

The techniques for determining the antenna gains G^p_j and feed calibration D-terms are discussed in Chapter 3. The calibrated cross-power spectra allow a determination of $\{\mathcal{RR},\mathcal{LL},\mathcal{RL},\mathcal{LR}\}$ and hence the visibility Stokes parameters $\{\mathcal{I},\mathcal{V},\mathcal{Q},\mathcal{U}\}$. The residual antenna phases are determined simultaneously in the final imaging using iterative self-calibration techniques (Wilkinson 1989). The imaging relation can be expressed in simplified form, here illustrated for total intensity I, after Sramek and Schwab (1986) as,

$$
\begin{aligned}
&[\mathcal{I}(u,v,\omega)+\mathcal{N}(u,v,\omega)]\sum_m \delta(u-u_m, v-v_m) \\
&\quad +[\mathcal{I}^*(u,v,\omega)+\mathcal{N}^*(u,v,\omega)]\sum_m \delta(u+u_m, v+v_m) \\
&\qquad \mathcal{F} \quad B_{\mathcal{I}}(\eta,\zeta,\omega)\star[I(\eta,\zeta,\omega)+N(\eta,\zeta,\omega)]
\end{aligned}
$$

where $\delta(u,v)$ is the Dirac delta function and $\mathcal{N}(u,v,\omega)$ denotes additive noise in the (u,v) plane. The transform of the sampling function to the image plane

is the so-called dirty beam $B_{\mathcal{I}}(\eta,\zeta,\omega)$. The $\star$ is used to denote convolution in the image plane (η,ζ) and $N(\eta,\zeta,\omega)$ is the Fourier counterpoint of $\mathcal{N}(u,v,\omega)$. This relation holds for all members of the set $(\mathcal{I},\mathcal{V},\mathcal{Q},\mathcal{U})$. All are Hermitian in the (u,v) plane and real in the image plane although only I is constrained to be positive. The (u,v) sampling is generally poor and non-linear deconvolution techniques such as CLEAN (Högbom 1974) are required to remove the effects of the dirty beam in the image plane.

It is useful to define the complex linear polarization in the image plane in terms of the quantity (Conway and Kronberg 1969),

$$P(\eta,\zeta,\omega) = Q(\eta,\zeta,\omega) + jU(\eta,\zeta,\omega) \tag{2.7}$$

which will be used later.

CHAPTER 3: DATA REDUCTION TECHNIQUES

Introduction

This chapter is concerned with data reduction techniques that can be used to remove the instrumental effects discussed in Chapter 2. The success of polarization VLBI experiments is heavily constrained by the degree to which these effects are determined and removed.

Existing data reduction techniques are discussed where necessary, as well as the extensions developed for the calibration and reduction of spectral line polarization VLBI observations. Data reduction techniques for single polarization spectral line VLBI data are discussed by Reid *et al.* (1980) and Diamond (1989). Partial spectral line polarization calibration of VLBI data was performed by Garcia-Barretto *et al.* (1988), and a review of calibration methods for continuum polarization VLBI data can be found in Cotton (1989).

The development and evaluation of techniques for reducing spectral line polarization VLBI data has been undertaken by the author within the Astronomical Image Processing System (AIPS) maintained by the National Radio Astronomy Observatory (NRAO). All post-correlation data reduction was performed within this system, including fringe-fitting. Several new AIPS tasks were developed in the course of this work and the specific software analysis path is discussed later in the chapter.

The AIPS system allows antenna-based calibration and the formalism of this method is adopted throughout the discussion.

3.1 Correlator Effects

The first step in the data reduction is the removal of several digital signal processing effects which result from the digital sampling and correlation of the recorded signals. The following corrections are applied to the data immediately after correlation.

In both the MK2 and MK3 systems the recorded signals are infinitely clipped thus losing all total power information. The measured cross-correlation coefficients ρ_c derived from the clipped data are related to the true correlation ρ by the Van Vleck relation (Van Vleck and Middleton 1966),

$$\rho = \sin(\frac{\pi}{2}\rho_c)$$

Autocorrelation data are further affected by clipper bias and the full Van Vleck relation, which is usually approximated in this case, is discussed by Davis (1974). The cross-correlation data are transformed to cross-power spectra and the autocorrelation functions to normalised autocorrelation spectra. The cross-power data are corrected for the residual fractional bit-shift error. In forming the cross-power and total power spectra, Hanning smoothing may be applied. A composite amplitude correction is applied to the spectra to correct for known digital losses within the correlator. The cross-power spectra are denoted by $r_{mn}(\omega, t_k)$, where (m, n) specifies the baseline antenna pair and t_k the centre time of the correlator accumulation period. Similarly the autocorrelation spectra are denoted by $r_{mm}(\omega, t_k)$. The dependence on t_k or equivalently (u_k, v_k) will be assumed implicit in the remainder of the chapter.

The MK2 correlator is described by Clark (1973) and the MK3 system by Whitney *et al.* (1976). Further details of the MK3 correlator corrections and the importing of MK3 data into AIPS can be found in Appendix A.

3.2 Bandpass Correction

The amplitude response of the composite bandpass can be derived from auto-correlation data alone and this approach has traditionally been used (Reid *et al.* 1980). This technique is limited if the video filters suffer from aliasing or if the phase response of the filter contains second order terms as a function of frequency. These conditions often afflict spectral line VLBI data, particularly when a narrow video bandwidth is used. An aliased signal $A(\omega)e^{j\omega t}$ sampled at the Nyquist rate $4\pi\omega_B$ and recorded in the upper sideband with bandpass response $B(\omega)$ extending to $\omega_B + \delta\omega_B$ can be represented as,

$$E(t) = \int_0^{\omega_B} B(\omega)A(\omega)e^{j\omega t}\ d\omega + \int_{\omega_B - \delta\omega_B}^{\omega_B} B^*(2\omega_B - \omega)A^*(2\omega_B - \omega)e^{j\omega t}\ d\omega$$

The cross-correlation $< E_1(t)E_2^*(t) >$ of two such signals is insensitive to the aliased power as the radio noise is stationary (Freeman 1958) and,

$$< A(\omega)A^*(\omega') >= \delta(\omega - \omega') < A(\omega)A^*(\omega) >$$

The aliased noise power appears however in the autocorrelation bandpass response and is appropriate for correcting the autocorrelation data.

The problems of aliasing and non-linear phase response can be overcome by determining a full complex composite bandpass response using the cross-power spectra for the continuum calibrators. This facility exists within AIPS and was found to be important for spectral line polarization VLBI data reduction. The data are pre-averaged after the removal of residual phase slopes in time and frequency (section 3.5.2) and an antenna-based simultaneous fit for each channel is performed which minimises,

$$\chi^2 = \sum_{m=1}^{N_a} \sum_{n=m+1}^{N_a} \sum_{l=1}^{N_c} ||r^{pp}_{mn}(\omega_l) - B^p_m(\omega_l) B^{p*}_n(\omega_l)||$$

where N_a is the number of antennas, N_c is the number of frequency channels, $r^{pp}_{mn}(\omega_l)$ is the pre-averaged parallel-hand calibrator cross-power spectrum at frequency ω_l for the baseline $(m-n)$ and $B^p_m(\omega_l)$ is the complex bandpass response at antenna m for polarization p as a function of frequency. The norm of the complex residual is denoted by $||\ \ ||$. The bandpasses are determined independently for each hand of polarization in spectral line polarization VLBI data reduction.

The complex bandpasses so determined are heavily smoothed using Hanning smoothing to prevent the introduction of systematic effects and are normalised over the band. Due to the prior removal of group delays the phase response contains only second order terms (Fig. 4.1). The solutions are antenna-based and the phase response of the reference antenna is consequently set to zero.

The cross-correlation data are corrected as,

$$r^{pq'}_{mn} = \frac{r^{pq}_{mn}(\omega)}{\sqrt{B^p_m(\omega) B^{q*}_n(\omega)}} \qquad 3.1$$

and the autocorrelation data as,

$$r^{pp'}_{mm} = \frac{r^{pp}_{mm}(\omega) - B^p_m(\omega)}{B^p_m(\omega)} \qquad 3.2$$

3.3 LSR Velocity Correction

As described in section (2.1.5) Earth rotation introduces a diurnal Doppler shift in the observed frequency band at each antenna. The effects of this shift are not generally removed during the course of the observations using frequency tracking due to the possibility of logistical or operator error. These corrections are

done offline. If the total velocity at antenna m with respect to the local standard of rest in the direction of the source at time t is,

$$V_{tot}(t) = V_{obs} + V_{dop}(t)$$

where V_{obs} is the desired line velocity and V_{dop} is the Doppler shift, then the spectrum needs to be shifted by,

$$\delta\nu = \nu_{obs} - \frac{\nu_0}{1 + \frac{V_{tot}(t)}{c}}$$

in the optical definition, where ν_{obs} is the observed frequency, ν_0 is the line rest frequency and c is the speed of light. In the radio definition $\delta\nu = \nu_{obs} - \nu_0(1 - \frac{V_{tot}(t)}{c})$.

This shift is accomplished by transforming the spectra to lag space and applying a phase slope across the band before transforming back to frequency (Reid *et al.* 1980) and this facility has been incorporated within AIPS by P. Diamond. In the case of the cross-power spectra the differential frequency shift is calculated with respect to the reference antenna which is fringe-rotated at the correlator. This convention differs between the MK2 and MK3 systems. The former rotates station B on each baseline and the latter station A.

3.4 Amplitude Calibration

The basic technique for determining the amplitude gains of the antennas in spectral line VLBI data reduction is discussed by Walker (1977), Reid *et al.* (1980) and Diamond (1989).

To calibrate the cross-power spectra in terms of correlated flux density requires an independent measure of the total power in each recorded signal before clipping occurs. After applying the Van Vleck correction and the bandpass correction the

correlated flux density can then be determined by multiplying by the geometric mean of the power in each signal,

$$S_{mn}(\omega) = b\sqrt{P_m(\bar{T}_{am} + T_{sm})P_n(\bar{T}_{an} + T_{sn})}\, r'_{mn}(\omega) \qquad 3.3$$

where P_m is the point source sensitivity of antenna m (in Jy/K), T_{sm} is the off-source system temperature and $\bar{T}_{am} = \frac{1}{\delta\omega}\int_0^{\delta\omega} B_m(\omega)T_m(\omega)d\omega$ is the averaged antenna temperature across the band due to the source emission. Residual, unmodelled correlation losses are included in the factor b.

In the case of autocorrelation data the total antenna temperature measured on the source is,

$$T_{on}(\omega) = B(\omega)T(\omega) + T_s B(\omega)$$

The normalised autocorrelation spectrum produced by the correlator is $r(\omega) = \frac{1}{\beta}T_{on}(\omega)$, where $\beta = \bar{T}_a + T_s$. In units of flux density,

$$S(\omega) = PT(\omega) = P(\bar{T}_a + T_s)r'(\omega) + P\bar{T}_a$$

Thus,

$$r'(\omega) = \frac{1}{P(\bar{T}_a + T_s)}S(\omega) - \frac{\bar{T}_a}{\bar{T}_a + T_s}$$

where $r'(\omega)$ is the bandpass corrected autocorrelation spectrum defined by (3.2). If a good template spectrum at high elevation $r'_{ref}(\omega)$ is well-determined at a reference antenna the cross-power gains $g_m = \frac{1}{\sqrt{P_m(\bar{T}_{am}+T_{sm})}}$ can be determined relative to this antenna by minimising,

$$\chi^2 = \sum_{\omega=\omega_1}^{\omega_2}\left[[(r'_{mm}(\omega) - g_m^2 r'_{ref}(\omega)]^2 + \alpha_0 + \sum_{k=1}^{n_p}\alpha_k\omega^k\right]$$

The polynomial term of order n_p is included to account for imperfect bandpass removal and includes the offset term $\alpha_0 = -\frac{\bar{T}_{am}}{\bar{T}_a + T_s}$, which can be used to estimate $\bar{T}_a$ if it is not known a priori. The parameter $\bar{T}_a$ can also be estimated by direct numerical integration of the line profile $\frac{1}{\delta\omega}\int_0^{\delta\omega} B_m(\omega)T_m(\omega)d\omega$. The coefficients α_k and g_m are estimated simultaneously in the fit over the frequency range (ω_1, ω_2) using standard linear least squares minimisation. The baseline-independent method developed here was found to be more robust than the traditional technique (Walker 1977) which requires an independent removal of residual baselines in the source and template spectra. In the case of spectral line observations over a narrow bandwidth it is often difficult to unambiguously identify and remove the residual baseline, which may introduce systematic errors in the fit or bias in the estimated gains. In addition, the effects of imperfect bandpass removal are usually time-variable due to the Doppler drift of the edge frequency of the source spectrum through the receiver bandpass.

Amplitude calibration using autocorrelation spectra is insensitive to source structure unlike standard continuum calibration techniques (Walker 1986), which use equation (3.3) for an unresolved source. In this case $T_a << T_s$ and,

$$\bar{S}_{mn} = b\sqrt{\overline{P_m T_{sm} P_n T_{sn}}}\ \bar{r}'_{mn}$$

where a bar denotes averaging over frequency. The ratio ξ of continuum cross-correlation and source autocorrelation amplitude gains relative to the reference antenna is therefore,

$$\xi = \sqrt{\frac{1+\kappa_m}{1+\kappa_{ref}}} \qquad 3.4$$

where $\kappa_m = \frac{\bar{T}_{am}}{T_{sm}}$. This ratio can be used to determine $\bar{T}_{am}$ if it is not known directly.

Autocorrelation gain factors do not model local oscillator coherence losses which are included in the residual b-factor in equation (3.3). This may be important at high frequencies. Severe satellite interference may complicate the use of autocorrelation gain fitting particularly for observations near 1612 MHz.

The absolute flux density scale is established by multiplying the gain correction curves $g_m^{-1}(t_k)$ by the calibrated flux density $P_{ref}(\bar{T}_a + T_s)_{ref}$ measured for the template scan. The method is thus less sensitive to individual system temperature measurements taken at each VLBI antenna throughout the run. For narrow bandwidth observations if the system temperature is not measured in the final video bandwidth an independent estimate of $\bar{T}_a$ is required.

In spectral line polarization VLBI the gain correction curves are determined separately for each hand of polarization using independent template spectra usually taken during the same reference scan. A uniform flux density scale is established by correcting for the differential polarization gain g_0^{R-L} of the reference antenna. To first order this is constant over the duration of typical VLBI observations. The differential gain at each antenna g_m^{R-L} can be estimated by a global minimisation of,

$$\chi^2 = \sum_{t_k} \sum_{m=1}^{N_a} \sum_{n=m+1}^{N_a} \left[\frac{g_m^{R-L} g_n^{R-L} |\bar{r}'^{LL}_{mn}(t_k)| - |\bar{r}'^{RR}_{mn}(t_k)|}{|\bar{r}'^{RR}_{mn}(t_k)| + g_m^{R-L} g_n^{R-L} |\bar{r}'^{LL}_{mn}(t_k)|} \right]^2 \qquad 3.5$$

where $|\bar{r}'^{RR}_{mn}(t_k)|$ is the amplitude of the continuum calibrator cross-power spectra coherently averaged over time and frequency after bandpass correction (3.1) and the removal of residual fringe rates and group delays (section 3.5.2)

3.5 Phase Calibration

Phase calibration involves determining and removing the instrumental and propagation phase terms contained in equation (2.4). An antenna-based factorization of residual complex antenna gains is used here. The complex gain for antenna

m in polarization p will be denoted by $G_m^p(\omega,t) = g_m^p(t)e^{j\phi_m^p(\omega,t)}$, where $g_m^p(t)$ is the amplitude gain discussed in the previous section and the data are considered already corrected for the complex bandpass response. The antenna phase $\phi_m(\omega,t)$ is approximated over short time intervals by linear slopes in time and frequency, defined respectively by the residual fringe rate and residual group delay,

$$\phi_m(\omega,t) = (\omega-\omega_0)(\tau_m - \tau_0) + (\dot{\phi}_m - \dot{\phi}_0)(t-t_0) + (\phi_m - \phi_0) \qquad 3.6$$

where ω_0 is the edge frequency of the band (assumed USB), τ_m is the residual group delay at antenna m, $\dot{\phi}_m$ is the residual fringe rate and ϕ_m is the residual phase. These quantities are referred to a reference antenna (subscript zero) and a reference time (t_0). This formalism will be used in the discussion below. The time interval used in (3.6) needs to be chosen for sufficient signal-to-noise ratio without violating the piece-wise linear phase approximation. A distinction is made here between the complex antenna gain $G_m^p(\omega,t)$ and the antenna gain correction $[G_m^p(\omega,t)]^{-1} = \frac{1}{g_m^p}e^{-j\phi_m^p(\omega,t)}$.

3.5.1 Parallactic Angle

The parallactic angle (2.2) is a known instrumental effect and is removed as the first step in the phase calibration by rotating the phase gain of each antenna, including the reference antenna, by,

$$G_m^{p'} = G_m^p\, e^{j s^p \alpha_m(t)} \qquad 3.7$$

where $\{s^{RCP} = -1, \quad s^{LCP} = +1\}$. This correction is zero for equatorially mounted antennas. If the parallactic angle is not removed as the first step in the polarization phase calibration, terms of the form $e^{j(\alpha_m - \alpha_0)}$ are carried forward in the analysis and complicate the smoothing of the calibration tables, which are then difficult to re-reference to a new reference antenna.

3.5.2 Fringe-fitting

The residual antenna phase $\phi_m(\omega, t)$ as given in equation (3.6) arises from errors in the correlator model and uncorrelated variations in the ionosphere, atmosphere and receiving electronics at each station (2.4). The resultant time-variable instrumental phase in the cross-power spectra is totally uncertain. The estimation of the residual fringe rate and delay in the cross-power data is known as fringe-fitting, and the purpose of fringe-fitting is to reduce the phase slopes in time and frequency sufficiently to allow the data to be coherently averaged. An antenna-based formalism allows global fringe-fitting using baselines where the source is well detected to improve the fringe-fitting of baselines with low signal-to-noise ratio (Schwab and Cotton 1983; Alef and Porcas 1986). This is not possible using baseline-based phase correction. The antenna-based formalism forces compliance with the phase closure relations (Rogers *et al.* 1974) which form the basis of self-calibration imaging. If the cross-power phase on baseline $(m - n)$ is modelled as $\Phi_{mn} = \vartheta_{mn} + (\phi_m - \phi_n)$, where ϑ_{mn} is the source structure phase at this (u, v) separation then the sum of cross-power phases and their derivatives about a closed triangle contains no instrumental or propagation effects,

$$\begin{aligned}
\Phi_{12} + \Phi_{23} - \Phi_{13} &= \vartheta_{12} + \vartheta_{23} - \vartheta_{13} \\
\dot{\Phi}_{12} + \dot{\Phi}_{23} - \dot{\Phi}_{13} &= \dot{\vartheta}_{12} + \dot{\vartheta}_{23} - \dot{\vartheta}_{13} \\
\frac{\partial \Phi_{12}}{\partial \omega} + \frac{\partial \Phi_{23}}{\partial \omega} - \frac{\partial \Phi_{13}}{\partial \omega} &= \frac{\partial \vartheta_{12}}{\partial \omega} + \frac{\partial \vartheta_{23}}{\partial \omega} - \frac{\partial \vartheta_{13}}{\partial \omega}
\end{aligned} \tag{3.8}$$

Global fringe-fitting requires an a priori model for the source structure phase ϑ_{mn}, which does not factorize uniquely in an antenna-based formalism except for linear phase slopes in u or v. The phase centre of the corrected data is located near the centroid of the emission and absolute position information is lost. Errors in

the fringe-fitting source model ϑ_{mn} are reflected in residual antenna phase errors $\varpi(t)$, later determined using self-calibration imaging.

In spectral line VLBI the residual group delays $\tau_m = \frac{\partial \phi_m}{\partial \omega}$ are determined from the continuum calibrator cross-power spectra. The measured delays $\tau_m(t_k)$ are smoothed over time and interpolated throughout the VLBI observations. The remaining instrumental phase corrections have a weak dependence on frequency across the band and the entire cross-power spectrum can be calibrated if the phase calibration is known for a given reference channel (Reid *et al.* 1980). As preparation for self-calibration imaging, residual fringe-rate phase solutions $(\dot{\phi}, \phi)$ are determined for a reference channel in the spectrum $r_{mn}(\omega_c)$ using global fringe-fitting. As these solutions are derived for the program source, interpolation thoughout the course of the VLBI observing run is considerably simplified.

3.5.3 Self-calibration

Removal of residual rates and delays allows the data to be averaged to improve the SNR but the residual antenna gain phase $\varpi_m(t)$ remains unknown. This precludes direct Fourier transform imaging which is possible at some level with connected-element interferometry.

Self-calibration is a technique whereby the source structure and residual antenna gains are estimated simultaneously in an iterative procedure. This minimises the sum (Wilkinson 1989),

$$\chi^2 = \sum_k \sum_{m=1}^{N_a} \sum_{n=m+1}^{N_a} a_{mn}(t_k)[r_{mn}(u_k, v_k, \omega_c) - d_m(t_k) d_n^*(t_k) \hat{r}_{mn}(u_k, v_k)]^2$$

where a_{mn} are weights, $r_{mn}(\omega_c, t_k)$ are the source visibilities at the reference channel frequency ω_c after fringe-fitting and amplitude calibration, $d_m(t_k) = |d_m(t_k)| e^{j\varpi_m(t_k)}$ are the residual antenna gains and $\hat{r}_{mn}(u_k, v_k)$ is the Fourier

transform of the trial source model in the image plane. The source model and antenna phase gains are varied iteratively in the fit (Pearson and Readhead 1984). The amplitude gain factors $|d_m(t_k)|$ may additionally be varied if the problem is well constrained. The technique requires an image deconvolution method such as CLEAN (Högbom 1974) or the Maximum Entropy Method (MEM, Narayan and Nityananda 1986) to remove the effects of poor sampling in the (u, v) plane. Self-calibration works best in the limit of a large number of antennas and simple source structure. In spectral line VLBI the reference frequency ω_c is chosen to satisfy the latter constraint as far as possible.

As self-calibration employs antenna-based gain corrections the closure phase relations (3.8) are automatically satisfied. The residual gain phases determined from self-calibration are added to the fringe phases (3.6) to derive the final phase calibration model.

The requirement of dual-polarization and MK3 capability limits the number of antennas in networks such as the European VLBI Network (EVN) that can participate in spectral line polarization observations. The resulting network is usually not well matched in sensitivity or (u, v) coverage. Inadequate frequency resolution may also ensure that there is no point-source reference channel due to spectral blending. At VLBI resolution, maser images typically consist of several compact components which may be spread over a relatively large field of view with respect to the synthesised beamwidth. For N antennas the ratio of visibility constraints to unknown self-calibration gains is $\frac{N-2}{2}$ (Cornwell 1986), which severely limits the quality of images obtained for small N. In particular, it may be difficult to obtain a satisfactory fit to the short baselines due to the limited sensitivity to extended emission. In addition, starting from a point-source model, the phase of the corrected visibilities is biased towards zero thus inducing false symmetrization in the image plane (Cornwell 1986; Linfield 1986). This is usually reduced by the

judicious application of constraints of positivity and compactness in the image plane (Wilkinson 1989), arguably at the cost of reproducibility.

An AIPS procedure VLB, derived from the procedure MAPIT written by G. Langston for mapping data from the Very Large Array, was developed with the aim of increasing the robustness of the reference channel imaging of spectral line sources using small antenna networks. This approach was possible partly due to the increase in high-speed computing power available to single users within AIPS (Bridle and Nance 1991) and exploits the fact that many systematic effects discussed above are reduced over a large number of self-calibration iterations (~ 30), although the convergence may be slow. Traditional VLBI self-calibration imaging techniques were used. The outer (u, v) plane received lower weighting and the antenna weights were set to $\frac{1}{\sqrt{P_m T_{s\,m}}}$. The starting model was chosen to be a point-source and an L1 solution was performed for the gain phases, keeping the amplitude fixed. A non-progressive self-calibration method was used i.e. the phase solution was always determined using the original (u, v) data set. Positive CLEAN components were used during the initial iterations, thereafter the number of CLEAN components was increased linearly to include negative CLEAN components. The solution interval was decreased linearly over the first ten iterations by an order of magnitude and then held constant.

The fit was assessed by comparing the closure-phase and amplitude plots of the model and original (u, v) data for the reference channel and other frequency channels after applying the phase solution to the data cube. A poor fit in the reference channel is indicated by systematic errors in other channels such as corrugations and sidelobes. Spurious symmetrization is best removed by the application of image plane constraints in the form of CLEAN boxes. The false, symmetrized components can be identified by their steady, albeit slow, decline in flux density as a function of iteration (Fig. 3.1). Alternatively, a phase solution derived from a

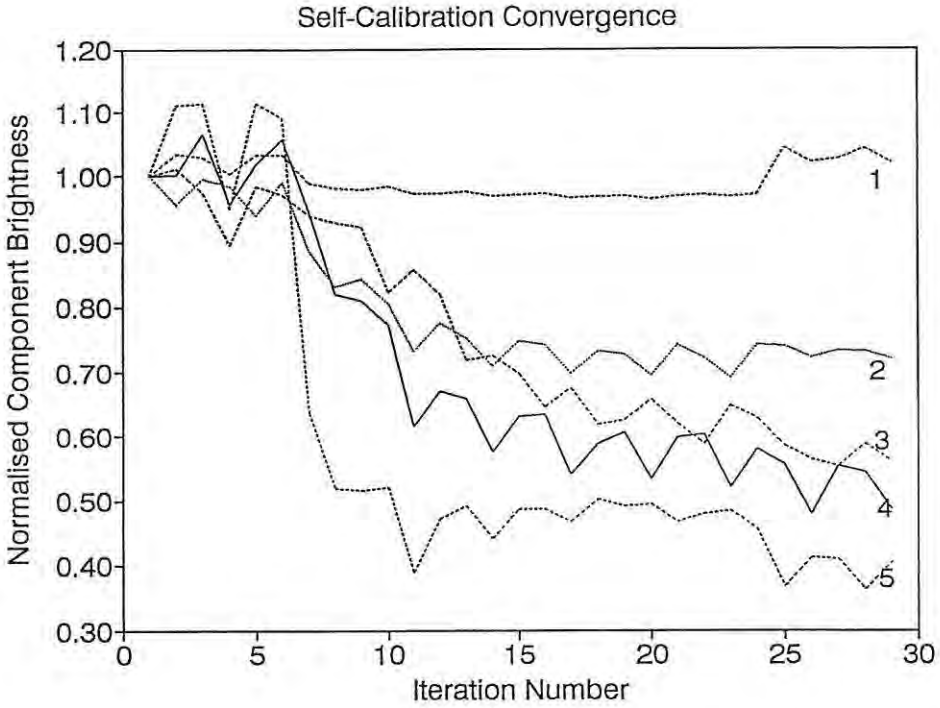

Fig. 3.1. The convergence of the AIPS self-calibration task VLB in trial imaging of a left-circularly polarized reference channel for the MK3 data set discussed in Chapter 5. The peak apparent brightness is plotted for five components, normalized to unity after the first iteration for clarity. This plot suggests that components 4 and 5 may be spurious although convergence is slow due to the limited network of five antennas. No CLEAN boxes were used as constraints in the (u, v) plane.

secondary channel applied to the reference channel may remove the symmetrized components if the source structure in the two channels is significantly different. The corrupted antenna gains that produce false symmetrization in one channel will not add coherently to induce symmetrization when acting on a different set of visibilities in another channel.

3.5.4 Spectral Line Polarization Phase Calibration

Spectral line polarization VLBI data reduction requires the determination of antenna phase gain terms $\phi_m^p(\omega,t)$ for each hand of polarization $p \in \{RCP, LCP\}$ that are aligned in the same phase frame. The residual group delays $\tau_m^p(t_k)$ are determined as before from the continuum calibrator scans but polarization fringe-fitting introduces several refinements.

In polarization VLBI the values of the crossed-polarization correlation pairs are a small fraction of the parallel-hand correlations if the linear polarization of the source is small, which is usually the case. The crossed-hand fringes are therefore difficult to detect if fringe-fitting in a baseline-based formalism. This problem can be ameliorated by using the parallel-hand fringes to predict the position of the crossed-hand fringes in $(\tau, \dot{\phi})$ space (Brown, Roberts and Wardle 1989) but global antenna-based fringe-fitting is more versatile. The antenna-based delay corrections are determined independently for each hand of circular polarization using only the parallel-hand data and the full sensitivity of global fringe-fitting is available with this technique. The independent delay solutions $\phi_m^p(\omega,t) = (\tau_m^p - \tau_0^p)(\omega - \omega_0)$ can be registered in the same phase frame by correcting for the R-L delay difference at the reference antenna $\delta\tau_0^{R-L}$,

$$\begin{aligned} \phi_m^L(\omega,t) &= (\tau_m^L - \tau_o^L)(\omega - \omega_0) \\ \phi_m^R(\omega,t) &= (\tau_m^R - \tau_o^R + \delta\tau_0^{R-L})(\omega - \omega_0) \end{aligned} \qquad 3.9$$

Both solutions have the same reference antenna and reference antenna polarization. It is assumed here that the continuum calibrators have no net circular polarization. The delay correction is applied and the fringe rate and phase calibration (including self-calibration) determined for a reference frequency channel

in one sense of polarization. This fringe-rate phase solution can be applied to the orthogonal polarization while retaining positional coincidence by correcting for the polarization fringe-rate and phase differences at each antenna $\delta\dot{\phi}_m^{R-L}, \delta\phi_m^{R-L}$. The total phase solution is therefore constructed as,

$$\begin{aligned}
\phi_m^L(\omega,t) &= (\tau_m^L - \tau_0^L)(\omega-\omega_0) + (\dot{\phi}_m^L - \dot{\phi}_0^L)(t-t_0) + (\phi_m^L - \phi_0^L) \\
\phi_m^R(\omega,t) &= (\tau_m^R - \tau_0^R + \delta\tau_0^{R-L})(\omega-\omega_0) + (\dot{\phi}_m^L - \dot{\phi}_0^L + \delta\dot{\phi}_m^{R-L})(t-t_0) \\
&\quad + (\phi_m^L - \phi_0^L + \delta\phi_m^{R-L}) \qquad 3.10
\end{aligned}$$

where,

$$\begin{aligned}
\delta\tau_m^{R-L} &= \tau_m^R - \tau_m^L \\
\delta\dot{\phi}_m^{R-L} &= \dot{\phi}_m^R - \dot{\phi}_m^L \\
\delta\phi_m^{R-L} &= \phi_m^R - \phi_m^L
\end{aligned}$$

In contrast, in continuum polarization VLBI the fringe-rate phase solutions can be determined independently for each polarization in the usual absence of net circular polarization in the continuum program source. This requires a correction for the differential fringe-rate and phase at the reference antenna alone (Cotton 1989). Polarization VLBI observation of continuum sources, or sources without appreciable circular polarization, is less complicated than that of circularly polarized sources commonly observed in spectral line VLBI. For the former sources, self-calibration in the RR and LL data can be performed using the same Stokes I image, thus ensuring positional coincidence in the two polarizations.

The delay offset $\delta\tau_0^{R-L}$ is the difference between the antenna-based delays for the right- and left-circular polarizations at the reference antenna. This can be determined from the baseline-based cross-hand delays $\tau_{mn}^{RL} = \frac{\partial\Phi_{mn}^{RL}}{\partial\omega}$ and $\tau_{mn}^{LR} =$

$\frac{\partial \Phi_{mn}^{LR}}{\partial \omega}$ which are directly estimated from the phase slopes across the cross-power spectra of the continuum calibrators using the relations (Brown, Roberts and Wardle 1989),

$$\begin{aligned}
\delta\tau_m^{R-L} &= \tau_{mn}^{RL} - \tau_{mn}^{LL} \\
\delta\tau_m^{R-L} &= \tau_{mn}^{RR} - \tau_{mn}^{LR} \\
\delta\tau_n^{R-L} &= \tau_{mn}^{RL} - \tau_{mn}^{RR} \\
\delta\tau_n^{R-L} &= \tau_{mn}^{LL} - \tau_{mn}^{LR}
\end{aligned} \qquad 3.11$$

The delay offset $\delta\tau_0^{R-L}$ is expected to be stable over the duration of a typical VLBI observation and can thus be determined from a single continuum scan where the cross-hand fringes are well-detected. The instrumental delay offset $\delta\tau_i^{R-L}$ (2.4) includes differences in cable length and video filter response in the differing electrical paths for each polarization at the reference antenna. The maximum delay offset due to ionospheric Faraday rotation $\mathcal{L}_g^{R-L}$ is $\sim -0.3 f_{GHz}^{-3}$ ns, obtained by extrapolating the results of Evans and Hagfors (1968) at 100 MHz. The phase change across a band $\delta\omega$ is $\delta\phi = \delta\omega\mathcal{L}_g^{R-L}$. For the OH line at 1612 MHz $\mathcal{L}_g^{R-L} \sim 40$ ps and $\delta\phi \sim 0.5$ milliradians across 2 MHz. These values are clearly negligible for the small video bandwidths used in spectral line VLBI observations. The estimate of $\mathcal{L}_g^{R-L}$ follows the method of Brown, Wardle and Roberts (1989) but differs slightly in the result.

Astrometric and geodetic VLBI requires a correction for the total ionospheric excess path delay $\mathcal{L}_g$ at each antenna due to the total electron content (TEC) along the line of sight. This can be estimated using either simultaneous observations at two frequencies, satellite Faraday rotation measurements, GPS ionospheric measurements or other ionosonde measurements (Gwinn 1984; Cotton 1989). In

spectral line polarization VLBI the total excess phase delay $\mathcal{L}_p$ and group delay $\mathcal{L}_g$ are removed as part of the reference polarization phase solution. The differential ionospheric Faraday rotation corrections $\mathcal{L}_g^{R-L}$ and $\mathcal{L}_p^{R-L}$ however do need to be determined. Ionospheric modelling (Chiu 1975) can be used if the total electron content cannot be estimated using the methods discussed above.

The fringe-rate offset $\dot{\phi}_0^{R-L}$ due to instrumental effects is expected to be negligible over periods in which the phase linearization (3.6) holds, due to the required phase stability in VLBI electronics. This was confirmed for the MK3 polarization observations reduced as part of this work. The effect of the atmosphere, clocks and geometric errors in the correlator model are polarization independent and can thus be ignored. The maximum fringe-rate offset $\dot{\mathcal{L}}_p^{R-L}$ due to ionospheric Faraday rotation can be estimated by assuming the change of $\dot{\mathcal{L}}_p^{R-L} \sim 0.15 f_{GHz}^{-3}$ discussed above occurs over the extreme case of one hour (Brown, Roberts and Wardle 1989). This leads to the relation $\dot{\mathcal{L}}_p^{R-L} \sim 40 f_{GHz}^{-2}\,\mu$Hz. At 1612 MHz this effect is $\sim 20\mu$Hz and can again be neglected.

The phase offset $\delta\phi^{R-L}$ is affected by slow drifts in the differential local oscillator phases for each independent sense of polarization, $(\theta_{0m}^R - \theta_{0n}^L)$ (2.4) and by ionospheric Faraday rotation γ_m^{R-L}. The former component depends partly on the temperature stability of the VLBI recording electronics at each station but is not expected to be large (Rogers 1990). Practical experience with the MK3 recording system indicates a maximum differential instrumental phase rate of $\leq 1\mu$Hz between independent video converters. Typical values are usually much less and this estimate may be contaminated by unmodelled ionospheric Faraday rotation. The ionospheric Faraday rotation component is expected to have a worst case value of $\mathcal{L}_p^{R-L} \sim 0.15 f_{GHz}^{-3}$ at solar maximum, which is $\sim$ 20 degrees of phase at 1612 MHz. Near solar minimum a value of $\sim$ 6 degrees at 1612 MHz is expected. This effect needs to be determined and removed using one of the

techniques discussed above. Ionospheric modelling may be adequate near solar minimum, including the use of phenomenological models of ionospheric electron density such as that developed by Chiu (1975). These models generally remove only the smoothly varying component of ionospheric Faraday rotation due to the regular ionosphere and do not correct for effects such as travelling ionospheric disturbances (TID's) or other local ionospheric effects (Gwinn 1984). These effects are generally evident on careful inspection of the data but can be more adequately removed by site-based ionospheric monitoring.

If the observations include a point-source polarization calibrator of known polarization position angle and the effects of feed contamination are removed (section 3.6), the phase offset $\delta\phi^{R-L}$ can be determined from the cross-hand and parallel hand correlations analogously to (3.11) as,

$$\begin{aligned}
\delta\phi_m^{R-L} &= \Phi_{mn}^{RL} - \Phi_{mn}^{LL} \\
\delta\phi_m^{R-L} &= \Phi_{mn}^{RR} - \Phi_{mn}^{LR} \\
\delta\phi_n^{R-L} &= \Phi_{mn}^{RL} - \Phi_{mn}^{RR} \\
\delta\phi_n^{R-L} &= \Phi_{mn}^{LL} - \Phi_{mn}^{LR}
\end{aligned}$$

Polarization calibrators with sufficient signal-to-noise ratio in the cross-hand correlations over the small video bandwidths used in spectral-line VLBI that are point sources at VLBI resolution are extremely rare. The instrumental phase offsets can be determined to within an additive constant using the parallel-hand cross-power phases alone, after the correction for ionospheric Faraday rotation, by solving the system of equations,

$$\Phi_{mn}^{RR} - \Phi_{mn}^{LL} = \delta\phi_n^{R-L} - \delta\phi_m^{R-L},\ m \in \{1..N_a\},\ n \in \{m+1..N_a\} \qquad 3.12$$

The equations are under-determined but can be solved for $\delta\phi_m^{R-L}$ + const. This method of phase calibration thus leaves the RCP and LCP phase solutions offset by an unknown constant of phase. This implies that the absolute position angle of the linearly polarized emission as observed on Earth is unknown but the relative position angle of different components within the image remains unaffected. In principle, the absolute position angle can be determined from a continuum polarization calibrator.

3.6 Feed Calibration

The contamination of orthogonal feeds is discussed in section 2.1.4. The system of equations (2.6), which forms the basis of the feed calibration, can be linearized by neglecting second-order terms such as $D_m D_n$ or $(\mathcal{Q}+j\mathcal{U})D_m$ on the basis that $|D_m|$ is typically ≤ 0.1 and $|\mathcal{Q}+j\mathcal{U}| \ll \mathcal{I}$. After applying the amplitude and phase corrections discussed in the preceding sections, including the parallactic angle correction (3.7), the system of equations reduces to,

$$
\begin{aligned}
r'^{RR}_{mn}(u,v,\omega) &= \mathcal{RR} \\
r'^{LL}_{mn}(u,v,\omega) &= \mathcal{LL} \\
r'^{RL}_{mn}(u,v,\omega) &= \mathcal{RL} + D_n^{L*}(\mathcal{RR})e^{j2\alpha_n}e^{-j\gamma_n^{R-L}} + D_m^{R}(\mathcal{LL})e^{j2\alpha_m}e^{-j\gamma_m^{R-L}} \\
r'^{LR}_{mn}(u,v,\omega) &= \mathcal{LR} + D_m^{L}(\mathcal{RR})e^{-j2\alpha_m}e^{j\gamma_m^{R-L}} + D_n^{R*}(\mathcal{LL})e^{-j2\alpha_n}e^{j\gamma_n^{R-L}}
\end{aligned}
\tag{3.13}
$$

where $r'^{pq}_{mn}(u,v,\omega) = [G_m^p\, G_n^{q*}\, e^{j(s^p\alpha_m + s^q\alpha_n)}]^{-1}\ r^{pq}_{mn}(u,v,\omega)$, are the cross-power spectra corrected for the complex antenna gains G_m^p after bandpass removal and $e^{js^p\alpha_m}$ are the parallactic angle corrections ($s^{RCP} = -1$; $s^{LCP} = +1$). The linearization (3.13) of the parallel-hand terms is implicit in the previous discussion of

fringe-fitting and self-calibration. High linear polarization in the reference channel may invalidate this assumption and necessitate a more sophisticated approach to fringe-fitting retaining the linear polarization terms in (2.6). The ionospheric terms γ_m^{R-L} are included for completeness but may be neglected if the ionospheric Faraday rotation is small.

The sub-system of equations,

$$r'^{RL}_{mn}(u,v,\omega) = \mathcal{RL} + D_n^{L*}(\mathcal{RR})e^{j2\alpha_n}e^{-j\gamma_n^{R-L}} + D_m^{R}(\mathcal{LL})e^{j2\alpha_m}e^{-j\gamma_m^{R-L}}$$
$$r'^{LR*}_{mn}(u,v,\omega) = \mathcal{LR}^* + D_m^{L*}(\mathcal{RR}^*)e^{j2\alpha_m}e^{-j\gamma_m^{R-L}} + D_n^{R}(\mathcal{LL}^*)e^{j2\alpha_n}e^{-j\gamma_n^{R-L}} \quad (3.14)$$

is linear in D_m^{L*} and D_m^R and can be solved by standard complex linear least squares techniques (Miller 1973) if the polarization structure $\{\mathcal{I},\mathcal{V},\mathcal{Q},\mathcal{U}\}$ of a calibrator source is well-determined. This technique requires that the signal-to-noise ratio of the cross-polarized fringes on the calibrator is sufficient to allow a solution. In practice, for a linearly polarized calibrator anything more complex than an ultra-compact point source renders such a fit unreliable. Such sources can be found for connected-element arrays such as the VLA but are considerably more difficult to locate for VLBI observations. The problem is compounded by the fact that if linearly polarized emission is associated with a compact source such as a quasar it is generally more likely to occur in the extended jet emission than the compact core (Wardle *et al.* 1986). The source OQ208 has however been mentioned in the literature as an ultra-compact polarization calibrator suitable for wide-band MK3 continuum observations at 5 GHz (Roberts, Brown and Wardle 1991). Spectral line polarization VLBI, however, uses a considerably reduced bandwidth compared to continuum VLBI and this places severe constraints on the required signal-to-noise ratio of the cross-polarized fringes. A totally unpolarized source could also be used but these are equally difficult to find at VLBI resolution.

A method was developed to provide an approximate D-term solution in the event that a suitable polarization calibrator cannot be found. The cross-power spectra for the spectral line program source can be used to calibrate the data if the expected linear polarization over a range of frequency channels is assumed low, i.e. $|\mathcal{Q}(\omega) + j\mathcal{U}(\omega)| \sim 0$ for $\omega \in [\omega_1,\ \omega_2]$. This is achieved by including each channel as an independent, purely circularly polarized source in a composite fit to equation (3.14). The source structure of the independent channels is obtained as $\mathcal{RR}(u,v,\omega) = r'^{RR}(u,v,\omega)$ and $\mathcal{LL}(u,v,\omega) = r'^{LL}(u,v,\omega)$.

The basis functions $e^{j2\alpha_m}$ are non-degenerate if the VLBI antennas are widely spaced in longitude and contain a mix of antennas with equatorial and alt-azimuth mounts. In small connected-element interferometers such as the VLA all antennas have almost identical parallactic angles and the degeneracy of the basis functions is removed by setting one D term to zero (Roberts, Brown and Wardle 1991). The degeneracy of the basis functions for a given network can be more accurately assessed by evaluating the condition of the curvature matrix in the complex least squares equations, which would be most generally solved by singular value decomposition. A Cholesky decomposition is currently used in the feed calibration software. The calibration technique discussed above using purely circularly polarized calibrators does not allow the determination of the absolute polarization position angle of the emission.

The D-terms could alternatively be obtained using a single spectral channel in the program source with a sufficiently simple linear polarization structure using a iterative technique. In this method the source structure and D-terms would be determined simultaneously. This may be a promising technique at high frequency resolution for isolated maser components with sufficient signal to noise ratio in the cross-polarized fringes. This was not pursued further in this work.

After the determination of the D-terms the data are corrected as,

$$\begin{pmatrix} \mathcal{RR} \\ \mathcal{LL} \\ \mathcal{RL} \\ \mathcal{LR} \end{pmatrix}_{mn} = \begin{pmatrix} 1 & 0 & 0 & 0 \\ 0 & 1 & 0 & 0 \\ -D_n^{L*}\, e^{j2\alpha_n}\, e^{-j\gamma_n^{R-L}} & -D_m^{R}\, e^{j2\alpha_m}\, e^{-j\gamma_m^{R-L}} & 1 & 0 \\ -D_m^{L}\, e^{-j2\alpha_m}\, e^{j\gamma_m^{R-L}} & -D_n^{R*}\, e^{-j2\alpha_n}\, e^{j\gamma_n^{R-L}} & 0 & 1 \end{pmatrix} \begin{pmatrix} r'^{RR} \\ r'^{LL} \\ r'^{RL} \\ r'^{LR} \end{pmatrix}_{mn} \tag{3.15}$$

This correction can only be made at a given point if the appropriate subset of uncorrected quantities all exist at that point. The corrected (u, v) data set may therefore be smaller than the uncorrected data set. Again the ionospheric Faraday rotation correction γ_m^{R-L} may be ignored if negligible.

Errors in the D-terms introduce errors in the cross-polarized data, excluding ionospheric Faraday rotation, of the general form,

$$\delta\mathcal{RL}_{mn} = \delta D_n^{L*}\, e^{j2\alpha_n}\, \mathcal{RR} + \delta D_n^{R}\, e^{j2\alpha_m}\, \mathcal{LL}$$
$$\delta\mathcal{LR}_{mn} = \delta D_m^{L}\, e^{-j2\alpha_m}\, \mathcal{RR} + \delta D_n^{R*}\, e^{-j2\alpha_n}\, \mathcal{LL}$$

For a limited range of parallactic angle α_m or for small networks the D-term errors may introduce leakage of $(\mathcal{I} + \mathcal{V})$ and $(\mathcal{I} - \mathcal{V})$ into the linearly polarized data. In general, however, these leakage terms have a variable non-zero phase offset and will not add coherently to produce spurious Q and U components in the image plane. Systematic leakage effects may be indicated if the percentage linear polarization is very similar for each I component in a given channel.

3.7 Imaging

The basic principles of self-calibration interferometric imaging are discussed in section 2.3.

The calibrated Stokes parameters in the (u, v) plane $\{\mathcal{I}, \mathcal{V}, \mathcal{Q}, \mathcal{U}\}$ are derived from the corrected correlations $\{\mathcal{RR}, \mathcal{LL}, \mathcal{RL}, \mathcal{LR}\}$ using the relations (2.5). VLBI

data often have unequal sampling in the four polarization correlation pairs due to correlator or observing errors and the size of the dataset is consequently reduced in forming the visibility Stokes parameters. The final images are generated by transforming to the image plane and correcting for the effects of (u,v) sampling using non-linear deconvolution techniques such as CLEAN or MEM. The imaged Stokes parameters $\{I,V,Q,U\}$ are real thus requiring only a half-plane transform of their Hermitian Fourier counterparts.

The $I(\eta,\zeta,\omega)$ and $V(\eta,\zeta,\omega)$ images are formed directly with this technique using the formal definition of $\mathcal{I}$ discussed above. A long history of continuum interferometry has led to a less rigorous definition of $\mathcal{I}$ which allows $\mathcal{I}$ to be formed from one parallel-hand correlation alone if neccessary, and assumes zero $\mathcal{V}$. This is inappropriate for spectral line polarization observations, where net circular polarization is often encountered.

In forming the Stokes $Q(\eta,\zeta,\omega)$ and $U(\eta,\zeta,\omega)$ images the unequal sampling of $\mathcal{RL}(u,v)$ and $\mathcal{LR}(u,v)$ can be overcome using the definition of complex brightness $P(\eta,\zeta) = Q(\eta,\zeta) + jU(\eta,\zeta)$ (2.7) defined by Conway and Kronberg (1969). The Fourier counterpart $\mathcal{P}(u,v)$, which is not Hermitian, satisfies the relations,

$$\mathcal{P}(u,v) = \mathcal{Q}(u,v) + j\mathcal{U}(u,v) = \mathcal{RL}(u,v)$$
$$\mathcal{P}(-u,-v) = \mathcal{Q}(u,v) - j\mathcal{U}(u,v) = \mathcal{RL}^*(u,v)$$

The complex image $P(\eta,\zeta)$ is generated by a full-plane complex transform of $\mathcal{P}(u,v)$ and deconvolved using the the CLEAN algorithm with the associated complex dirty beam,

$$B(\eta,\zeta) \quad \mathcal{F} \quad S_{RL}(u,v) + S_{LR}(-u,-v)$$

where $S_{RL} = \sum_k \delta_{RL}(u_k, v_k)$ and $S_{LR} = \sum_k \delta_{LR}(u_k, v_k)$ are the (u, v) sampling functions for the $\mathcal{RL}$ and $\mathcal{LR}$ correlations respectively, neglecting weighting. The imaginary part of the dirty beam is zero for equal sampling $S_{RL} = S_{LR}$.

The Conway and Kronberg technique can be implemented using half-plane interferometric mapping procedures by forming the Hermitian quantities $\mathcal{Q}'(u, v)$ and $\mathcal{U}'(u, v)$ (Cotton 1991), where,

$$\begin{aligned}
\mathcal{Q}'(u,v) &= \frac{1}{2}[\mathcal{RL}(u,v)S_{RL}(u,v) + \mathcal{LR}(u,v)S_{LR}(u,v) \\
&\quad + \mathcal{RL}^* S_{RL}(-u,-v) + \mathcal{LR}^*(u,v)S_{LR}(-u,-v)] \\
\mathcal{U}'(u,v) &= \frac{j}{2}[\mathcal{LR}(u,v)S_{LR}(u,v) - \mathcal{RL}(u,v)S_{RL}(u,v) \\
&\quad - \mathcal{LR}^*(u,v)S_{LR}(-u,-v) + \mathcal{RL}^*(u,v)S_{RL}(-u,-v)]
\end{aligned}$$

These are transformed to the image plane to yield real images $Q'(\eta, \zeta) = \mathcal{R}e[P(\eta, \zeta)]$ and $U'(\eta, \zeta) = \mathcal{I}m[P(\eta, \zeta)]$. Now,

$$\begin{aligned}
\mathcal{P}'(u,v) &= \mathcal{Q}'(u,v) + j\mathcal{U}'(u,v) \\
&= \mathcal{RL}(u,v)S_{RL}(u,v) + \mathcal{LR}^*(u,v)S_{LR}(-u,-v) \\
\mathcal{F} \quad & Q(\eta,\zeta) + jU(\eta,\zeta)
\end{aligned}$$

The real and imaginary parts of the complex dirty beam $B(\eta, \zeta)$ can be similarly formed by setting the existing $\mathcal{RL}$ and $\mathcal{LR}$ correlations to unity, and transforming to the image plane as described above. The resulting complex dirty beam needs to be normalised to unit modulus at the beam centre and the complex dirty image needs to be adjusted by the same factor. The Högbom CLEAN algorithm was designed for the deconvolution of real images but can be extended directly to complex quantities. This has been implemented within AIPS by W.D. Cotton.

3.8 Data Reduction within AIPS

The schematic data reduction path within AIPS is shown in Fig. 3.2. The tasks that required modification for use with spectral line polarization data are marked with an asterisk. The task MK3IN is prominent within this set. Several new tasks were developed including BPCOR for smoothing complex bandpass tables, FRPLT for plotting fringe-rate spectra and visibility time series, SPCAL for spectral line polarization feed calibration and VLB for reference channel self-calibration imaging (derived from MAPIT).

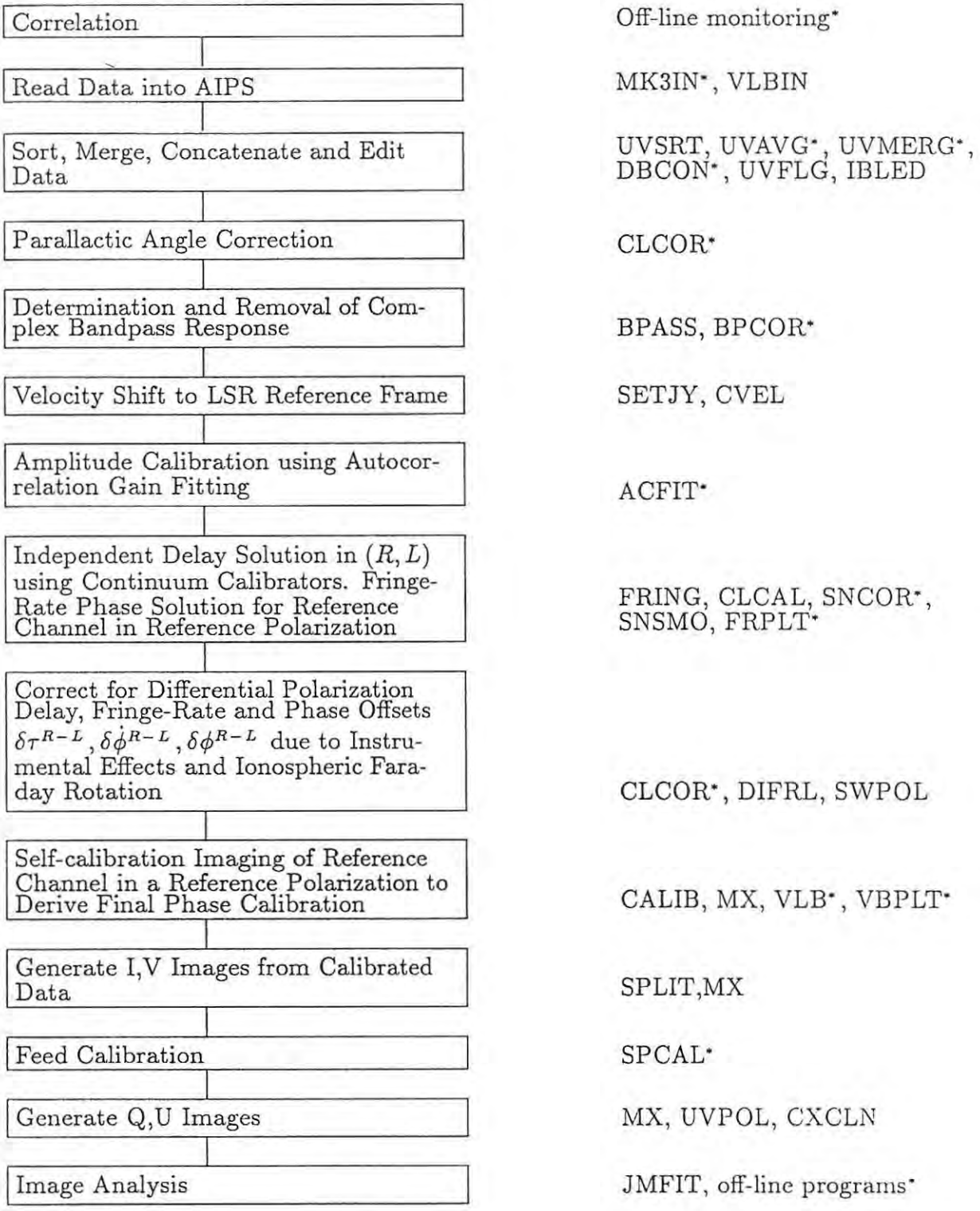

Fig. 3.2. The schematic data reduction path within AIPS for spectral line polarization data. The tasks that required modification for spectral line polarization data are marked with an asterisk.

CHAPTER 4: MK2 OBSERVATIONS OF IRC+10420

Introduction

This chapter describes MK2 observations of IRC+10420 conducted in 1982 using a network of telescopes in the EVN. The data reduction method is discussed and the resulting images are presented. The astrophysical interpretation of these results is given in Chapter 7.

4.1 Observations

MERLIN observations of IRC+10420 by Diamond, Norris and Booth (1983) revealed unusual structure in the circumstellar shell including possible bipolarity. Subsequent VLBI observations were scheduled using the EVN antennas at Jodrell Bank, Effelsberg, Onsala and Dwingeloo and the EVN affiliate station at Crimea with P. Diamond, R. Norris, R. Booth and L. Matveyenko as principal investigators. The data from Crimea were not used in the reduction, due to the absence of calibrator scans. The system parameters for the resulting antenna network are given in Table 4.1.

TABLE 4.1

Antenna Parameters

Station	Diameter (m)	J^1_{sys} (Jy)
Effelsberg	100	31
Jodrell MkIA	76	115
Onsala 85	26	260
Dwingeloo	26	335

[1] Nominal zenith system temperature in Janskys

The observations were performed during the period 17 Oct 1982 UT 10:30 to 18 Oct 1982 UT 00:30 using the MK2 VLBI system. A net upper-sideband video bandwidth of 250 kHz was recorded at each antenna centered on an LSR velocity of $\sim +48$ kms^{-1}, assuming a line rest frequency of 1612.23109 MHz. Left-circular polarization was recorded at each site. The source coordinates are listed in Table 4.2. The continuum source BL_Lac was observed as a delay and bandpass calibrator at the beginning and end of the run.

TABLE 4.2

Source Coordinates

Source	α (1950.0)	δ (1950.0)
IRC+10420	$19^h\ 24^m\ 26.7^s$	$11^\circ\ 15^m\ 10.0^s$
BL_Lac	$22^h\ 00^m\ 39.4^s$	$42^\circ\ 02^m\ 08.6^s$

System temperature measurements were requested at the start of each thirty minute scan. This was a relatively early spectral line VLBI observation and frequency tracking was attempted. The edge frequency of the recorded video band was consequently changed at the beginning of each scan to track the diurnal Doppler shift more accurately. This practice has generally fallen out of favour in spectral line VLBI due to the attendant logistical difficulties.

4.2 Data Reduction

The data were correlated by P. Diamond at the Bonn MK2 correlator which was operated by the Max-Planck Institute for Radio Astronomy (MPI). The cross-correlation functions were transformed to 128-channel cross-power spectra on-line by the NOVA control computer and corrected for Van Vleck and fractional bit shift errors. No on-line corrections were applied to the autocorrelation data. The data were pre-averaged to 10s and baseline-based residual fringe rates were erroneously removed before the data were archived on magnetic tape as CDC Cyber data files in the MPI spectral line VLBI data format.

Subsequent processing of the data began in earnest in 1989. The CDC Cyber 60-bit data on tape were decoded and converted to the spectral line data format adopted by the Smithsonian Astrophysical Observatory (SAO) in collaboration with the NRAO. The data were corrected for several non-closing phase errors known to be associated with the MPI MK2 correlator including a local oscillator rounding error, fringe rate glitch and phase error introduced by a zero'th order geometric delay calculation (Norris *et al.*1984). The non-closing fringe rates removed in error in earlier processing were restored. Existing software written by P. Diamond for the conversion of CDC data to the NRAO/SAO format was used but required several refinements.

The data in SAO format were imported into AIPS using the task VLBIN. At this point the autocorrelation functions were transformed to autocorrelation spectra and corrected for 1-bit sampling and clipper bias. The subsequent data reduction within AIPS followed the path discussed in Chapter 3 but without the need for polarization corrections such as parallactic angle removal, spectral line polarization phase calibration or feed calibration. The data reduction strategy is briefly discussed below.

The data were first edited to remove discrepant points. The complex cross-correlation bandpass response was determined for each antenna using the cross-power spectra for the continuum calibrator source BL_Lac and are plotted in Fig. 4.1. The autocorrelation bandpass response is not shown here but was used to correct the autocorrelation spectra. The autocorrelation and cross-correlation data were corrected for the residual diurnal Doppler shift at each antenna and centred on an LSR velocity of +48.4 kms^{-1}. The antenna amplitude gains were determined as composite antenna gains with respect to the averaged Effelsberg autocorrelation spectrum for the scan 17:30 - 18:30 UT using the baseline-independent template fitting technique discussed in section 3.4. A ten minute solution interval was used

and bad gains were removed on inspection. The absolute flux density scale was established using system temperature measurements at Onsala, which appeared to be the most reliable. The averaged antenna temperature across the band due to the source emission, $\bar{T}_a$, was determined from the offset term in the bandpass-corrected autocorrelation spectrum and by direct numerical integration across the spectrum. These methods are discussed in section 3.4. The estimated error in the absolute flux scale is $\sim 20\%$. The scaled template spectrum at Effelsberg is shown in Fig. 4.2.

The residual group delays were determined from the BL_Lac data, interpolated and applied to the IRC+10420 data. The reference channel at $V_{LSR} = 45.49$ kms^{-1} in the IRC+10420 spectrum was used to derive residual fringe rate corrections. Hanning smoothing was applied to the calibrated data yielding a spectral resolution of 0.73 kms^{-1}. The residual antenna phase gains were determined from self-calibration imaging of the reference channel using the mapping techniques discussed in section 3.5.3. The relative fit of the reference channel (u,v) data to the source model in closure-phase and correlated amplitude is shown in Fig. 4.3 and Fig. 4.4 The phase gains from the reference channel were applied to the other frequency channels in the data cube to derive the final calibrated (u,v) data set.

4.3 Imaging

The calibrated data were transformed to the image plane and deconvolved using the CLEAN algorithm. The dirty beam is shown in Fig. 4.5 and the final image cube is plotted in Fig. 4.6. Each map is 512 x 512 pixels with a pixel spacing of 6 mas.

The list of components in Table 4.3 was derived from the final images by selecting all components in each channel with apparent peak brightness greater than the absolute value of the deepest negative in the channel. Each component was fitted as a two-dimensional elliptical Gaussian in relative right ascension and

declination, after interactively constraining the fit to a rectangular region tightly enclosing the component in the image plane. The apparent size of the components was estimated from the fit after deconvolution to remove the known elliptical CLEAN beam. Upper limits to the apparent size are enclosed in parentheses. The velocity width was determined in an independent fit over velocity at the position of the peak component brightness assuming a Gaussian line profile. The velocity fit was performed interactively using multiple Gaussian components where necessary.

TABLE 4.3
List of Components

V^a	δV^b	X^c	Y^c	θ^d_{maj}	θ^d_{min}	PA^e	LCP^f
64.06	.79	.793	-.770	17.0	3.1	152.3	1.02
64.16	.70	.498	.215	(8.5)	(8.5)	(180.0)	.975E-01
63.12	.76	.486	.201	9.7	4.5	71.4	.691E-01
63.07	.87	1.230	-.451	8.1	4.3	79.0	.442
62.94	.67	.596	.236	13.3	6.8	106.6	.121
62.42	.90	.564	.232	18.5	6.1	71.5	.248
62.23	.47	-.211	-.389	11.8	5.6	75.3	.440E-01
62.06	.96	-.265	.268	23.4	3.9	55.3	2.30
61.16	.45	-.236	.259	(9.4)	(9.4)	(180.0)	.133
60.93	.65	1.137	-.337	5.7	4.6	26.4	.167
61.01	.97	.813	-.838	8.9	4.4	122.6	.392
60.22	.60	1.271	-.560	9.6	.8	167.3	.155
60.34	.78	.996	-.470	(9.5)	(9.5)	(180.0)	.913E-01
60.19	.61	.654	.127	17.2	7.0	162.6	.497E-01
59.50	.78	-.418	.113	15.1	8.7	72.5	2.69
59.44	.61	.318	-1.351	(11.8)	(11.8)	(180.0)	.110
59.33	.93	.813	-.861	23.6	5.7	132.9	.338
59.46	.80	1.159	-.227	6.5	4.9	109.4	.255
58.43	.81	.996	-.402	(3.9)	(3.9)	(180.0)	2.28
58.37	.58	-.441	.010	32.8	17.9	116.8	.159
57.92	.74	-.238	.263	8.7	7.0	117.8	.205
57.86	.77	-.455	-.055	16.7	5.8	69.0	2.04
57.66	1.47	1.021	-.499	(18.5)	(18.5)	(180.0)	4.46
57.65	.58	.864	-.169	(4.9)	(4.9)	(180.0)	.168
56.56	1.73	.998	-.392	8.7	7.4	169.7	5.86
56.87	.85	.350	-1.159	9.6	4.0	161.0	.316
56.80	.75	-.259	.241	7.4	3.8	127.3	1.02
56.75	.83	-.420	-.071	(8.1)	(8.1)	(180.0)	.388
56.11	.70	.965	-.810	(10.9)	(10.9)	(180.0)	.403
55.85	.73	-.087	-.435	10.2	1.3	128.9	.477
55.65	1.00	1.002	-.502	49.4	18.0	130.7	2.55
55.68	.69	-.416	-.010	8.7	6.3	45.9	.249
55.28	.77	.645	-.048	7.2	4.6	97.2	.843
55.24	1.60	-.375	.065	29.8	5.7	89.9	2.69
54.64	.72	1.069	-.603	12.6	5.8	57.5	.423
54.68	.75	-.322	.050	11.3	5.5	113.0	3.07
54.47	.84	-.396	-.028	(7.9)	(7.9)	(180.0)	1.51
54.34	1.29	.983	-.480	50.8	3.3	15.0	1.55
54.21	.76	.770	.048	(6.2)	(6.2)	(180.0)	1.40
53.91	.79	1.042	-.603	11.2	2.9	130.1	.578
54.04	.96	.989	-.384	(29.6)	(29.6)	(180.0)	.924
53.39	.56	.723	-1.218	(8.9)	(8.9)	(180.0)	.152
53.33	1.06	.990	-.371	(11.8)	(11.8)	(180.0)	1.02
53.38	.77	-.382	.016	50.0	17.8	.1	1.59
53.43	.71	-.195	-.540	6.5	3.2	91.3	.468
52.98	.75	.978	-.435	(17.7)	(17.7)	(180.0)	1.78
53.23	.90	.575	.212	7.9	5.1	140.7	.935
52.83	.67	1.031	-.617	(11.8)	(11.8)	(180.0)	.585
52.59	1.00	.558	-1.161	6.1	3.2	9.7	.483
52.67	.85	.973	-.399	(20.1)	(20.1)	(180.0)	.251

52.40	1.11	.964	-.221	24.4	5.9	118.3	2.70
52.56	.64	.533	.205	8.8	5.5	97.3	.334
52.45	.93	-.368	.036	22.3	3.5	91.3	1.48
52.39	.83	-.389	-.144	(8.7)	(8.7)	(180.0)	.350
52.02	.72	.967	-.660	8.4	4.4	127.6	2.58
52.15	.97	.904	-.560	19.7	4.7	157.1	5.76
51.61	.81	.869	-.117	10.4	6.3	148.3	.385
51.18	.71	.987	-.319	11.3	7.0	37.4	1.34
51.45	.73	.568	.204	7.0	2.5	89.1	2.06
51.24	.90	-.366	-.037	3.4	.6	13.6	.670
51.47	.85	-.117	-.382	16.3	4.9	156.5	4.83
50.88	.60	.923	-.179	7.2	2.6	155.9	.322
50.97	.97	-.113	-.395	35.9	3.6	164.7	2.15
50.46	.91	.962	-.381	9.4	6.5	75.2	4.12
50.73	.81	.864	-.120	5.3	3.1	42.7	.533
50.56	1.14	.611	.138	9.4	4.9	166.1	.547
50.64	.76	.540	.151	(9.8)	(9.8)	(180.0)	1.62
50.54	1.06	-.424	-.120	10.3	7.8	48.0	3.70
50.18	.71	.816	-.968	(11.7)	(11.7)	(180.0)	.206
50.36	.72	.895	-.511	(7.0)	(7.0)	(180.0)	.460
50.18	.77	.571	-.167	6.5	4.9	110.7	.635
50.29	.73	.020	-.327	10.2	3.3	136.8	1.37
49.81	.85	.879	-.595	(9.3)	(9.3)	(180.0)	.425
49.79	.86	.961	-.253	10.2	1.1	144.3	2.17
49.79	.82	.916	-.178	(13.2)	(13.2)	(180.0)	1.49
50.01	.78	.361	-.619	(6.1)	(6.1)	(180.0)	.634
49.88	.49	.372	.247	5.6	2.8	81.8	.198
49.92	.62	-.404	.016	(13.3)	(13.3)	(180.0)	.595
49.39	.93	.628	.143	(23.7)	(23.7)	(180.0)	.607
49.53	.78	-.420	-.082	11.2	4.7	8.5	2.40
49.23	1.00	.885	-.519	10.3	2.5	136.3	.918
49.12	.87	.965	-.462	(9.6)	(9.6)	(180.0)	.208
48.94	.80	.596	.118	23.5	9.7	69.8	2.80
49.07	.73	.335	-.066	10.6	4.5	51.5	1.39
48.74	1.05	-.395	-.061	5.7	3.2	49.4	.640
48.43	1.06	.979	-.277	16.4	2.6	146.6	.181
48.24	.71	.968	-.359	5.8	3.6	50.3	.239
48.35	.79	.616	.021	9.1	3.9	137.8	1.50
48.55	.92	.009	-.307	7.7	5.8	141.0	.364
48.34	.47	-.158	-.365	34.2	4.2	91.7	.209
48.10	.62	.696	-.683	(17.3)	(17.3)	(180.0)	.597
48.17	.68	.567	-.166	9.9	2.6	134.0	.843
47.92	.84	.284	-.635	7.8	5.1	130.6	14.9
48.02	.81	-.109	-.369	17.5	7.3	152.4	1.65
47.59	.88	.544	-.660	20.4	2.6	92.1	8.33
47.77	.81	-.560	-.138	8.6	3.5	78.4	.606
47.25	.66	.084	-.349	11.7	4.4	2.2	.857
47.37	.77	-.351	-.056	(9.9)	(9.9)	(180.0)	.739
46.84	.62	.660	-.153	7.8	5.0	165.5	1.07
47.10	.69	.278	-.587	45.0	10.1	8.6	2.24
46.96	.81	-.161	-.434	21.7	7.0	127.0	21.2
46.78	.58	-.350	-.131	(8.6)	(8.6)	(180.0)	.716
46.44	.81	.545	-.649	5.9	4.4	114.7	3.15
46.40	.81	.295	-.551	15.4	6.3	144.6	10.0
46.15	.98	.274	-.610	27.9	11.9	53.9	2.19

46.31	.76	.329	-.594	14.5	3.0	149.3	9.80
46.25	.67	-.191	-.466	29.5	3.8	48.3	1.84
45.45	1.05	.204	-.254	16.6	6.6	38.3	21.7
45.46	.54	.197	-.183	14.2	5.9	170.2	1.88
45.53	.78	.000	.003	7.2	1.4	177.4	27.9
45.27	.73	.263	-.754	56.0	7.6	35.0	7.84
45.03	.65	.107	-.257	(7.0)	(7.0)	(180.0)	4.66
44.94	1.02	.217	-.243	10.1	4.3	151.7	17.7
44.33	.76	.228	-.735	15.8	1.1	2.9	15.4
44.35	.61	.228	-.660	4.1	2.2	163.4	1.55
44.20	.72	.226	-.792	(19.4)	(19.4)	(180.0)	15.2
43.96	.76	.252	-.252	28.6	10.7	90.7	25.2
43.62	.89	-.029	-.119	16.1	7.4	159.7	3.18
43.32	.65	.000	-.079	11.3	.6	38.6	2.19
43.03	1.48	.223	-.738	(5.3)	(5.3)	(180.0)	1.29
42.55	.82	.238	-.670	10.4	4.9	142.1	.613
42.46	.59	.336	.499	(10.6)	(10.6)	(180.0)	.664E-01
42.14	.62	-.060	-.429	7.2	6.7	65.3	.165
41.88	.42	.233	-.672	(6.8)	(6.8)	(180.0)	.357
41.15	.72	.350	-.588	6.9	3.1	94.0	.293

[a] Centre LSR velocity of the component, assumed to have a Gaussian velocity profile (kms^{-1}).

[b] The full width at half maximum of the Gaussian line profile (kms^{-1}).

[c] Relative angular separation (X, Y) of the peak component brightness with respect to the map centre in the direction of increasing right ascension and declination of date respectively (arcsec).

[d] The estimated apparent size of the component along the major and minor axes after deconvolution by the CLEAN restoring beam (mas). Upper limits are given in parentheses.

[e] Position angle of the component major axis (measured from north to east) (deg).

[f] Peak apparent brightness of the component in left circular polarization (Jy per beam). The beam solid angle is $\Omega_{beam} = 1.133\ \theta_{maj}^{beam}\ \theta_{min}^{beam}$, where $\theta_{maj}^{beam} = 31.50$ mas and $\theta_{min}^{beam} = 27.78$ mas.

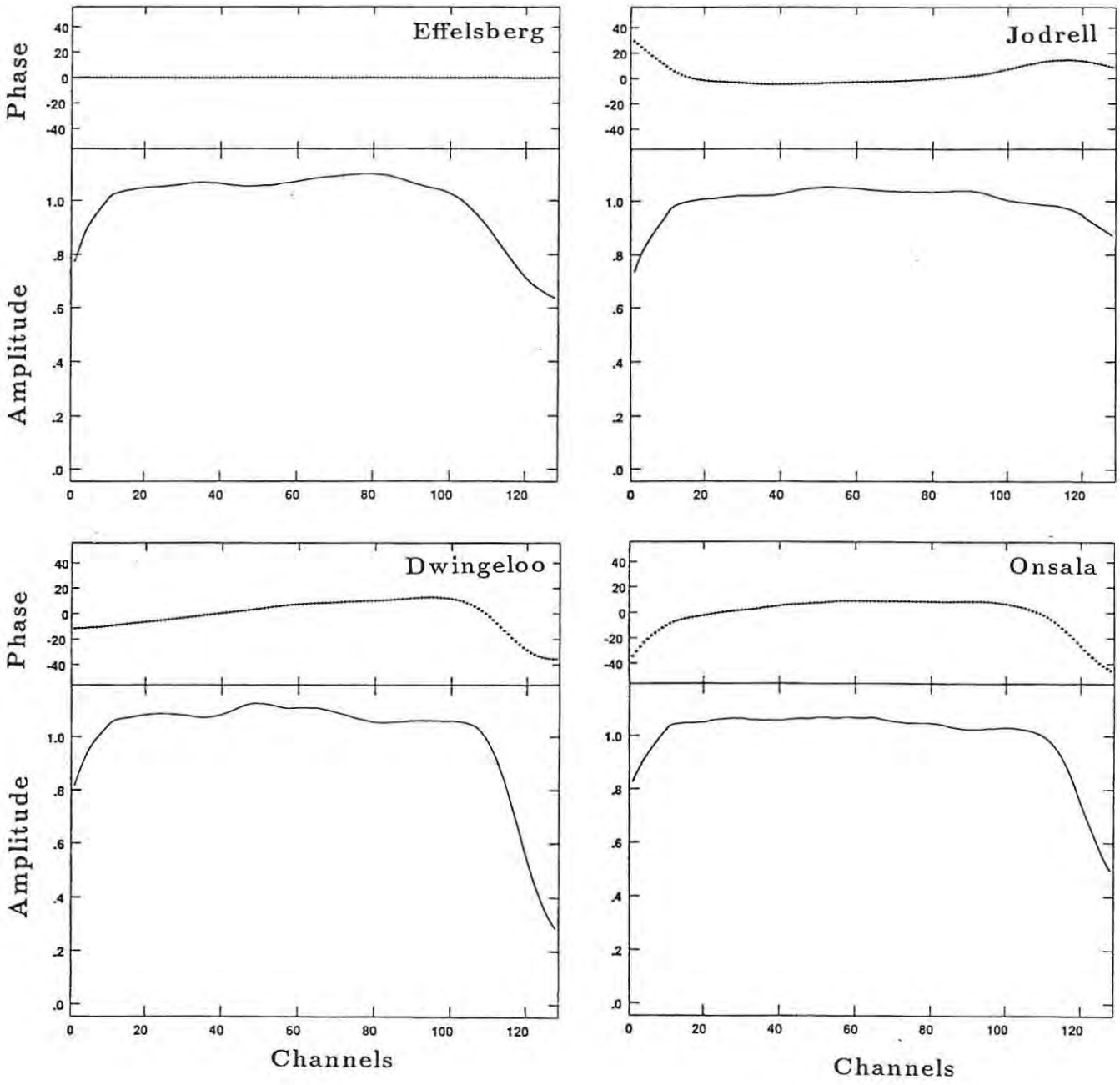

Fig. 4.1. The normalised cross-correlation complex bandpass response for the antennas involved in the MK2 VLBI observations of IRC+10420. The $x-$axis is in units of frequency channel number. The solutions were obtained from the cross-power data for Bl_Lac and have been smoothed using a 20-channel complex Hanning window.

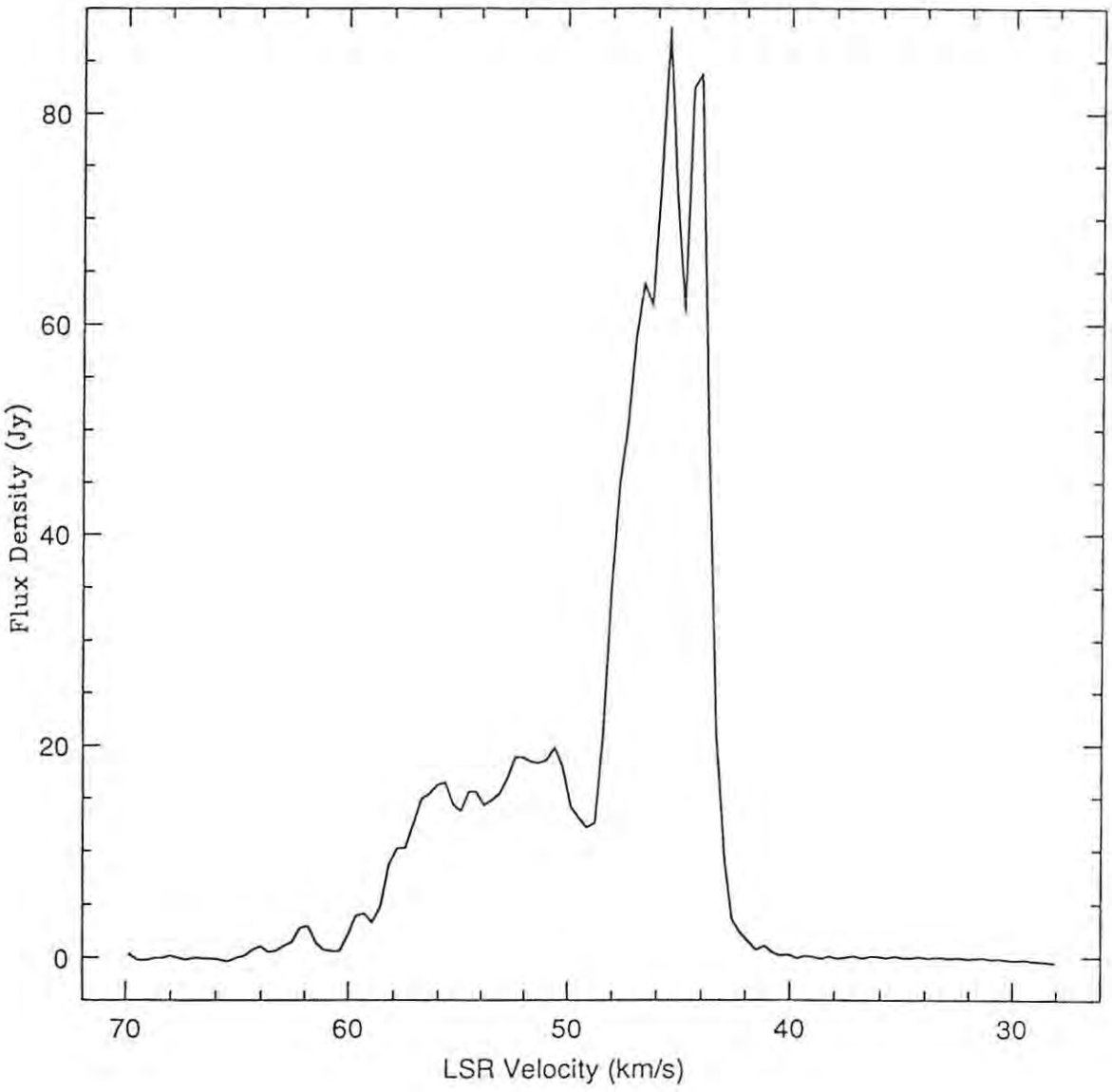

Fig. 4.2. The single-dish autocorrelation spectrum in left-circular polarization of the OH maser emission at 1612 MHz towards IRC+10420. The spectrum is derived from the Effelsberg autocorrelation data for the MK2 VLBI experiment on 17 October 1982. The spectral resolution after Hanning smoothing is 0.73 kms^{-1} and the estimated error in the absolute flux density scale is $\sim$ 20%.

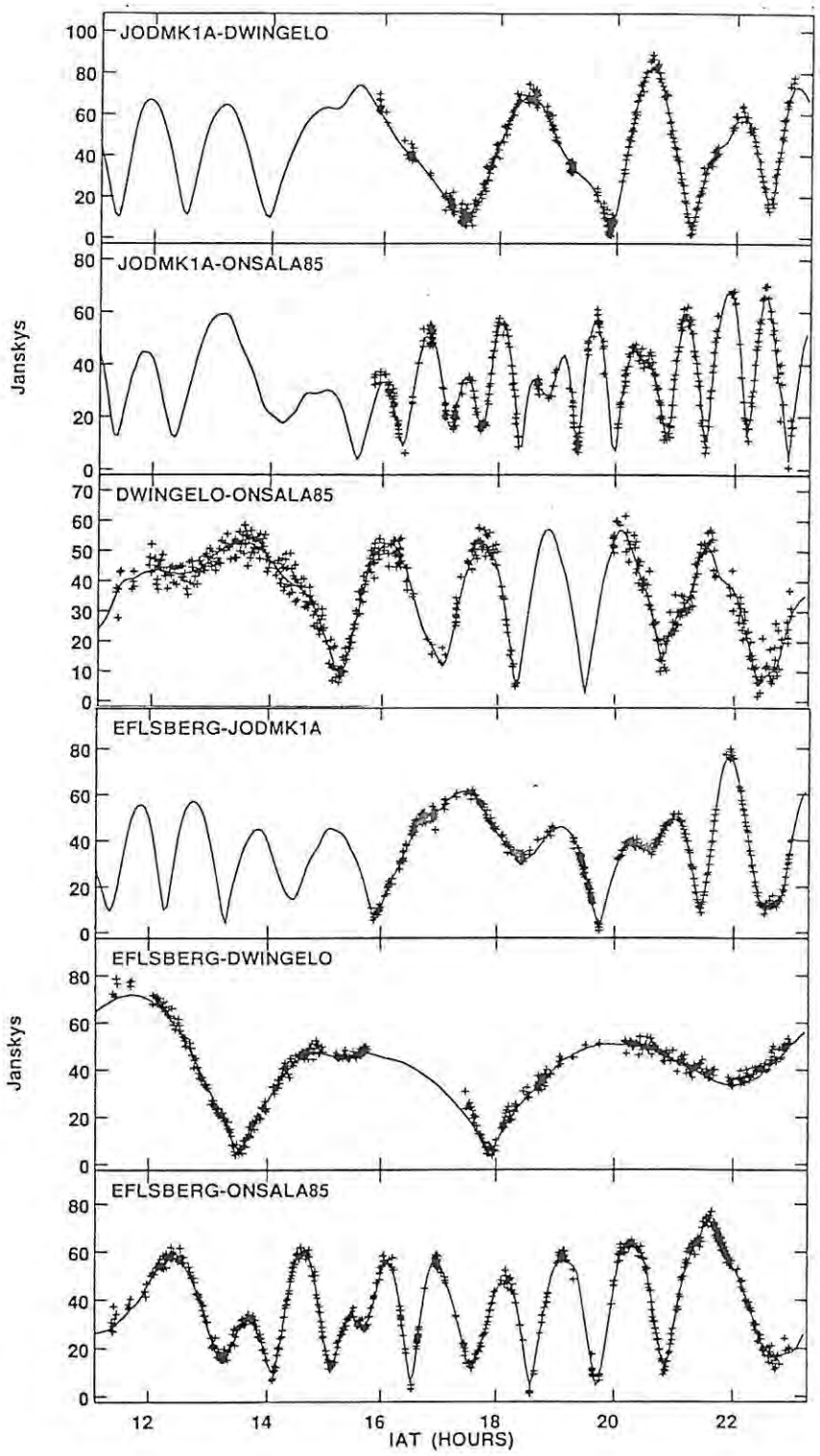

Fig. 4.3. The fit to the source model in correlated amplitude for the reference channel at $V_{LSR} = 45.49$ kms^{-1}. The $x-$axis is in units of International Atomic Time (IAT).

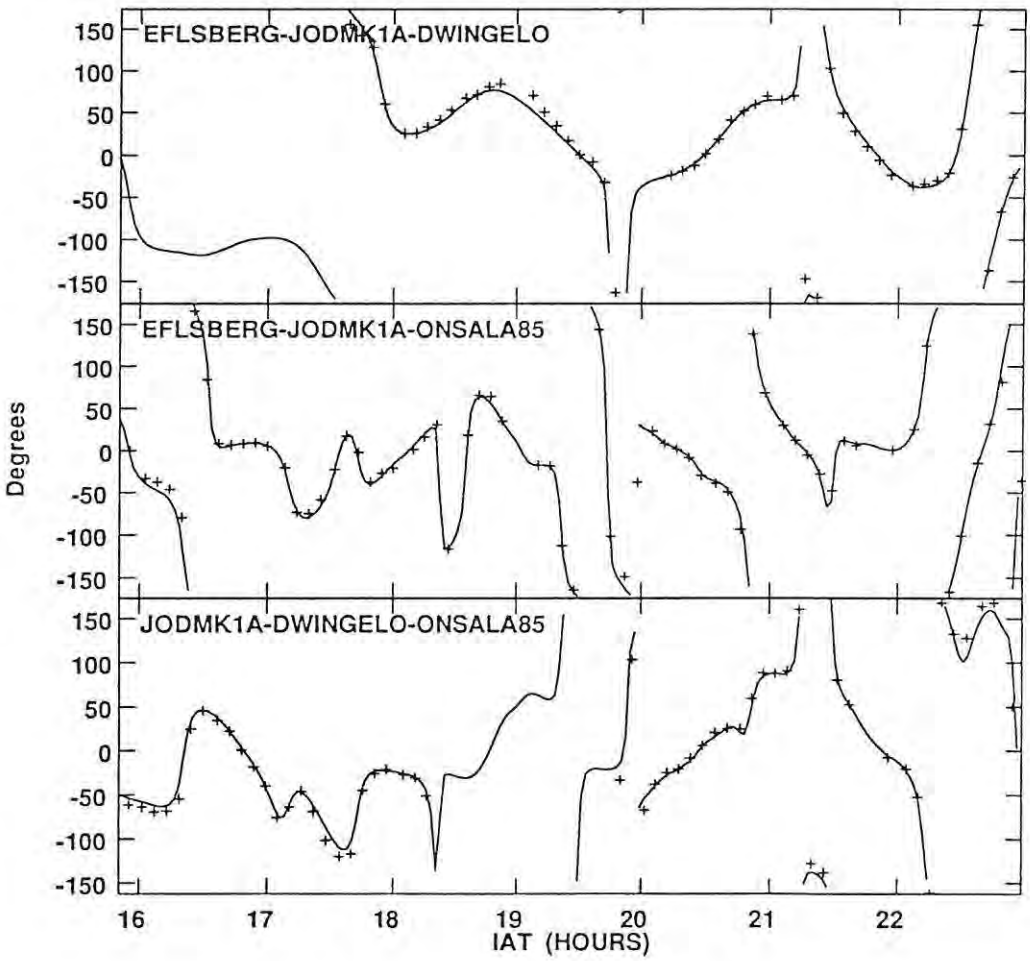

Fig. 4.4. The fit to the source model in closure phase for the reference channel at $V_{LSR} = 45.49$ km^{-1}. The $x-$axis is in units of International Atomic Time (IAT).

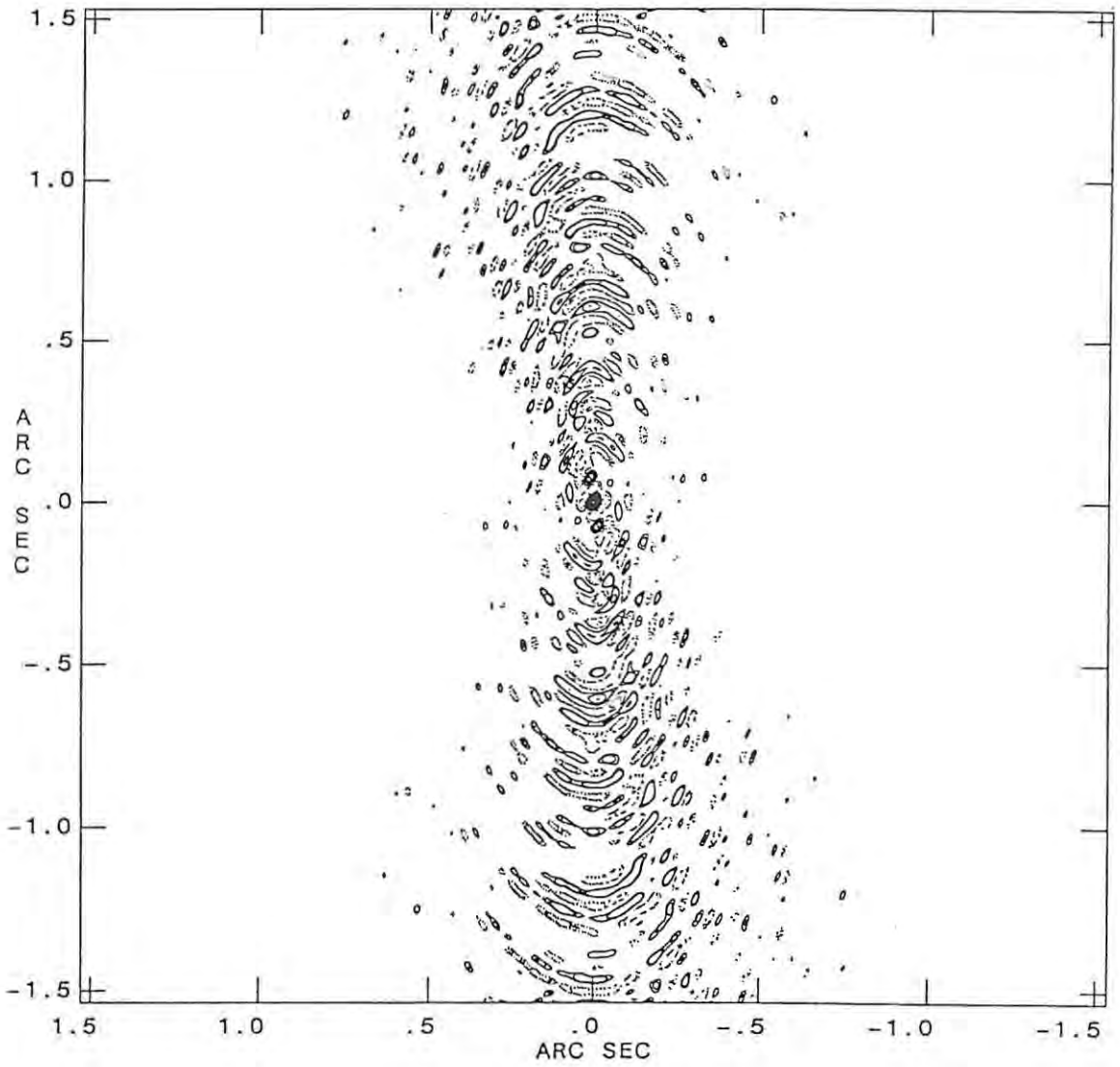

Fig. 4.5. The point spread function or dirty beam for the (u, v) sampling in the MK2 VLBI observations of IRC+10420. The contours are plotted at (-20, -10, -7.5, 7.5, 10, 20, 30, 40, 50, 60, 70, 80, 90, 100) % of the peak unit brightness.

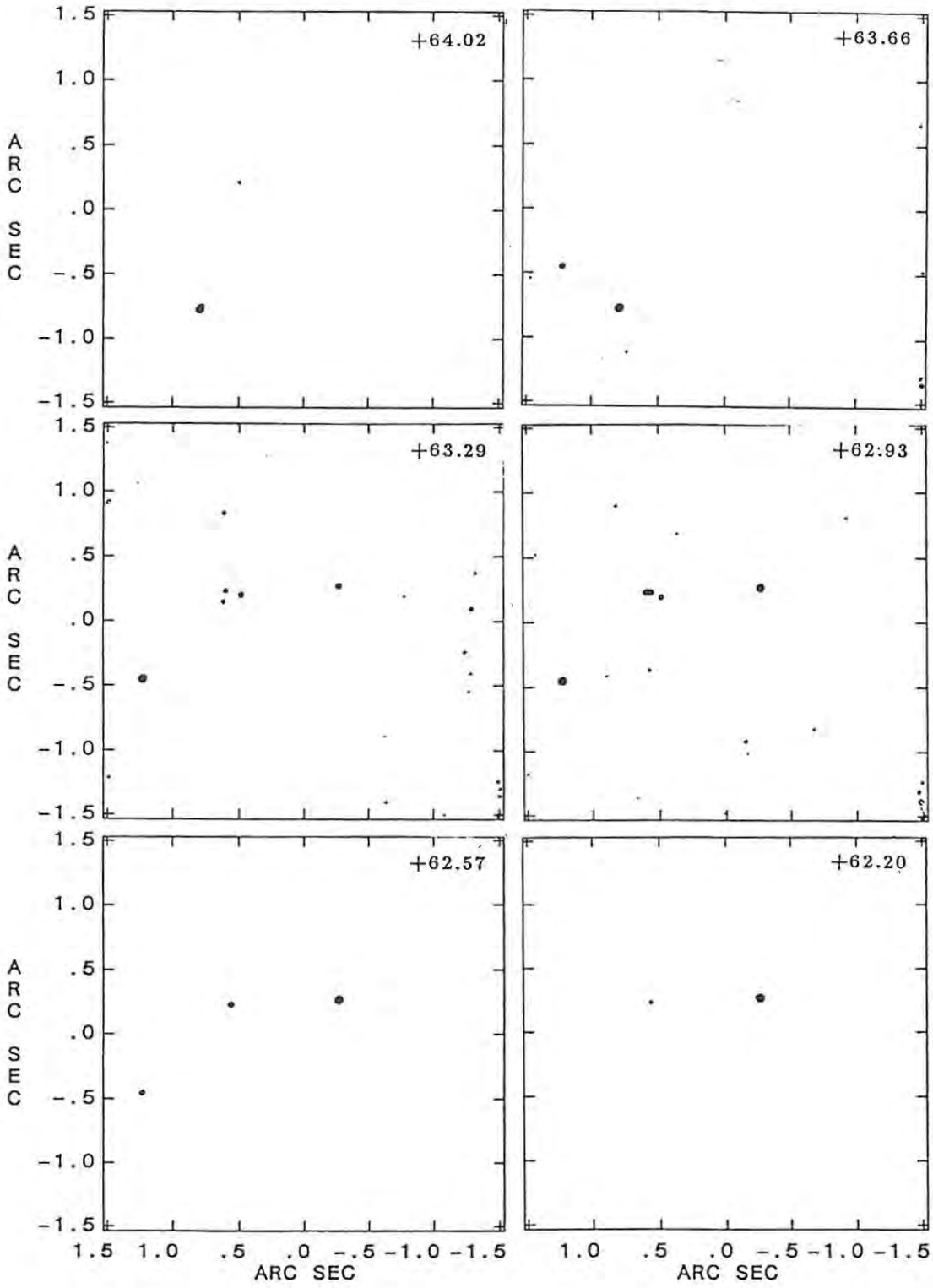

Fig. 4.6. The channel maps in left-circular polarization of the 1612 MHz OH maser emission towards IRC+10420 as obtained from the MK2 VLBI observations of October 1982. The LSR velocity is indicated in the upper right-hand corner of each channel map in units of kms^{-1}. The contour levels were chosen at (-20, -10, -7.5, 7.5, 10, 20, 30, 40, 50, 60, 70, 80, 90, 100) % of the peak brightness in each channel.

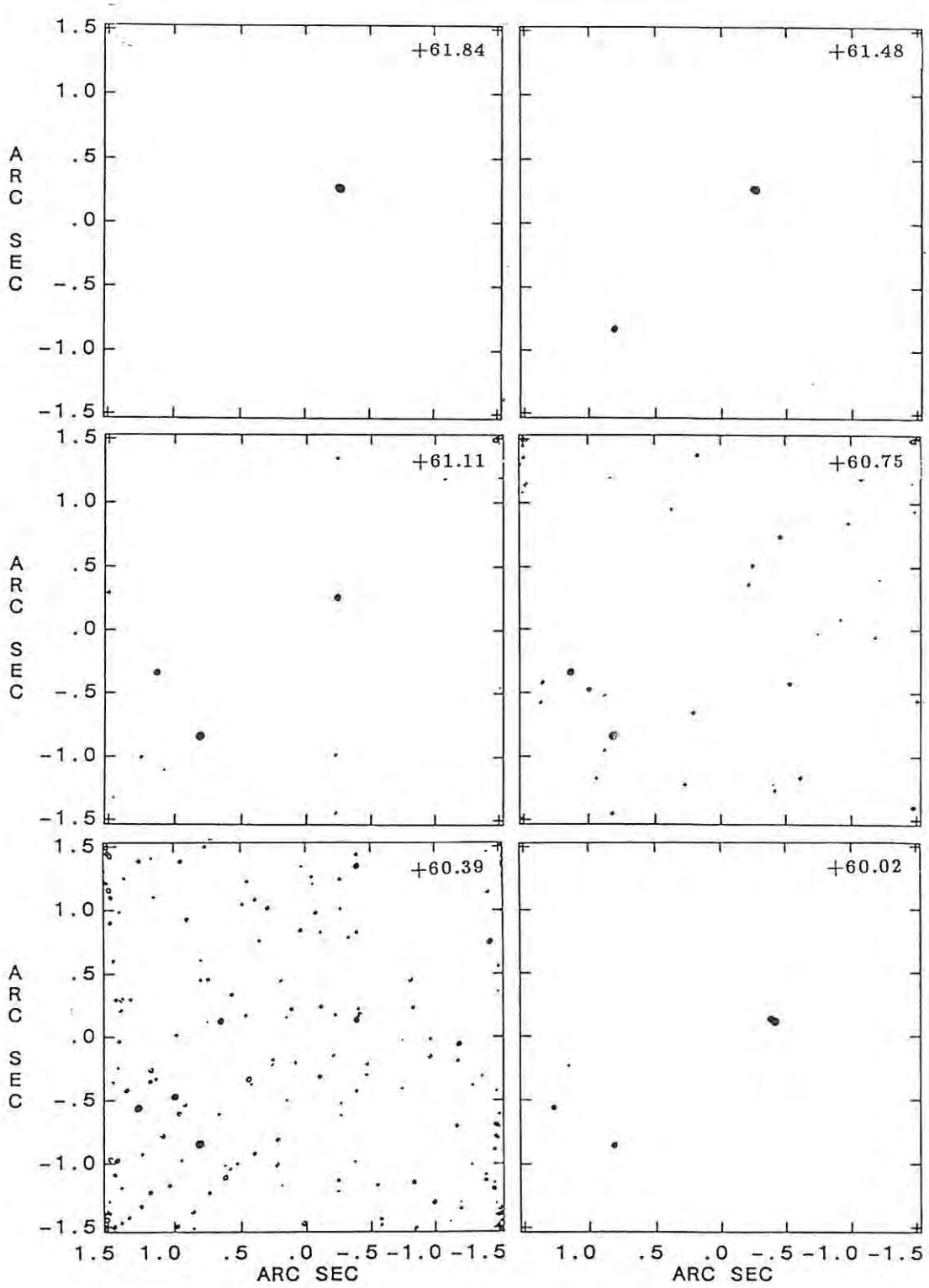

Fig. 4.6. *(continued).*

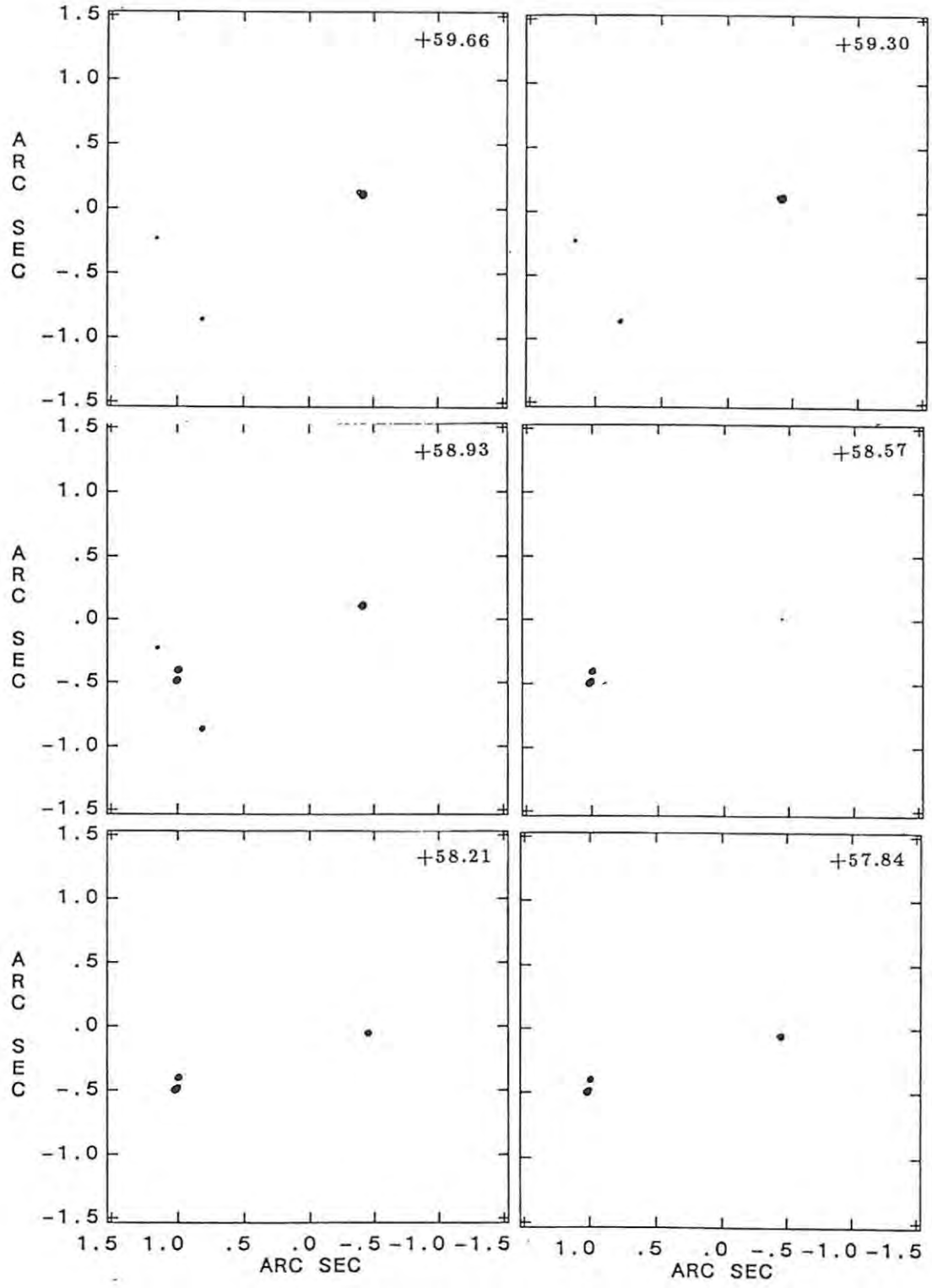

Fig. 4.6. *(continued).*

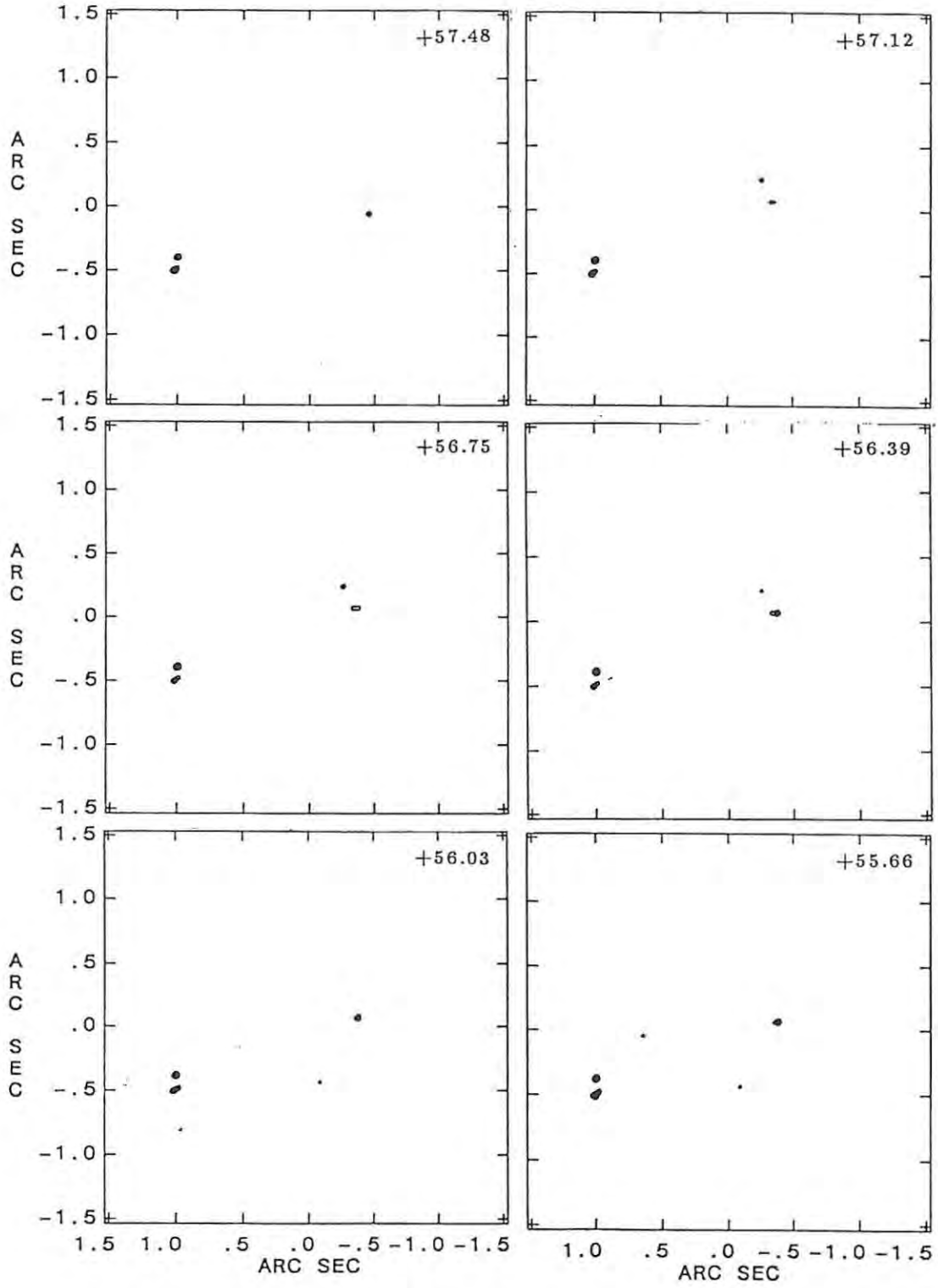

Fig. 4.6. *(continued).*

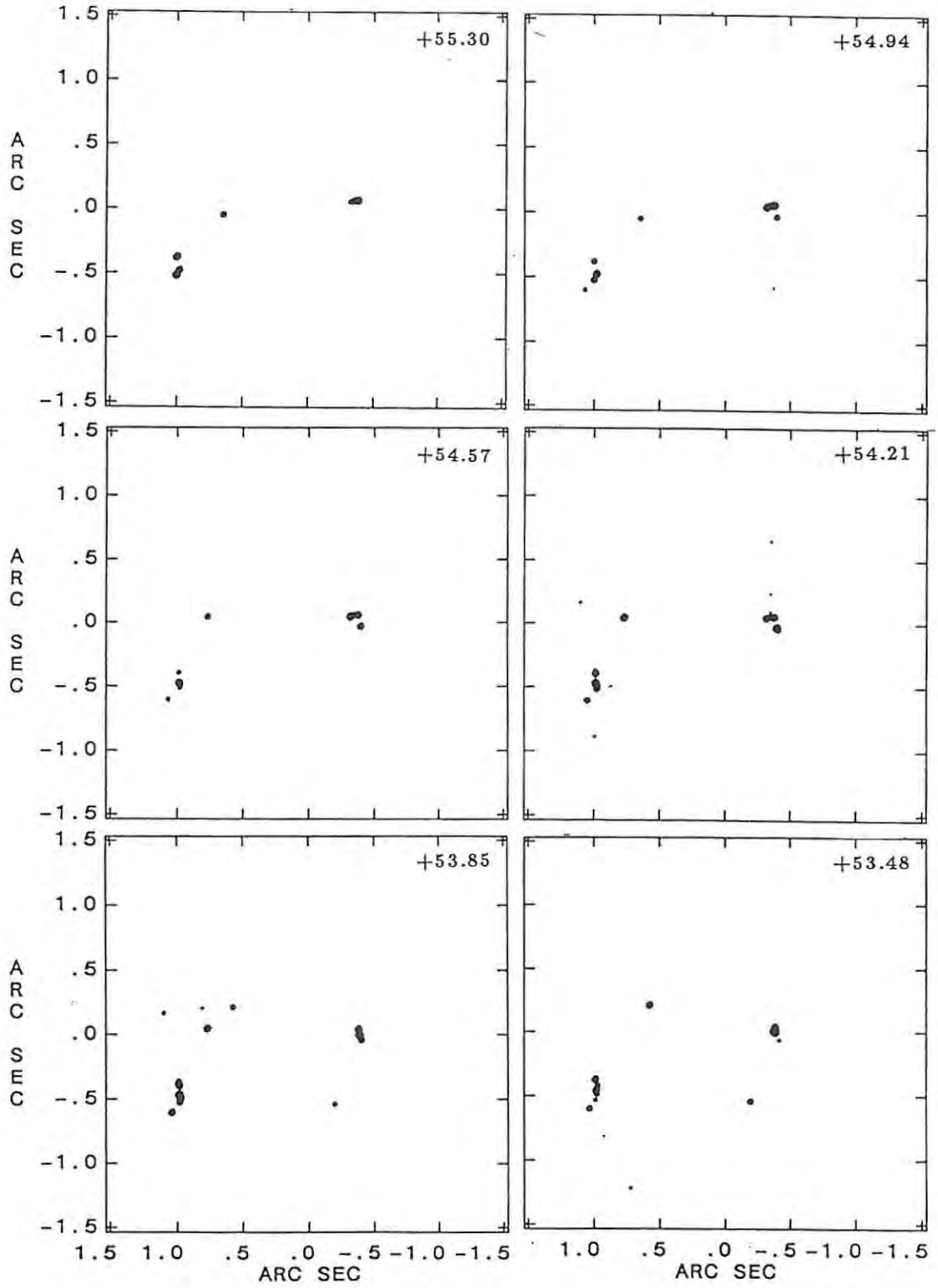

Fig. 4.6. *(continued).*

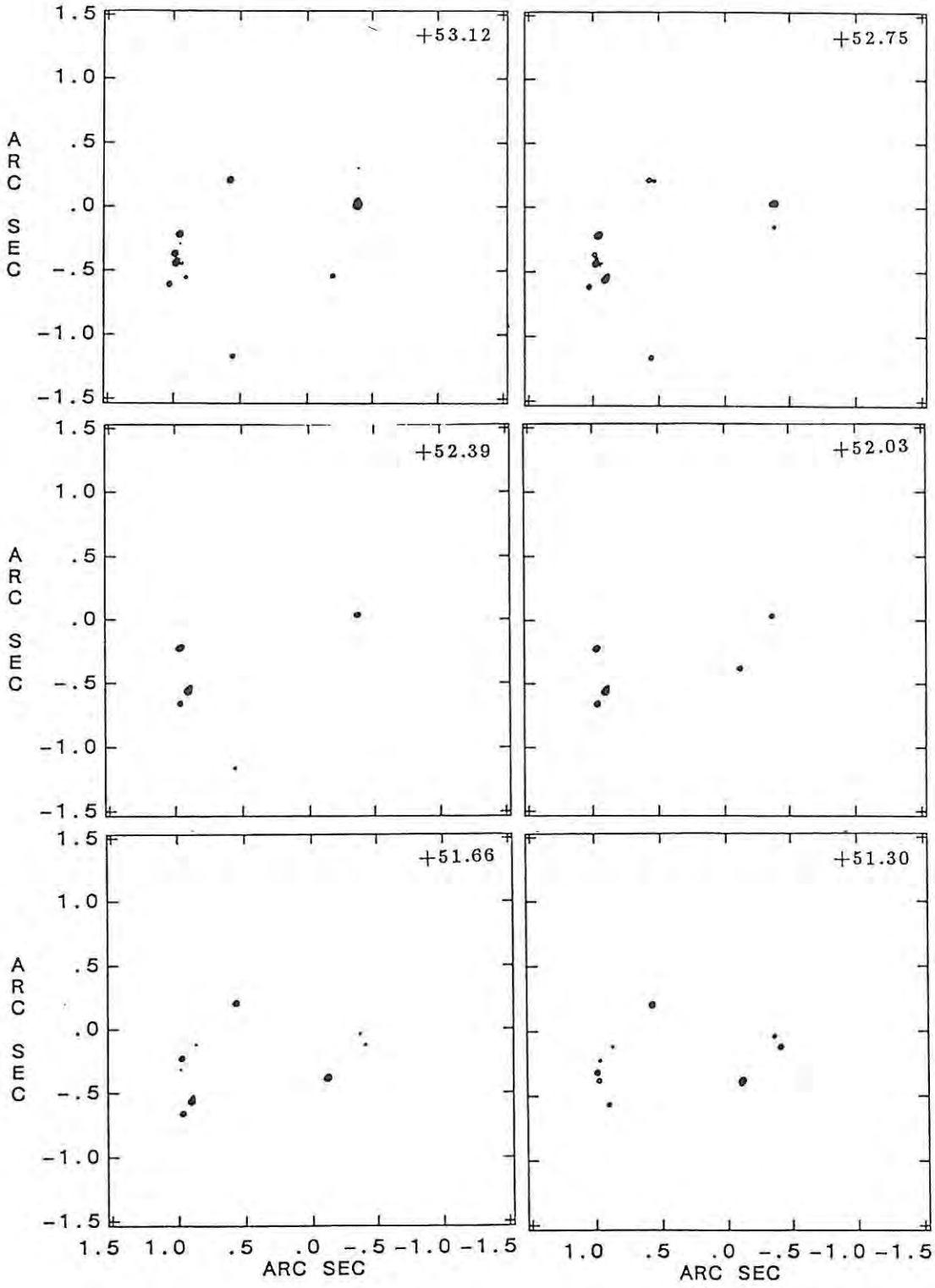

Fig. 4.6. *(continued).*

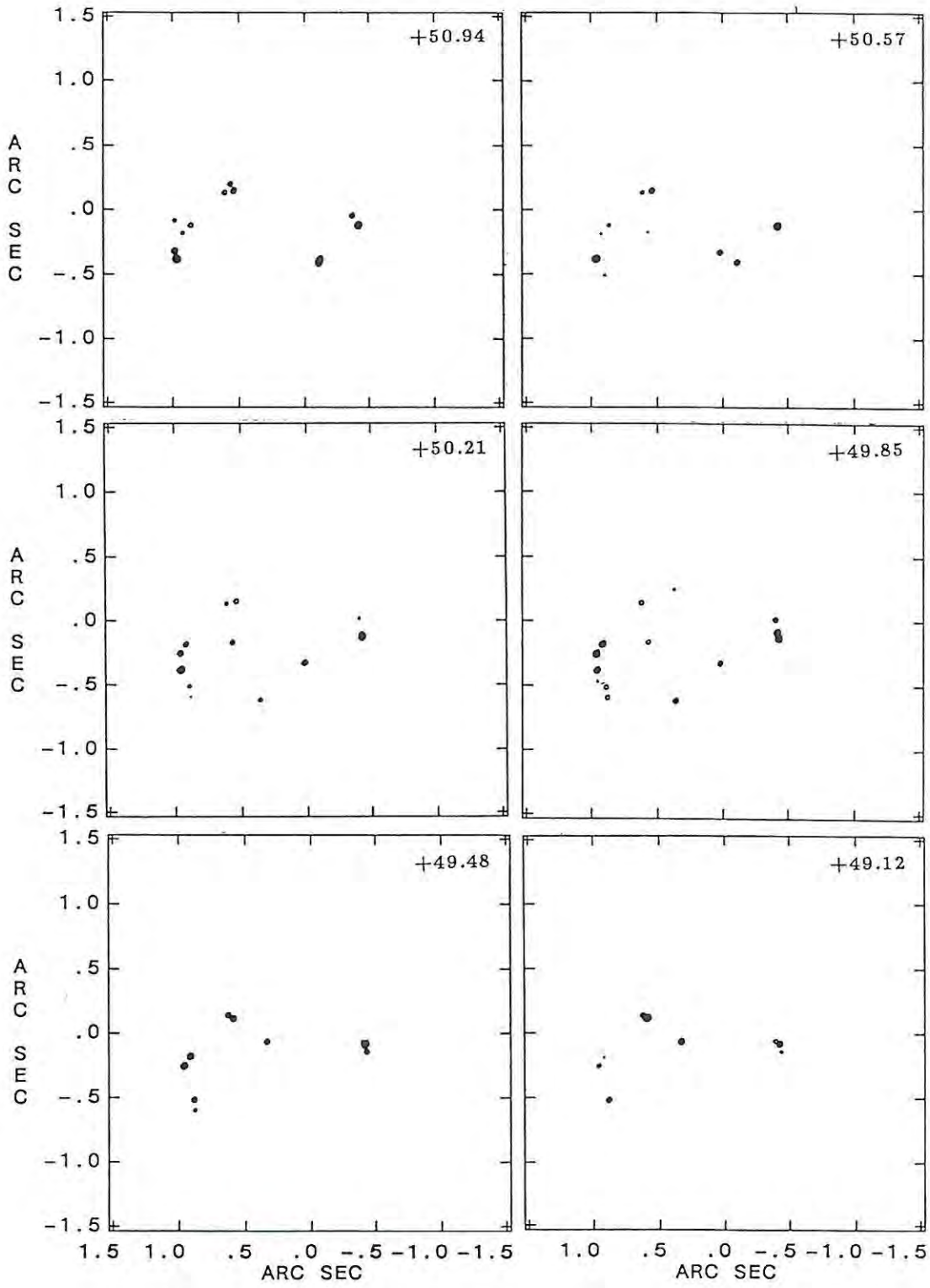

Fig. 4.6. *(continued).*

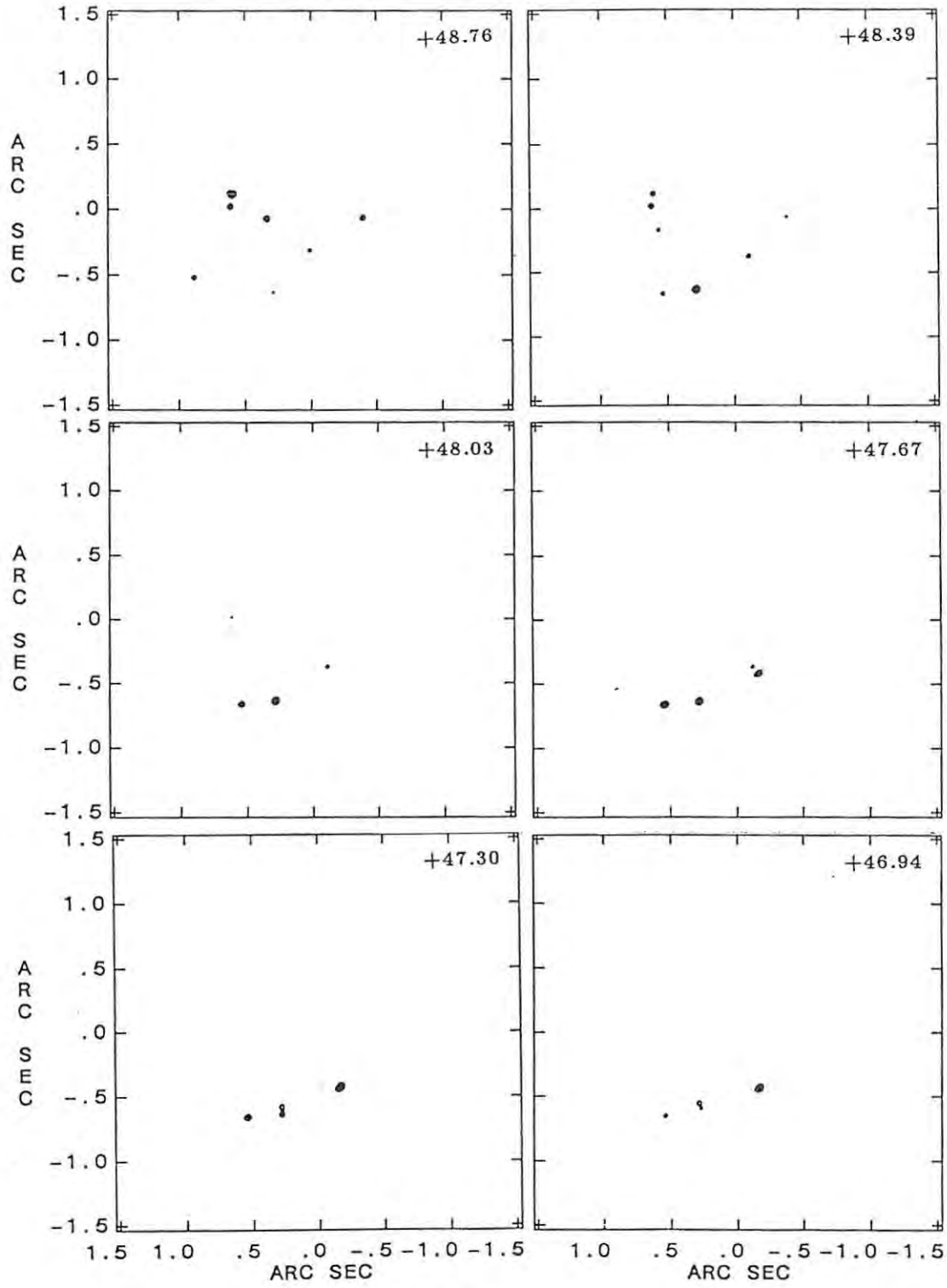

Fig. 4.6. *(continued).*

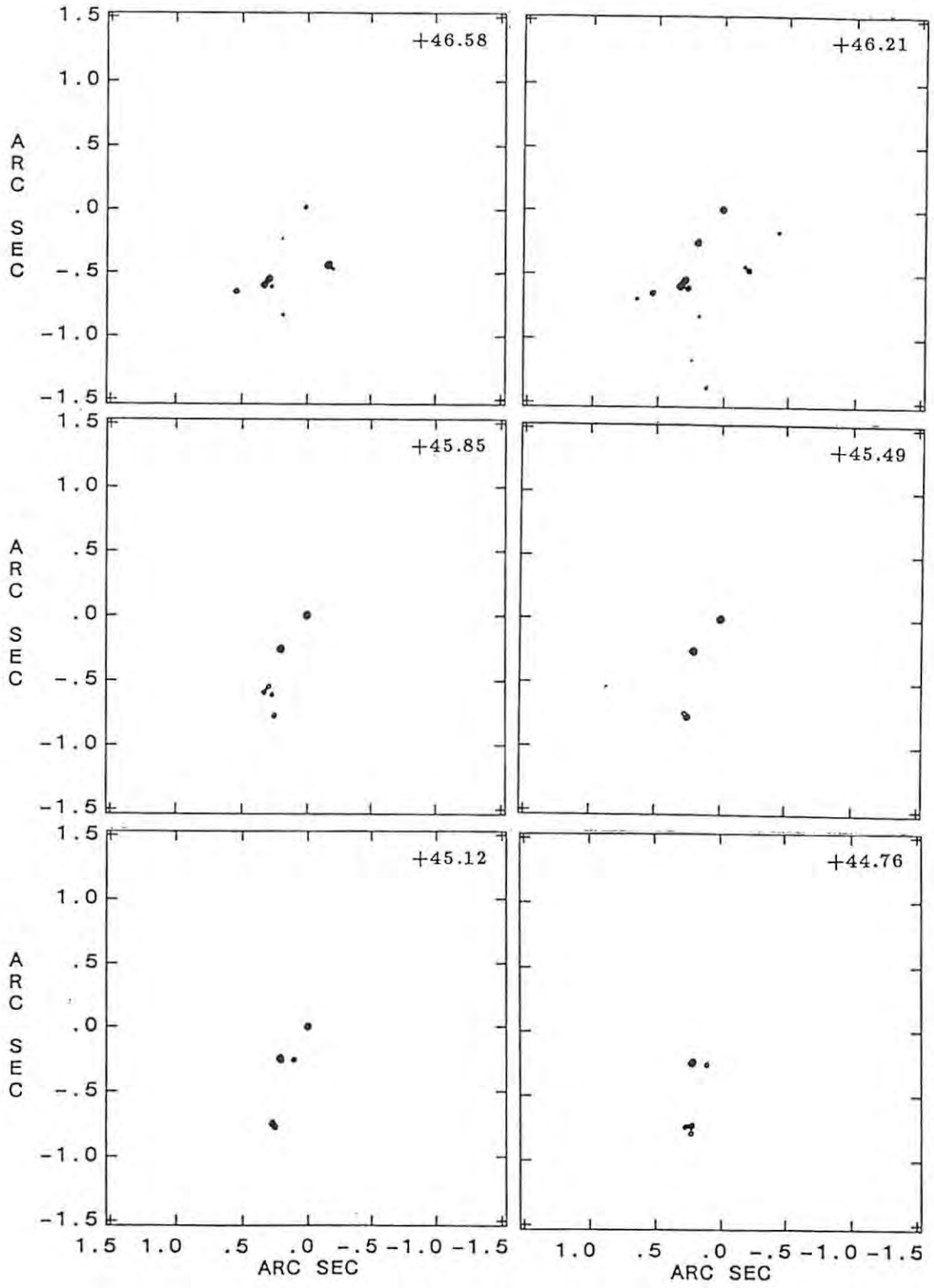

Fig. 4.6. *(continued).*

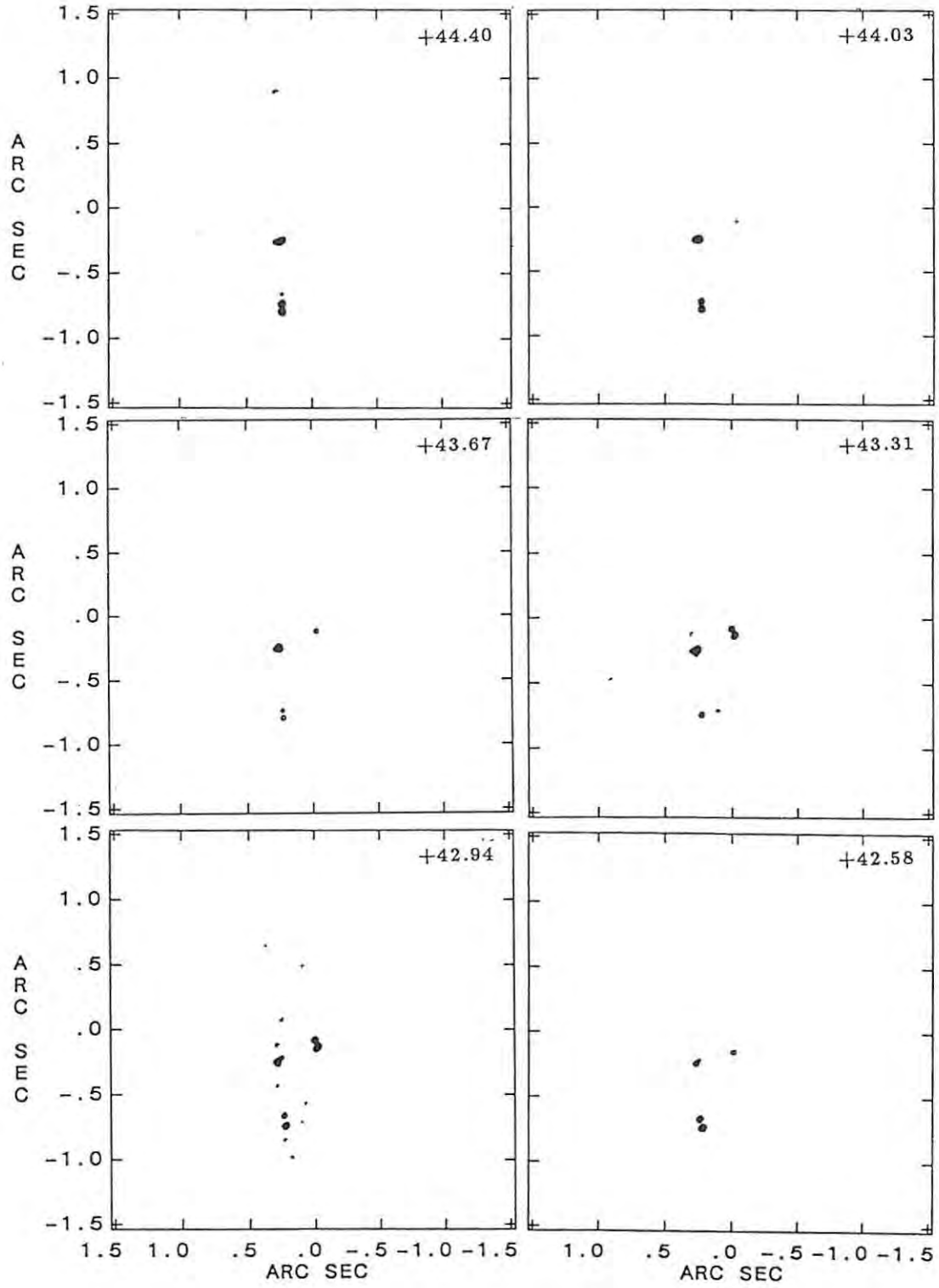

Fig. 4.6. *(continued).*

CHAPTER 5: MK3 OBSERVATIONS OF IRC+10420

Introduction

This chapter describes dual polarization MK3 observations of IRC+10420 conducted using a network of EVN telescopes in March 1987. The data reduction technique is discussed and the results are presented. The astrophysical interpretation of the results as well as further image analysis is discussed in Chapter 7.

5.1 Observations

Simultaneous, full polarization VLBI observations of the three principal OH maser transitions towards IRC+10420 at 1612, 1665 and 1667 MHz were proposed in 1986 using the MK3 recording system. The proposers were P. Diamond, D. A. Graham, R.J. Cohen, R.S. Booth, R.T. Schilizzi and F. Mantovani. The aim of the experiment was to map the four Stokes parameters in each transition and by so doing locate the possible Zeeman pairs throughout the circumstellar envelope and allow an estimate of the magnetic field. We consider here only the reduction of the 1612 MHz data as the 1665 MHz and 1667 MHz data proved too weak to image reliably. All post-correlation data reduction was undertaken by the author.

The observations were successfully conducted on 1 March 1987 from 03:00 - 14:30 UT using a network of EVN telescopes comprising Effelsberg, Jodrell MkIA, the Westerbork phased array, Onsala and Medicina. All stations observed both right- and left-circularly polarized emission except Medicina where only left-circularly polarized data were recorded. The system parameters for each station are given in Table 5.1.

The observations were conducted in MK3 mode C recording a net upper sideband video bandwidth of 250 kHz for each polarization at each transition. The data were sampled at 500 kHz resulting in a tape speed $\frac{1}{8}$th of normal. The 1612

TABLE 5.1

Antenna Parameters

Station	Diameter (m)	J^1_{sys} (Jy)	Mount type
Effelsberg	100	27	Alt/Az
Jodrell MkIA	76	84	Alt/Az
Westerbork Array	~ 55	170	Ha/Dec
Onsala 85	26	330	Ha/Dec
Medicina	32	~ 1450	Alt/Az

[1] Nominal zenith system temperature in Janskys

MHz bandwidth was centred on an LSR velocity of $\sim +50$ kms^{-1}. The continuum sources 3C345, 1611+343 and BL_Lac were observed as delay and bandpass calibrators approximately every three hours throughout the run. System temperature measurements were requested at the start of each thirty minute scan and frequency tracking was not employed. The source coordinates are given in Table 5.2.

TABLE 5.2

Source Coordinates

Source	α (1950.0)	δ (1950.0)
IRC+10420	$19^h\ 24^m\ 26.74^s$	$11^\circ\ 15^m\ 11.2^s$
3C345	$16^h\ 41^m\ 17.6^s$	$39^\circ\ 54^m\ 10.81^s$
1611+343	$16^h\ 11^m\ 47.92^s$	$34^\circ\ 20^m\ 19.83^s$
BL_Lac	$22^h\ 00^m\ 39.4^s$	$42^\circ\ 02^m\ 08.6^s$

5.2 Data Reduction

The data were correlated at the MK3 correlator at Haystack Observatory, initially by P. Diamond and subsequently in absentee mode. The correlator A-tapes

were read directly into AIPS using the task MK3IN, which was substantially modified as part of this work to deal with spectral line polarization data as discussed in Appendix A. The 112-channel cross-power spectra were formed using uniform weighting yielding a resolution of ~ 0.50 kms^{-1}. The correlator load was increased eight-fold over normal due to the 250 kHz bandwidth. This led to high correlator error rates despite a relatively long correlator accumulation period of 6s. This necessitated frequent re-correlation in single-baseline mode and off-line monitoring of correlator data quality and completeness.

The data, once loaded into AIPS, were merged, concatenated and edited to remove outlying points. The subsequent data reduction path follows that described in Chapter 3 for spectral line polarization data and will be discussed only in brief here.

The complex cross-correlation bandpass response at each antenna in each sense of polarization $B_m^p(\omega)$ was determined from the respective pre-averaged parallel-hand cross-power spectra for the continuum calibrator sources 3C345, 1611+343 and BL_Lac. The bandpass response at each antenna was assumed time-independent and was removed from the cross-correlation data using the relation (3.1). The autocorrelation bandpass response was determined separately and used to correct the autocorrelation data as in (3.2). The residual geometric Doppler shift at each antenna was removed and the autocorrelation and cross-correlation spectra centred on an LSR velocity of $V_{LSR} = +50$ kms^{-1}.

The antenna-based amplitude gains were determined separately in each sense of polarization with respect to a set of reference RCP and LCP autocorrelation template scans at Effelsberg from 07:00 - 07:30 UT using the baseline-independent fitting method described in section 3.4. The autocorrelation spectra were badly contaminated by GLONASS satellite interference and poorly sampled in time due to correlator errors. To synthesise more complete gain corrections the shape of the

gain curve at each antenna was assumed independent of polarization except for a constant scaling factor. The scaling factors were determined using least squares minimisation to align the two gain curves in each polarization and a more complete composite gain curve was then generated.

The functional form of the Jodrell gain curve was derived from the 1665 MHz autocorrelation gain data due to severe interference at 1612 MHz. The autocorrelation gain at Jodrell for the two polarizations at 1612 MHz was established using the cross-correlation data for the point-source calibrator 1611+343, subject to the relation (3.4).

The differential gain of the two 1612 MHz template scans at the reference antenna was determined using (3.5). The relative gain of the two polarizations is estimated to be good to within a few percent. The absolute flux density scale was established using system temperature measurements and an estimate of the mean integrated antenna temperature due to the source, $\bar{T}_a$, derived from the offset in the bandpass-corrected autocorrelation spectra and the ratio of cross-correlation to autocorrelation gains. The scaled I and V autocorrelation spectra at the reference antenna Effelsberg are shown in Fig. 5.1.

The first step in the phase calibration proper was the removal of parallactic angle phases in each sense of polarization. The phase-calibration system was disabled during the observations as the 10 kHz signal interferes with spectral line observing and these gains were set to unit modulus and zero phase. The residual group delays were determined independently in each polarization using global fringe-fitting to the cross-power data for the continuum calibrators. The delay offset $\delta\tau_0^{R-L}$ at the reference antenna (Effelsberg) was determined from the residual group delays on the Effelsberg-Jodrell baseline for the scans on the continuum calibrator 3C345 at 5^h and 11^h UT using the relations (3.11). The cross-polarized fringes for these scans were well-detected and a value of $\delta\tau_0^{R-L} = (182 \pm 4.5)$ ns

was obtained, which was assumed constant throughout the observing run. This was used to correct the independent delay solutions in each polarization as indicated in equation (3.9), thus locating the parallel- and cross-polarized fringes in the same delay frame. The delay solution was smoothed, interpolated and applied to the program source IRC+10420.

The residual fringe rate corrections were determined by using global fringe-fitting on a selected reference channel in the source spectrum at $V_{LSR} = 44.18$ kms^{-1} using only the left-circularly polarized data r_{mn}^{LL}. The differential phase offset at each antenna $\delta\phi_m^{R-L}$ consists of an instrumental term due to the independent phase offsets for each video converter in the MK3 system and a component due to ionospheric Faraday rotation. The Faraday rotation was removed using a phenomenological model of ionospheric electron density (Chiu 1975; UAG 1981) which takes the Zurich sunspot number R_Z as input. The observations were performed relatively close to the minimum for solar cycle 22 which started in September 1986. A sunspot number of $R_Z = 14$ (NGDC 1987) was used which predicts a peak ionospheric phase rotation of ~ 6 deg (Fig. 5.2). The software to compute the ionospheric Faraday rotation was incorporated into AIPS by C. Flatters and uses a standard model for the Earth's magnetic field (Valley 1965). The differential video converter phases were determined using the phase difference between the parallel-hand cross-power spectra of the continuum calibrator sources by solving the equations (3.12). As discussed previously this introduces an unknown constant phase offset at the reference antenna as the system of equations is under-determined. This is however the only approach possible in the absence of a suitable polarization calibrator. The relative phases of the video converters displayed a slow drift with time which did not exceed 1 μ Hz in the worst case although this may be contaminated by unmodelled ionsopheric Faraday rotation. The differential fringe rate $\delta\dot{\phi}_m$ was assumed negligible for reasons discussed in

section 3.5.4. The fringe rate and phase solution for the reference channel in the reference polarization (LCP) was corrected for the differential polarization phase offsets discussed above using the relation (3.10), thus deriving a phase solution for the orthogonal polarization (RCP) in the same phase frame.

5.3 Imaging

The residual antenna gain phases were determined by self-calibration imaging of a reference channel at $V_{LSR} = 44.18$ kms^{-1} in RR. The mapping strategy described in section 3.5.3 was used, although Medicina was excluded to provide balanced (u, v) coverage in each sense of polarization. The gain phases were applied to the data cube to derive the calibrated data set suitable for generating the (I,V) images. The fit to the reference channel in amplitude and closure phase is shown in Fig. 5.3 and Fig. 5.4. The dirty beam for the (I, V) images is plotted in Fig. 5.5. The natural restoring beam, obtained by fitting an elliptical Gaussian fit to the centre lobe of the dirty beam, was used in the CLEAN deconvolution step. The final I images are plotted in Fig. 5.6. Each map is 512 x 512 pixels with a pixel spacing of 6 mas.

The calibrated data were used to determine the instrumental feed contamination as parametrized by the D-terms in equations (3.13). The observed continuum sources were unsuitable as polarization calibrators either as a result of poor parallactic angle coverage, resolved or extended polarized emission or inadequate SNR in the cross-polarized fringes due to the limited video bandwidth. As a result the spectral line program source IRC+10420 was used to derive an approximate D-term solution using the technique discussed in section 3.6. The velocity range $V_{LSR} = \{40.03, \quad 64.94\}$ kms^{-1} of the source cross-power spectrum was used for the fit to equation (3.14) with each channel treated as an independent linearly unpolarized source. This approach was motivated by the apparent absence of significant intrinsic linear polarization in the uncorrected cross-polarized data when

TABLE 5.3

Feed Polarizations

Station	D^R		D^L	
	$\|D^R\|$	$\arg(D^R)$ (deg)	$\|D^L\|$	$\arg(D^L)$ (deg)
Effelsberg	0.0527	23.4	0.123	140.4
Jodrell MkIA	0.0107	61.4	0.0099	-56.4
Westerbork Array	0.0483	-178.3	0.0522	-45.7
Onsala 85	0.0370	174.2	0.0681	-16.1

plotting ratios of the form $\frac{\mathcal{RL}(\omega)}{\mathcal{RR}(\omega)}$ and $\frac{\mathcal{LR}(\omega)}{\mathcal{LL}(\omega)}$. A solution interval of 10 min was used in the fit. The ionospheric Faraday rotation terms γ_m^{R-L} were considered negligible compared to the noise in the cross-polarized data and were not corrected in the fit. Tests where an ionsopheric Faraday rotation model was included did not lead to significantly lower post-fit residuals. The resulting D-terms are given in Table 5.3.

The data were corrected using the relation (3.15), again neglecting the ionospheric Faraday rotation terms. The Q and U images were obtained from the corrected data using the method described in section (3.7). The real and imaginary parts of the complex dirty beam are plotted in Fig. 5.7 and Fig. 5.8. The same CLEAN restoring beam and antenna weights were used as for the I and V images. Table 5.4 contains a list of all components in the I images with peak apparent brightness greater than the absolute value of the deepest negative in the velocity channel. The Stokes I components were fitted as elliptical Gaussians in relative right ascension and declination over an interactively defined rectangular region tightly enclosing the component in the image plane. The apparent size of the I components was estimated from the fit by removing the effects of the CLEAN restoring beam using straightforward algebraic formulae for the deconvolution of

two elliptical Gaussians. Deconvolved sizes that are upper limits are enclosed in parentheses.

The velocity width in Stokes I was determined by an independent fit over velocity at the position of peak component brightness (X, Y). The velocity fit was performed interactively using one or more Gaussian components to fit the line profile. The apparent component brightness in Stokes Q, U and V was taken to be the pixel value at the position of the peak I brightness (X, Y). This approach was adopted to avoid systematic bias which is likely if fitting an elliptical Gaussian with a peak less than four times the root mean square (rms) error in the map (Fomalont 1986). The components are assumed to have the same angular size in each Stokes parameter.

The fractional circular and linear polarization of each component, m_c and m_l, given in Table 5.4 are defined as,

$$m_c = \frac{V}{I}$$
$$m_l = \frac{P}{I} = \frac{\sqrt{Q^2 + U^2}}{I}$$

Both m_c and m_l have non-Gaussian probability distributions (Wardle and Kronberg 1974; McIntosh 1987) and the significance of a detection needs to be carefully determined. The measured off-peak rms noise in each velocity channel will be denoted by $\sigma_I^0(\omega), \sigma_V^0(\omega), \sigma_Q^0(\omega)$ and $\sigma_U^0(\omega)$. These measures were taken in corner regions of each channel image and do not adequately describe the noise statistics across central parts of the image where systematic imaging errors dominate. These are caused by inadequate (u, v) sampling and possible calibration and deconvolution errors. The poor sampling results from the limited number of antennas and correlator data losses in this recording mode, as evidenced in Fig.

5.3. Systematic effects may show up as regions of negative brightness in the I images which have no physical interpretation or as corrugations or striping. Broadly speaking, systematic imaging errors often add a non-Gaussian tail to the noise distribution. The deepest negative pixel in each I channel image provides some measure of the systematic error. Assuming a Gaussian noise distribution, the magnitude of the deepest negative, $|I_{neg}|$ implies a noise variance of $\sigma_I \sim |I_{neg}|/4.6212$, for a map of 512x512 pixels. This was used in a strictly non-rigorous manner to broaden the rms noise estimates as $\sigma_I = \beta\sigma_I^0, \sigma_V = \beta\sigma_V^0, \sigma_Q = \beta\sigma_Q^0, \sigma_U = \beta\sigma_U^0$, where $\beta = \frac{|I_{neg}|}{4.6212\sigma_I^0}$. The frequency dependence of these quantities is assumed implicit in what follows. The Stokes parameters $\{I, V, Q, U\}$ for each component are assumed in this analysis to be drawn from normal distributions with the above variances.

The hypothesis that the calculated fractional circular polarization $\frac{V}{I}$ is drawn from a zero-mean population can be rejected at a 95% level of significance if $\frac{V}{I} > u_c$, where u_c is obtained by solving $\int_{-u_c}^{u_c} \phi_0^c(m_c)\, dm_c = 0.95$, and $\phi_0^c(m_c)$ is the probability distribution for m_c with $V = 0$. To within a few percent, $u_c \sim \frac{1.96\sigma_V}{I}$ if $I >> \sigma_I$, which is true for most of the data in Table 5.4. For completeness $\phi_0^c(m_c)$ is given by,

$$\phi_0^c(m_c) = \frac{1}{2\pi\sigma_V\,\sigma_I {m_c}^2}\left[\frac{1}{p}e^{\frac{I^2}{2\sigma_I^2}} + \frac{q}{p}\sqrt{\frac{\pi}{p}}e^{\frac{q^2}{p}-\frac{I^2}{2\sigma_I^2}}\Phi(\frac{q}{\sqrt{p}})\right]$$

where $p = \frac{1}{2\sigma_V^2} + \frac{1}{2\sigma_I^2 m_c^2}$, $q = \frac{I}{2\sigma_I^2 m_c}$ and $\Phi(x)$ is the error function. This probability distribution was derived using standard statistical techniques for functions of continuous distributions (Hamilton 1964, p.19).

In this definition of m_c the distribution is symmetric about zero and no correction for bias needs to be made. The detection limit u_c was derived by numerical integration of $\phi_0^c(m_c)$ as described above. If $\frac{|V|}{I} < u_c$ then m_c was set to zero in Table 5.4.

The fractional linear polarization m_l has a Rice probability distribution (Wardle and Kronberg 1974). The hypothesis that m_l is zero can be rejected at a 95% level of significance if $\frac{\sqrt{Q^2+U^2}}{I} > u_l$, where u_l is obtained by solving $\int_0^{u_l} \phi_0^l(m_l)\, dm_l = 0.95$ and $\phi_0^l(m_l)$ is the probability distribution for m_l with $Q = U = 0$. The linear polarization $P = \sqrt{Q^2 + U^2}$ has a Raleigh type probability distribution $\phi_0^P(P)$ if Q and U are zero-mean Gaussian variables. This can be derived as,

$$\phi_0^P(P) = \frac{P e^{\frac{-P^2}{2\sigma_U^2}}}{2\pi\sigma_Q\sigma_U}[2\pi + \varrho]$$

$$\varrho = \sum_{k=1}^{\infty}(-1)^k \frac{\alpha^k}{k!}\left[\frac{2\pi}{2^{2k}}\binom{2k}{k} + \frac{2}{2^{2k-1}}\sum_{l=0}^{k-1}\binom{2k}{l}\frac{\sin(2\pi(k-l))}{2k-2l}\right]$$

where $\alpha = P^2[\frac{1}{2\sigma_Q^2} - \frac{1}{2\sigma_U^2}]$. The less general case is considered by TMS (p.260). Assuming $\sigma_Q \sim \sigma_U$, as is typically the case for these data, then $\sigma_{QU} = \sqrt{\sigma_Q\sigma_U}$ and $\phi_0^l(m_l)$ takes the form,

$$\phi_0^l(m_l) = \frac{1}{\sqrt{2\pi}\sigma_{QU}^2\,\sigma_I m_l^2}\left[\frac{be^{-\frac{I^2}{2\sigma_I^2}}}{a^2} + \sqrt{\frac{\pi}{a^5}}\frac{(2b^2+a)}{2}e^{\frac{b^2}{a}-\frac{I^2}{2\sigma_I^2}}\Phi(\frac{b}{\sqrt{a}})\right]$$

where $a = \frac{1}{2\sigma_{QU}^2} + \frac{1}{2\sigma_I^2 m_l^2}$ and $b = \frac{I}{2\sigma_I^2 m_l}$. The 95% detection limit u_l was derived by numerical integration of $\phi_0^l(m_l)$ as described above. If $\frac{\sqrt{Q^2+U^2}}{I} < u_l$ then m_l was set to zero in Table 5.4. The detection limit u_l can be approximated by a range estimate,

$$u_l = \frac{1.65}{\sqrt{2}}\left[\frac{P+\sigma_P}{I-\sigma_I} - \frac{P-\sigma_P}{I+\sigma_I}\right]$$

where the factor 1.65 derives from a one-tailed test on an assumed normal distribution and $\sigma_P = \frac{\sqrt{Q^2\sigma_Q^2+U^2\sigma_U^2}}{P}$. This approximation typically underestimates

u_l by up to $\sim$ 10% for $m_l < 0.05$ but may overestimate u_l by up to $\sim$ 35% for $m_l \sim 0.2$ for the signal to noise ratios of the data in Table 5.4

The fractional linear polarization is positive with a non-Gaussian distribution and the calculated value $m_l = \frac{\sqrt{Q^2+U^2}}{I}$ needs to be corrected for bias (Wardle and Kronberg 1974). The true fractional linear polarization m_l' was accordingly calculated as (TMS p.262),

$$m_l' = \frac{\sqrt{Q^2 + U^2 - \sigma_{QU}^2}}{I}$$

If $m_l > 0$ then the position angle of the linearly polarized emission was calculated as (McIntosh 1987),

$$\chi = \frac{1}{2} \arctan\left(\frac{U}{Q}\right)$$

.

The probability distribution for χ is symmetric (Wardle and Kronberg 1974) and no correction for bias is necessary.

TABLE 5.4
List of Components

V^a	$\triangle V^b$	X^c	Y^c	θ^d_{maj}	θ^d_{min}	PA^e	I^f	V^f	Q^f	U^f	m^g_c	m'_l	χ^h
64.53	0.91	0.192	0.622	(26.9)	(26.9)	(180.0)	0.089	0.006	-0.002	-0.001	0.0	0.0	0
64.10	0.50	0.257	0.471	(14.3)	(14.3)	(180.0)	0.287	0.081	0.001	0.011	28.3	0.0	0
64.10	0.51	0.493	-0.673	(26.8)	(26.8)	(180.0)	0.124	-0.033	0.001	-0.007	-26.5	0.0	0
63.99	0.75	0.558	-0.521	10.3	6.9	118.4	0.985	-0.354	-0.007	-0.004	-35.9	0.0	0
62.90	0.33	-0.514	0.528	17.3	7.0	61.6	0.322	0.110	-0.002	0.003	34.0	0.0	0
62.90	0.48	1.019	-0.196	(8.1)	(8.1)	(180.0)	0.545	-0.079	-0.010	-0.040	-14.4	7.4	-52
62.48	0.49	0.342	0.500	(26.3)	(26.3)	(180.0)	0.300	-0.072	0.003	0.000	-24.0	0.0	0
61.88	0.61	-0.509	0.531	45.3	8.8	52.4	1.058	0.681	-0.003	-0.001	64.4	0.0	0
61.79	0.65	-0.409	0.667	(41.8)	(41.8)	(180.0)	0.138	0.042	0.004	-0.004	0.0	0.0	0
61.45	0.60	0.257	-1.253	(7.8)	(7.8)	(180.0)	0.427	0.082	0.005	0.001	19.2	0.0	0
61.44	0.71	-0.548	0.520	(19.7)	(19.7)	(180.0)	0.197	0.196	-0.005	0.013	99.9	0.0	0
61.36	0.59	1.154	-0.354	(19.9)	(19.9)	(180.0)	0.366	-0.005	-0.022	-0.005	0.0	0.0	0
60.72	0.37	-0.496	0.540	(20.8)	(20.8)	(180.0)	0.398	0.037	-0.004	-0.013	0.0	0.0	0
60.57	0.97	0.581	-0.595	(15.3)	(15.3)	(180.0)	0.171	0.110	-0.006	-0.017	64.3	0.0	0
60.34	0.59	-0.549	0.435	(13.4)	(13.4)	(180.0)	0.378	0.269	-0.001	-0.005	71.1	0.0	0
60.23	0.62	1.037	-0.311	(9.8)	(9.8)	(180.0)	0.817	0.023	-0.035	-0.025	0.0	5.0	-72
59.85	0.58	-0.643	0.395	(26.2)	(26.2)	(180.0)	1.278	0.256	0.000	-0.030	20.0	2.1	-45
59.62	0.53	-0.787	-0.119	(11.8)	(11.8)	(180.0)	0.095	-0.008	0.007	0.015	0.0	0.0	0
59.51	0.75	0.582	-0.611	(11.6)	(11.6)	(180.0)	0.288	0.152	-0.012	-0.007	52.8	0.0	0
59.50	0.53	-0.670	0.372	26.6	7.6	68.8	2.855	-0.223	0.078	-0.008	-7.8	2.6	-2
59.30	0.58	0.076	-1.104	(14.4)	(14.4)	(180.0)	0.180	0.010	0.005	-0.002	0.0	0.0	0
59.22	0.57	1.053	-0.337	(29.7)	(29.7)	(180.0)	0.308	0.020	-0.012	0.008	0.0	0.0	0
59.21	0.27	0.779	-0.241	(12.3)	(12.3)	(180.0)	0.236	-0.060	0.008	0.008	-25.3	0.0	0
59.09	0.65	0.766	-0.149	(11.9)	(11.9)	(180.0)	0.491	-0.022	0.003	-0.027	0.0	0.0	0
59.05	0.59	0.224	0.718	(15.3)	(15.3)	(180.0)	0.852	0.222	0.000	0.002	26.0	0.0	0
58.70	0.62	-0.716	0.286	42.5	7.3	137.0	0.411	0.043	0.008	0.001	0.0	0.0	0
58.66	0.61	0.129	-1.154	(9.9)	(9.9)	(180.0)	0.412	-0.112	0.002	-0.013	-27.2	0.0	0
58.48	0.68	-0.701	0.264	29.2	5.0	171.1	0.263	0.003	0.002	-0.005	0.0	0.0	0
58.27	0.48	0.779	-0.242	13.0	4.9	112.3	2.358	-0.679	0.009	-0.022	-28.8	0.0	0
57.90	0.54	-0.701	0.206	(35.9)	(35.9)	(180.0)	0.469	0.044	-0.001	-0.001	0.0	0.0	0
57.89	0.78	-0.738	0.407	21.2	1.1	75.8	0.351	0.050	-0.002	0.011	0.0	0.0	0
57.85	0.49	-0.488	0.524	17.6	11.4	24.9	0.287	-0.032	0.010	-0.007	0.0	0.0	0
57.68	0.64	0.221	0.714	(15.2)	(15.2)	(180.0)	0.265	0.042	0.003	0.006	0.0	0.0	0
57.60	0.61	0.906	-0.330	(11.4)	(11.4)	(180.0)	0.289	-0.010	-0.014	-0.006	0.0	0.0	0
57.53	0.78	0.797	-0.857	10.8	6.3	158.8	0.146	-0.016	0.007	-0.005	0.0	0.0	0
57.49	0.48	1.104	-0.452	(18.2)	(18.2)	(180.0)	0.302	0.025	-0.004	-0.006	0.0	0.0	0
57.47	0.47	-0.629	0.327	6.6	4.2	116.5	1.029	-0.453	-0.004	-0.009	-44.0	0.0	0
57.40	1.34	0.781	-0.247	23.3	2.9	128.0	1.663	-0.224	0.021	-0.018	-13.5	0.0	0
57.11	0.56	-0.660	0.216	(14.0)	(14.0)	(180.0)	0.208	0.037	-0.010	0.005	0.0	0.0	0
56.69	0.61	-0.512	0.487	42.1	5.2	33.1	0.692	0.055	0.007	0.011	7.9	0.0	0
56.65	0.47	0.110	-0.922	(6.7)	(6.7)	(180.0)	0.553	0.029	-0.008	-0.010	0.0	0.0	0
56.65	0.48	-0.581	0.328	18.5	6.7	72.8	0.674	0.045	-0.003	0.015	6.6	0.0	0
56.43	0.66	0.839	-0.117	(76.4)	(76.4)	(180.0)	0.069	0.030	-0.002	-0.006	0.0	0.0	0
56.32	0.64	-0.625	0.324	15.5	2.3	95.8	2.544	-0.852	0.005	0.035	-33.5	0.0	0
56.27	0.71	0.485	0.659	6.7	2.6	74.8	0.871	-0.210	-0.038	-0.037	-24.1	0.0	0
56.11	1.26	0.717	-0.636	(16.6)	(16.6)	(180.0)	0.264	-0.022	0.002	-0.020	0.0	0.0	0
55.92	0.66	-0.540	0.378	(17.7)	(17.7)	(180.0)	0.174	-0.014	0.001	-0.024	0.0	0.0	0
55.89	1.08	0.762	-0.126	(9.7)	(9.7)	(180.0)	3.538	-0.354	0.120	0.102	-10.0	4.4	20
55.87	0.56	0.743	0.079	12.1	10.1	106.7	0.575	0.186	-0.013	-0.022	32.4	0.0	0
55.82	0.54	-0.486	0.558	(6.1)	(6.1)	(180.0)	0.823	-0.006	0.008	0.012	0.0	0.0	0

55.80	0.57	-0.544	0.360	(31.0)	(31.0)	(180.0)	0.441	0.041	0.007	0.009	0.0	0.0	0
55.69	0.58	0.576	0.457	(7.2)	(7.2)	(180.0)	0.287	-0.353	-0.008	-0.005	-123.1*	0.0	0
55.44	0.83	-0.629	0.319	18.6	4.5	98.7	3.019	0.012	0.008	0.031	0.0	0.0	0
55.40	0.56	0.124	-0.918	12.4	3.6	100.4	1.853	-0.136	-0.063	0.028	-7.3	0.0	0
55.40	0.74	0.757	-0.251	(55.9)	(55.9)	(180.0)	0.584	0.006	-0.036	-0.028	0.0	0.0	0
55.37	0.58	0.629	0.449	11.9	4.6	91.9	0.345	0.021	0.004	0.003	0.0	0.0	0
54.96	0.54	0.578	0.498	13.3	4.1	10.7	0.270	-0.031	0.007	-0.005	0.0	0.0	0
54.59	0.51	0.137	-0.919	45.8	3.3	119.4	0.869	-0.024	-0.016	0.018	0.0	0.0	0
54.59	0.61	-0.570	0.306	(12.5)	(12.5)	(180.0)	1.455	-0.145	0.001	0.015	-10.0	0.0	0
54.51	0.75	0.741	-0.226	(9.2)	(9.2)	(180.0)	2.287	0.988	0.058	0.033	43.2	2.7	14
54.44	0.66	-0.650	0.227	(14.4)	(14.4)	(180.0)	0.548	-0.088	0.008	0.011	-16.0	0.0	0
54.41	0.76	0.623	0.430	(13.6)	(13.6)	(180.0)	1.083	0.039	0.007	-0.006	0.0	0.0	0
54.39	0.91	0.828	-0.348	(6.8)	(6.8)	(180.0)	0.533	0.013	0.013	-0.017	0.0	0.0	0
54.23	0.71	-0.626	0.307	(11.8)	(11.8)	(180.0)	1.521	-0.106	0.003	0.019	0.0	0.0	0
54.20	0.64	0.525	0.305	7.2	3.0	98.6	3.649	0.039	0.035	0.009	0.0	0.0	0
54.00	0.69	0.807	-0.347	(8.4)	(8.4)	(180.0)	1.706	-0.048	0.031	-0.015	0.0	0.0	0
54.00	0.88	0.780	-0.439	8.9	1.8	173.0	0.350	0.206	0.011	-0.003	58.8	0.0	0
53.73	0.46	-0.486	0.413	(66.2)	(66.2)	(180.0)	0.417	0.085	-0.004	-0.018	0.0	0.0	0
53.66	0.61	0.749	-0.122	(48.3)	(48.3)	(180.0)	0.604	-0.306	0.107	-0.064	-50.8	19.6	-15
53.33	0.91	-0.401	0.513	12.1	8.8	39.3	0.696	0.050	0.011	-0.017	0.0	0.0	0
53.32	0.45	0.481	-0.970	13.4	8.9	88.2	1.012	-0.098	0.017	-0.003	-9.7	0.0	0
53.25	0.55	0.695	0.050	(52.2)	(52.2)	(180.0)	0.313	-0.057	0.006	0.004	0.0	0.0	0
53.24	0.56	0.439	-0.987	45.9	6.3	57.1	0.651	-0.236	-0.012	-0.003	-36.2	0.0	0
53.09	0.84	-0.630	0.291	23.6	7.1	176.0	1.208	-0.050	-0.007	0.015	0.0	0.0	0
53.05	0.66	-0.542	0.339	(12.3)	(12.3)	(180.0)	0.520	-0.054	0.003	0.001	0.0	0.0	0
53.00	0.59	0.451	-1.002	17.8	6.2	117.3	0.556	-0.215	-0.002	0.001	-38.7	0.0	0
53.00	0.77	0.737	-0.180	(7.2)	(7.2)	(180.0)	1.255	-0.462	-0.014	-0.030	-36.8	0.0	0
52.92	0.51	0.405	-0.991	23.0	5.8	97.4	0.465	-0.015	0.016	-0.004	0.0	0.0	0
52.90	0.46	0.695	-0.695	(10.2)	(10.2)	(180.0)	0.509	0.030	0.006	-0.008	0.0	0.0	0
52.83	0.56	0.208	0.481	10.1	1.8	134.9	1.403	-0.355	0.064	-0.003	-25.3	0.0	0
52.79	0.71	0.792	-0.360	7.2	1.7	137.0	0.561	-0.070	0.018	-0.005	0.0	0.0	0
52.59	0.61	0.644	-0.089	(11.0)	(11.0)	(180.0)	0.377	0.010	-0.004	0.004	0.0	0.0	0
52.50	0.63	-0.619	-0.312	(14.3)	(14.3)	(180.0)	0.551	0.014	0.001	0.023	0.0	0.0	0
52.48	0.46	0.463	0.601	(11.2)	(11.2)	(180.0)	0.469	0.049	-0.005	-0.034	0.0	0.0	0
52.46	0.80	0.720	0.035	19.0	0.9	94.6	2.886	-0.174	-0.077	0.047	-6.0	3.0	74
52.26	0.63	-0.252	0.526	(8.6)	(8.6)	(180.0)	2.509	-0.130	-0.004	0.004	-5.2	0.0	0
52.18	0.78	-0.627	0.289	(47.7)	(47.7)	(180.0)	1.315	-0.015	-0.004	0.020	0.0	0.0	0
52.11	0.57	0.719	-0.396	46.7	5.2	142.4	0.693	0.057	0.021	-0.061	0.0	0.0	0
52.09	0.75	0.662	-0.305	11.3	8.8	139.0	4.185	-0.189	0.008	-0.158	-4.5	3.7	-43
52.00	0.64	0.600	-0.468	(11.5)	(11.5)	(180.0)	0.573	0.006	-0.008	-0.014	0.0	0.0	0
51.75	0.27	0.191	0.498	(13.5)	(13.5)	(180.0)	0.370	0.093	0.003	-0.007	25.1	0.0	0
51.72	0.59	-0.240	0.555	(13.7)	(13.7)	(180.0)	0.467	0.291	0.016	-0.030	62.4	0.0	0
51.66	0.44	0.491	0.299	10.0	4.9	133.7	0.367	0.097	-0.016	0.010	26.5	0.0	0
51.57	0.54	0.323	0.460	6.4	4.4	156.0	3.073	-0.283	0.056	-0.005	-9.2	0.0	0
51.53	0.61	-0.101	0.601	(11.2)	(11.2)	(180.0)	1.982	0.027	0.010	0.035	0.0	0.0	0
51.26	0.48	-0.316	0.591	26.2	5.3	83.7	0.859	0.170	0.020	-0.008	19.8	0.0	0
51.23	0.46	0.014	0.604	(10.5)	(10.5)	(180.0)	1.253	-0.049	0.085	0.028	0.0	6.7	9
51.23	0.46	0.279	0.434	18.9	5.5	57.5	0.774	0.007	-0.132	-0.070	0.0	18.9	-76
51.10	0.64	0.745	-0.073	(8.8)	(8.8)	(180.0)	1.937	0.712	0.084	-0.088	36.8	6.1	-23
50.91	0.91	-0.128	0.616	(61.1)	(61.1)	(180.0)	0.717	0.078	0.011	0.014	0.0	0.0	0
50.82	0.45	0.283	0.607	(9.9)	(9.9)	(180.0)	0.767	-0.010	-0.007	0.009	0.0	0.0	0
50.73	0.62	0.736	-0.120	29.7	8.0	14.5	1.884	0.445	0.001	-0.009	23.6	0.0	0
50.68	0.64	0.192	0.483	11.3	4.3	110.0	6.585	0.114	-0.024	0.093	1.7	1.4	52
50.53	0.78	-0.145	0.631	10.8	4.6	48.0	0.728	-0.005	0.014	0.001	0.0	0.0	0
50.41	0.51	0.281	-0.957	5.1	3.6	0.2	2.335	0.151	0.024	-0.007	6.5	0.0	0

50.40	0.83	-0.673	0.132	8.7	4.4	98.5	5.108	0.065	0.038	-0.007	0.0	0.0	0
50.38	1.44	0.683	0.075	(5.0)	(5.0)	(180.0)	0.886	0.324	0.002	0.005	36.5	0.0	0
50.15	0.84	0.492	-0.844	(8.3)	(8.3)	(180.0)	0.389	-0.001	-0.006	-0.009	0.0	0.0	0
50.14	0.75	0.134	0.507	10.4	2.9	130.6	4.435	-1.025	-0.013	0.025	-23.1	0.0	0
49.99	0.47	0.271	0.765	8.3	3.6	59.9	0.467	-0.075	-0.009	-0.004	0.0	0.0	0
49.95	0.52	0.720	0.005	(19.2)	(19.2)	(180.0)	0.950	-0.061	0.028	-0.024	0.0	0.0	0
49.84	0.83	0.636	-0.336	(7.2)	(7.2)	(180.0)	1.128	-0.042	0.006	-0.007	0.0	0.0	0
49.82	0.61	-0.655	0.264	(9.4)	(9.4)	(180.0)	0.747	0.090	0.025	-0.001	0.0	0.0	0
49.61	0.51	0.687	-0.243	(17.5)	(17.5)	(180.0)	0.430	0.016	0.004	0.021	0.0	0.0	0
49.53	0.56	-0.669	0.169	8.1	6.6	5.8	3.613	-0.031	0.077	-0.118	0.0	3.8	-28
49.49	0.63	-0.176	0.615	(14.5)	(14.5)	(180.0)	1.393	-0.403	0.015	-0.009	-28.9	0.0	0
49.21	0.68	0.644	-0.260	(11.1)	(11.1)	(180.0)	0.459	0.042	0.006	0.005	0.0	0.0	0
49.20	0.67	0.569	-0.710	12.5	3.7	121.9	0.951	0.888	0.002	0.008	93.4	0.0	0
49.13	0.54	0.362	0.367	12.6	10.8	124.7	0.415	0.025	0.008	-0.008	0.0	0.0	0
49.10	0.56	0.096	0.190	(12.7)	(12.7)	(180.0)	0.408	-0.005	-0.004	0.008	0.0	0.0	0
49.08	0.68	0.697	0.042	(10.2)	(10.2)	(180.0)	0.907	0.621	-0.018	-0.004	68.4	0.0	0
49.01	0.91	-0.247	0.372	5.6	5.2	145.2	3.780	0.166	0.114	-0.039	4.4	3.0	-9
48.84	0.73	0.721	-0.206	13.8	9.0	126.7	0.567	0.021	-0.002	0.002	0.0	0.0	0
48.63	0.64	-0.642	0.185	(26.2)	(26.2)	(180.0)	0.745	0.352	0.007	0.005	47.2	0.0	0
48.34	0.65	-0.659	0.115	(22.2)	(22.2)	(180.0)	0.536	0.045	0.008	0.001	0.0	0.0	0
48.32	0.56	-0.726	0.135	(6.2)	(6.2)	(180.0)	1.276	0.132	0.001	-0.013	10.3	0.0	0
48.31	0.60	-0.355	-0.124	10.1	5.8	148.2	2.678	0.215	0.021	0.013	8.0	0.0	0
47.99	0.58	0.452	-0.432	(5.8)	(5.8)	(180.0)	1.159	-0.309	-0.002	0.005	-26.7	0.0	0
47.89	0.49	-0.810	0.118	(6.3)	(6.3)	(180.0)	1.251	-0.064	0.015	0.006	0.0	0.0	0
47.88	0.54	0.333	-0.459	(89.8)	(89.8)	(180.0)	0.108	0.022	-0.001	-0.007	0.0	0.0	0
47.57	0.88	0.291	0.193	(90.0)	(90.0)	(180.0)	0.206	-0.061	-0.005	-0.008	0.0	0.0	0
47.52	0.83	0.294	-0.408	(21.1)	(21.1)	(180.0)	15.659	-3.926	0.010	-0.269	-25.1	1.6	-43
47.21	0.83	0.378	-0.511	(12.9)	(12.9)	(180.0)	1.245	0.214	-0.004	-0.005	17.2	0.0	0
47.19	0.68	-0.408	-0.161	(13.2)	(13.2)	(180.0)	1.613	0.004	0.056	-0.086	0.0	0.0	0
47.17	0.57	-0.366	-0.353	(9.3)	(9.3)	(180.0)	2.363	-0.310	0.004	-0.012	-13.1	0.0	0
47.15	0.56	-0.666	0.101	(11.6)	(11.6)	(180.0)	0.919	-0.270	0.035	-0.008	-29.4	0.0	0
47.06	0.57	-0.410	-0.180	16.5	9.4	97.3	5.136	-0.258	0.141	-0.107	-5.0	3.3	-18
47.01	0.56	-0.475	0.169	(17.5)	(17.5)	(180.0)	0.795	0.289	0.013	0.017	36.4	0.0	0
46.86	0.84	0.114	-1.086	(10.1)	(10.1)	(180.0)	0.600	-0.076	-0.001	-0.009	-12.6	0.0	0
46.78	0.62	-0.741	0.106	(24.5)	(24.5)	(180.0)	0.871	-0.286	0.004	-0.008	-32.8	0.0	0
46.68	0.44	0.510	-0.288	(7.3)	(7.3)	(180.0)	0.882	0.472	-0.001	-0.005	53.5	0.0	0
46.60	0.69	0.437	-0.457	(19.4)	(19.4)	(180.0)	0.863	-0.015	-0.021	0.003	0.0	0.0	0
46.39	1.03	0.052	-0.493	8.9	6.7	173.2	1.068	0.001	-0.016	0.006	0.0	0.0	0
46.37	0.63	0.299	-0.400	8.4	4.7	52.2	5.286	-3.301	0.009	-0.071	-62.4	0.0	0
46.36	0.71	-0.803	0.109	(12.5)	(12.5)	(180.0)	1.629	-0.110	0.005	-0.017	0.0	0.0	0
46.24	0.49	0.384	0.148	(19.9)	(19.9)	(180.0)	0.594	-0.090	0.010	-0.015	0.0	0.0	0
46.24	0.50	-0.697	0.076	(32.5)	(32.5)	(180.0)	0.963	0.216	0.003	0.006	22.4	0.0	0
46.23	0.59	-0.232	0.270	(6.4)	(6.4)	(180.0)	3.128	-0.051	-0.005	-0.051	0.0	0.0	0
46.03	0.66	-0.445	-0.098	22.6	7.0	133.6	1.040	0.151	0.044	-0.033	14.5	0.0	0
45.92	0.59	0.417	-0.449	(19.6)	(19.6)	(180.0)	2.752	0.180	-0.017	0.014	6.5	0.0	0
45.84	0.56	-0.083	0.229	(15.8)	(15.8)	(180.0)	1.046	-0.088	-0.010	0.014	-8.4	0.0	0
45.80	0.51	0.471	-0.628	19.4	8.9	45.8	0.962	-0.008	0.003	0.006	0.0	0.0	0
45.52	0.76	-0.046	-0.002	28.3	5.7	107.8	15.544	-1.195	0.049	0.201	-7.7	1.2	38
45.51	0.57	-0.247	0.258	6.2	2.6	65.9	9.248	0.984	-0.054	0.109	10.6	0.0	0
45.22	0.69	0.016	-0.515	41.2	4.7	28.3	6.537	0.204	-0.028	0.004	3.1	0.0	0
45.16	0.66	0.377	0.146	13.1	7.4	33.2	1.230	-0.283	0.011	0.001	-23.0	0.0	0
45.02	0.44	0.054	-0.432	(6.6)	(6.6)	(180.0)	3.162	-0.246	0.042	-0.015	-7.8	0.0	0
44.93	0.68	0.024	-0.490	(21.9)	(21.9)	(180.0)	2.353	0.139	0.011	0.001	0.0	0.0	0
44.68	0.81	-0.033	0.011	19.5	12.4	96.8	9.106	-1.073	0.013	0.073	-11.8	0.0	0
44.21	0.51	-0.002	-0.603	(11.1)	(11.1)	(180.0)	1.133	-0.057	-0.021	-0.011	0.0	0.0	0

44.17	0.48	0.018	0.603	(34.2)	(34.2)	(180.0)	1.850	-0.016	-0.035	-0.011	0.0	0.0	0
44.06	0.64	-0.074	-0.042	(7.9)	(7.9)	(180.0)	4.653	0.286	-0.008	-0.009	6.2	0.0	0
43.96	0.86	0.000	-0.001	28.6	6.4	104.6	12.508	-0.820	-0.148	-0.071	-6.6	0.0	0
43.78	0.47	0.108	0.122	29.3	2.2	39.3	0.877	-0.004	-0.009	0.009	0.0	0.0	0
43.35	0.46	-0.270	0.126	9.2	3.5	117.2	4.983	-0.057	0.014	-0.060	0.0	0.0	0
43.35	0.60	-0.106	-1.060	(21.5)	(21.5)	(180.0)	0.955	0.015	0.003	0.024	0.0	0.0	0
43.01	0.60	-0.071	-0.045	36.5	6.8	78.9	3.625	0.061	-0.025	0.032	0.0	0.0	0
42.95	0.44	0.016	0.012	45.1	22.6	109.2	1.691	0.052	-0.012	-0.001	0.0	0.0	0
42.79	0.71	-0.104	0.143	(16.4)	(16.4)	(180.0)	0.341	0.008	-0.004	0.004	0.0	0.0	0
42.59	0.52	-0.070	-0.660	(11.5)	(11.5)	(180.0)	0.341	-0.007	0.000	0.010	0.0	0.0	0
42.55	0.76	-0.039	-0.049	(15.5)	(15.5)	(180.0)	1.937	-0.044	-0.002	0.009	0.0	0.0	0
42.48	0.51	-0.357	-0.128	(11.3)	(11.3)	(180.0)	0.386	-0.027	0.005	-0.008	0.0	0.0	0
42.11	0.83	-0.060	-0.049	10.7	1.8	116.1	1.955	0.009	-0.004	0.011	0.0	0.0	0
42.08	0.28	0.021	-0.002	(16.1)	(16.1)	(180.0)	0.398	0.005	-0.007	-0.006	0.0	0.0	0
42.05	0.62	-0.248	0.136	(17.0)	(17.0)	(180.0)	0.500	0.007	0.006	-0.002	0.0	0.0	0
41.70	0.46	-0.258	0.083	24.1	4.2	18.3	0.286	-0.068	0.013	0.002	0.0	0.0	0
41.54	0.74	0.017	-0.180	(11.2)	(11.2)	(180.0)	0.438	0.064	0.001	0.011	0.0	0.0	0
41.32	0.67	-0.065	-0.060	(12.7)	(12.7)	(180.0)	1.084	-0.022	-0.024	0.015	0.0	0.0	0
41.11	0.67	0.107	-0.339	(12.3)	(12.3)	(180.0)	0.832	0.046	0.007	0.006	0.0	0.0	0
40.45	0.54	-0.047	-0.172	(10.8)	(10.8)	(180.0)	0.985	0.214	0.019	-0.014	21.7	0.0	0

[a] Centre LSR velocity of the component, assumed to have a Gaussian velocity profile (kms^{-1}).

[b] The full width at half maximum of the Gaussian component in velocity (kms^{-1}).

[c] Relative angular separation (X, Y) of the peak component brightness in I with respect to the map centre in the direction of increasing right ascension and declination (J2000) respectively (arcsec).

[d] The estimated apparent size of the component along the major and minor axes after deconvolution by the CLEAN restoring beam (milliarcsec (mas)). Upper limits are given in parentheses.

[e] Position angle of the component major axis (measured from north to east) (deg).

[f] Peak apparent brightness of the component in the four Stokes parameters measured at the position of maximum brightness in I (Jy/beam).The beam solid angle is $\Omega_{beam} = 1.133\ \theta_{maj}^{beam}\ \theta_{min}^{beam}$, where $\theta_{maj}^{beam} = 38.86$ mas and $\theta_{min}^{beam} = 29.46$ mas.

[g] Degree of circular polarization in percent. The component marked with an asterisk has a formal error of $\sim 30\%$, and is thus consistent with an upper limit of 100%.

[h] Degree of linear polarization in percent m_l' after correction for bias, and the relative position angle of the polarized emission χ (deg). The absolute position angle is not known due to the method of polarization phase calibration, as discussed in the text.

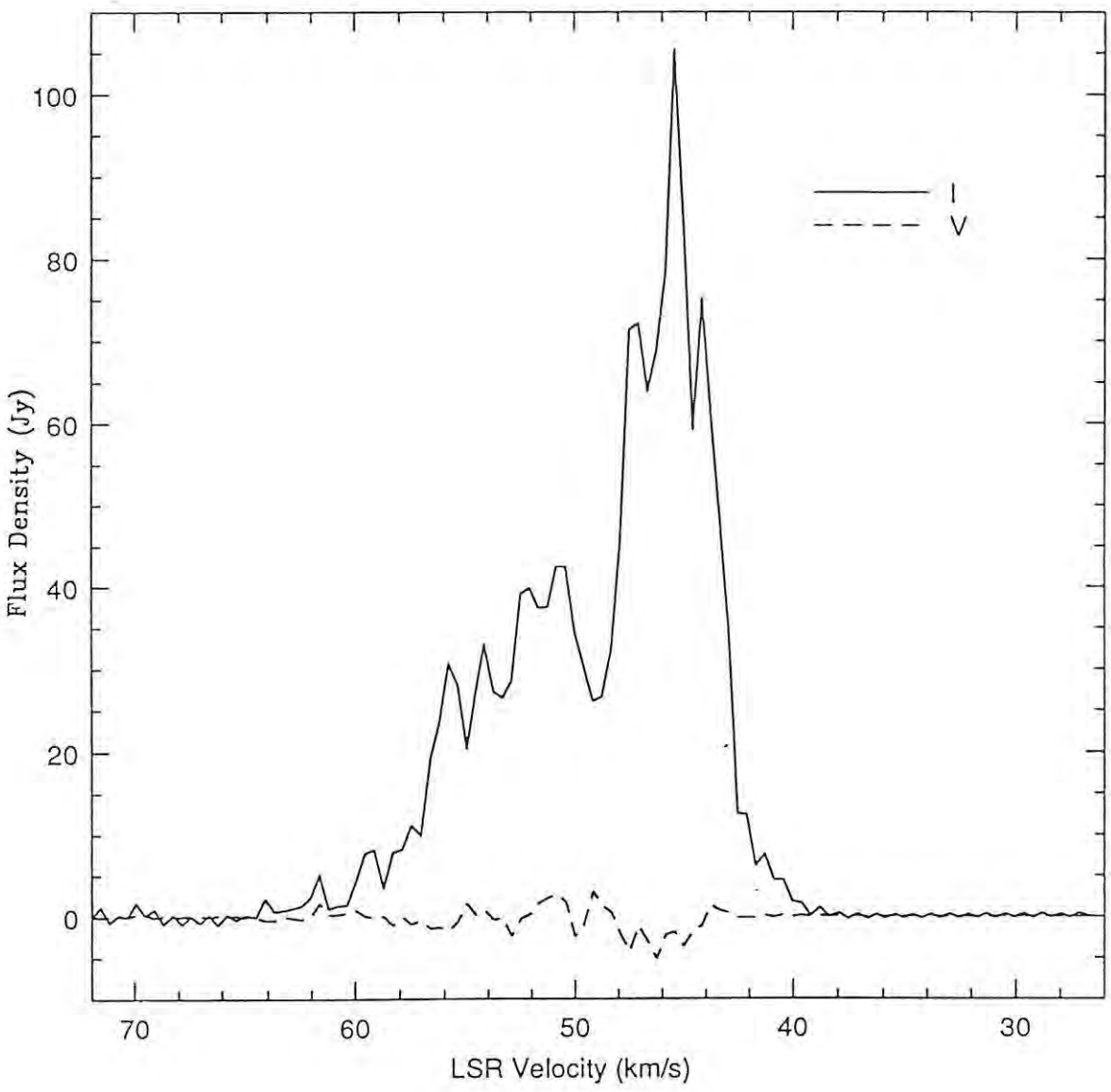

Fig. 5.1. Single-dish autocorrelation spectra in Stokes I and V of the 1612 MHz OH maser emission towards IRC+10420. These spectra were derived from the Effelsberg autocorrelation VLBI data taken on 1 March 1987. The spectral resolution is ~ 0.50 kms^{-1} and the error in the absolute flux density scale in I is estimated to be $\sim 20\%$.

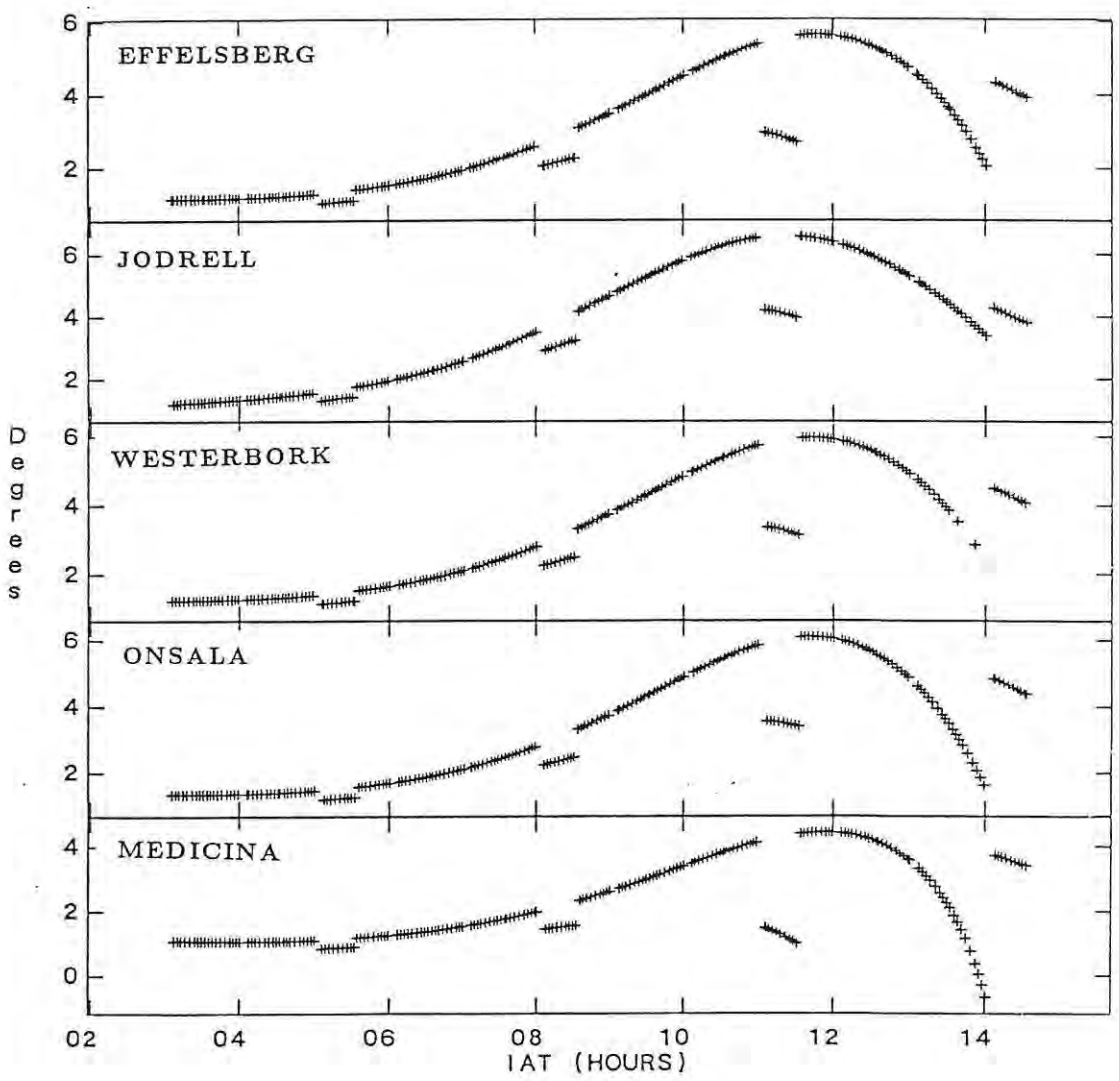

Fig. 5.2. The predicted ionospheric Faraday rotation over the course of the MK3 VLBI observations for a Zurich sunspot number, $R_Z = 14$, as used in the polarization phase calibration. The discontinuities in the phase function mark the continuum calibrator scans. The model used here (Chiu 1975; UAG 1981) was implemented within AIPS by C. Flatters.

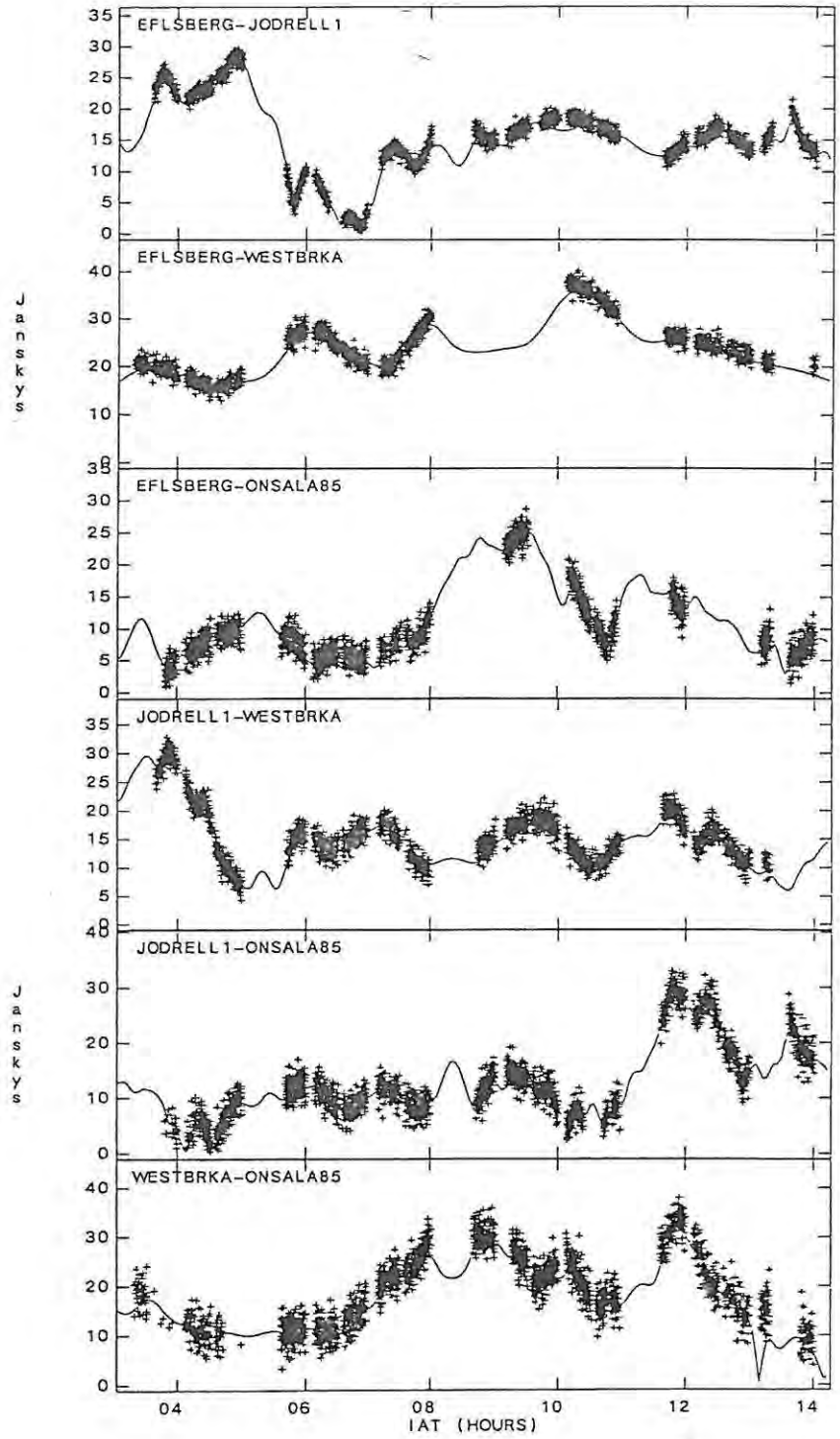

Fig. 5.3. A plot of the correlated amplitude in Stokes I for the (u, v) data in the reference channel at $V_{LSR} = 44.18$ kms^{-1} as a function of time. The $x-$axis is in units of International Atomic Time (IAT). The source model is plotted as a continuous line.

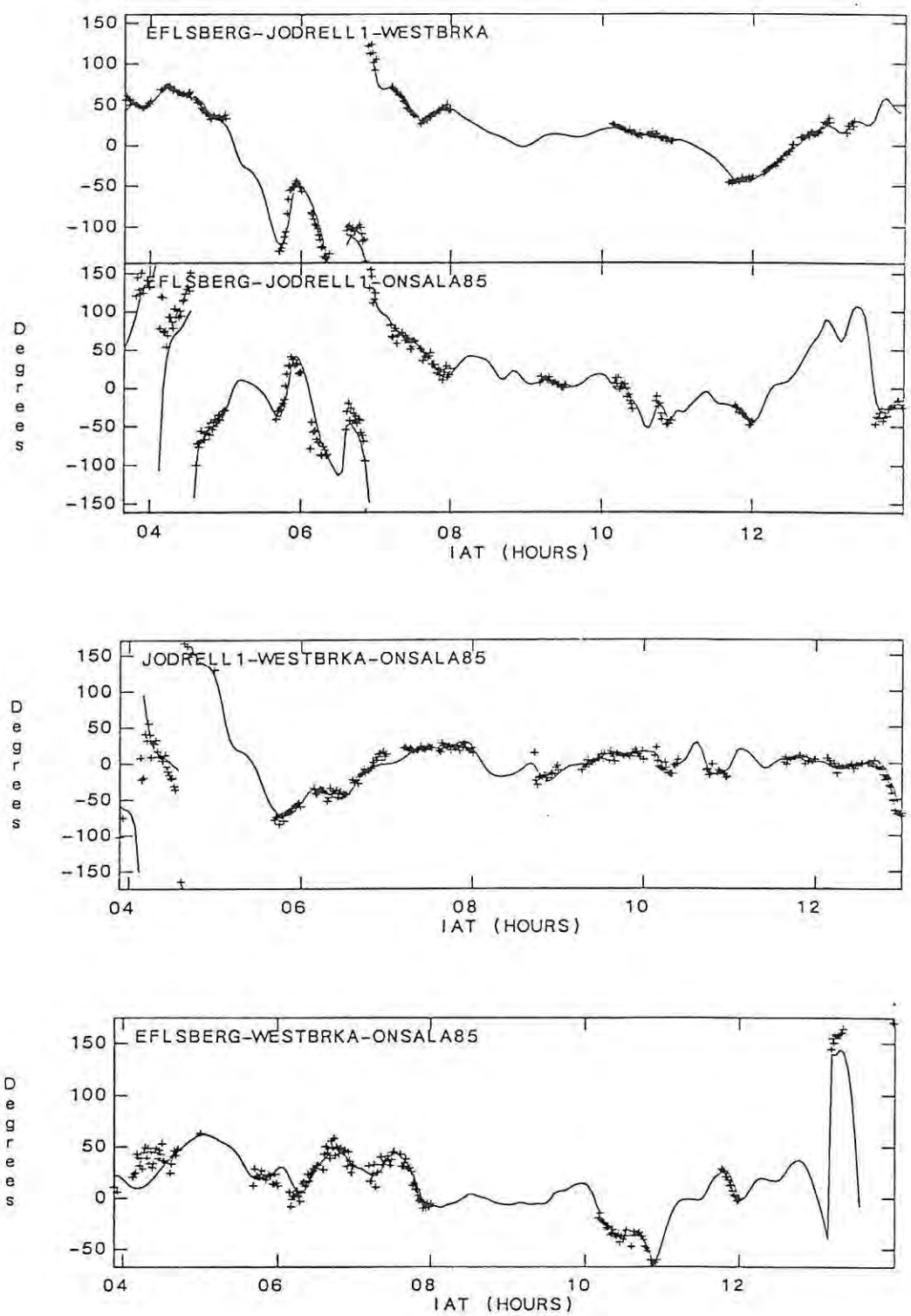

Fig. 5.4. A plot of the closure phases in Stokes I for the (u, v) data in the reference channel at $V_{LSR} = 44.18$ kms^{-1} as a function of time. The $x-$axis is in units of International Atomic Time (IAT). The closure phase predicted by the source model is plotted as a solid line.

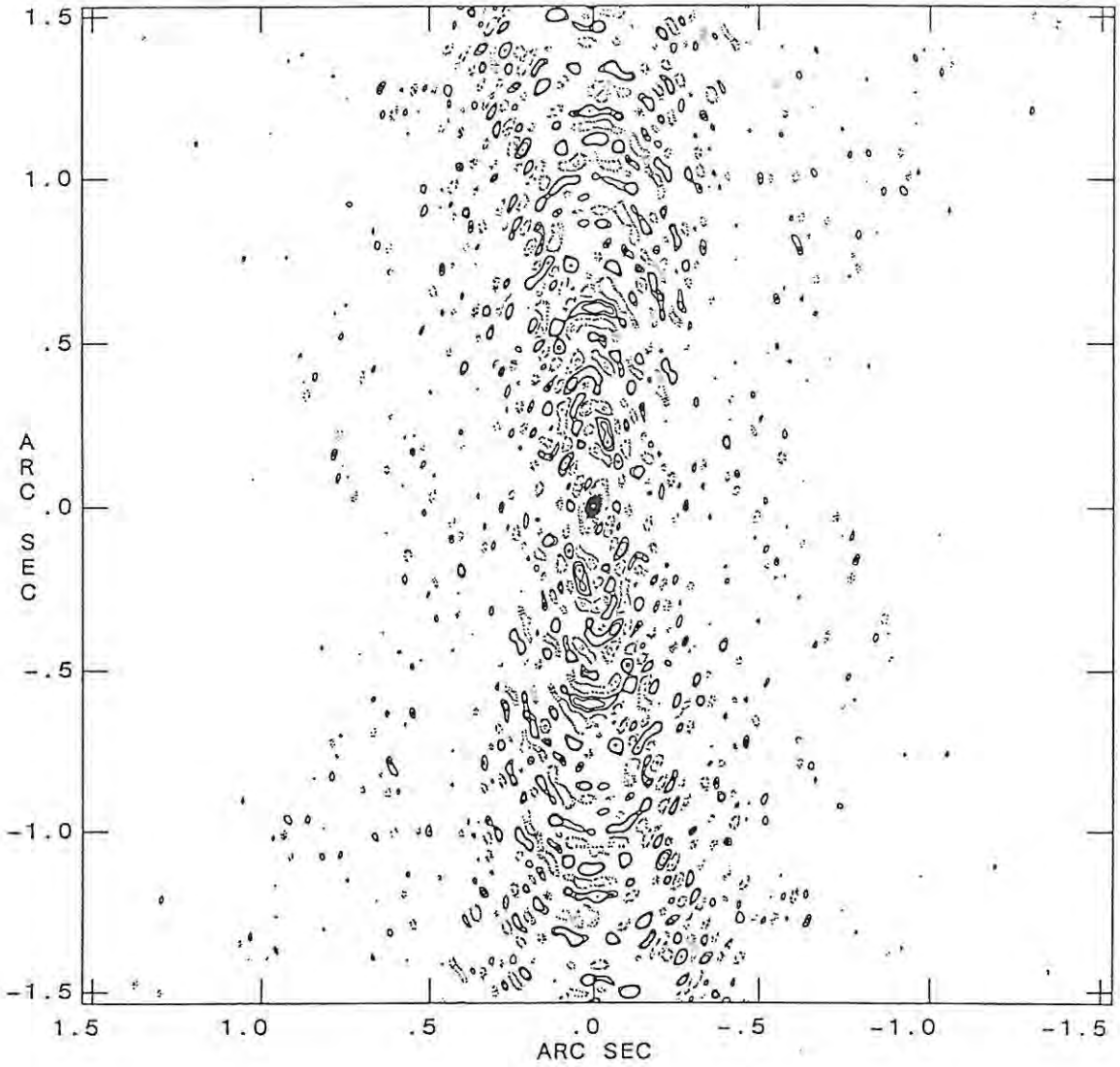

Fig. 5.5. The point spread function or dirty beam in Stokes I for the MK3 VLBI data. Contours are plotted at (-100, -90, -80, -70, -60, -50, -40, -30, -20, -10, -7.5, 7.5, 10, 20, 30, 40, 50, 60, 70, 80, 90, 100) % of the peak unit brightness.

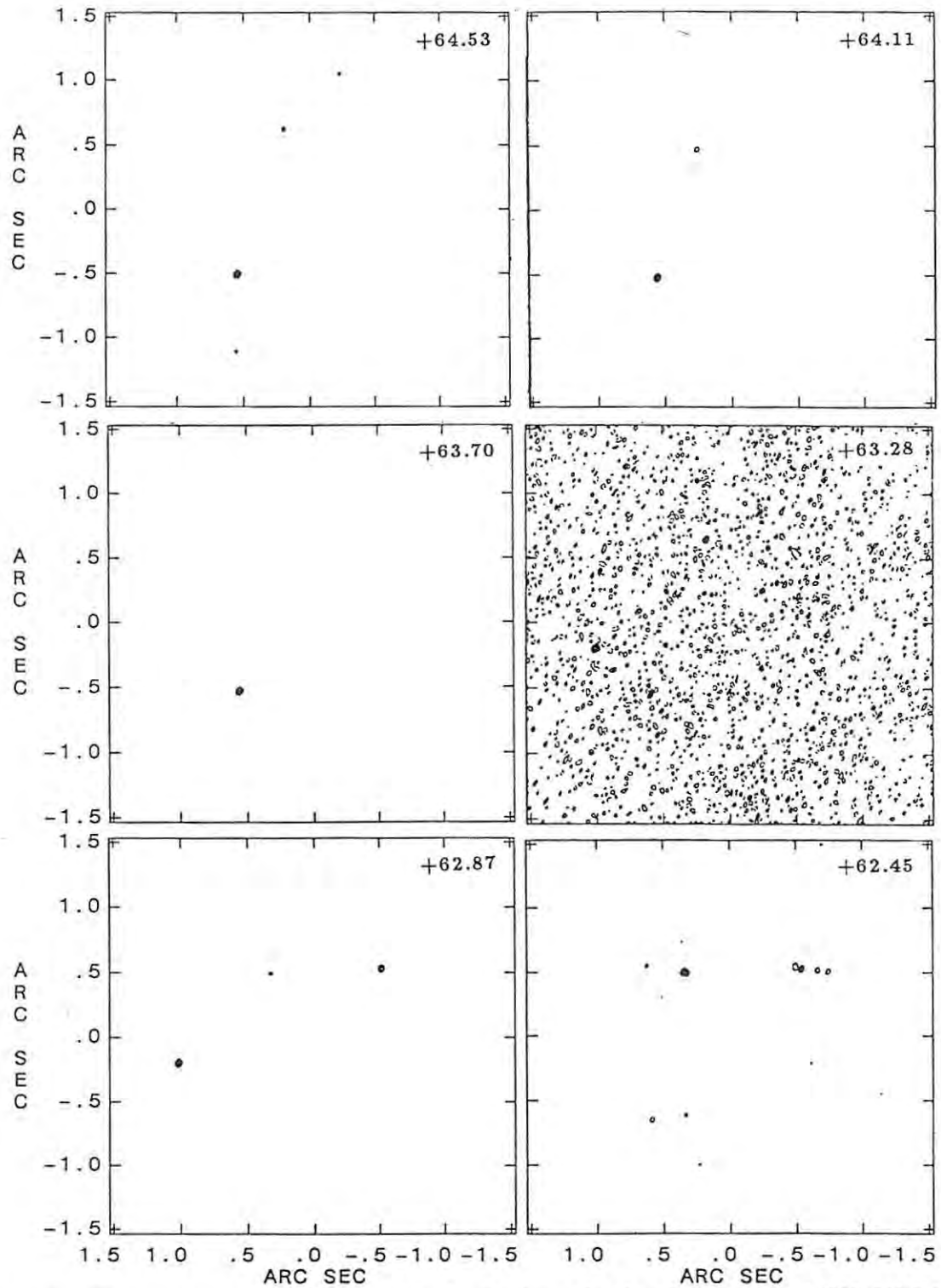

Fig. 5.6. Channel maps in Stokes I polarization obtained from the MK3 VLBI observations of the 1612 MHz OH maser emission towards IRC+10420. The LSR velocity is plotted in the upper right-hand corner of each channel in units of kms^{-1}. The contour levels were chosen at (-30,-15, 15, 30, 45, 60, 75, 90, 100) % of the peak brightness in each channel.

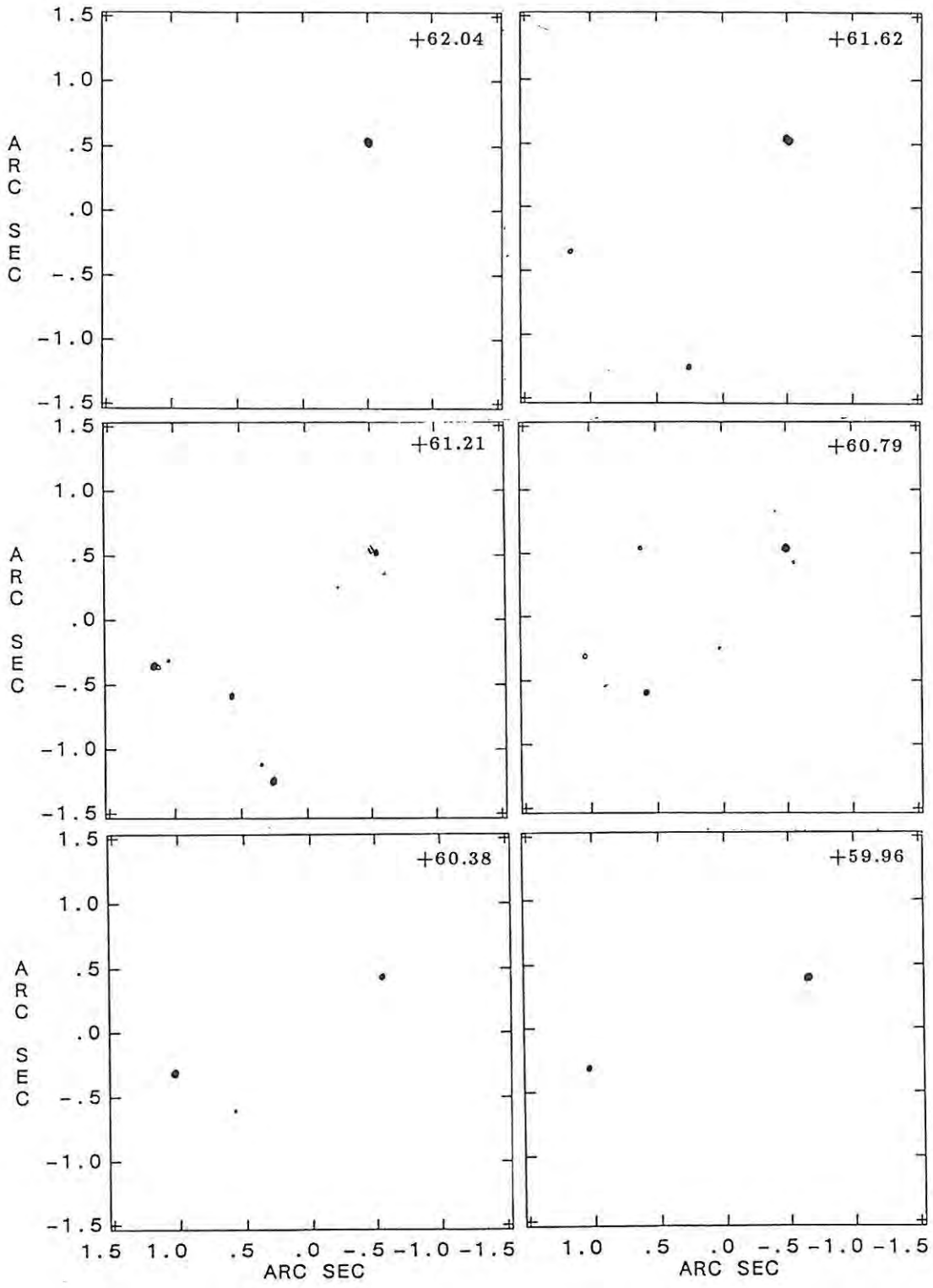

Fig. 5.6. *(continued).*

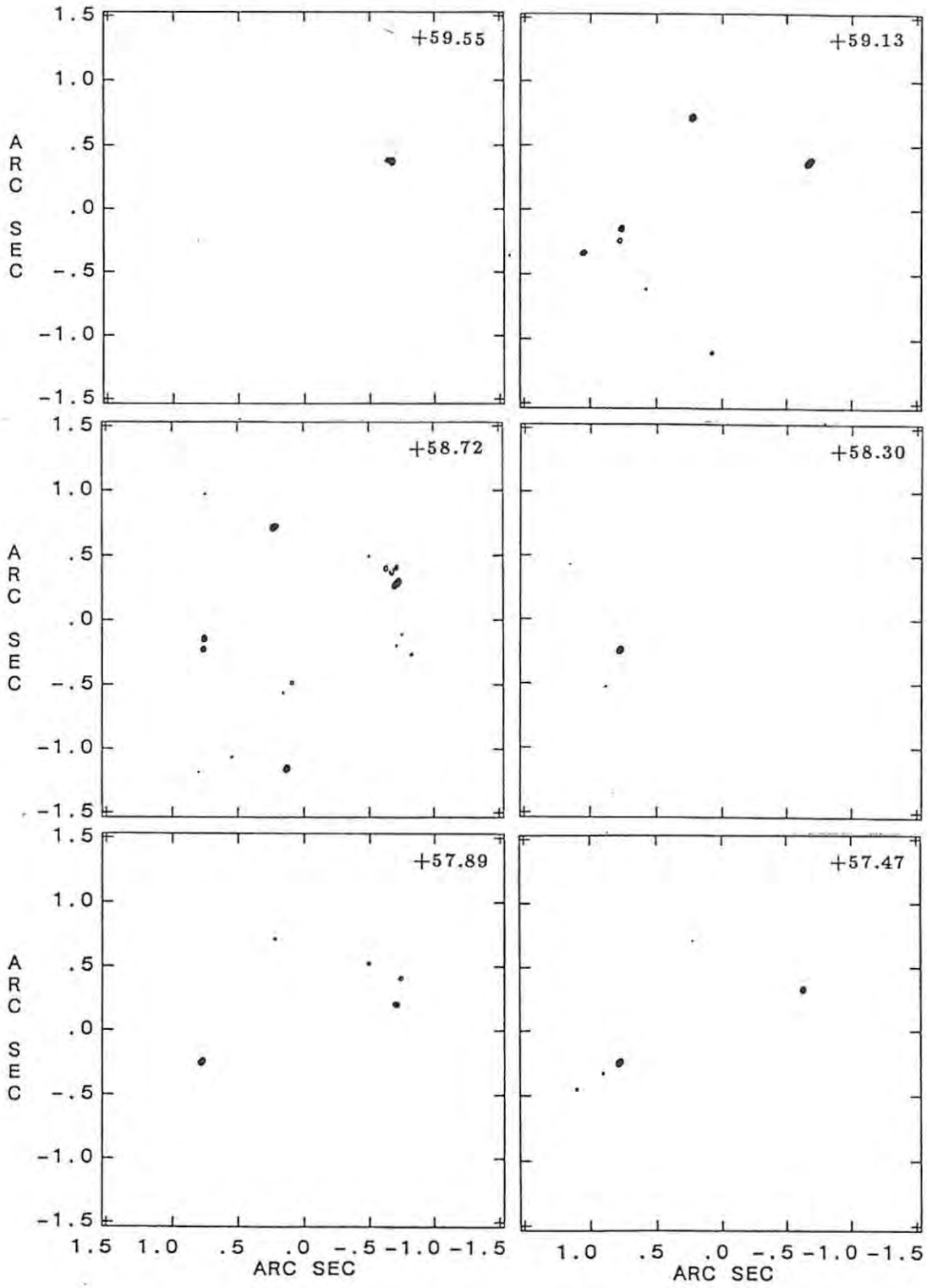

Fig. 5.6. *(continued).*

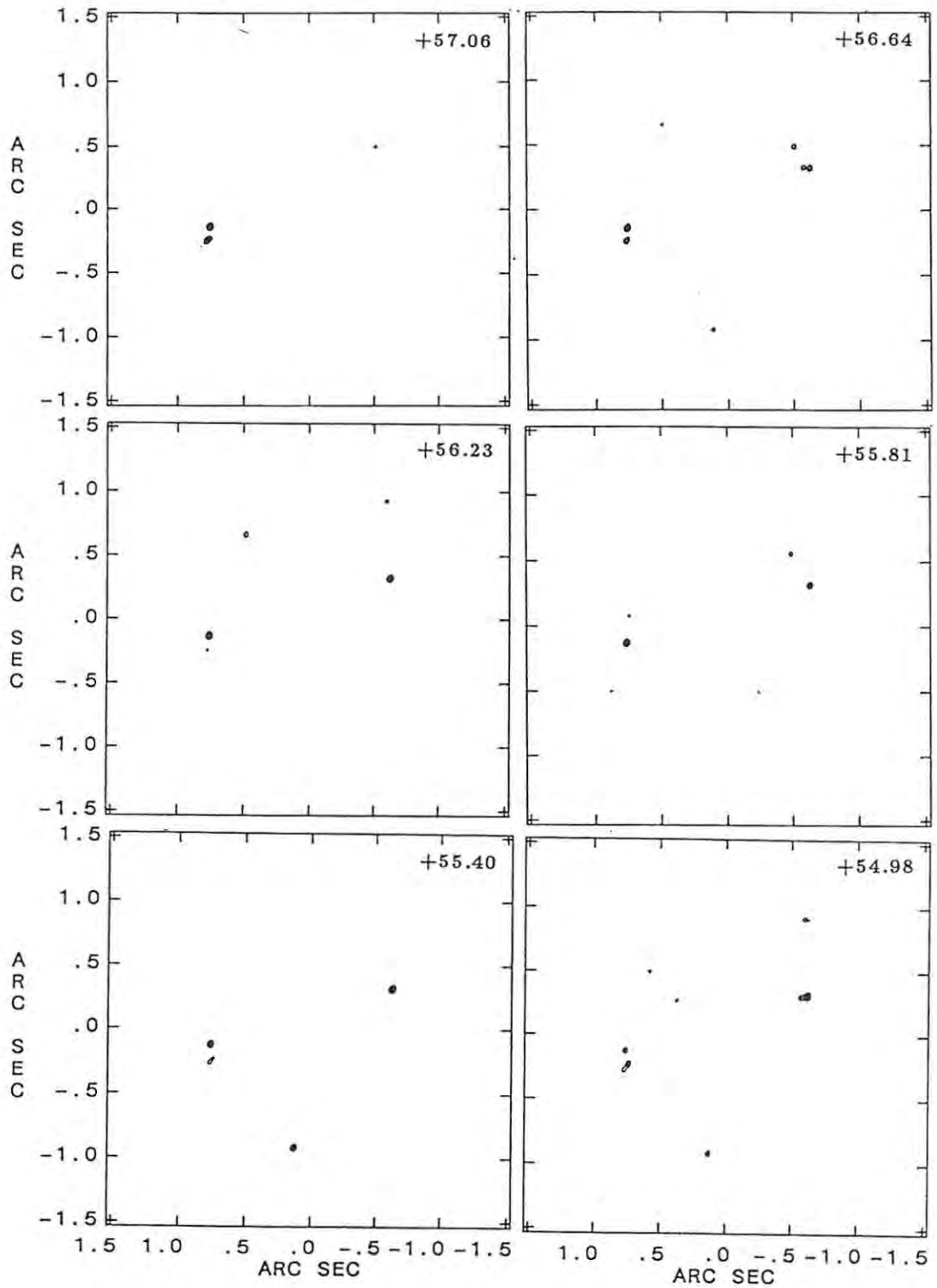

Fig. 5.6. *(continued).*

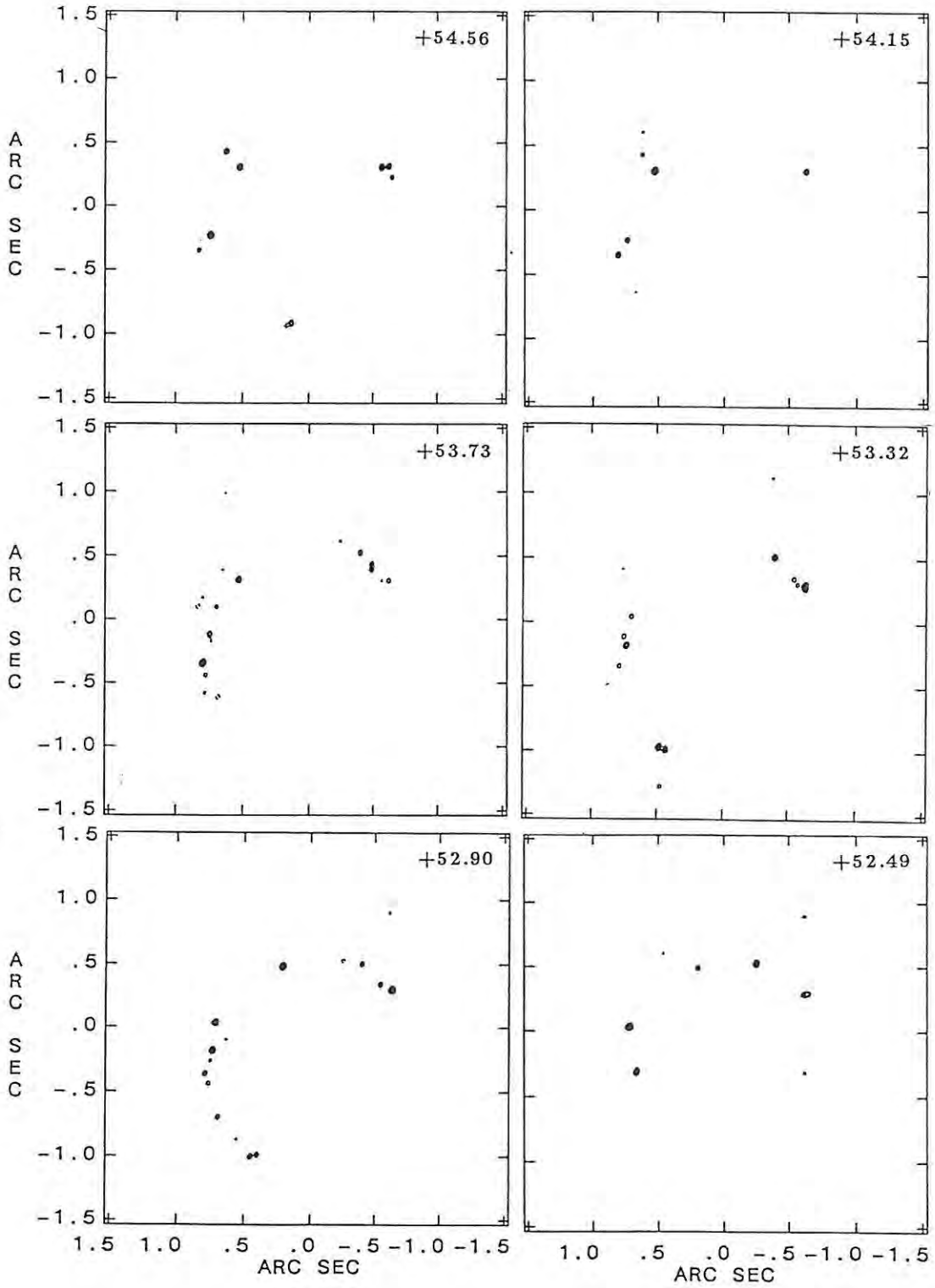

Fig. 5.6. *(continued).*

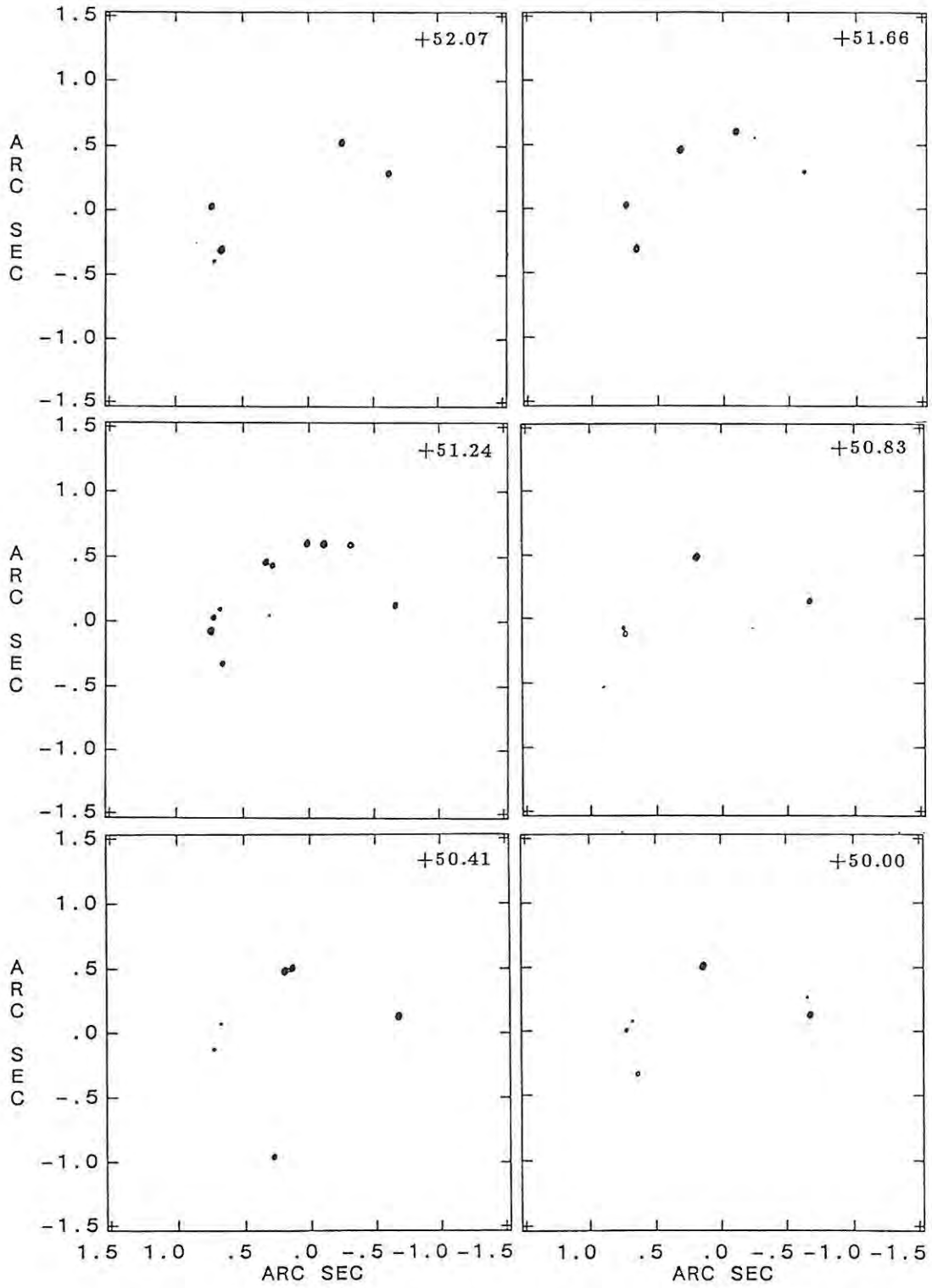

Fig. 5.6. *(continued).*

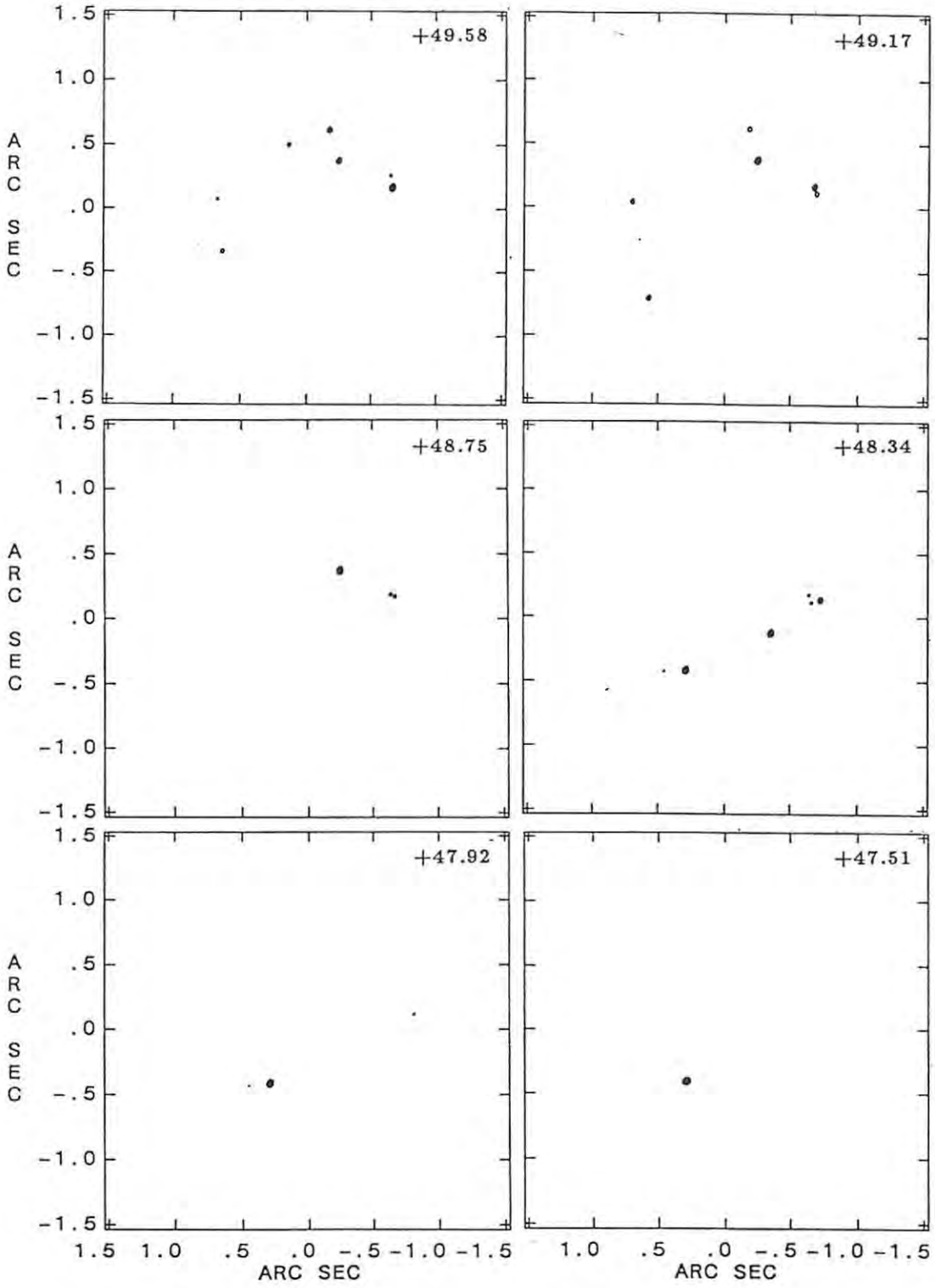

Fig. 5.6. *(continued).*

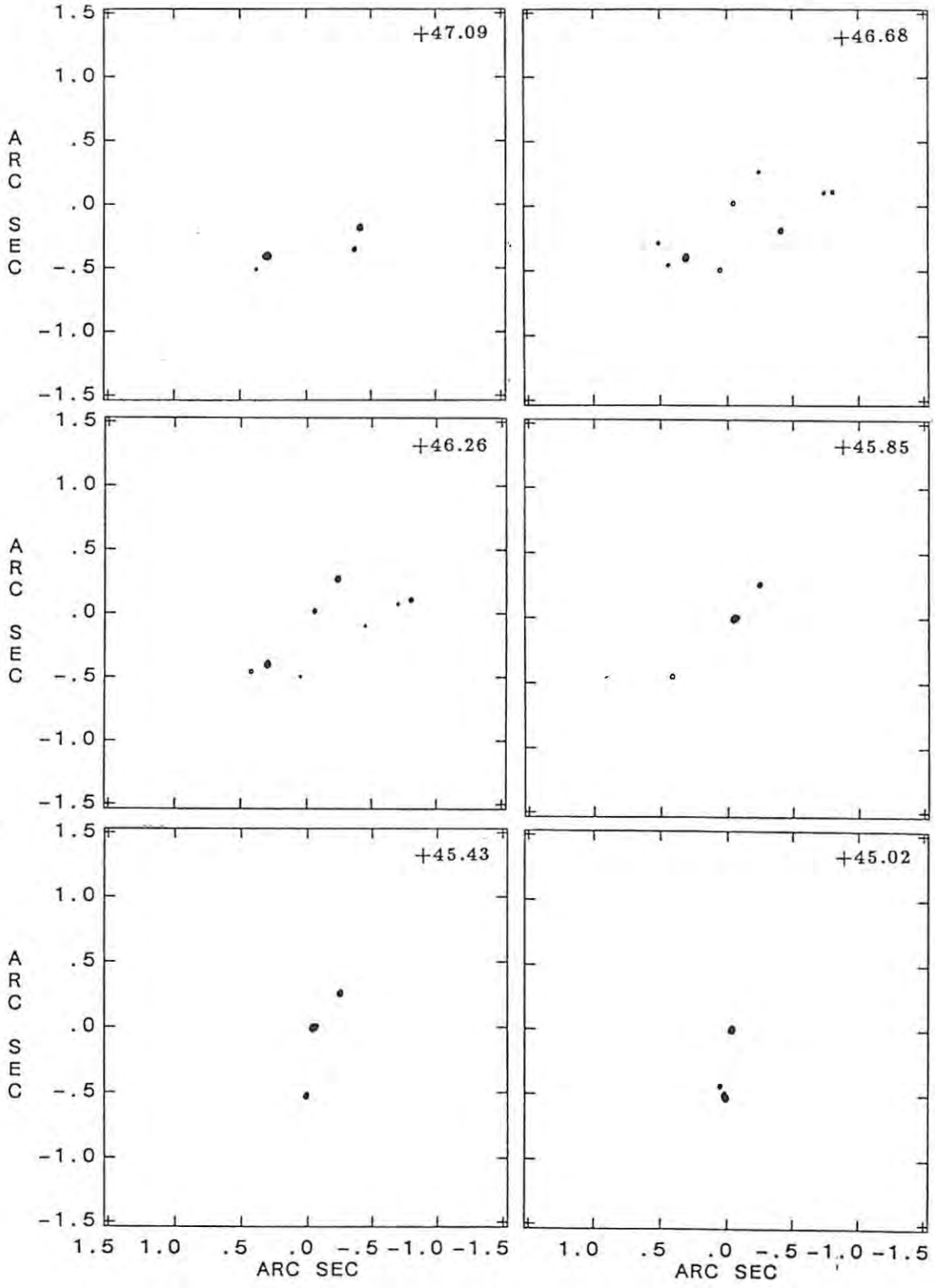

Fig. 5.6. *(continued).*

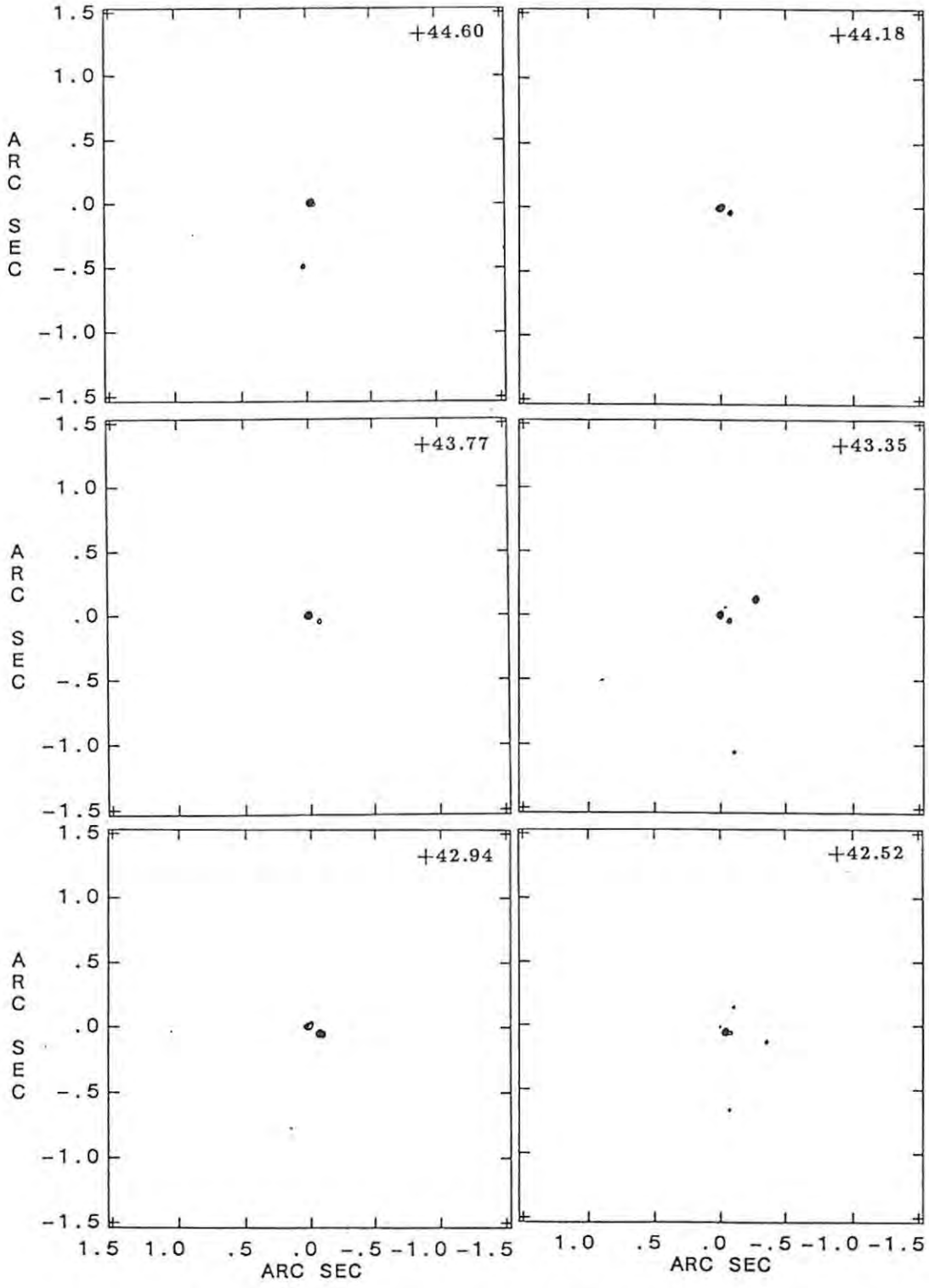

Fig. 5.6. *(continued).*

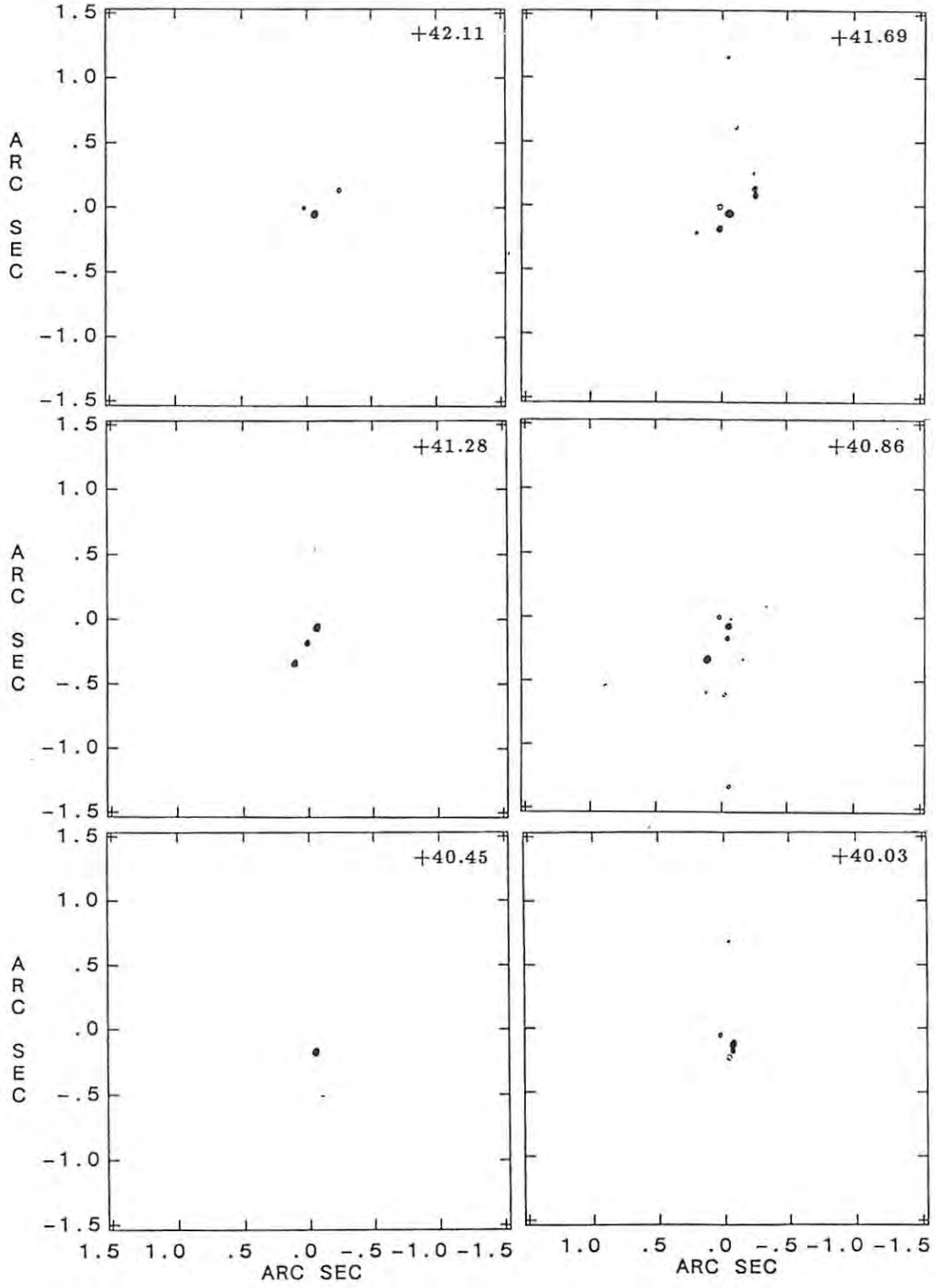

Fig. 5.6. *(continued).*

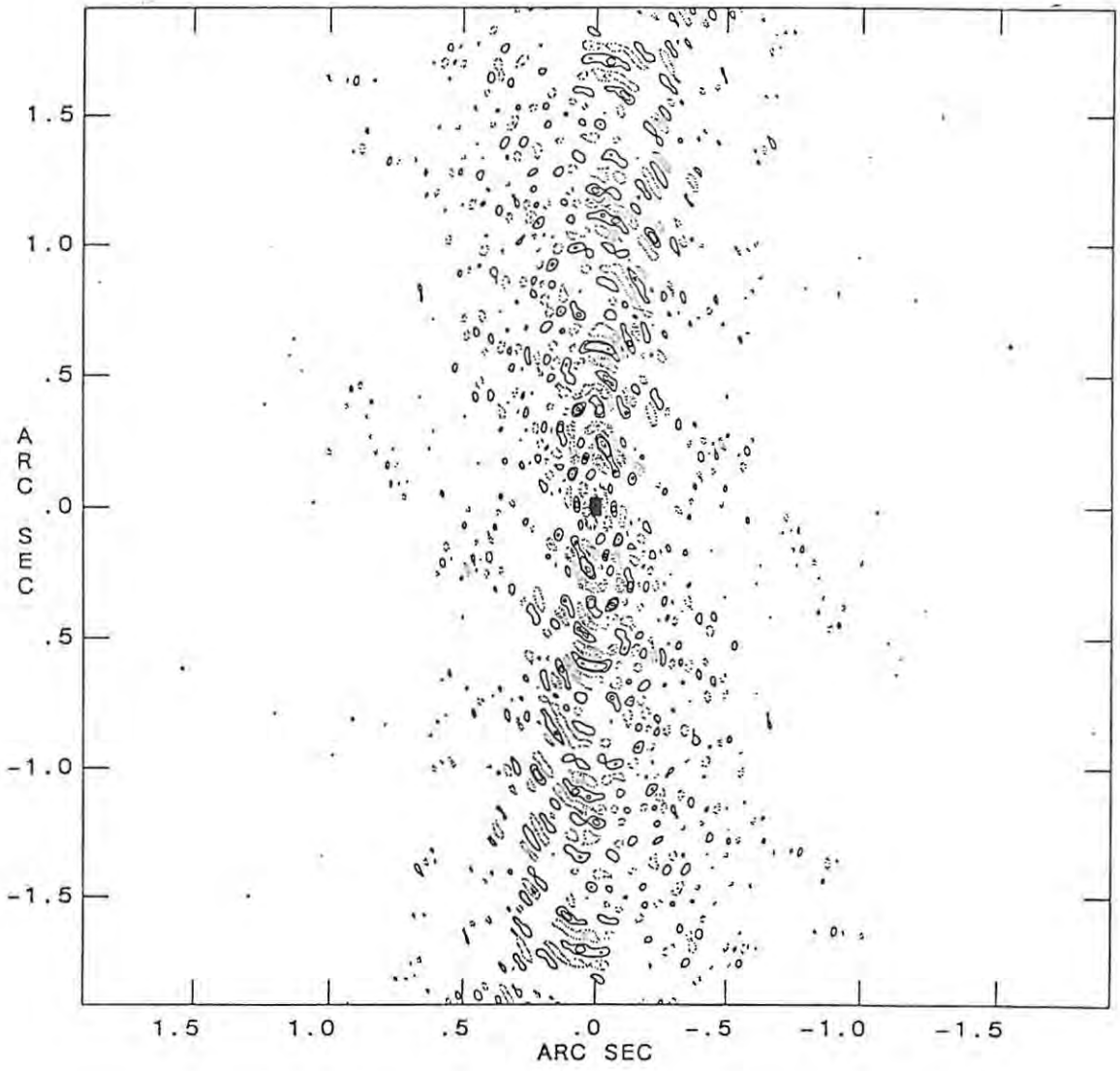

Fig. 5.7. The real part of the complex dirty beam for the (u, v) sampling of the MK3 VLBI observations. The contours are plotted at (-30, -20, -10, 10, 20, 30, 40, 50, 60, 70, 80, 90, 100) % of the peak brightness.

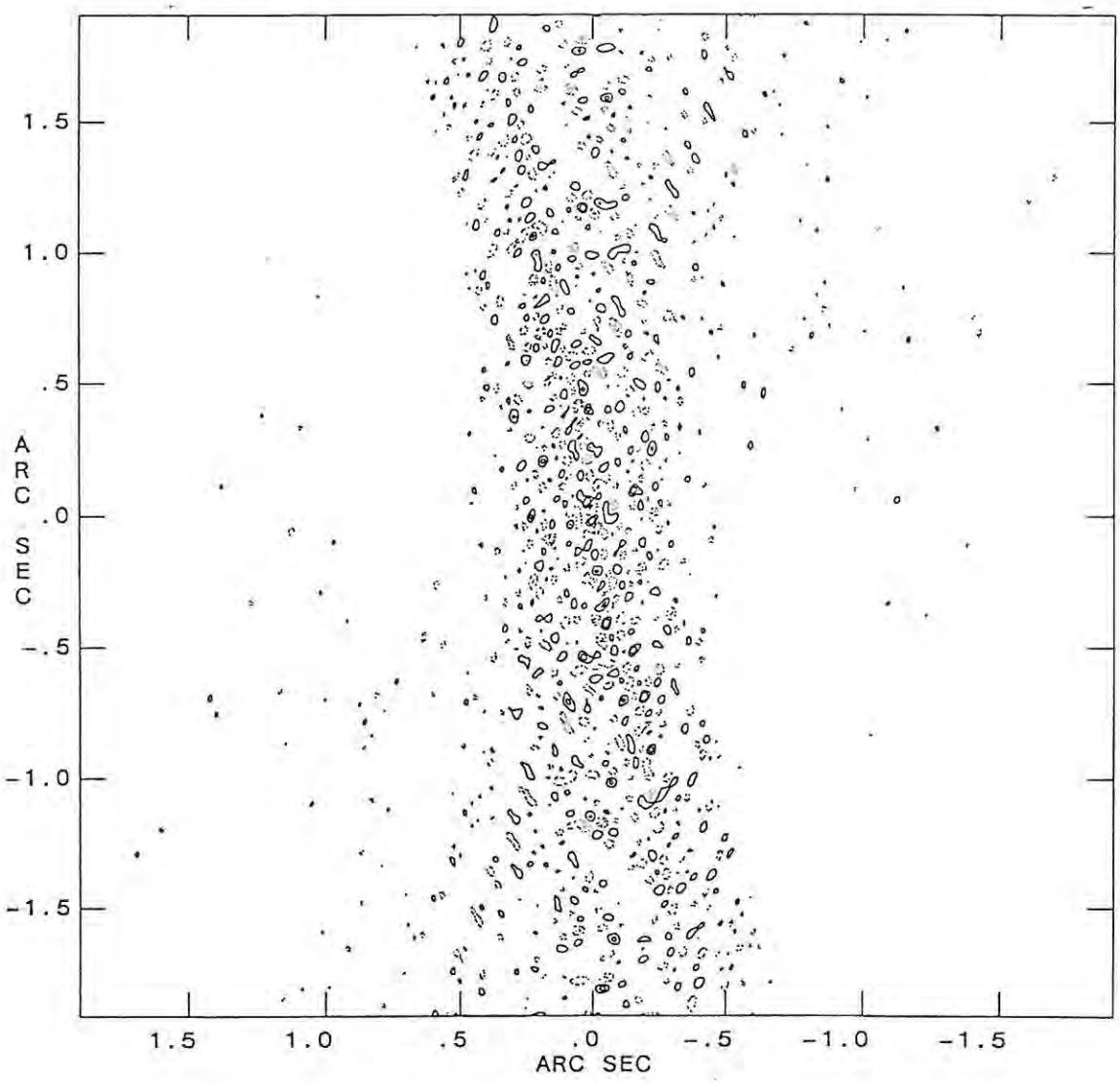

Fig. 5.8. The imaginary part of the complex dirty beam for the (u, v) sampling of the MK3 VLBI observations. The contours are plotted at (-100, -66, -33, 33, 66, 100) % of the peak brightness. The overall normalisation of the complex dirty beam is discussed in the text.

CHAPTER 6: IRC+10420: REVIEW OF SOURCE PROPERTIES

Introduction

IRC+10420 is an unusual, strong infra-red (IR) source which is widely held to be a candidate proto-planetary nebula or post-AGB transitional object. There is bright associated OH maser emission at 1612 MHz which is unusual for its polarization properties and the early spectral type F of the central star. IRC+10420 is a good candidate for spectral line VLBI observations and the first VLBI maps of the source using closure-phase imaging techniques are presented in Chapters 4 and 5. The latter observations were reduced using a full polarization synthesis as part of the evaluation and development of spectral line polarization VLBI data reduction techniques.

This chapter contains a review of the literature for the source IRC+10420, with particular reference to the interpretation of the VLBI observations presented as part of this work.

6.1 General Properties

IRC+10420 appears as a strong source in the 2μm IRC sky survey of Neugebauer and Leighton (1969), and was subsequently classified as an F8 Ia supergiant by Giguere, Woolf and Webber (1976). An absorption line optical spectrum of normal appearance was found with a high luminosity star further indicated by a strong, blended O I triplet at 7774 $\dot{A}$, typical of late B, A and F supergiants (Humphreys *et al.* 1973). Brackett absorption in H is present, consistent with an F8 type (Thompson and Boroson 1977). Initial IR spectra revealed emission lines from neutral Na, Mg and Fe (Thompson and Boroson 1977) but more prominent emission features in Hα, Ca II and [Ca II] have recently appeared (Irvine 1986).

Craine *et al.* (1976) measured an apparent visual magnitude $m_v = 11.84$ and a normal reddening curve with $A_v \sim 6.9$. Assuming an absolute visual magnitude of $M_v = -8$ expected for an F8 Ia star this implies a photometric distance of $D \sim 3.9$ kpc (Mutel *et al.* 1979), unless the extinction curve in the circumstellar shell differs greatly from the interstellar medium (Fix 1981). Using more recent values $m_v = 11.2$ and $A_v \sim 7.3$ derived by Ridgway *et al.* (1986) assuming a G0 I type, this calculation can be repeated to yield a photometric distance estimate of $D \sim 2.4$ kpc, emphasising the inherent uncertainty in this method.

Gottlieb and Liller (1978) report a linear increase in the annual mean B magnitude of ~ 0.025 magnitudes per year from 1925 to 1978. Before 1925 the star varied irregularly between 14th and 15th magnitude.

6.2 Emission

6.2.1 OH Maser Emission

The detection of OH maser emission at 1612, 1665 and 1667 MHz by Giguere, Woolf and Webber (1976) placed the source as a strong supergiant OH/IR star. A highly asymmetric double-peaked spectrum was detected at 1612 MHz in February 1975 with a velocity separation of ~ 58 km s^{-1} and a blue-shifted peak I flux density of ~ 44 Jy at a velocity resolution of 0.37 km s^{-1} . No emission was detected at 1720 MHz. The velocity separation is comparable to other supergiant OH/IR stars such as VY CMa, NML Cyg and VX Sgr but distinct from the Mira OH stars which have lower expansion velocities (Mutel *et al.* 1979; Giguere, Woolf and Webber 1976). The flux density variations at 1612, 1665 and 1667 MHz are tabulated by Nedoluha and Bowers (1992). The 1612 MHz emission is known to vary on timescales as short as ten months and the peak blue-shifted flux density has increased overall by a factor of $\sim 2-3$ since discovery (Nedoluha and Bowers 1992). A prominent feature of the time evolution at 1612 MHz has been the development of a plateau of emission at $V_{LSR} = 50-60$ km s^{-1} which was absent

on discovery but has since increased substantially (Lewis, Terzian and Eder 1986). By 1985 half of the 1612 MHz blue-shifted OH flux was emitted in the plateau at $V_{LSR} > 50$ km s^{-1} (Lewis, Eder and Terzian 1985). The mean flux density of the plateau reached $\sim$ 30% of the peak flux density in 1989 and the increase in the 1612 MHz emission has been compared to the flare event in U Ori (Nedoluha and Bowers 1992).

6.2.2 Other Maser Lines

There is no associated water maser emission at 22 GHz (Giguere, Woolf and Webber 1976; Nyman, Johansson and Booth 1986). Searches for SiO maser emission at 43 GHz and 86 GHz have similarly been unsuccessful (Dickinson *et al.* 1978; Jewell *et al.* 1984; Nyman, Johansson and Booth 1986; Engels and Heske 1989).

Excited state OH maser emission has not been detected for this source either from the $^2\Pi_{3/2}, J = 5/2$ rotational state at 6.0 GHz or the $^2\Pi_{1/2}, J = 1/2$ state at 4.7 GHz (Jewell, Schenewerk and Snyder 1985).

6.2.3 Thermal Molecular Emission

A list of the detected molecular lines is given in Table 6.1, including derived velocity parameters where possible. A list of molecular species which have not been detected in the circumstellar envelope is given in Table 6.2. Detection limits are not given here due to the heterogeneous nature of the observations.

6.2.4 Infra-Red Emission

IRC+10420 has a significant IR excess with emission peaks near 10 μm and 20 μm , indicative of circumstellar silicate dust (Forrest, McCarthy and Houck 1979). It is designated as IRAS 19244+1115 in the IRAS catalogue where it is listed as a non-variable source (Olnon *et al.* 1986). A composite spectrum including IRAS data and ground-based observations is given by Hrivnak, Kwok and Volk

TABLE 6.1

Detected Thermal Molecular Emission

	Transition	V_*^a	V_e^b	$\triangle V^c$	References
CO	J=1-0	80.9	51.7	103	Knapp and Morris (1985)
SiO	ν=0,J=2-1	79	35	70	Olofsson *et al.* (1982)
HCN	J=1-0	78	39	78	Jewell, Snyder and Schenewerk (1986)
$HCN/H^{13}CN$	J=1-0	77.6	33	66	Nercessian *et al.* (1989)
SO_2	3(1,3)-2(0,2)	75	37	74	Guilloteau *et al.* (1986)

[a] Estimated stellar LSR velocity (km s^{-1})

[b] Estimated expansion velocity (km s^{-1})

[c] Velocity range of emission (km s^{-1})

TABLE 6.2

Non-Detections

	Transition	References
SiS	J=5-4	Olofsson *et al.* (1982)
HNC	J=1-0	Olofsson *et al.* (1982)
		Nercessian *et al.* (1989)
HC_3N	J=10-9	Oloffson *et al.* (1982)
HI		Knapp and Bowers (1983)
MgO,TiO,ClO,CCl		Millar *et al.* (1987)
SO		Guilloteau *et al.* (1986)

(1989). Photospheric and chromospheric lines including Brackett H, Mg I and Fe II are present at $\lambda < 2$ μm while the spectrum is dominated by circumstellar dust emission for $\lambda > 2$ μm (Fix and Cobb 1987).

IR speckle interferometry reveals no convincing evidence of spatial asymmetry and suggests an inner dust shell radius $\theta(3.8\ \mu\text{m}) \sim 0.155$ arcsec and a dust temperature of $\sim$ 750 K (Dyck *et al.* 1984; Ridgway *et al.* 1986; Cobb and Fix 1987; Fix and Cobb 1988; LeVan and Sloan 1989). The angular diameter in the IR scales approximately as $\theta \propto \lambda^{\alpha}$, where $\alpha \sim 1.2$. This relation includes 50 μm and 100 μm sizes obtained from high resolution airborne imaging (Harvey *et al.* 1991).

The source is classified non-variable in the IRAS survey but a $\sim$ 40% increase at 24 μm in 1985 is reported by Lewis, Terzian and Eder (1986) which may be connected with the OH maser flare. No further information concerning IR variability is available in the literature.

6.2.5 Continuum Emission

Sensitive VLA observations of the source reveal no associated continuum emission ($<$ 3.9 mJy at λ = 1.5cm) (Sahai, Claussen and Masson 1989).

6.3 Radio Interferometry at 1612 MHz

Early VLBI observations of IRC+10420 at 1612 MHz were reported by Reid *et al.* (1979), Mutel *et al.* (1979) and Benson *et al.* (1979). The latter observations were reduced using the fringe-rate mapping technique and provide point component positions for features with high SNR. A compact feature was detected at $V_{LSR} \sim 45.4$ km s^{-1} with some evidence for disk-like structure in the blue-shifted emission. At an assumed distance of 3.4 kpc (Mutel *et al.* 1979) the overall extent of the maser emission is 5 x 10^{16} cm which is comparable to other OH/IR supergiants. The red-shifted emission at $V_{LSR} \sim 100$ km s^{-1} was not detected

at VLBI resolution. Reid *et al.* (1979) confirmed the stellar position as coincident with the OH maser emission.

MERLIN observations of the blue-shifted emission using closure-phase imaging techniques were reported by Diamond, Norris and Booth (1983). No clear evidence of a symmetric shell structure was found. The extreme blue-shifted emission was found to be aligned approximately N-S with an E-W disk at position angle $\sim 72°$ apparent at larger LSR velocities. This was interpreted as an equatorial disk in an overall bipolar outflow. The MERLIN radius-velocity data $\theta(V)$ when fitted as an expanding shell are consistent with a stellar velocity $V_* \sim 76$ km s^{-1} , expansion velocity $V_e \sim 37$ km s^{-1} and an angular radius $\theta_R \sim 1.25$ arcsec ($= 6 \times 10^{16}$ cm at 3.4 kpc).

An accurate OH position was established in a survey of OH/IR stars by Bowers, Johnston and Spencer (1981). Further VLA observations by Bowers (1984) covering the full range of emission revealed a complex kinematic structure not necessarily consistent with a bipolar outflow. The disk position angle shown in the MERLIN images of Diamond, Norris and Booth (1983) was found not to persist at higher LSR velocities. A spherical geometry was proposed where mass loss occurs without a preferred direction. The joint kinematic data at 1612 and 1667 MHz were modelled using three shells of differing radii consistent with the parameters $V_* \sim 76.5$ km s^{-1} and $V_e \sim 32.5$ km s^{-1} . Such discrete mass loss in random directions is consistent with the model of Alcock and Ross (1986) as discussed by Fix (1987).

VLA observations in right- and left-circular polarization at 1612 and 1665 MHz were performed by Nedoluha and Bowers (1992). The flux density had increased sufficiently by the time of the observations in December 1988 to allow imaging across the entire velocity profile and particularly near the stellar velocity $V_* \sim 80$ km s^{-1} . These maps show that the emission at 1612 MHz is unresolved

at $V_{LSR} < 46$ km s^{-1} and has the same E-W morphology between $V_{LSR} = 46-60$ km s^{-1} as reported by Diamond, Norris and Booth (1983). Incomplete shell structures occur over the velocity range $V_{LSR} = 63 - 95$ km s^{-1}, while at the stellar velocity $V_* \sim 80$ km s^{-1} the emission is predominantly E-W at a position angle of 90°. The emission at $V_{LSR} \sim 100 - 103$ km s^{-1} appears to indicate two shells with a N-S orientation of the stronger components. There is evidence for near-far and E-W asymmetry in the velocity field.

Nedoluha and Bowers (1992) interpret the circumstellar outflow as an oblate shell with an anisotropic radial velocity field (Bowers 1991). The outflow velocity is modelled as $\propto \rho_0^{-2}$, where ρ_0 is the outer radius of the ellipsoid and the nearside of the equatorial plane is tilted above the line of sight. The model parameters were derived by fitting the $\theta(V)$, $I(V)$ and position angle-velocity data $PA(V)$ derived from the images.

6.4 Polarization Properties of the 1612 MHz OH Maser Emission

6.4.1 Observational Properties

The OH/IR stars as a class have not been observed to show strong circular polarization in the 1612 MHz OH maser line, with the notable exception of the supergiant sources such as IRC+10420, VY CMa, VX Sgr and NML Cyg (Cohen *et al.* 1987; Zell and Fix 1989) and the Mira variable U Orionis (Reid *et al.* 1979; Cohen 1989). The observed degree of circular polarization in single dish spectra is strongly dependent on the velocity resolution of the observations. Cohen *et al.* (1987) estimate a lower limit to the component maser linewidth of ~ 0.1 km s^{-1}based on high resolution spectroscopy. At high velocity resolution (0.06 km s^{-1}) the supergiant sources mentioned above show peak circular polarization of $\sim$ 25-45% in single dish observations (Cohen *et al.* 1987). The extent of depolarization caused by spatial blending is uncertain (Zell and Fix 1991).

From the earliest observations, IRC+10420 has been known to exhibit strong circular polarization at high velocity resolution (Reid *et al.* 1979; Mutel *et al.* 1979; Benson *et al.* 1979; Cohen *et al.* 1987). Individual cross-power spectra contain highly circularly polarized features (Mutel *et al.* 1979), but this estimate of the degree of polarization does not properly account for source structure. The net circular polarization across the spectrum as a whole is non-zero and variable (Benson *et al.* 1979; Lewis, Eder and Terzian 1985). There is weak ($< 5\%$) linear polarization at 1612 MHz (Mutel *et al.* 1979).

Reid *et al.* (1979) estimate a circumstellar magnetic field strength of $\sim$ 10 mG by interpreting two adjacent features of opposite sign in their single dish V spectrum as a Zeeman pair. This Zeeman identification is not interferometric, however, and the magnetic field estimate is uncertain as a result.

6.4.2 Polarization Mechanisms

The molecular structure of hydroxyl is discussed by Herzberg (1950) and Cook (1977). The OH molecule has one unpaired electron and the first order quantum mechanical addition of the electronic and nuclear angular momenta implies two rotational series of the electronic groundstates $^2\Pi_{1/2}$ and $^2\Pi_{3/2}$. The state $^2\Pi_{3/2}$, $J = \frac{3}{2}$ has the lowest energy and is further split into a quartet by the combined effects of $\Lambda-$doubling and the hyperfine interaction between the electrons and the proton (Cook 1977). The $\Lambda-$doublet states have opposite parity and the total quantum number F takes the values $\{1,\ 2\}$ in each of these states. The discussion is confined to the $^2\Pi_{3/2}$, $J = \frac{3}{2}$, $F = 1 - 2$ transition at 1612.231 MHz in what follows.

A small magnetic field, B, splits each F state into $2F + 1$ magnetic substates with magnetic quantum number $m_F \in \{-F,\ -F+1,\ ...,\ F-1, F\}$. The magnetic substates are offset in energy by $\triangle E = g_F^{\pm} \mu_B B m_F$, where μ_B is the Bohr magneton and $g_F^{\pm}$ the Lande splitting factor (Cook 1977; Lis, Goldsmith and

Predmore 1989). The Lande factor takes the values $\{g^+_{F=2} = 0.935(\frac{3}{4}),\ g^+_{F=1} = 0.935(\frac{5}{4}),\ g^-_{F=2} = 0.936(\frac{3}{4}),\ g^-_{F=1} = 0.936(\frac{5}{4}),\}$, where the superscript denotes the parity of the $\Lambda-$doublet (Cook 1977). The Zeeman substates are depicted in Fig. 6.1. Transitions are allowed with $m_F = (-1,\ 0,\ 1)$ and are known as $(\sigma^-, \pi, \sigma^+)$ components respectively. The Zeeman patterns for propagation parallel and perpendicular to the magnetic field are shown in Fig. 6.2. The pure σ^- and σ^+ components are in general left- and right-elliptically polarized respectively, with the semi-major to semi-minor axial ratio of the polarization ellipse given by $\cos\psi$, where ψ $(< \frac{\pi}{2})$ is the angle between the magnetic field and line of sight (Lis, Goldsmith and Predmore 1989). The pure π components are linearly polarized parallel to the projected magnetic field and are zero for $\psi = 0$.

The transport of polarized maser emission in a full Zeeman multiplet is a complex problem with many theoretical considerations. These include the evolution of the molecular density matrix, radiative transfer of the maser emission, cross-relaxation caused by trapped infra-red radiation and the effects of Faraday rotation. This model was originally considered by Goldreich, Keeley and Kwan (1973a,b). The effect of velocity gradients was further developed by Deguchi and Watson (1986), Nedoluha and Watson (1990) and references therein.

Neglecting Faraday rotation and velocity gradients, a saturated astrophysical OH maser subject to Zeeman splitting appreciably greater than the maser linewidth $\Delta\omega$ will have non-zero components (Goldreich, Keeley and Kwan 1973b),

$$\begin{aligned}
\left(\frac{V}{I}\right)_{\sigma^\pm} &= \pm\frac{2\cos\psi}{(1+\cos^2\psi)} \\
\left(\frac{Q}{I}\right)_{\sigma^\pm} &= \frac{\sin^2\psi}{(1+\cos^2\psi)} \\
\left(\frac{Q}{I}\right)_{\pi} &= -1
\end{aligned} \tag{6.1}$$

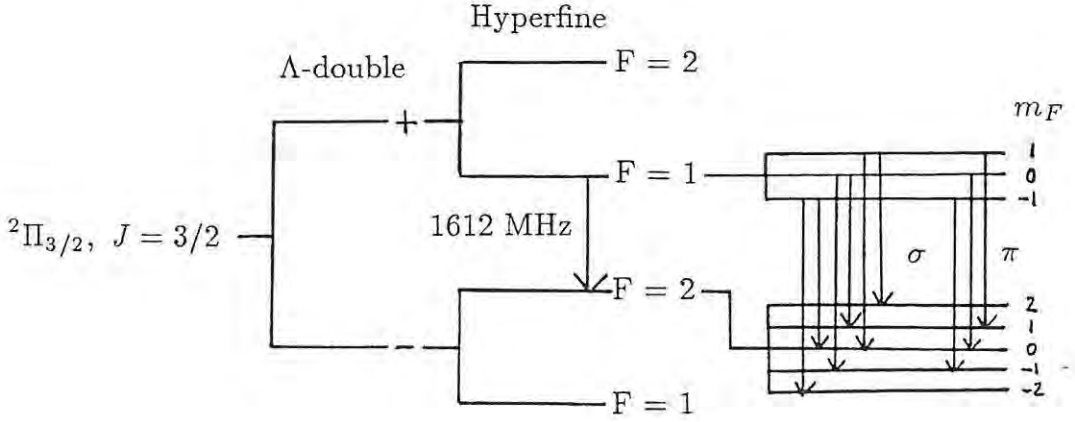

Fig. 6.1. The Zeeman substates for the groundstate $^2\Pi_{3/2}$, $J = \frac{3}{2}$ of the OH molecule.

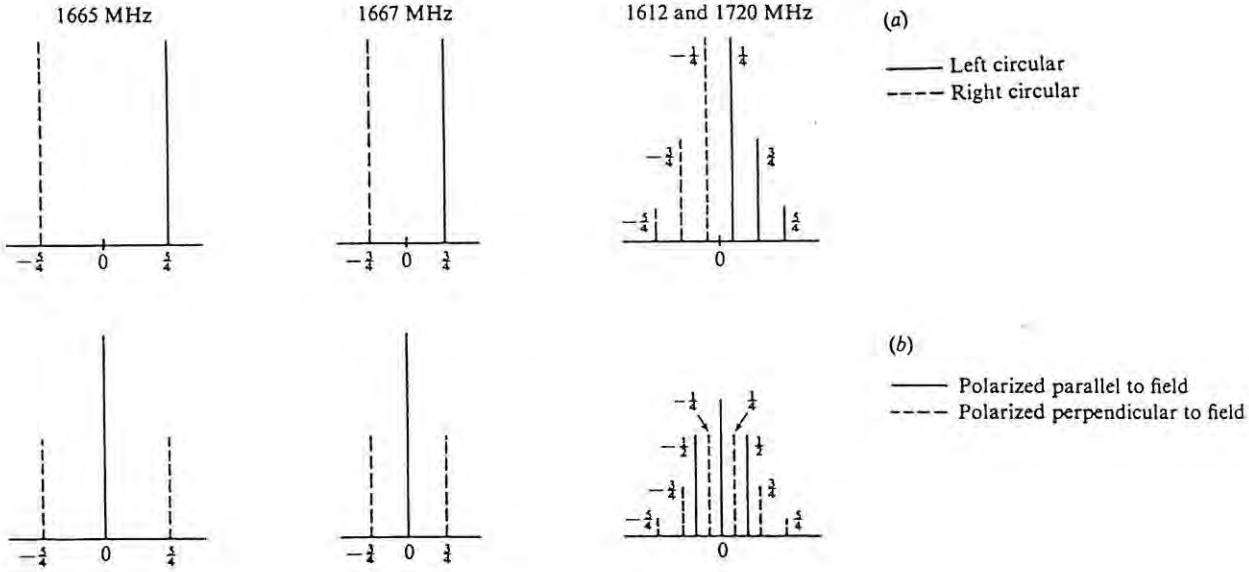

Fig. 6.2. The Zeeman components of the transitions in the Λ− doublet of the $^2\Pi_{3/2}$, $J = \frac{3}{2}$ state of OH; (a) observation parallel to the field, (b) observation perpendicular to the field (from Cook (1977)).

The σ components dominate for $\psi < 55°$ while the π components dominate at larger angles. Significant Faraday rotation suppresses the linear polarization to produce non-zero components (Goldreich, Keeley and Kwan 1973b),

$$\left(\frac{V}{I}\right)_{\sigma^{\pm}} = \pm 1$$
$$\left(\frac{V}{I}\right)_{\pi} = \kappa, \qquad (-1 < \kappa \leq 1)$$

Here, π components dominate for $\psi > 72°$.

The effects of velocity gradients on maser polarization has been considered by Deguchi and Watson (1986) and Nedoluha and Watson (1990), partly to explain the absence of full Zeeman patterns in polarization observations of OH masers. In this model where the overlap of different Zeeman components is considered, the degree of linear and circular polarization depends on several factors including the dimensionless ratio Δv_z of the Zeeman splitting to the thermal line breadth Δv_{th}, the velocity gradient Δv_g, the degree of saturation and optical depth of the maser, and the angle, ψ, between the magnetic field and line of sight. The main predictions of the theory are (Nedoluha and Watson 1990),

(a) High net circular polarization (50−100%) will be observed if $\Delta v_z \geq 1$ and Δv_g is a few times Δv_{th}. The components may be narrowed with no clear Zeeman pattern. The degree of net circular polarization increases with higher maser saturation and optical depth. Significant net circular polarization $(25 - 50\%)$ is possible for $\Delta v_z < 1$ in certain circumstances (Deguchi and Watson 1986).

(b) Net circular polarization is possible for large ψ and linear polarization at small ψ, contrary to the basic model discussed above.

(c) Faraday rotation will reduce the degree of linear polarization expected from (6.1) but numerical models indicate lower associated net circular polarization in this case.

(d) The degree of linear polarization will be uncorrelated with ψ contrary to the basic model for Zeeman components. This may introduce a high degree of randomness in the polarization position angle of elliptically polarized components.

6.5 Evolutionary Status

The OH/IR stars are widely held to be the progenitors of planetary nebulae on the basis of their luminosities, mass-loss rates and location on the AGB (Habing 1990). Several candidate sources have been proposed as post-AGB transitional objects or proto-planetary nebulae, including IRC+10420 (Knapp 1989). The nature of the transitional phase is reviewed by Habing (1990) and Rodriguez (1987). It is generally believed that the progenitor objects undergo a period of high mass-loss towards the end of their AGB evolution, depleting the remnant hydrogen shell (Jura 1987). The central star is expected to contract and increase in temperature, causing the object to move towards the blue and increase in visual magnitude as the expanding shell becomes thinner. The exposure of the stellar core leads to a high-velocity, hot stellar wind (Rodriguez 1987) and also the ionisation of the inner shell. The appearance of hydrogen recombination lines and forbidden metallic lines concludes the transition to planetary nebula (Volk and Kwok 1989).

The high mass-loss phase is modelled either as a "superwind" (Renzini 1981) or by invoking the interaction between the fast and slow stellar winds (Kwok 1982). The proto-planetary nebulae are found to have a typical size of 7 x 10^{17} cm (Bujarrabal *et al.* 1988).

The defining characteristics of proto-planetary nebulae are uncertain (Rodriguez 1987), with a wide range of accepted criteria. The evidence for the transitional nature of IRC+10420 is examined below. The early spectral type $F8$ and position in the IRAS two colour plot of $\log\left(\frac{F_{60\mu m}}{F_{25\mu m}}\right)$ versus $\log\left(\frac{F_{25\mu m}}{F_{12\mu m}}\right)$ indicates

an object intermediate between the Miras and the young planetary nebulae (Chapman 1988; Volk and Kwok 1989). The object has IRAS colours typically indicative of OH/IR stars with 10 μm absorption rather than the observed 10 μm emission (Volk and Kwok 1989). This may indicate an unusual circumstellar shell or a low initial optical depth in the shell (Hrivnak, Kwok and Volk 1989). The source has a high expansion velocity and a mass-loss rate $\sim 10^{-4} M_{\odot}$ /yr determined from OH and CO observations (Knapp 1989), providing evidence of a "superwind" phase (Bujarrabal, Gomez-Gonzalez and Planesas 1989). Radiation-driven mass-loss calculations and models of the spectral energy distribution indicate that the mass-loss may have terminated recently (Knapp 1989; Hrivnak, Kwok and Volk 1989). The high expansion velocity and early spectral type delineate the source quite strongly amongst the OH/IR stars as a class (Hekkert, Chapman and Zijlstra 1992)

The interferometric OH maser observations show asphericity without unambiguously confirming a bipolar outflow (Diamond, Norris and Booth 1983; Bowers 1984). The strong asymmetry between the blue- and red-shifted peaks in the total power spectra and the flare in peak flux density may further indicate evolution in the circumstellar envelope structure (Nedoluha and Bowers 1992). No continuum emission has been detected to indicate ionization of the inner shell (Drake and Linsky 1989), although Fix and Cobb (1987) suggest that the Mg and Fe emission lines arise from a precursor to a fast stellar wind. The absence of H_2O and SiO masers, which form closer to the star can be explained in terms of disruption in the density and mass-loss in the inner shell (Lewis 1989). An outer fossil shell from an earlier M-giant phase has been predicted (Mutel *et al.* 1979). The detection of HCN and SO_2 in the envelope may indicate more advanced circumstellar chemistry (Jewell, Snyder and Schenewerk 1986). Molecular emission may persist for $\sim$ 300 years after the onset of the planetary nebula phase (Bujarrabal *et al.* 1988).

A distinct class of candidate proto-planetary nebulae are the so-called 89 Her objects, a set of high galactic latitude F supergiants (Parthasarathy and Pottasch 1986; Hrivnak, Kwok and Volk 1989). These may be low or intermediate mass stars that display supergiant spectral characteristics due to temporary extension of the stellar atmosphere as a result of high mass-loss (Pottasch and Parthasarathy 1988). IRC+10420 may be a low-latitude counterpart to these objects.

The planetary nebulae typically have bipolar or ellipsoidal structure and this asymmetry is believed to arise during the AGB evolution of the progenitor (Habing 1990). Several mechanisms have been proposed including magnetic confinement and binarity (Bowers, Johnston and de Vegt 1988) but this issue remains unresolved.

This 10 mG estimate of the magnetic field in the envelope of IRC+10420 by Reid *et al.* (1979) has been interpreted to imply a stellar magnetic field of $\sim 10^2 - 10^3$ G (Reid 1990) based on the assumption that the magnetic field strength varies as the square of the distance from the stellar surface. Barvainis, McIntosh and Predmore (1987) provide evidence of supergiant stellar magnetic fields $\leq$ 100 G from the detection of circular polarization in circumstellar SiO maser emission. The implied magnetic energy density in the circumstellar envelope has important dynamical implications for the circumstellar outflow (Chapman and Cohen 1986; Barvainis, McIntosh and Predmore 1987; Nedoluha and Bowers 1992). The association of OH maser polarization with the supergiant OH/IR stars may have important implications for their structure and evolutionary status. The exact nature of this connection is unknown.

CHAPTER 7: KINEMATICS AND POLARIZATION

Introduction

This chapter concerns the astrophysical interpretation of the VLBI results presented in Chapters 4 and 5. This includes a discussion of the morphology, variability and kinematics of the source. The polarization structure is considered and estimates are presented for the circumstellar magnetic field.

7.1 Variability and Morphology

The profile shape and peak flux density of the total power spectra obtained from the MK2 and MK3 VLBI data, shown in Fig. 4.2 and Fig. 5.1 respectively, when compared to previously published observations, confirm the short-term variability and the remarkable long-term flare activity known for this source (Nedoluha and Bowers 1992). The plateau emission at V_{LSR} = 50-60 km s^{-1} has increased by a factor of 2 in peak flux density between the two VLBI epochs considered as part of this work. Unpublished spectra for epochs 1985.8 and 1986.3 (Gaylard and West 1991) confirm that there is short-term variability on time-scales at least as short as six months.

The VLBI maps in Fig. 4.6 and Fig. 5.6 show clearly that the source structure has varied between the two epochs. In general, however, both sets of VLBI images follow closely the overall morphology of the MERLIN maps (Diamond, Norris and Booth 1983) and previous VLA observations (Bowers 1984; Nedoluha and Bowers 1992). The VLBI images trace the most compact maser emission in the source with little sensitivity to extended emission and thus provide useful complementary information on the source morphology.

In the velocity range V_{LSR} = 40-45 km s^{-1} both epochs show compact emission with a N-S orientation. A prominent triplet is evident in both sets of

maps at $V_{LSR} \sim 45.4$ km s^{-1} . The central component of this triplet has been postulated as the stellar position (McLaren and Betz 1980; Bowers 1984; Nedoluha and Bowers 1992). In the range $V_{LSR} = 46-49$ km s^{-1} the emission is distributed in an E-W disk-like structure at an approximate position angle of $\sim -70°$ measured N through E right ascension. There is E-W asymmetry in the component position angles. The disk is clearly shown in the MERLIN images of Diamond, Norris and Booth (1983).

The E-W disk morphology persists in general form through $V_{LSR} \sim 59$ km s^{-1} , but a striking shell structure is evident in the MK3 images in the range $V_{LSR} = 49-55$ km s^{-1} . The channel map at $V_{LSR} = 52.9$ km s^{-1} delineates the shell clearly and is reproduced at higher resolution in Fig. 7.1. There is some evidence for the shell structure in the MK2 images over the corresponding velocity range but it is neither pronounced or complete. In the range $V_{LSR} = 59-64$ km s^{-1} the VLBI maps are in good agreement with the VLA maps of Nedoluha and Bowers (1992), showing larger, partially complete ring structures superimposed on the E-W disk emission evident at lower LSR velocities.

The primary variation in the source morphology between the two epochs is the clear enhancement of the northern shell emission in the range $V_{LSR} \sim 49-55$ km s^{-1} . New shell components are particularly evident between a position angle of +27° and -58° towards the NW edge of the shell. The western components of the E-W disk-like emission have decreased somewhat in peak brightness between the two epochs.

7.2 Proper Motion and Kinematics

This section considers the kinematics of IRC+10420, including proper motion. Previous proper motion studies of OH main-line masers have included MERLIN observations of U Orionis (Chapman, Cohen and Saikia 1991) and VLBI observations of the star-forming region W3(OH) (Bloemhof, Reid and Moran 1992).

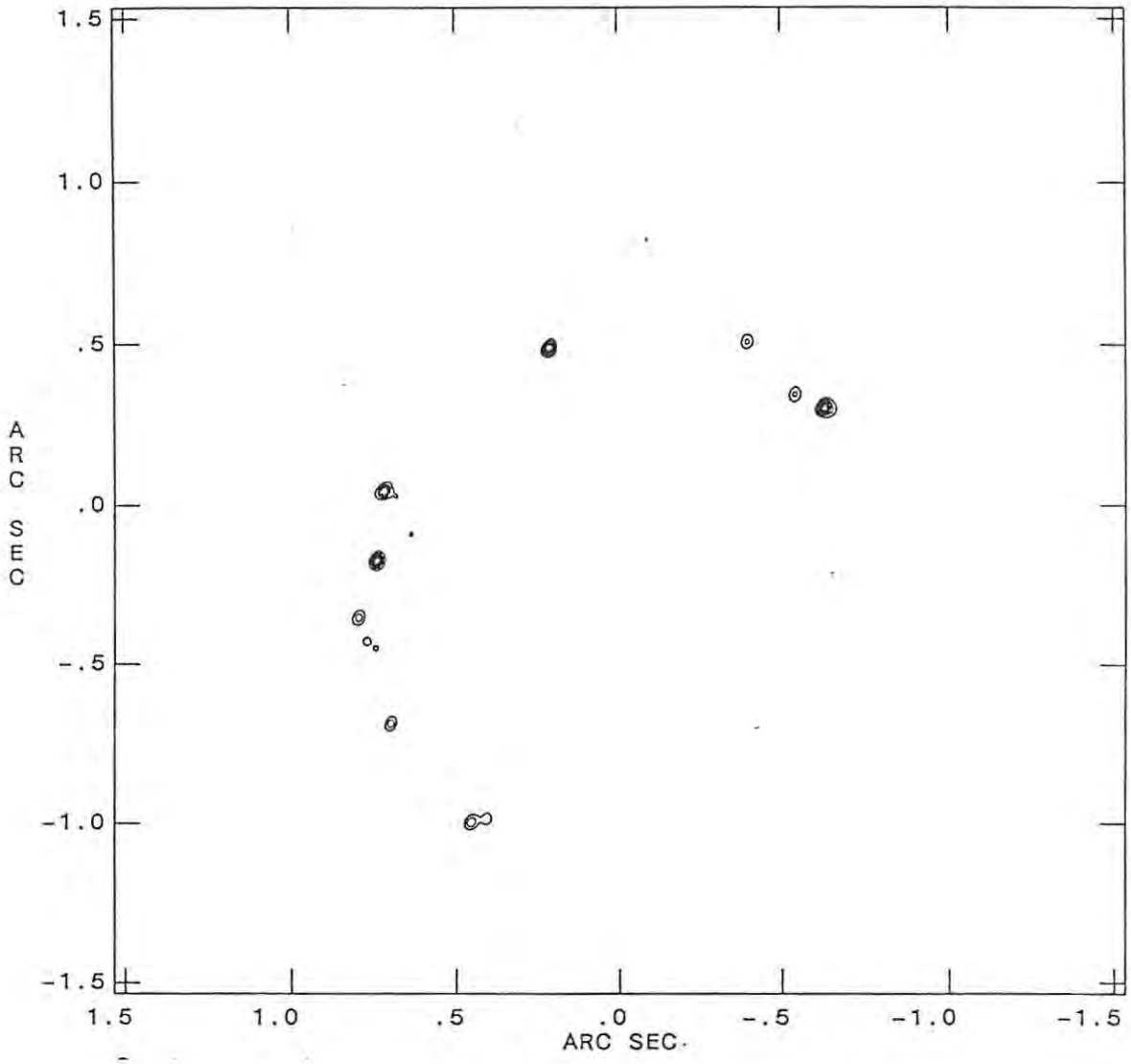

Fig. 7.1. Channel map of the Stokes I emission at $V_{LSR} = 52.90$ km s^{-1} obtained from the 1987 MK3 VLBI observations. Contour levels are at (15%, 30%, 45%, 60%, ,75%, 90%, 100%) of the peak channel brightness.

Results are presented for what is believed to be the first VLBI determination of proper motion for 1612 MHz OH masers towards an OH/IR star.

7.2.1 Proper Motion Determination

Two separate VLBI observations of IRC+10420 have been reduced as part of this work, and the results for each epoch are presented in Chapters 4 and 5. This suggests the possibility of determining bulk proper motions in the source, a topic which is of considerable interest due to the complex kinematics of IRC+10420 (Diamond, Norris and Booth 1983; Nedoluha and Bowers 1992). The experiment design was not optimised for proper motion determination due to the heterogeneous VLBI recording systems and correlators used at each epoch, although both data sets were processed within AIPS using a comparable software path. These differences are not ideal but do not preclude the determination of proper motion.

The two epochs were observed in 1982.80 and 1987.17, yielding a time interval, $\triangle t = 4.37$ yr over which to detect proper motions. A measured angular separation $\triangle\theta$ at a distance D implies a velocity of,

$$\left(\frac{V}{km\ s^{-1}}\right) \sim 1731.5 \left(\frac{\triangle\theta}{mas}\right)\left(\frac{D}{kpc}\right)\left(\frac{\triangle t}{days}\right)^{-1} \qquad 7.1$$

As discussed in Chapters 4 and 5 the component positions at each epoch in each velocity channel were derived by fitting elliptical Gaussians to each component over a tightly constrained, interactively defined region in the image, using the AIPS task JMFIT. Note that Tables 4.3 and 5.4 contain consolidated component lists after fitting in velocity to obtain the peak component velocity and linewidth. In contrast, the individual component fits in each channel are used in what follows. The error in the fitted Gaussian component peak positions in each channel is,

$$\epsilon_{X,Y} \sim \frac{\theta_{beam}}{2\ SNR} \qquad 7.2$$

where SNR is the signal-to-noise ratio in the images (Bloemhof, Reid and Moran 1992; Fomalont 1986). This relation excludes gross systematic imaging errors. Each component typically persists over several velocity channels n_c and, if matched components exist at each epoch in each channel, a channel average of the proper motion vectors can be performed to derive an averaged proper motion for the component. Assuming an equal SNR for each component in each channel, the minimum SNR required to measure a proper motion velocity of $V_{1\sigma}$ is, from (7.1),

$$SNR \sim \frac{1731.5}{\sqrt{2n_c}} \left(\frac{\theta_{beam}}{mas}\right) \left(\frac{D}{kpc}\right) \left(\frac{V_{1\sigma}}{km\ s^{-1}}\right)^{-1} \left(\frac{\triangle t}{days}\right)^{-1} \qquad 7.3$$

Distance estimates for IRC+10420 vary from 3.4 to 5.8 kpc (Mutel *et al.* 1979; Bowers 1984; Nedoluha and Bowers 1992) while the geometric mean of the major and minor axes of the synthesised beams at each epoch are comparable at $\sim$ 30 mas. Previous studies of the kinematics of IRC+10420 have consistently estimated the expansion velocity in the circumstellar envelope to be $\sim$ 35 kms^{-1}. For a 10% uncertainty in the proper motion velocity of 3.5 kms^{-1} equation (7.3) indicates a required SNR of $\sim \frac{6.6}{\sqrt{n_c}} \left(\frac{D}{kpc}\right)$. This condition is satisfied by sufficient components in the VLBI images at each epoch even with single-channel detection at the maximum distance estimate of 5.8 kpc. The constraint defined by equation (7.3) is clearly more severe in sources with lower representative bulk velocities or that are at smaller distances.

The MK2 experiment was observed in left-circular polarization. The MK3 Stokes I components were used in the proper motion analysis. No significant systematic error is expected from this. The I and V component positions converge where there is sufficient signal-to-noise ratio to allow a comparison.

The absolute astrometric position of the phase centre in the VLBI images is unknown due to the nature of the VLBI data reduction technique as discussed

in Chapter 3. The maps were aligned by translating the MK2 maps to provide coincidence between the compact central component of the triplet which occurs at both epochs near $V_{LSR} \sim 45.5$ km s^{-1} . The position of this component, which is compact and persists over several channels, has been postulated as the stellar position based on kinematic and other arguments (Bowers 1984; Nedoluha and Bowers 1992) but this is not conclusive. All derived proper motions are uncertain by a constant, additive velocity offset due to the uncertainty in the astrometric position of the phase centre at each epoch, or equivalently the unknown proper motion of the reference component used for alignment (Bloemhof, Reid and Moran 1992).

The AIPS analysis software does not transform the (u, v, w) geocentric coordinates of date to a quasi-inertial reference frame such as the solar system barycentre. The component positions thus need to be referred to a reference epoch and angular coordinate frame before deriving proper motions. Over a small field the angular coordinate distortion is approximately a translation and rotation about the field centre. The first order translation is absorbed in the unkown constant velocity offset discussed above and the higher order terms can be removed by correcting for the differential effects of precession, nutation, annual aberration and general relativistic solar gravitational deflection (Bloemhof, Reid and Moran 1992). For the two data sets considered here the differential effects are ~ 0.7 mas at a radius of 1500 mas from the field centre and are estimated to have been corrected to a precision well within the errors in the component positions. A reference epoch of 1950.0 was used in the differential coordinate corrections. The analytic form of these corrections can be found in the Explanatory Supplement to the Astronomical Almanac and other references (Taff 1981), but were performed numerically using general precession routines. The uncertainty in the assumed stellar position is quoted as ~ 0.2 arcsec by Nedoluha and Bowers (1992) based on VLA observations. This uncertainty contributes less than 0.1 μas error to the differential

coordinate corrections. In contrast, a simple coordinate rotation to remove differential effects leaves residual errors of $\sim$ 0.1 mas and is inadequate for proper motion determination.

The matching of components at each epoch was performed by inspection using an interactive graphics program. A total bandwidth of 250 kHz was recorded at both epochs. The MK2 experiment was correlated over 128 frequency channels while the MK3 observations were correlated over 112 frequency channels. The MK3 component positions were interpolated over velocity to derive new MK3 component positions at the MK2 channel velocities. This is equivalent to padding one of the cross-correlation lag functions with zeros. Component identifications for each MK2 component in each velocity channel were accepted subject to the following criteria:

(a) The associated MK3 component is detected in two adjacent velocity channels on either side of the MK2 component velocity to allow linear interpolation of the MK3 component position.

(b) The angular separation of the two MK3 components used for interpolation is less than $\frac{\theta_{beam}}{3} \sim 10$ mas.

(c) The ratio of major to minor axes of the elliptical Gaussian fitted to each component before deconvolution is less than 2:1.

The derived proper motions in each channel were further averaged over velocity using minimum variance weighting to produce averaged proper motions for each component. All error calculations were based on the approximate relation (7.2) using noise variance estimates derived from the deepest negative pixel in each channel at each epoch as discussed in section 5.3. These estimates of noise variance are somewhat conservative but are more representative of possible systematic imaging errors than standard off-peak noise variance estimates.

Further to the component identification criteria, the averaged proper motions were rejected if:

(d) The modulus of the proper motion error vector exceeds 3.5 km s^{-1} which is 10% of the outflow velocity.

The list of components satisfying the above conditions is given in Table 7.1 for an assumed distance of 3.4 kpc (Mutel *et al.* 1979). In cases where the apparent position of the major axis of the component can be derived in the strongest channel by deconvolution of the synthesised beam this value is included in the table. The position angles of the matched component pairs in each channel are plotted against each other in Fig. 7.2. There is a good linear correlation between the position angles at each epoch ($r = 0.72$), thus lending credence to the component identifications and to the interpretation that bulk proper motions in the circumstellar gas are being observed.

The morphology of the OH maser components is sufficiently persistent over the time interval between the observations to allow relatively reliable identification of associated components at each epoch. There is some variation of component brightness between the epochs but this was not pursued further due to limitations imposed by systematic imaging errors.

The proper motion vectors for assumed distances of 3.4 kpc and 5.8 kpc are plotted in Fig. 7.3 and Fig. 7.4 respectively.

7.2.2 Kinematics

The standard model for the kinematics of OH/IR circumstellar shells is that of a thin expanding sphere with a constant radial outflow velocity (Reid *et al.* 1977). The angular extent of the shell at a velocity V_{LSR} is given by,

$$\theta(V_{LSR}) = \theta_R \sqrt{1 - \frac{(V_{LSR} - V_*)^2}{V_e^2}} \qquad 7.4$$

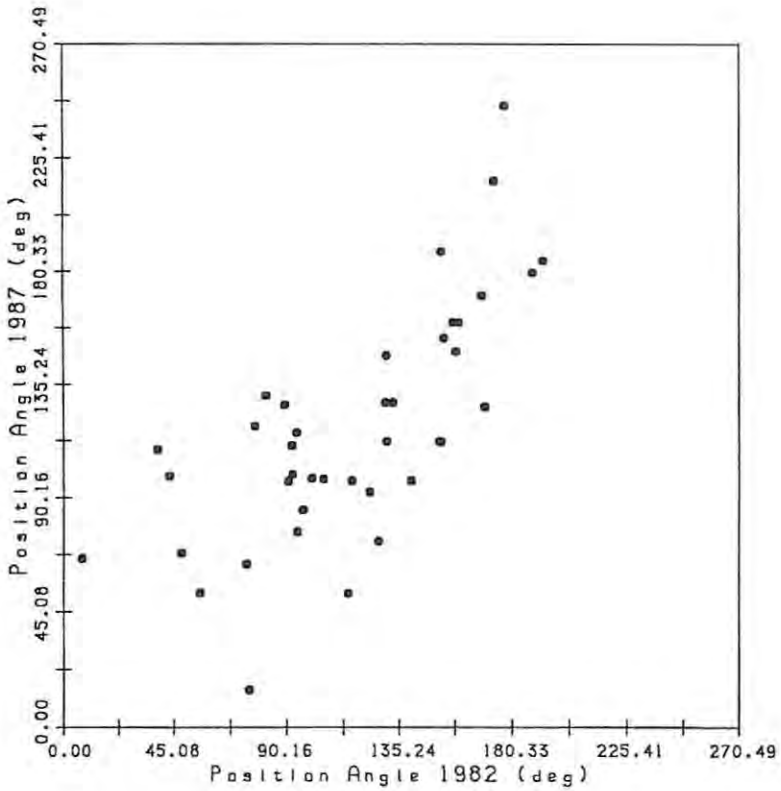

Fig. 7.2. The correlation of the apparent component position angles between the two epochs, after deconvolution by the synthesised beam.

where θ_R is the angular radius of the shell, V_* is the LSR velocity of the central star, and V_e is the radial expansion velocity. This model is an idealization and the kinematics of OH/IR shells are generally more complex. It does provide a useful reference however.

The proper motion diagrams shown in Fig. 7.3 and Fig. 7.4 are subject to an unknown constant vector velocity offset and need to be interpreted carefully as a result. In the standard model (7.4) an error $\Delta\theta$ in the assumed stellar position used to align the maps would imply a velocity offset of magnitude $\sim V_e \sin \Delta\theta$. The proper motion diagrams do however provide clear evidence for overall expansion in the circumstellar outflow despite marked E-W asymmetry in the velocity field. The proper motion vectors increase in magnitude as V_{LSR} approaches $V_* \sim 80$ km s^{-1} , in common with the standard model.

TABLE 7.1
Table of Proper Motions

X^a	Y^a	V^b	ΔX^c	ΔY^c	$\epsilon^d_{\Delta X,\Delta Y}$	PA_2^e	PA_3^e
0.542	-0.519	64.02	14.24	-6.27	0.24	152.3	112.2
-0.513	0.522	61.84	7.59	11.92	0.25	55.3	52.4
-0.665	0.367	59.30	-5.21	8.06	0.28	104.7	97.4
0.768	-0.245	57.85	10.83	-2.67	0.11		128.0
0.748	-0.138	56.48	8.94	-0.32	0.14	169.7	126.2
-0.623	0.321	55.74	-0.89	2.08	0.23	91.9	
0.750	-0.128	55.59	9.97	0.10	0.22		151.0
0.733	-0.228	54.63	5.56	-3.74	0.44	17.9	
0.522	0.299	54.11	5.99	4.83	0.53		118.8
0.791	-0.353	53.85	8.91	4.88	0.83	130.1	146.6
0.728	-0.184	53.12	6.56	1.33	0.87		151.9
-0.630	0.285	52.99	0.54	12.67	0.57	173.3	216.3
0.709	0.032	52.76	7.77	0.55	0.74	123.4	92.2
-0.616	0.290	52.26	-4.32	1.39	0.47	91.3	
0.654	-0.309	52.06	7.45	-1.95	0.20	157.1	159.8
0.724	0.027	51.92	13.21	-1.31	0.41	116.2	96.7
0.320	0.456	51.30	8.36	2.42	0.75	89.1	127.0
0.712	-0.131	50.58	22.58	5.20	0.69	75.2	14.5
-0.673	0.134	50.44	1.83	0.76	0.18	48.0	68.2
0.669	0.069	49.98	10.60	-0.66	0.72		135.5
-0.669	0.173	49.48	-0.44	-0.85	0.30	188.5	179.6
-0.358	-0.118	48.33	2.09	-3.63	0.65	152.4	188.1
0.293	-0.408	47.70	-1.52	-3.83	0.18	92.1	110.7
-0.411	-0.180	46.94	-1.24	-1.39	0.36	127.0	72.8
0.294	-0.397	46.58	8.24	-3.46	0.95	114.7	52.2
-0.249	0.256	45.49	3.22	3.57	0.41	177.4	245.9
-0.046	-0.001	45.49	-0.70	-0.03	0.30	38.3	109.1
-0.032	0.010	44.76	-0.78	-0.67	0.25	151.7	112.3
0.004	0.001	43.90	-0.36	-1.72	0.18	90.7	96.4
0.100	-0.336	41.13	5.70	-2.05	0.92	94.0	115.8

[a] Averaged angular position (X, Y) of the MK2 component with respect to the map centre, with X and Y increasing in the direction of increasing relative 1950.0 right ascension and declination respectively (arcsec).

[b] Averaged LSR velocity of the component (kms^{-1}).

[c] The proper motions for the component in X and Y, in the sense $(X_{1987} - X_{1982},\ Y_{1987} - Y_{1982})$ in mas.

[d] The estimated errors in ΔX and ΔY (mas).

[e] The position angle of the brightest channel in the component after deconvolution by the synthesised beam for the MK2 and MK3 data respectively, measured N through E (deg).

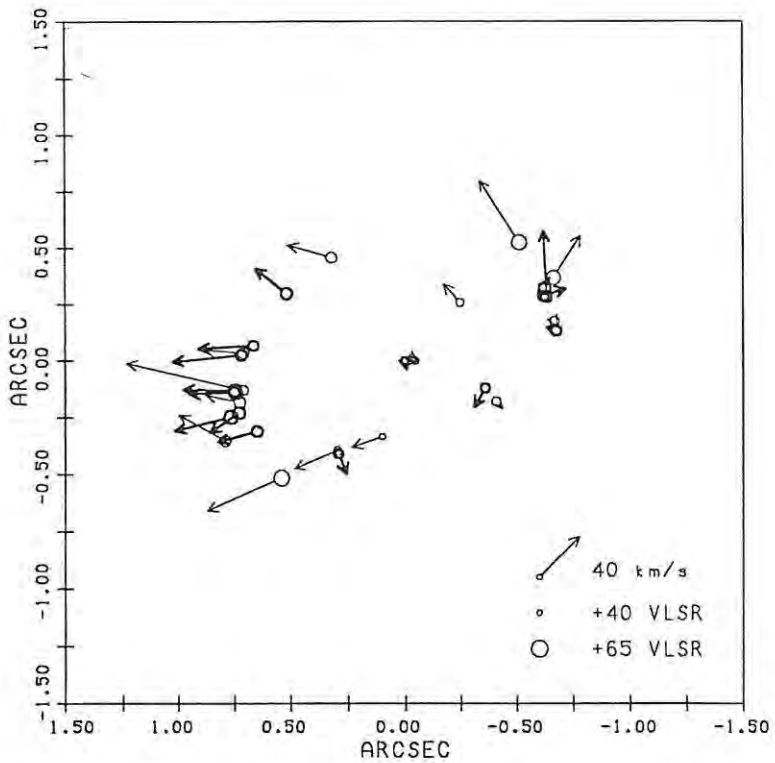

Fig. 7.3. The angular distribution of the proper motion velocity vectors for an assumed distance $D = 3.4$ kpc. The radius of the circle at the base of the arrow indicates the LSR velocity of the component.

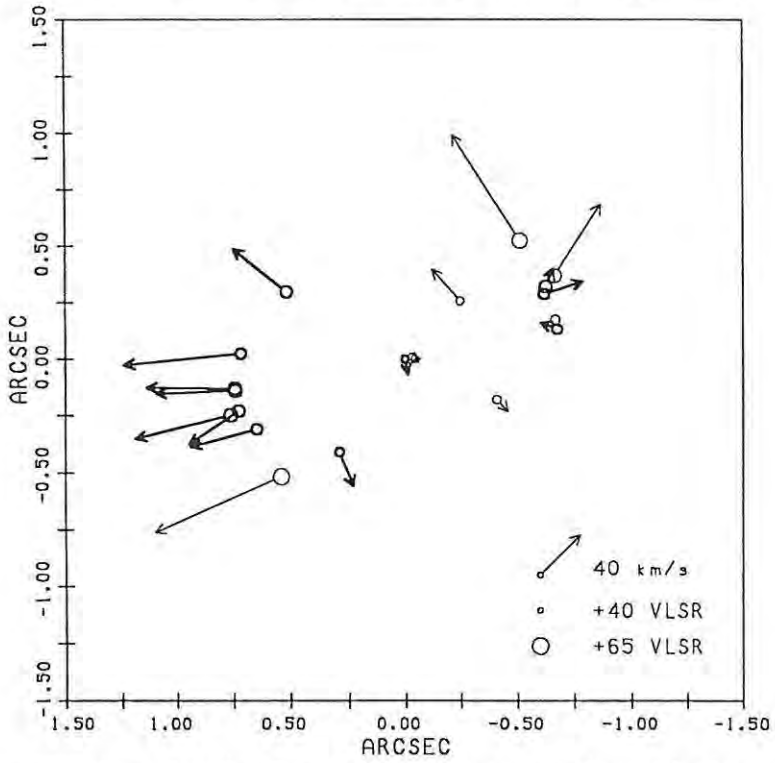

Fig. 7.4. The angular distribution of the proper motion velocity vectors for an assumed distance $D = 5.8$ kpc. The radius of the circle at the base of the arrow indicates the LSR velocity of the component.

The overall expansion in the envelope is further confirmed by examining the distribution of the change in pair-wise separation between the two epochs for all independent component pairs in Table 7.1. This technique was used by Bloemhof, Reid and Moran (1992) and Chapman, Cohen and Saikia (1991) and is non-parametric in the sense that it does not require a model for the velocity field or alignment of the two maps. We plot the distribution of,

$$|\mathbf{X}_{3i} - \mathbf{X}_{3j}| - |\mathbf{X}_{2i} - \mathbf{X}_{2j}|, \qquad i = 1, n; \quad j = i + 1, n$$

where $\mathbf{X}_{2i} = (X_{2i},\ Y_{2i})$ and $\mathbf{X}_{3i} = (X_{3i},\ Y_{3i})$ and $(\mathbf{X}_{2i},\ \mathbf{X}_{3i})$ are assumed to be matched components at each epoch. This distribution is plotted in Fig. 7.5. The non-zero mean of the distribution provides further clear evidence for expansion. The exact shape of the distribution however depends strongly on the uniformity of the sampling and cannot reliably be used to derive kinematic parameters, even if a standard model of the velocity field is assumed.

The radius velocity $\theta(V_{LSR})$ and position angle velocity $PA(V_{LSR})$ diagrams derived from the VLBI data are plotted in Fig. 7.6 and Fig. 7.7 respectively. These diagrams are consistent with their VLA counterparts published by Nedoluha and Bowers (1992), reproduced here as Fig. 7.8. The best-fit parameters to the standard model (7.4) are given by Nedoluha and Bowers (1992) as $\theta_R = 1.27$ arcsec, $V_e = 31.0$ km s^{-1} and $V_* = 79.3$ km s^{-1} , and this model is plotted as a solid curve in both sets of $\theta(V_{LSR})$ diagrams. The limited range in LSR velocity covered by the VLBI observations renders a re-determination of these parameters unreliable and probably misleading. The standard model is clearly a poor fit to the kinematics of IRC+10420.

The E-W disk-like emission discussed in section 7.1 is evident in the $PA(V_{LSR})$ diagrams and both E and W components persist over the velocity range covered

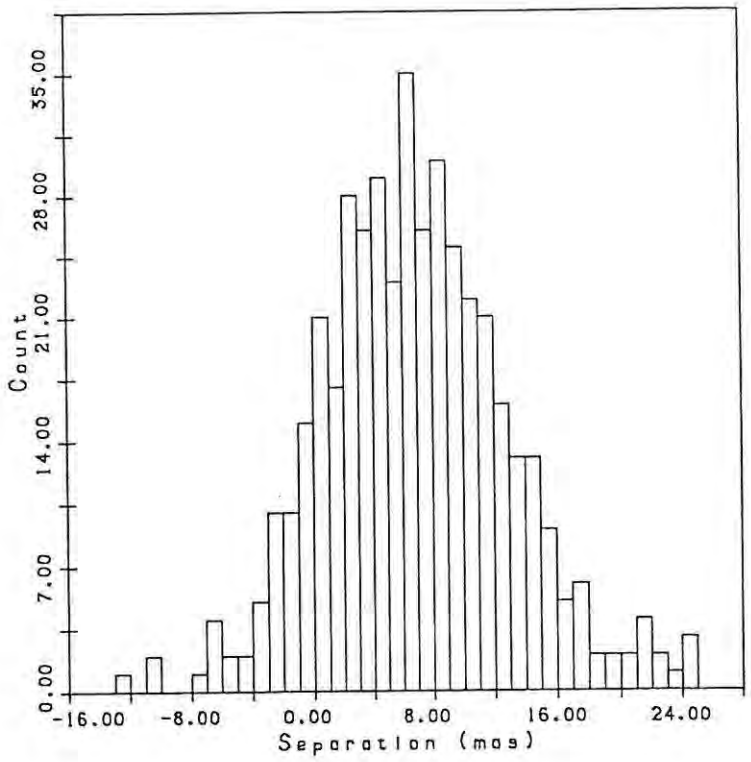

Fig. 7.5. The distribution of the change in pair-wise separation between the two epochs for all independent component pairs in Table 7.1.

by the VLBI observations. The position angle of the eastern component shows a linear decrease with increasing V_{LSR} at both epochs. The shell structure between $V_{LSR} \sim$ 49-55 km s^{-1} is evident in the increased scatter in the $PA(V_{LSR})$ plots over this velocity range.

The inadequacies of the standard expanding shell model have prompted more complex models of OH/IR circumstellar kinematics (Bowers and Johnston 1988; Bowers, Johnston and de Vegt 1989). These include biconical outflows and more generally, inclined ellipsoidal models with an anisotropic radial velocity field including acceleration and rotation (Bowers 1991). A discussion of possible physical reasons for non-sphericity or asymmetry is given by Diamond *et al.* (1985). Nedoluha and Bowers (1992) have proposed an elliptical model for the kinematic structure of IRC+10420 and we consider these models in more detail below.

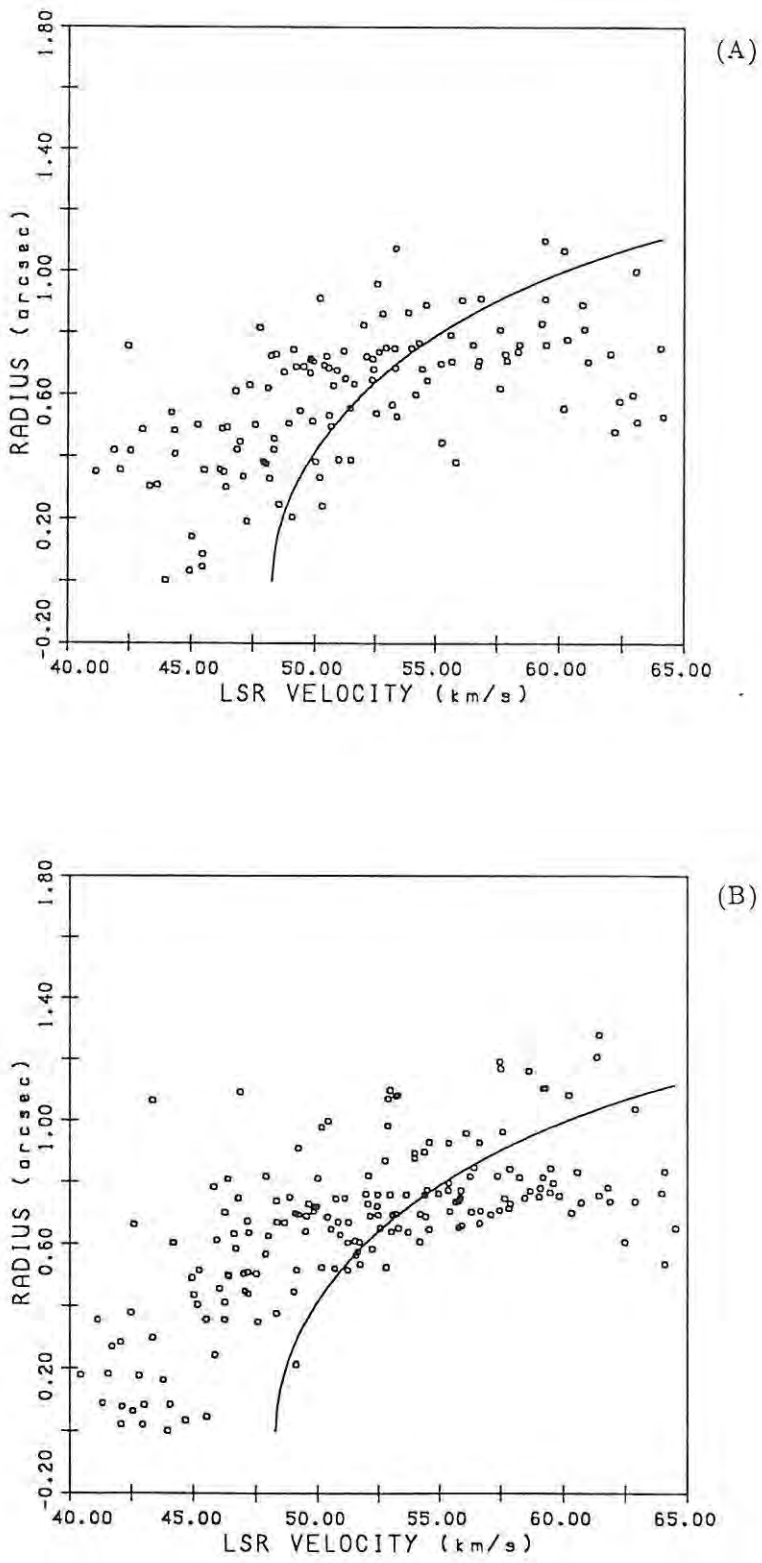

Fig. 7.6. The angular radius - velocity diagrams for the MK2 (a) and MK3 (b) VLBI observations of IRC+10420. The best fit to the standard model obtained by Nedoluha and Bowers (1992) with $\theta_R = 1.27$ arcsec, $V_e = 31.0$ km s^{-1} and $V_* = 79.3$ km s^{-1} is plotted as a solid line.

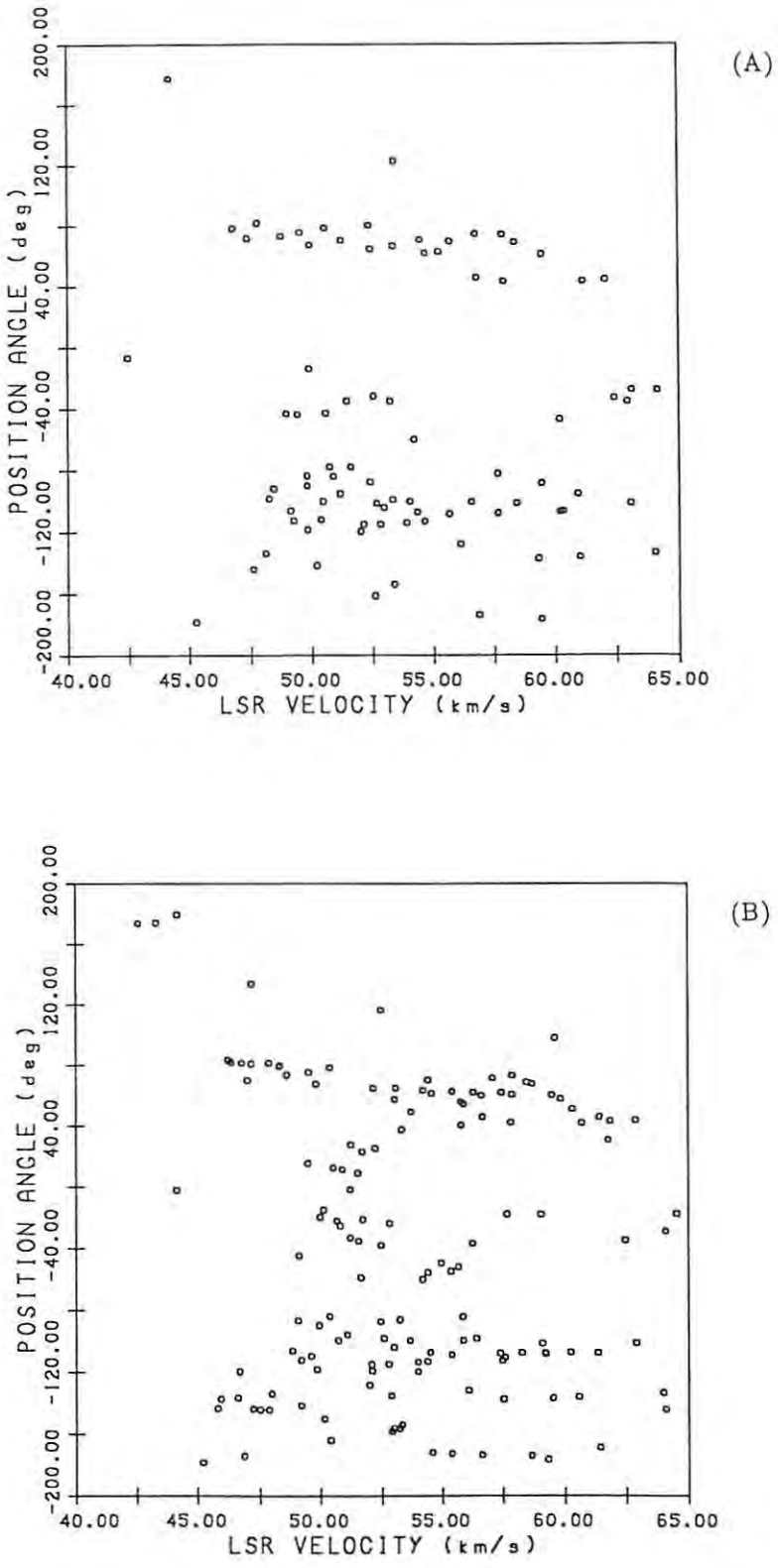

Fig. 7.7. The position angle - velocity diagrams for the MK2 (a) and MK3 (b) VLBI observations of IRC+10420. Position angles are only plotted for components with a projected radial distance greater than 0.5 arcsec.

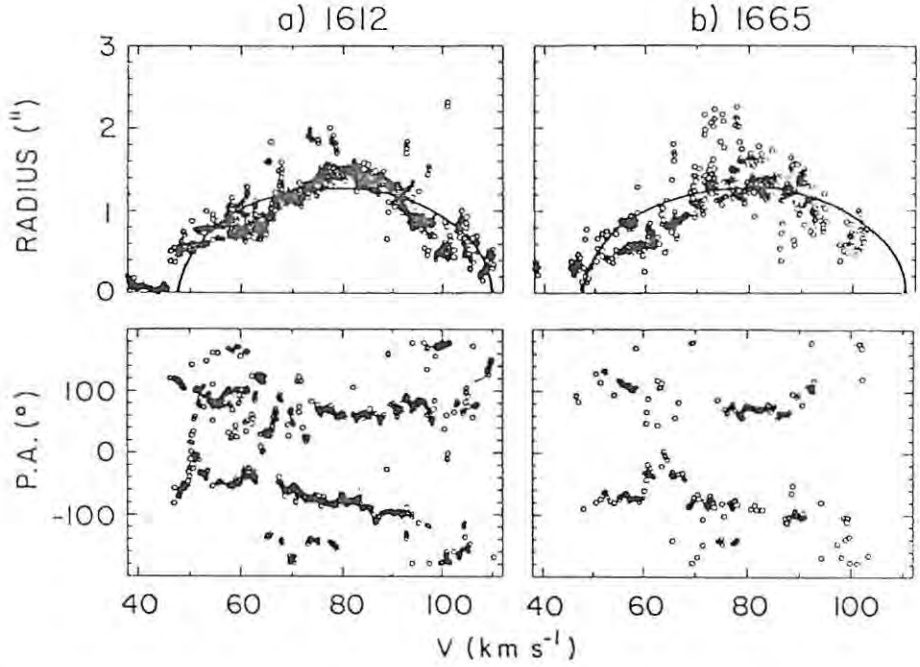

Fig. 7.8. Best-fit Gaussian positions of (a) 1612 MHz and (b) 1665 MHz emission. The top graphs give the distance from the inferred VLA stellar position as a function of velocity. The bottom panels give the position angle as a function of velocity for all features at least 0.5 arcsec from the inferred stellar position (from Nedoluha and Bowers (1992)).

The original model formulation of Bowers (1991) can be extended by allowing arbitrary three-dimensional rotations of the ellipsoid and by relaxing the constraint that it be an ellipsoid of revolution. We consider here a generalised model (Fig. 7.9) with the OH gas uniformly distributed between the surfaces,

$$\frac{x^2}{a_\pm^2} + \frac{(y\cos\beta - z\sin\beta)^2}{b_\pm^2} + \frac{(y\sin\beta + z\cos\beta)^2}{c_\pm^2} - 1 = 0 \qquad 7.5$$

where $a_+ = a_- + \Delta_s$, $b_+ = b_- + \Delta_s$ and $c_+ = c_- + \Delta_s$, with Δ_s the uniform shell thickness and β the angle of rotation about the $z-$axis. The rotation (θ_0, ϕ_0) about the $x-$ and $y-$ axes is achieved by locating the observer at $(D\cos\theta_0\cos\phi_0, D\cos\theta_0\sin\phi_0, D\sin\theta_0)$, where D is the distance to the source. The radial velocity field is anisotropic and takes the form given by Bowers (1991),

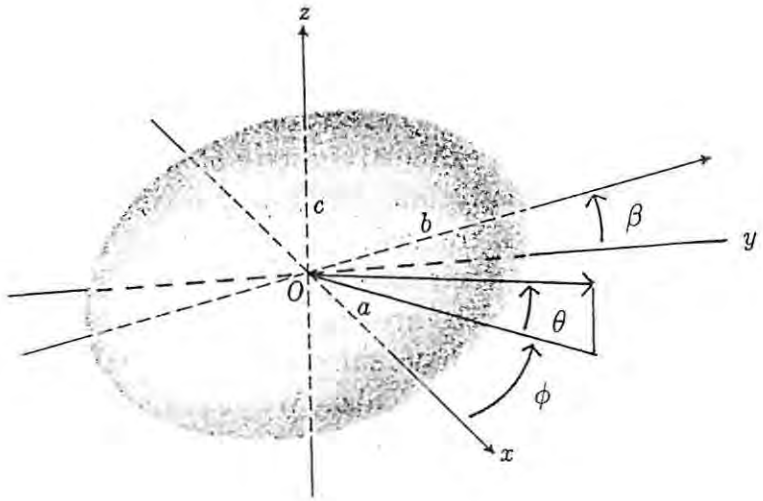

Fig. 7.9. The ellipsoidal kinematic model for the circumstellar outflow.

$$\mathbf{V}_{rad}(x,y,z) = V_{r0}\,\rho_0^n(x,y,z) \qquad 7.6$$

where ρ_0 is the outer radius of the ellipsoid along a line segment passing through the origin and the point (x,y,z) and V_{r0} is a constant which can be expressed equivalently as $V_{r0} = V_a a^{-n}$, where V_a is the desired radial velocity along the $x-$axis at $(\pm a, 0, 0)$. The outflow velocity along the other axes can be derived from equation (7.6) given above.

The model allows rotation in the equatorial plane with a constant tangential velocity. The rotating equatorial gas is assumed to rise to higher latitudes λ above the plane by thermal expansion, retaining the tangential velocity of the gas in the plane (Bowers 1991). All gas above a cut-off latitude λ_0 is assumed to have zero rotation where λ_0 is expressed in terms of the ratio between the thermal velocity dispersion normal to the plane and the radial expansion velocity (Bowers

1991). We generalise this constraint for $a \neq b \neq c$ by requiring zero rotation for $\tan\lambda > \left(\frac{a}{\rho_0}\right)^n \tan\lambda_0$.

The line of sight for relative angular coordinates (X, Y) with respect to the field centre (θ_0, ϕ_0) is given by,

$$\frac{x - D\cos\theta_0\cos\phi_0}{\cos(\theta_0 - Y)\cos(\phi_0 + Y\sec\theta_0)} = \frac{y - D\cos\theta_0\sin\phi_0}{\cos(\theta_0 - Y)\sin(\phi_0 + Y\sec\theta_0)} = \frac{z - D\sin\theta_0}{\sin(\theta_0 - Y)}$$

For each point along the parametrized line of sight, $(x(s), y(s), z(s))$, we define an orthogonal unit vector basis $(\mathbf{e}_l, \mathbf{e}_X, \mathbf{e}_Y)$ whose vectors point away from the observer and in the direction of increasing X and Y respectively. The corresponding components of velocity are given by $V_l = \mathbf{e}_l \cdot \mathbf{V}_{rad}$, $V_X = \mathbf{e}_X \cdot \mathbf{V}_{rad}$ and $V_Y = \mathbf{e}_Y \cdot \mathbf{V}_{rad}$, where $\mathbf{V}_{rad}$ is the radial velocity outflow vector. The intersection of the line of sight with the inner and outer ellipsoid surfaces is obtained from (7.5), with s scaled for numerical convenience. For a velocity V along the line of sight the coherent maser path length is computed as,

$$L(X,Y) = \int_s e^{-4\ln 2\frac{(V - V_l)^2}{\sigma_V^2}}\, ds$$

where σ_V is the intrinsic Doppler width of the line and the integration along the line of sight s takes into account the boundaries of the inner and outer ellipsoids. Bowers (1991) determines $L(X,Y)$ using a sharp cut-off at $\pm\frac{\sigma_V}{2}$ without assuming a Gaussian line profile or performing a numerical integration. The intensity at velocity V is calculated using the relation given by Bowers (1991) motivated by the work of Alcock and Ross (1985),

$$I(X,Y) = \text{const. } L^3(X,Y)$$

In order to model the proper motion data the respresentative gas velocity at V is determined by taking the weighted averages,

$$V_X(X,Y,V) = \frac{1}{L(X,Y)} \int_s (\mathbf{e}_X \cdot \mathbf{V}_{rad}) e^{-4 \ln 2 \frac{(V-V_l)^2}{\sigma_V^2}} ds \tag{7.7}$$

$$V_Y(X,Y,V) = \frac{1}{L(X,Y)} \int_s (\mathbf{e}_Y \cdot \mathbf{V}_{rad}) e^{-4 \ln 2 \frac{(V-V_l)^2}{\sigma_V^2}} ds \tag{7.8}$$

which are set to zero if $L(X,Y) = 0$.

Nedoluha and Bowers (1992) derive an ellipsoidal model for IRC+10420 with parameters $a = b = 8700$ AU, $c \sim 5856$ AU, $D = 5.8$ kpc, $\triangle_s \sim 4350$ AU, $\theta_0 = -25°$, $\phi_0 = 0$ and $\beta = 0$, anisotropy index $n = -2$, $V_* = 80$ km s^{-1} and $V_a = 28$ km s^{-1} . They set $\sigma_V = 0.9$ km s^{-1} based on independent considerations. These parameters were derived by fitting the $\theta(V_{LSR})$, $PA(V_{LSR})$ and $I(V_{LSR})$ profiles. The agreement between this kinematic model and the VLBI data is shown in Fig.7.10. The assumed stellar velocity V_* and the expansion velocity V_e are in good agreement with other molecular lines listed in Table 6.1. The shell thickness is consistent with the IR estimate of the inner dust shell radius.

The agreement between the Nedoluha and Bowers model and the MK3 VLBI data is clearly not ideal. A search over a range of parameter values using the extended ellipsoid model yielded some improved fits to the VLBI data but none decisively so. This task was hampered by the limited velocity range of the VLBI data and the inherent complexity of the models. In particular, an improved fit was obtained using the extended ellipsoid model with $\phi = -5.0°$, $\beta = 0.2°$, and $b = 1.32$ arcsec while retaining the model parameters of Nedoluha and Bowers (1992) given above. This does not affect the qualitative interpretation of the kinematics and the original model is retained in what follows.

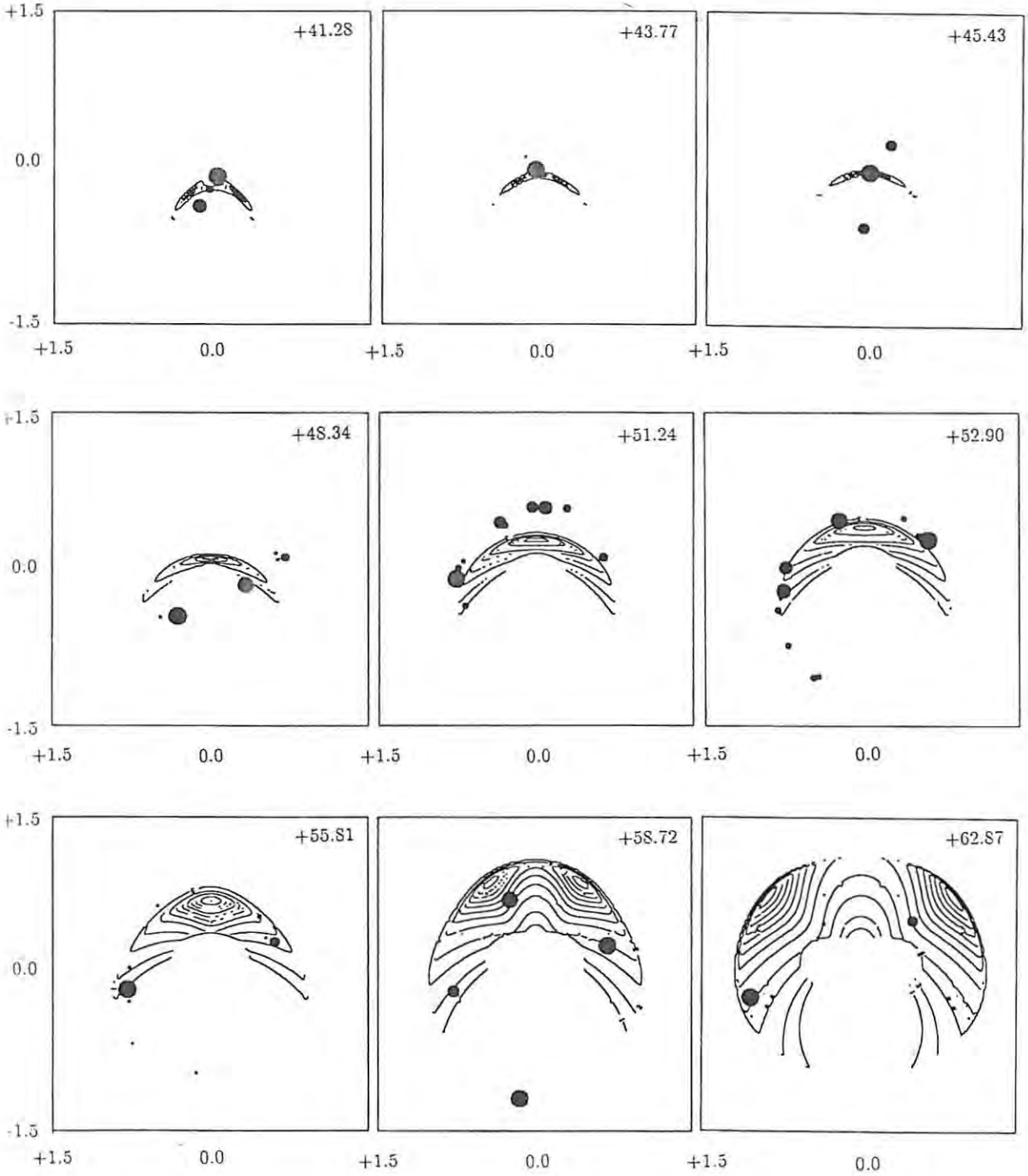

Fig. 7.10. The agreement between the ellipsoidal kinematic model of Nedoluha and Bowers (1992) and the Stokes I MK3 VLBI data for a range of channel velocities. Contour levels are plotted at $(1\%, 2\%, 5\%, 10\%, 20\%, 30\%, 40\%, 50\%, 60\%, 70\%, 80\%, 90\%, 100\%)$ of the peak model intensity for each channel. The radius of the circle plotted for each VLBI component is proportional to brightness and scaled relative to the strongest component in the channel.

If the kinematic structure of the source is known the proper motion data can be used to derive a distance estimate by using the technique of expanding cluster parallax (Genzel *et al.* 1981). A weighted least squares minimization was performed to fit the proper motion data to the transverse model velocities calculated using (7.7) and (7.8). For the Nedoluha and Bowers ellipsoid model a source distance of $D \sim 3.3$ kpc was obtained with a small formal error. The uncertainty in this parameter is dominated by unknown systematic errors in the kinematic model for the source but this estimate agrees well with the result of Mutel *et al.* (1979). In a systematic grid search of parameter space there is strong support for a distance $D \sim 3$ kpc for a range of ellipsoid model parameters.

The model velocities are plotted in Fig. 7.11 assuming a distance $D = 3.3$ kpc. The model reproduces several important features in the proper motion data satisfactorily, particularly the apparent E-W anisotropy in the transverse outflow velocity which appears to be mostly an orientation effect.

7.3 Polarization and Magnetic Field

Table 5.4 indicates that the individual maser components are significantly circularly polarized at VLBI resolution. This is consistent with the preliminary estimates of the degree of polarization obtained by Mutel *et al.* (1979). Taken in conjunction with the single-dish results of Cohen *et al.* (1987) and the VLA polarization observations of Nedoluha and Bowers (1992) this confirms that spatial blending is an important factor in determining the observed degree of circular polarization in circumstellar OH masers.

The angular distribution of components that are significantly polarized with ($\sqrt{(m_c^2 + m_l^2)} > 10\%$) and have peak brightness greater than 1 Jy/beam is shown in Fig. 7.12. There is some evidence that the more polarized components lie on the outer edges of the E-W disk. The components with measurable elliptical polarization are typically located on the edges of the maser region, particularly

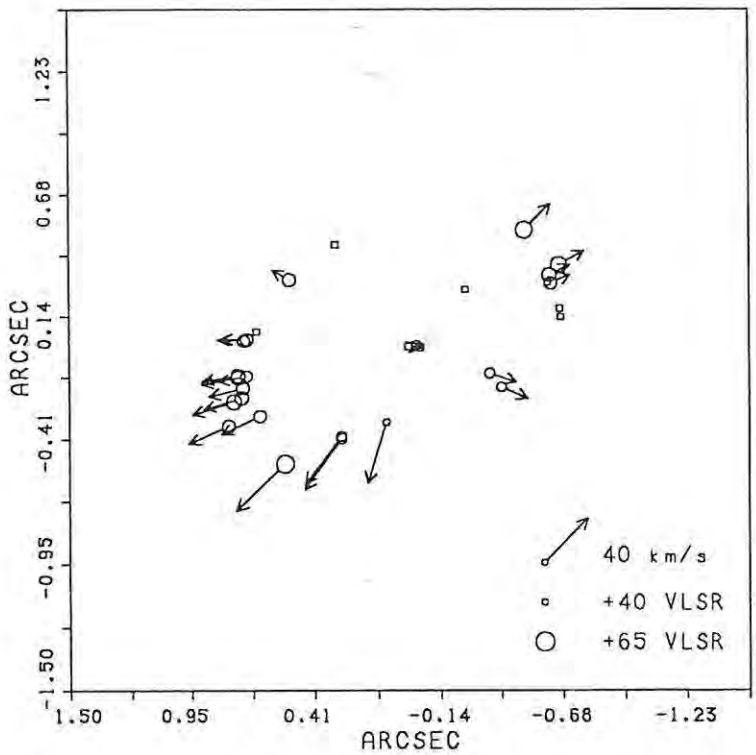

Fig. 7.11. The expected model proper motion vectors for an assumed distance $D = 3.3$ kpc for the ellipsoidal kinematic model of Nedoluha and Bowers (1992). Squares denote component positions where the model velocities are undefined.

the eastern edge of the disk structure. In the basic model of Goldreich, Keeley and Kwan (1973a,b) enhanced circular polarization is expected from σ-components in regions where the magnetic field has a greater longitudinal component and a small angle to the line of sight. This distribution could be interpreted as evidence for a generally azimuthal magnetic field in the source, as predicted by the theoretical models of Pascoli (1992). Faraday rotation may explain the possible suppression of linear polarization in the central regions of the source. The Faraday rotation ψ along a path L, with longitudinal magnetic field $B_{\|}$ and electron density n_e is given by Garcia-Barreto *et al.* (1988),

$$\left(\frac{\psi}{deg}\right) = 0.5 \left(\frac{n_e}{cm^{-3}}\right) \left(\frac{B}{mG}\right) \left(\frac{L}{10^{15} cm}\right) \left(\frac{\lambda}{18cm}\right)^2$$

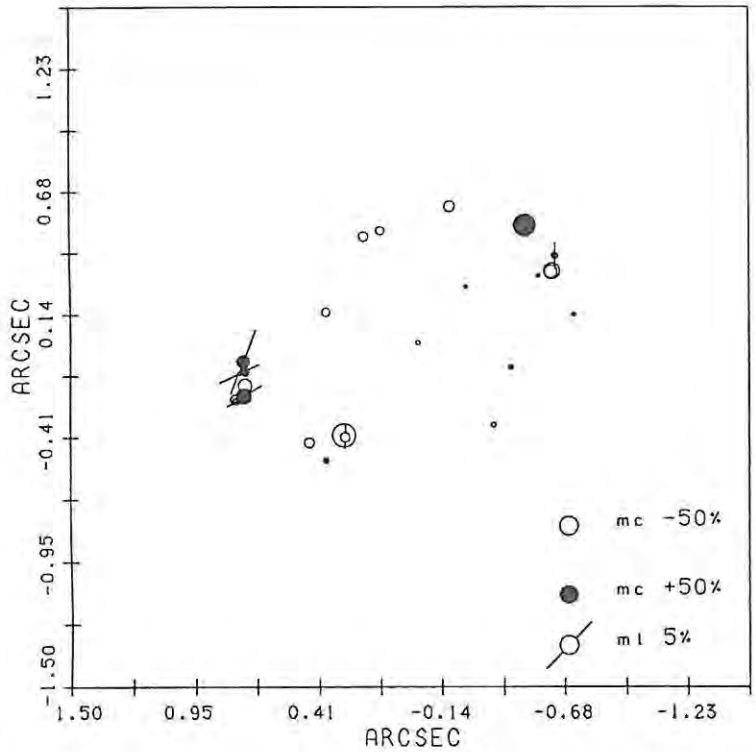

Fig. 7.12. The angular distribution of significantly polarized components as determined by the MK3 VLBI observations. Components are plotted with peak component brightness exceeding 1 Jy/beam and polarization ($\sqrt{(m_c^2 + m_l^2)} > 10\%$). The radius of the circle plotted for each component is proportional to the degree of circular polarization m_c. Filled circles denote a positive sense of circular polarization and empty circles a negative sense of circular polarization. The degree of linear polarization m_l is denoted by the length of the diagonal line segment which is plotted at the polarization position angle of the component. The legend denotes radii for 50% circular polarization and 5% linear polarization.

The detection of components with non-zero linear polarization implies an upper limit to the electron density of $n_e \sim 10$ cm^{-3} along these lines of sight if the Faraday rotation < 1 rad, the maser path length is 10^{16} cm and the longitudinal component of the magnetic field is 1 mG. This is consistent with the estimate $n_e < 15$ cm^{-3} derived by Barvainis, McIntosh and Predmore (1987) from SiO maser observations of late-type stars.

There is no clear evidence of full Zeeman multiplets in the VLBI data, in common with main-line OH masers in star-forming regions where Zeeman pairs are difficult to identify. In addition, the multiplet structure at 1612 MHz is con-

siderably more complex. The absence of easily identifiable Zeeman structure has been explained by Deguchi and Watson (1986) in terms of velocity gradients in the maser region. As discussed in section 6.4.2 this theory predicts significant polarization ($\sim 50 - 100\%$) if $\Delta v_z \sim 1$ and there are appreciable velocity gradients. Assuming $\Delta v_{th} \sim 0.9$ kms^{-1} (Nedoluha and Bowers 1992), the detection of significant circular polarization in the VLBI observations implies a magnetic field of $B \sim 1 - 3$ mG. This method of magnetic field estimation is often used for maser transitions of non-paramagnetic molecules such as SiO and H_2O, where low circular polarization is observed (Barvainis, McIntosh and Predmore 1987; Güsten and Fiebig 1990). Single dish polarization observations of main-line OH emission from IRC+10420 yields similar estimates for the magnetic field (Claussen and Fix 1982).

The estimation of magnetic field strength from Zeeman observations depends on the ratio r_z of the splitting to the observed linewidth $\Delta\Phi$, the signal to noise ratio of the data and the frequency resolution of the observations. In the limit of small splitting the approximation given by Troland and Heiles (1982) can be used,

$$V(V_{LSR}) = \alpha B_{\parallel} \frac{dI(V_{LSR})}{dV_{LSR}} + \beta I(V_{LSR}) \qquad 7.9$$

where for the 1612 MHz OH line, $\alpha = 0.236$ km s^{-1} per mG (Davies 1974) obtained from a weighted average of the multiplet components and β accounts for differential polarization gain errors. The applicability and numerical properties of this technique have been exhaustively considered by Sault *et al.* (1990). The technique breaks down for $r_z > 0.1$ or if the sampling interval is greater than $\frac{\Delta\Phi}{10}$ (Sault *et al.* 1990). For $\Delta v_z >> 1$ the individual Zeeman components should be clearly identifiable as separate components.

TABLE 7.2

Magnetic Field Estimates

V_{LSR}	X	Y	$B_{\parallel}$
kms^{-1}	arcsec	arcsec	mG
50.68	+0.192	0.483	-1.1
50.38	+0.683	0.075	2.7

The circumstellar OH masers at 1612 MHz are intermediate to these two cases with $r_z \sim 1$ and neither estimation method is directly applicable. The VLBI observations considered here have poor velocity resolution due to technical limitations on spectral line observations within the MK3 system. The poor sampling renders the approximation (7.9) unreliable (Sault *et al.* 1990). In addition, for the observed linewidths the small splitting constraint precludes magnetic field estimates exceeding $0.3 - 0.4$ mG.

A conservative technique was consequently used in deriving magnetic field estimates. The I and V spectra were split into sum and difference components and the Zeeman splitting was estimated as the difference between the centroids of these components. Errors were derived by Monte Carlo simulation using the off-peak noise variance derived from the deepest negative in the I channel as discussed in Chapter 5. A 3-σ significance test was applied to the estimated Zeeman splitting. In addition the B field estimate was rejected if the ratio $r_{\pm}$ of the mean intensity of the sum and difference components lies outside the range $\frac{3}{4} < r_{\pm} < \frac{4}{3}$. Only spectrally isolated components were considered in this analysis. The I and V spectra for the resulting two components where a B-field estimate proved possible are shown in Fig. 7.13.

The initial estimate of 10 mG for the magnetic field strength B_{maser} in the masing region (Reid *et al.* 1979) appears to have been overestimated. No evidence

for a Zeeman splitting of this order was found in the VLBI data. Similarly the range 15 mG $> B >$ $\frac{1}{6}$ mG derived by Nedoluha and Bowers (1992) can probably be narrowed to 4-5 mG $> B >$ $\frac{1}{6}$ mG.

Assuming a radial dependence $B_* = B_{maser}\left(\frac{R_{maser}}{R_*}\right)^2$ (Reid 1990) and $\frac{R_{maser}}{R_*} = 100$, yields a surface photospheric magnetic field of $\sim 10 - 30$ G for B_{maser} = 1-3 mG. This is closer to the estimates of Barvainis, McIntosh and Predmore (1987) for typical magnetic field strengths in late-type stars ($B < 100$ G) derived from SiO maser observations than the 1-3 kG fields for IRC+10420 indicated by previous work (Reid etal 1990; Nedoluha and Bowers 1992). The estimate of the stellar magnetic field is subject to several uncertainties in the assumed parameters, particularly the radial dependence of the magnetic field strength. An exponent of two is adopted for comparison with earlier estimates by Reid (1990). The implied magnetic energy density in the circumstellar envelope still however has important dynamical implications for the circumstellar outflow (Chapman and Cohen 1986).

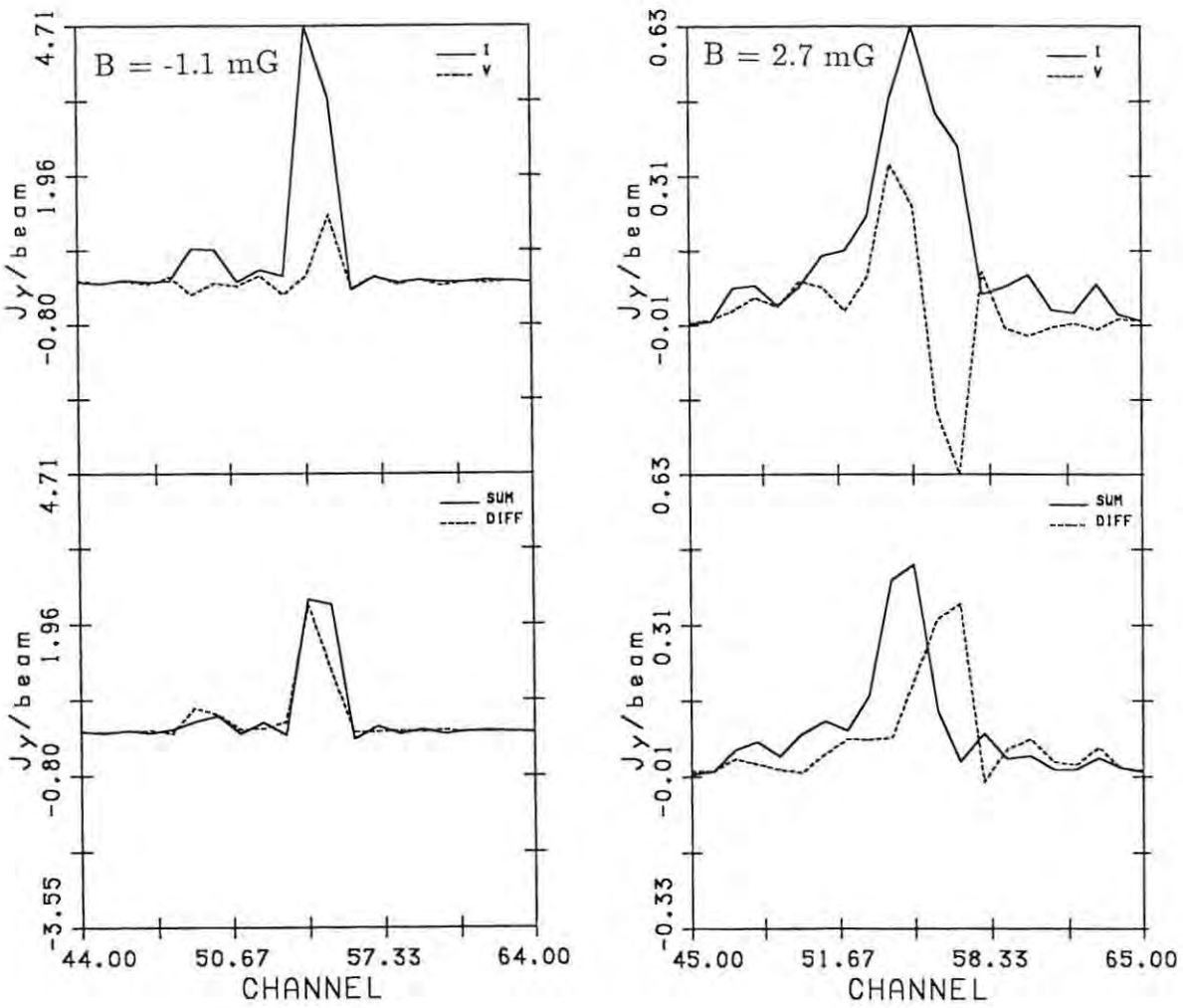

Fig. 7.13. The I, V, sum and difference spectra for the components listed in Table 7.2. The spectra have been averaged over a 30 x 30 mas region centered on the component position and are plotted against channel number.

CHAPTER 8: CONCLUSIONS

8.1 Summary of Results

This work has concerned the implementation and evaluation of techniques for the calibration and imaging of spectral line polarization VLBI data.

This has included a review of the instrumental and propagation effects which need to be removed in the course of calibrating such observations, with particular reference to their polarization dependence. This includes propagation through the ionosphere and troposphere, instrumental feed contamination and differential propagation effects through the receivers and associated electronics in each polarization channel. In addition, digital signal processing in the correlator introduces artificial effects which need to be removed.

The development and evaluation of techniques for reducing spectral line polarization VLBI data has been undertaken within the Astronomical Image Processing System (AIPS) maintained by the National Radio Astronomy Observatory. All post-correlation data reduction was performed within the AIPS system, including fringe-fitting. Several new AIPS tasks were developed in the course of this investigation, and others were adapted to the requirements of spectral line polarization calibration. Specific attention has been devoted to the problem of processing spectral line polarization observations using the MK3 VLBI system within this framework.

The fact that all post-correlation data reduction was performed within the same software environment using an antenna-based formalism has allowed considerable flexibility in investigating new data reduction strategies for spectral line polarization observations. The direct transfer of MK3 correlator output into the

AIPS system allowed improved corrections for known correlator effects such as the fractional bit shift error and a more complete monitoring of correlator data quality.

A full complex bandpass response was determined for each antenna in each polarization and an enhanced technique was developed for amplitude calibration for spectral line VLBI data recorded over a narrow bandwidth. The differential polarization amplitude gain was established using data taken on the continuum calibrators. The antenna-based factorization of residual complex antenna gains was particularly advantageous in the phase calibration process. The phase calibration process includes a correction for parallactic angle, global fringe-fitting to determine residual fringe rates and delays, self-calibration of a reference channel to determine a phase solution and the removal of differential phase terms introduced by differing paths through the atmosphere and receiving electronics for each sense of polarization. A robust technique was developed for self-calibration imaging of the reference channel suited to the difficulties posed by spectral line observations using small antenna networks and exploiting the increasing computing power available to single users within AIPS. Global polarization fringe-fitting within an antenna-based formalism was found to have many advantages over baseline-based fringe-fitting typically used in continuum polarization VLBI. The differential polarization phase corrections were determined using an ionospheric model for Faraday rotation and the continuum calibrator data to determine phase and delay corrections within the MK3 recording electronics. The unique problems posed by instrumental feed calibration for spectral line polarization VLBI observations were considered and a technique was developed to provide an approximate feed calibration in the absence of a suitable continuum polarization calibrator. The imaging of polarization data was investigated and a full complex imaging method was adopted which is particularly advantageous for poorly sampled cross-polarization data.

The evaluation of spectral line polarization reduction methods provided important insights into the difficulties and possibilities of this technique. In particular the MK3 system was found to be not ideal for narrow bandwidth spectral line polarization observations despite the multi-band capacity of the system which is well-suited to polarization observations in general. The fixed playback rate at the correlator renders processing of narrow bandwidth data problematic. The capacity to record at different sampling rates in each band would also greatly improve the possibilities in spectral line polarization calibration by allowing the surplus bandwidth to be used for observations of continuum polarization calibrators. These deficiencies of the MK3 system should be resolved by the new VLBA recording system and this will have an important impact on the possibilities for spectral line polarization observations in the future.

The requirements for differential ionospheric phase correction impose constraints on spectral line polarization observations at relatively low frequencies such as 1.6 GHz. Such observations should be scheduled during sunspot minima and preferably at night. Model corrections for ionospheric Faraday rotation were found to be inadequate for polarization calibration in the general case of significant rotation. This problem is most easily resolved by ground-based monitoring at each VLBI antenna of the total electron content along the line of sight.

The question of instrumental feed calibration for spectral line polarization VLBI poses unique difficulties due to the narrow recorded bandwidths and the scarcity of suitable polarization calibrators at VLBI resolution. The latter problem affects continuum polarization VLBI observations in equal measure. On the other hand the problem is rendered somewhat more tractable in spectral line VLBI by the higher intrinsic brightness of maser sources. This allows the determination of approximate feed solutions as discussed above and may ultimately allow improved continuum polarization calibration using compact, bright maser components that

are spectrally isolated and have simple polarization structure as polarization calibrators. Instrumental feed calibration is greatly assisted by including a small number of equatorially mounted antennas in the VLBI network.

The data set used in this evaluation comprised 1612 MHz MK3 observations of the OH masers towards the unusual OH/IR source IRC+10420. The properties of this source were reviewed including its evolutionary status. Single polarization MK2 observations of the same source at an earlier epoch were also reduced. These are the first VLBI images obtained of the source using closure-phase imaging techniques. This allowed an investigation of the source morphology at VLBI resolution and the determination of changes in the source structure between the two epochs. In particular a full proper motion determination was performed after a rigorous correction for differential angular coordinate distortion. This clearly shows expansion in the circumstellar envelope and appears to support an ellipsoidal kinematic model for the source with an anisotropic radial velocity field. The expanding cluster parallax technique has allowed an independent estimate of the distance to the source of $D \sim 3.3$ kpc. The angular distribution of polarized emission has been determined in this maser transition and a new estimate of the magnetic field of $1-3$ mG has been obtained. This interferometric Zeeman determination indicates that previous single dish estimates of 10 mG are probably overestimates. There is some evidence for an azimuthal magnetic field in the source.

8.2. Future Work

Data reduction techniques for spectral line polarization observations need further investigation, particularly the problem of instrumental feed calibration where an iterative calibration technique may prove useful. The problem of VLBI polarization calibrators is exceedingly important particularly for continuum observations at frequencies higher than 10 GHz and spectral line calibration techniques may

assist in this regard as discussed above. In addition, fringe fitting of sources that are significantly linearly polarized needs further development.

The existing techniques need to be used in observations of maser transitions at other frequencies such as SiO and H_2O masers, where the angular distribution of polarized emission is poorly known. Polarization information is also important in the unambiguous identification of proper motions. Zeeman estimates of the magnetic field distribution using VLBI techniques may provide important dynamical information for maser sources in general.

The techniques hold great promise for the future, particularly with the advent of new instruments such as the VLBA.

APPENDIX A: MK3 SPECTRAL LINE POLARIZATION DATA

Introduction

This appendix contains reference material relating to the processing of spectral line polarization data within the MK3 system. Particular reference is given to the importing of the MK3 correlator output data directly into AIPS using the task MK3IN. This has the advantage of allowing all post-correlation data processing to be performed within AIPS, including global fringe-fitting. This was an important step in the spectral line polarization data processing. A considerable amount of effort was expended modifying MK3IN and ensuring that it functioned correctly for spectral line polarization data.

A.1 MK3 Correlator System

The MK3 correlator system is described elsewhere (Whitney *et al.* 1976; Alef 1989) and in internal Haystack Observatory memoranda and only a brief introduction is given here. The MK3 system allows the recording of up to 28 simultaneous independent tracks of maximum 2 MHz bandwidth and was primarily designed for geodetic applications. The correlator has a modular design with independent 8-lag complex cross-correlator modules that can be flexibly assigned under computer control to combinations of recorded track pairs on each baseline. In geodetic applications with 4 MHz sampling one module is assigned per recorded track pair on each baseline. The larger lag range required for spectral line observations is obtained by assigning multiple correlator modules, offset in delay, to each baseline track pair. Each module decodes the video data to generate bit streams for station A and station B. These are corrected respectively for fringe rotation and the model delay before the data are cross-correlated and accumulated. The MK3 correlator applies a band-centre fractional bit shift correction by incrementing or

decrementing the fringe rotator phase by $\frac{\pi}{2}$ at each bit shift. At the end of each accumulation period (AP) the complex correlation coefficients are stored and subsequently written to the correlator output tape (A-tape).

The A-tape format is based on the Hewlett Packard HP 1000 file structure where each file consists of a root extent to which extents of the same size and type are added as the file is expanded. Modifications to the HP file handling by Haystack Observatory, however, allow MK3 data file extents to have arbitrary size and type and allows an enhanced tape archive system (known as SAVEM). The correlator output format is described in the "COREL and "SAVEM data files on the correlator computer. In brief, extents of type 50 contain record types with scan information, antenna baseline tables, track frequencies and the correlator model geometry. The output records from each complex cross-correlator module are written in associated type 51 extents, indexed on module number, baseline number and time.

The AIPS task MK3IN, written by W.D. Cotton, was enhanced to deal with MK3 spectral line polarization data. This task decodes the HP correlator output tapes, corrects the data for residual digital correlation effects and converts the data to the AIPS format. This allows all post-correlation calibration including fringe-fitting to be performed within AIPS. The cross-correlation functions, formed by concatenating the normalised output of separate correlator modules, are corrected for amplitude losses and transformed to cross-power spectra. A correction is applied for the residual fractional bit shift phase error. The baseline-based geometric model used by the correlator is converted to an antenna-based formalism and stored in the associated AIPS calibration table. The error statistics are compiled for each scan and global correlator parameters such as clock offsets are monitored for consistency. A brief description of the technical details of this process are given in the following sections.

A.2 Correction for Correlator Effects

The correlator fringe-fitting software is described in the "FRNGE file on the correlator computer, primarily written by A.R. Whitney and A.E.E. Rogers. The Fourier transform conventions and digital corrections applied by MK3IN are discussed in this section.

A.2.1 Cross-Correlation Functions

Each module produces a set of 8-lag complex cross-correlation counts centred about the delay offset of the module. The counts are written to tape for each module, along with the delay offset and FBS parameters for the module and the correlator counts for the sine and cosine channels. The data read from tape for each module are:

r'_k = Unnormalized complex cross − correlation counts
in decreasing lag order , $k = 1, 8$

τ_k = Lag for channel k
$= \tau_0 + 5 - k$ (bits)

τ_0 = Module delay offset of $5 - $th channel (bits)

$\Sigma\cos$ = Total no of bits correlated in cosine channel

$\Sigma\sin$ = Total no of bits correlated in sine channel

f_s = Fringe rate sign bit. This bit is set if the fringe rate is negative but the correlator performs a positive fringe rotation, thus conjugating the correlation function. (The MK3 correlator performs only + ve fringe rotation; MK3A performs both + ve

and $-$ ve rotation and does not set this bit)

f_n = Normalisation (Whitney *et al.* 1976)

$= f_1 f_2 f_3 f_4$

$= (\frac{\pi}{2})(\frac{3}{4})(\frac{\pi}{4\cos\frac{\pi}{8}})(1-\frac{\pi^2}{288})^{-1} = 1.03705$

f_1 = Van Vleck clipping correction

f_2 = Fraction of AP that $3-$level rotator is not zero

f_3 = Fringe rotator loss factor

f_4 = Loss factor for band $-$ centre FBS correction

The counts from each correlator module are normalised, corrected for correlator losses, clipping and fringe rotation effects to yield normalised complex cross-correlation values r_k,

$$Re(r_k) = \sin\left(\frac{f_n(2Re(r'_k) - \Sigma\cos)}{\Sigma\cos}\right)$$
$$Im(r_k) = -\sin\left(\frac{f_n(1-2f_s)(2Im(r'_k) - \Sigma\sin)}{\Sigma\sin}\right)$$

The full cross-correlation function, R_j, is constructed by concatenating the output of the correlator modules in increasing lag order.

R_k = Normalised complex XC function in increasing lag order

N = No of lags in the full cross $-$ correlation function

τ_k = Lag no of k $-$ th channel

$= \left(-\frac{N}{2}+1\right) + (k-1)$

The maximum cross-correlation lag range symmetric about zero lag is used in practice but in this discussion the lag range is assumed symmetric for clarity. The cross-correlation function is then transformed to a cross-power spectrum as:

$$S_l'(m) = \sum_{k=1}^{N} R_k e^{-2\pi j(k-\frac{N}{2})(\frac{m-1}{N})} \quad \text{(LSB)}$$

$$S_u'(m) = \sum_{k=1}^{N} R_k e^{2\pi j(k-\frac{N}{2})(\frac{m-1}{N})} \quad \text{(USB)}$$

The cross-power spectra are corrected for the fractional bit shift effect as,

$$S_u(m) = S_u'(m)e^{-2\pi j(m-(\frac{N}{4}+1))\frac{\delta_{FBS}}{N}}$$

$$S_l(m) = S_l'^{*}(m)e^{-2\pi j(m-(N-\frac{N}{4}+1))\frac{\delta_{FBS}}{N}}$$

where δ_{FBS} is the average fractional bit shift delay error over the AP (in bits), and is discussed later.

If both sidebands are present, the upper and lower sidebands are joined and written to the output file as $S_{u+l}(k)$,

$$S_{u+l}(k = \frac{N}{2} + m - 1) = S_u(m), \quad m = 2, 3, .., \left(\frac{N}{2}\right)$$

$$S_{u+l}(k = m - \frac{N}{2} - 1) = S_l(m), \quad m = \frac{N}{2} + 2, .., N$$

$$S_{u+l}(k = \frac{N}{2}) = 0$$

where the channel frequency $\omega_k = [(\frac{2-N}{N}) + (k-1)\frac{2}{N}]\,\Delta\omega \quad , k = 1, (N-1)$.

If only a single USB is present the output spectrum $S_{out}(k)$ is written as,

$$S_{out}(k = m) = S_u(m), \quad m = 2, \frac{N}{2}, \quad \omega_k = (k-1)\frac{2\Delta\omega}{N}$$

$$S_{out}(k = 1) = 0$$

A.2.2. Autocorrelation Functions

The autocorrelation functions are computed by a set of 8-lag complex cross-correlator modules covering half the cross-correlation lag range. The MK3 correlator modules can produce 16-lag autocorrelation output but this is not yet fully supported by the correlator software.

Using the notation of section A.2.1, the data from each correlator module are normalized and corrected for correlator losses to yield a set of normalized real autocorrelation values, r_k.

$$Re(r_k) = f_a \left(\frac{2Re(r'_k) - \Sigma \cos}{\Sigma \cos} \right)$$
$$Im(r_k) = 0$$

where $f_a = f_1 = \frac{\pi}{2}$. The half autocorrelation function is constructed by concatenating the output of the correlators in increasing lag order. The AC bias, β, is determined as the average of the outer third of the lag function. The data are mirrored about the centre lag, which is set to unity, to produce a symmetric AC function R_k^a over the same range as the cross-correlation functions, the Van Vleck clipping correction is applied and the bias is removed,

$$R_k^a = \frac{\sin R'^a_k - \beta}{1 - \beta}$$

The autocorrelation function is transformed to an autocorrelation spectrum as,

$$S_l^a(m) = \sum_{k=1}^{N} R_k^a e^{-2\pi j(k - \frac{N}{2})(\frac{m-1}{N})} \quad (LSB)$$
$$S_u^a(m) = \sum_{k=1}^{N} R_k^a e^{2\pi j(k - \frac{N}{2})(\frac{m-1}{N})} \quad (USB)$$

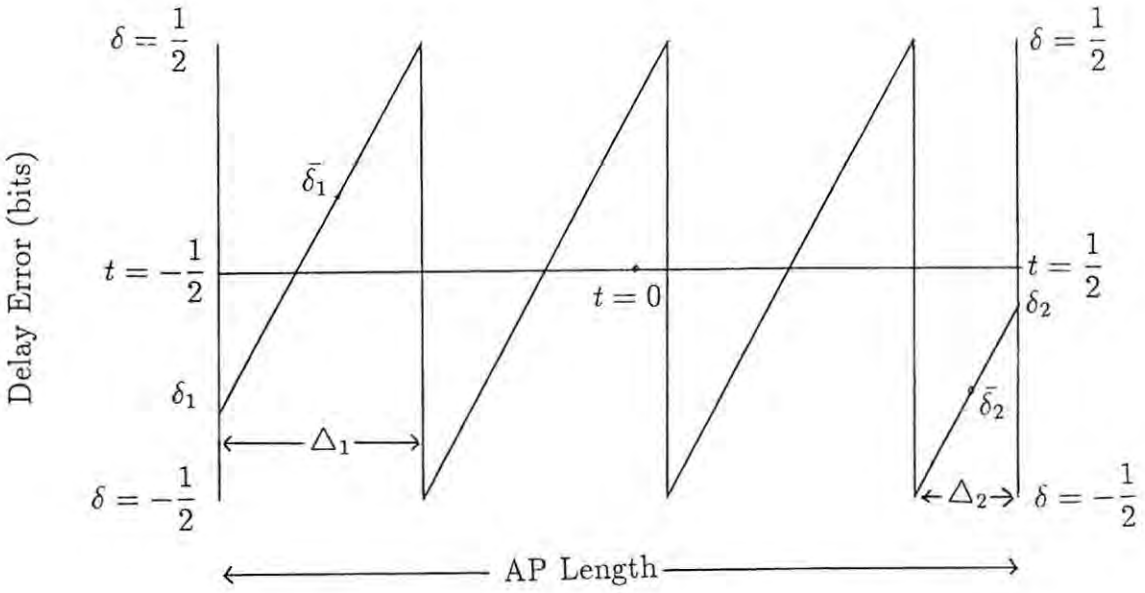

Fig. A.1. The fractional bit shift delay error over an accumulation period (after Rogers 1983).

No FBS correction is applied and the data are output in the same format as the cross-correlation functions.

A.2.3. Fractional Bit Shift Correction

The MK3 correlator applies a band-centre FBS correction by incrementing or decrementing the fringe rotator phase by $\frac{\pi}{2}$ at each bit shift. This is referred to as "automatic bit-shift mode" in the MK3 documentation (Rogers 1983).

The following notation will be used:

δ_0 = FBS error at center of AP (bits)

s = Bit shift rate (bits/AP)

$$
\begin{aligned}
N_1 &= \text{No of bit shifts in 1st half of AP} \\
&= \text{int}\left[\left|-\frac{s}{2}+\delta_0\right|+\frac{1}{2}\right] \\
N_2 &= \text{No of bit shifts in 2nd half of AP} \\
&= \text{int}\left[\left|\frac{s}{2}+\delta_0\right|+\frac{1}{2}\right]
\end{aligned}
$$

From Figure A.1,

$$\delta = st + \delta_0$$

and,

$$
\begin{aligned}
\delta_1 &= -\frac{s}{2} + \delta_0 + N_1 \\
\delta_2 &= \frac{s}{2} + \delta_0 - N_2 \\
\Delta_1 &= \frac{1}{s}(\frac{1}{2} - \delta_1) \\
\Delta_2 &= \frac{1}{s}(\delta_2 + \frac{1}{2})
\end{aligned}
$$

The average delay error, $\bar{\delta_1}$, in the first sub-interval and $\bar{\delta_2}$ in the last sub-interval are given by,

$$
\begin{aligned}
\bar{\delta_1} &= (\frac{1}{2} - \delta_1)\frac{1}{2} + \delta_1 \\
\bar{\delta_2} &= \frac{1}{2}(-\frac{1}{2} + \delta_2)
\end{aligned}
$$

The average delay error over the AP is given by,

$$
\begin{aligned}
\delta_{FBS} &= \bar{\delta_1}\Delta_1 + \bar{\delta_2}\Delta_2 \\
&= \left[\delta_0 + \frac{(N_1 - N_2)}{2}\right]\left[1 - \frac{(N_1 + N_2)}{s}\right] \\
&= [\delta_0 + f_d]\left[1 - \frac{(N_1 + N_2)}{s}\right]
\end{aligned}
$$

Now, $|N_1 - N_2| << 1$, and therefore,

$$N_1 = N_2 \quad \text{then} \quad f_d = 0$$

$$N_1 = N_2 + 1 \quad \text{then } \delta_0 < 0, \text{ and } f_d = 0.5$$

$$N_1 = N_2 - 1 \quad \text{then } \delta_0 > 0, \text{ and } f_d = -0.5$$

An example of the FBS phase correction is shown in Figure A.2.

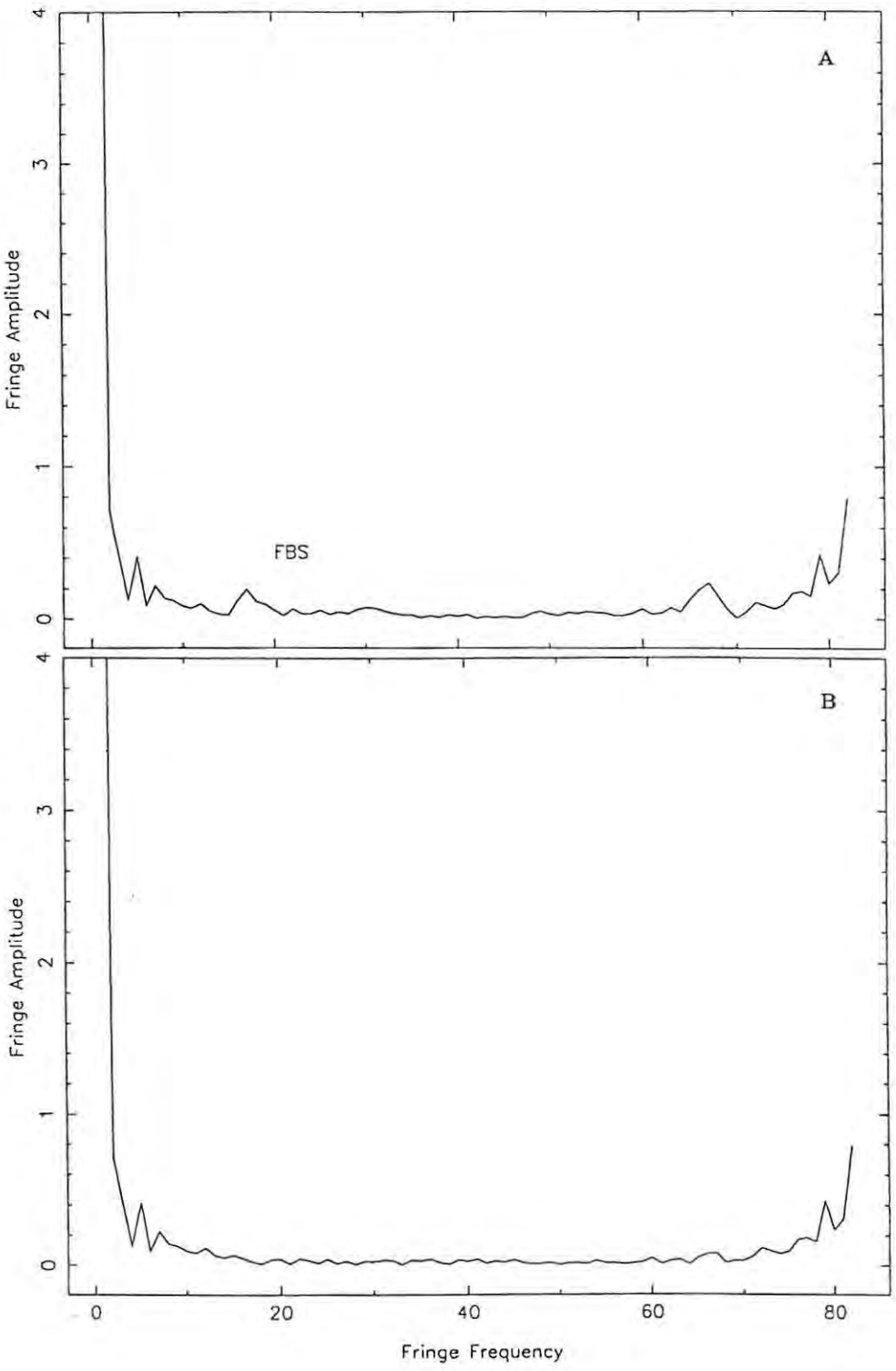

Fig. A.2. The fringe rate spectrum at 500 kHz (total bandwidth 2 MHz) for 5 GHz observations of 3C84 on the baseline Haystack-VLA before (a) and after (b) the correction for the residual fractional bit shift error. The fringe rate spectrum amplitude is in arbitrary units and is truncated near zero frequency. The fringe frequency is also in arbitrary units.

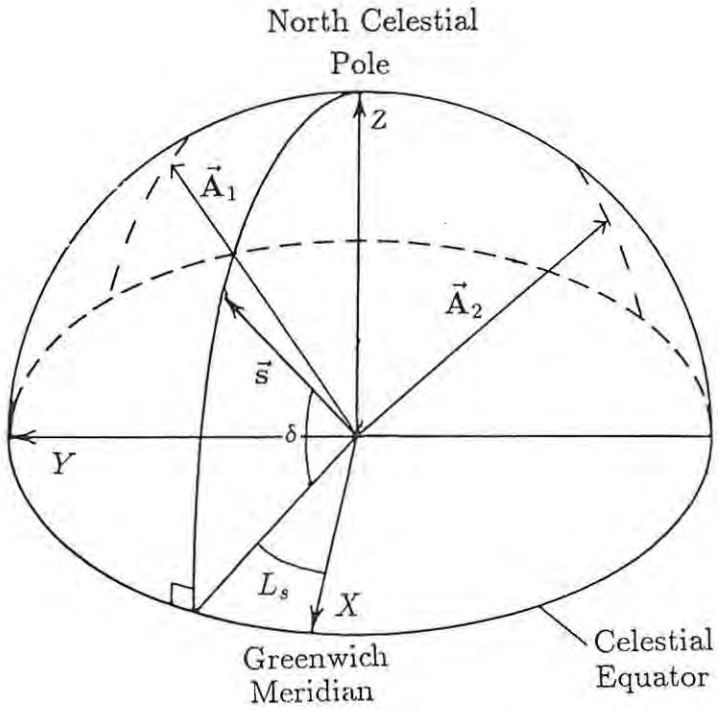

Fig. A.3. Geometry used in the discussion of the MK3 correlator model (adapted from TMS p.87).

A.3 Correlator Model

This is a brief description of the calculation of the antenna-based geometric delays, rates and accelerations for the AIPS calibration table using the MK3 correlator model, as deduced from the Haystack routines XELAY and ATMOS. For consistency, the antenna based delays are compared to the baseline based delays which are recorded for each scan reference time on the A-tape.

Notation

$$\vec{A}_i' = \text{Station i vector wrt } 1900 - 1905 \text{ CIO pole.}$$

$$= (A_{xi}, A_{yi}, A_{zi})\ (\mu s)$$

$(\Delta x, \Delta y)$ = X, Y components of polar motion (rad)

$\delta_s(t)$ = Apparent declination of source at time t (rad)

$\alpha_s(t)$ = Apparent right ascension of source at time t (rad)

$\frac{d\delta_s}{dt}$ = Derivative of apparent declination wrt UT (rad/s)

$L_s(t)$ = Greenwich hour angle of source at time t (rad)

$\frac{dL_s}{dt}$ = Hour angle rate (rad/s)

t_E = Processing reference time (s)

$GAST(t_E)$ = Greenwich apparent sidereal time at t_E (rad)

$\frac{dGAST}{dt}$ = Derivative of GAST wrt UT (rad/s)

τ_{ci}^0 = Clock offset for station $i > 0$ = early (μs)

$\dot{\tau}_{ci}$ = Clock rate for station $i > 0$ = fast (s/s)

τ_{ci}^E = Clock epoch for station i

ρ_i = Zenith atmosphere electrical delay (μs)

$\theta_i(t)$ = Source elevation from station i (rad)

$\Delta_{UT1-UTC}$ = UT1 − UTC (rad)

λ_i, ϕ_i = Latitude and west longitude for station i

ω_e = Sidereal rate (rad/s)

$L_{si}(t)$ = Hour angle of source at station $i$at time t

A.3.1 Geometry

All quantities are referred to a quasi-Lorentzian reference frame at the centre of the Earth. The geometric properties of each wavefront are identified by the UTC geocentric arrival time t for the wavefront.

A left hand set of (x, y, z) coordinates is used with the z-axis through the North Celestial Pole, the x-axis through the Greenwich meridian and an orthogonal y-axis.

The station vectors as read from tape, $\vec{\mathbf{A}}_i'$, refer to the 1903 CIO pole and need to be corrected for polar motion,

$$\vec{\mathbf{A}}_i = \begin{pmatrix} 1 & 0 & -\Delta x \\ 0 & 1 & -\Delta y \\ \Delta x & \Delta y & 1 \end{pmatrix} \vec{\mathbf{A}}_i'$$

The unit vector in the direction of the source is,

$$\vec{\mathbf{s}}(t) = \cos\delta_s(t)\cos L_s(t)\vec{\mathbf{x}} + \cos\delta_s(t)\sin L_s(t)\vec{\mathbf{y}} + \sin\delta_s(t)\vec{\mathbf{z}}$$

where,

$$\begin{aligned} L_s(t) &= GAST(t_E) - \alpha_s(t_E) + \Delta_{UT1-UTC} + (t - t_E)\frac{dL_s}{dt} \\ &= L_{s0} + (t - t_E)\frac{dL_s}{dt} \\ &= L_{s0} + \Delta L_s \end{aligned} \qquad (A.1)$$

A.3.2. Geocentric Delay

The total geocentric delay for each station is given by,

$$\tau_i(t) = \tau_{gi} + \tau_{ci} + \tau_i^a \qquad (A.2)$$

where τ_{gi} is the geometric delay, τ_{ci} contains clock terms and τ_i^a is the neutral atmosphere delay. The geometric contribution can be approximated as,

$$\begin{aligned} \tau_{gi}(t) &\sim -\vec{\mathbf{s}}(t - \tau_{gi}(t)).\vec{\mathbf{A}}_i \\ &\sim \tau_{0i} - a_q\tau_{0i} \\ &\sim \tau_{0i} + \tau_{da} \end{aligned}$$

where $\tau_{0i} = -\vec{s}(t).\vec{A}_i$ and the diurnal aberration term is $\tau_{da} = -\frac{d[\vec{s}(t).\vec{A}_i]}{dt}\tau_{0i}$.

Now, τ_{0i} can be expanded as,

$$\begin{aligned}\tau_{0i} &= -\vec{s}(t).\vec{A}_i \\ &= -\cos\delta_s(t)(A_{xi}\cos L_{s0} + A_{yi}\sin L_{s0})\cos\Delta L_s \\ &\quad -\cos\delta_s(t)(-A_{xi}\sin L_{s0} + A_{yi}\cos L_{s0})\sin\Delta L_s - A_{zi}\sin\delta_s(t)\end{aligned}$$

If δ_s is known at epoch t_E then,

$$\delta_s(t) = \delta_s(t_E) + (t - t_E)\frac{d\delta_s}{dt}$$

where $\frac{d\delta_s}{dt}$ is the rate of change of apparent declination wrt UT (rad/s). Therefore,

$$\begin{aligned}\cos\delta_s(t) &= \cos\delta_s(t_E) - (t - t_E)\frac{d\delta_s}{dt}\sin\delta_s(t_E) \\ \sin\delta_s(t) &= \sin\delta_s(t_E) + (t - t_E)\frac{d\delta_s}{dt}\cos\delta_s(t_E)\end{aligned} \qquad (A.3)$$

Using (A.1) and (A.3),

$$\begin{aligned}\tau_{0i} &= B_c - B_x + B_y(t - t_E) \\ &= \tau'_{0i} + B_y(t - t_E)\end{aligned}$$

where,

$$\begin{aligned}B_a &= \cos\delta_s(t_E)(A_{xi}\cos L_{s0} + A_{yi}\sin L_{s0}) \\ B_b &= \cos\delta_s(t_E)(-A_{xi}\sin L_{s0} + A_{yi}\cos L_{s0}) \\ B_c &= -A_{zi}\sin\delta_s(t_E) \\ B_x &= B_a\cos\Delta L_s + B_b\sin\Delta L_s \\ B_y &= \dot{B}_c - \dot{B}_a\cos\Delta L_s - \dot{B}_b\sin\Delta L_s \\ \dot{B}_a &= -\sin\delta_s(t_E)(A_{xi}\cos L_{s0} + A_{yi}\sin L_{s0})\frac{d\delta_s}{dt} \\ \dot{B}_b &= -\sin\delta_s(t_E)(-A_{xi}\sin L_{s0} + A_{yi}\cos L_{s0})\frac{d\delta_s}{dt} \\ \dot{B}_c &= -A_{zi}\cos\delta_s(t_E)\frac{d\delta_s}{dt}\end{aligned}$$

The diurnal aberration term can be expanded as,

$$\tau_{da} \sim -a_q \tau'_{0i}$$

where,

$$a_q = \frac{dGAST}{dt} \cos\delta_s(t_E)(A_{yi} \cos L_s(t) - A_{xi} \sin L_s(t))$$

Using (A.1),

$$a_q = B_{qd} \cos\Delta L_s + B_{qe} \sin\Delta L_s$$

where,

$$B_{qd} = \frac{dGAST}{dt} \cos\delta_s(t_E)(A_{yi} \cos L_{s0} - A_{xi} \sin L_{s0})$$
$$B_{qe} = \frac{dGAST}{dt} \cos\delta_s(t_E)(-A_{yi} \sin L_{s0} - A_{xi} \cos L_{s0})$$

The clock terms are,

$$\tau_{ci}(t) = \tau^0_{ci} + \dot{\tau}_{ci}(t - t^E_{ci}) + \tau_i(t)\dot{\tau}_{ci}$$

The last term is added after the call to the Haystack correlator routine XELAY.

A.3.3 Delay Rate

The delay rate is obtained by differentiating (A.2),

$$\dot{\tau}_i = \frac{d\tau_i}{dt} = (B_a \sin\Delta L_s - B_b \cos\Delta L_s)\frac{dL_s}{dt} + \dot{B}_y(t - t_E) + B_y + a_q\dot{\tau}'_{0i} + \dot{a}_q\tau'_{0i} + \dot{\tau}_{ci} + \dot{\tau}^a_i$$

where,

$$\dot{B}_y = (\dot{B}_a \sin\Delta L_s - \dot{B}_b \cos\Delta L_s)\frac{dL_s}{dt}$$
$$\dot{\tau}'_{0i} = (B_a \sin\Delta L_s - B_b \cos\Delta L_s)\frac{dL_s}{dt}$$
$$\dot{a}_q = (B_{qd} \sin\Delta L_s - B_{qe} \cos\Delta L_s)\frac{dL_s}{dt}$$

A.3.4 Delay Acceleration

Now,

$$\frac{d^2\tau_{0i}}{dt^2} \sim \frac{dL_s}{dt}(\frac{dL_s}{dt}B_x - B_y + \dot{B}_c) + 2\dot{B}_y$$

and,

$$\ddot{\tau}_i = \frac{d^2\tau_{0i}}{dt^2} + a_q\frac{d^2\tau_{0i}}{dt^2} + 2\dot{\tau}'_{0i}\dot{a}_q - \tau'_{0i}a_q(\frac{dL_s}{dt})^2 + \ddot{\tau}^a_i$$

A.3.5 Neutral Atmosphere Delay

A modified cosecant law is used to compute the atmospheric delay τ^a_i (Robertson 1975; Chao 1970),

$$\tau^a_i(t) = \rho_i[\sin\theta_i + \frac{0.00143}{\tan\theta_i + 0.0445}]^{-1} \qquad (A.4)$$

where $\theta_i(t)$ is the elevation of the source from station i at time t, and ρ_i is the zenith electrical delay at station i (typically 7ns).

The elevation is computed as,

$$\sin\theta_i(t) = \sin\lambda_i \sin\delta_s(t_E) + \cos\lambda_i \cos\delta_s(t_E)\cos L_{si}(t)$$

where $\lambda_i = \arctan\frac{A_{yi}}{A_{xi}}$ and $\phi_i(t) = \arctan\frac{A_{yi}}{A_{xi}}$. The source hour angle is computed relative to the meridian passage,

$$L_{si}(t) = \omega_e(t - t_{mer})$$

where,

$$t_{mer} = \frac{1}{\omega_e}(\alpha_s(t_E) - GAST(t_E) + \frac{dGAST}{dt}t_E + \phi)$$

The atmosphere delay rate is obtained by differentiating (A.4).

$$\dot{\tau}^a_i = -\rho_i s^{-2} s'\dot{\theta}_i$$

where

$$s = \sin\theta_i + \frac{0.00143}{\tan\theta_i + 0.0445}$$

$$s' = \frac{ds}{d\theta} = \cos\theta_i - \frac{0.00143}{[\sin\theta_i + 0.0445\cos\theta_i]^2}$$

$$\dot{\theta}_i = \frac{\omega_e}{\cos\theta_i}\cos\lambda_i\cos\delta_s(t_E)\sin L_{si}(t)$$

The atmosphere delay acceleration is obtained by differentiating $\dot{\tau}_i^a$.

A.3.6 Baseline-Based Delay

A baseline delay is written on the A-tape for each scan reference time t_E. This is the baseline-based delay $\Delta\tau_b$ for the wavefront arriving at station 1 at UTC time t_E. The baseline delay is calculated as above but using differenced station vectors and clocks (remote-reference) by the correlator control computer. The differential antenna based delay $\Delta\tau_a(t_E) = \tau_2(t_E) - \tau_1(t_E)$, where $\tau_i(t_E)$ is the total geocentric delay at antenna i, is the baseline delay for the wavefront arriving at the Earth centre at t_E. Therefore,

$$\Delta\tau_b(t_E) = \Delta\tau_a(t_E - \Delta\tau)$$

where $\Delta\tau$ is the geocentric propagation time for station 1. A consistency error is reported by MK3IN if the antenna-based delays used by MK3IN differ by more than 1ps when corrected to the baseline-based formalism.

A.4 Correlator Errors

This is a list of conditions under which MK3IN rejects type 51 data records. These conditions should agree with the MK3 FRNGE data rejection criteria (Whitney 1990). All bit addresses in this list refer to the type 51 records. Data are discarded if any of the following bits are set:

Bit 14 word 2: Correlate suppress.

Bit 13 word 2: Tapes out of sync.

Bit 12 word 2: A priori array overrun.

Bit 14 word 1: Overrun in AP arrays.

Bit 7 word 2: No PP update.

Bit 5 word 2: Y slipped sync.

Bit 4 word 2: X slipped sync.

Bit 1 word 2: No Y clock.

Bit 0 word 2: No X clock.

Bit 2 word 6: Tape disagreement between tape time and
expected tape time.

Bit 3 word 6: Error correction attempt initiated.

Bit 1 word 6: CRCC error in remote station sync block.

Bit 0 word 6: CRCC error in reference station sync block.

Bits 15-8 word 3: MK3A error conditions.

Data are also discarded if any of the following conditions are met:

a) Type 51 record time exceeds nominal scan length.

b) Time offset from scan start time differs from integral number of AP intervals by more than 1 ms. Integral second offsets are ignored.

c) The parity error count for the module exceeds the maximum allowed parity error rate. Max parity error count = (Sample rate (bits/s)) * (AP length (s)) * Max PER / 8. The max parity error rate (PER) default is 0.01.

d) Fewer than the allowed fraction of the nominal number of bits are correlated within the AP. Min correlator count = (Sample rate (bits/s)) * (AP length (s)) * (Dropout level). Dropout level default is 0.5. This test is applied to

both sine and cosine channels of the correlator except for AC functions in which case the test is applied only to the cosine channel.

e) Module termination status bad (any operator terminated code).

The option was added to MK3IN to allow CRCC and slipped synchronization error codes to be ignored. Numerous tests indicated that these error flags did not seem to be correlated with bad data in amplitude or phase when correlating narrow bandwidth spectral line data. In this case the correlator computer is under heavy load and the communication with the correlator modules is sometimes impaired. Other error flags, especially time errors, were clearly associated with bad data. The load on the correlator computer can be reduced by increasing the AP length and by correlating in single-baseline mode.

REFERENCES

Alcock, C., and Ross, R.R.: 1986, *Ap. J.*, **305**, 837.

Alef, W., and Porcas, R.W.: 1986, *Astr. Ap.*, **168**,365.

Alef, W.: 1989, Introduction to Phase-Reference Mapping in *Very Long Baseline Interferometry. Techniques and Applications, NATO ASI Series C*, **283**,Eds. M. Felli and R.E. Spencer, Kluwer Academic Publishers, Dordrecht, p. 261.

Bartel, N.: 1990, *in press.*

Barvainis, R., McIntosh, G., and Predmore, C.R.: 1987, *Nature* , **329**, 613.

Benson, J.M., Mutel, R.L., Fix, J.D., and Claussen, M.J.: 1979, *Ap. J.*, **229**, L87.

Bloemhof, E.E., Reid, M.J., and Moran, J.M.: 1992, *Ap. J.*, **397**, 500.

Bowers, P.F.: 1984, *Ap. J.*, **279**, 350.

Bowers, P.F.: 1991, *Ap. J. Suppl.*, **76**, 1099.

Bowers, P.F., and Johnston, K.J.: 1988, *Ap. J.*, **330**, 339.

Bowers, P.F., Johnston, K.J., and Spencer, J.H.: 1981, *Nature* , **291**, 382.

Bowers, P.F., Johnston, K.J., and de Vegt, C.: 1989, *Ap. J.*, **340**, 479.

Bridle, A.H., and Nance, J.: 1991, AIPS Memorandum 70, NRAO, Charlottesville, USA.

Brown, L.F., Roberts, D.H., and Wardle, J.F.C.: 1989, *A.J.*, **97**,1522.

Bujarrabal, V., Gomez-Gonzalez, J., Bachiller, R., and Martin-Pintado, J.: 1988, *Astr. Ap.*, **204**, 242.

Bujarrabal, V., Gomez-Gonzalez, J., and Planesas, P.: 1989, *Astr. Ap.*, **219**, 256.

Chao, C.C.: 1970, Report TM 391-129, Jet Propulsion Laboratory, NASA.

Chapman, J.M.: 1988, *M.N.R.A.S.* , **230**, 415.

Chapman, J.M., and Cohen, R.J.: 1986, *M.N.R.A.S.* , **220**, 513.

Chapman, J.M., Cohen, R.J., and Saikia, D.J.: 1991, *M.N.R.A.S.* , **249**, 227.

Chiu, Y.T.: 1975, *J. Atm. Terr. Phys.*, **37**, 1563.

Cimerman, M.: 1979, *Ap. J.*, **234**, 891.

Clark, B.G.: 1973, *Proc. IEEE*, **61**,1242.

Clark, B.G.: 1986, Introduction and Basic Theory in *Synthesis Imaging*, Eds. R.A. Perley, F.R. Schwab and A.H. Bridle, NRAO, Green Bank USA, p.1.

Claussen, M., and Fix, J.: 1982, *Ap. J.*, **263**, 153.

Cobb, M.L., and Fix, J.D.: 1987, *Ap. J.*, **315**, 325.

Cohen, R.J., Downs, G., Emerson, R., Grimm M., Gulkis, S., Stevens, G., and Tarter, J.: 1987, *M.N.R.A.S.* , **225**, 491.

Cohen, R.J.: 1989, *Rep. Prog. Phys.*, **52**, 881.

Conway, R.G., and Kronberg, P.P.: 1969, *M.N.R.A.S.* , **142**, 11.

Cook, A.H.: 1977, *Celestial Masers*, Cambridge University Press, Cambridge.

Cornwell, T.: 1986, Self-Calibration in *Synthesis Imaging*, Eds. R.A. Perley, F.R. Schwab and A.H. Bridle, NRAO, Green Bank USA, p.137.

Cotton, W.D., Geldzahler, B.J., Marcaide, J.M., Shapiro, I.I., Sanroma, M., and Rius, A.: 1984, *Ap. J.*, **286**, 503.

Cotton, W.D.: 1989, Polarimetry in *Very Long Baseline Interferometry. Techniques and Applications*, Eds. M. Felli, and R.E. Spencer, Kluwer Academic Publishers, Dordrecht, p. 275.

Cotton, W.D.: 1991, personal communication.

Craine, E.R., Schuster, W.J., Tapia, S., and Vrba, F.J.: 1976, *Ap. J.*, **205**, 802.

Davies, K.: 1965, *Ionospheric Radio Propagation: National Bureau of Standards Monograph 80*, US Govt. Printing Office, Washington DC 20402, USA.

Davies, R.D.: 1974, in *Galactic Radio Astronomy*, Eds. F.J. Kerr and S.C. Simonson III, IAU, p. 275.

Davis, W.F.: 1974, *Astr. Ap. Suppl.* , **15**,381.

Deguchi, S., and Watson, W.D.: 1986, *Ap. J.*, **300**, L15.

Diamond, P.J.: 1989, Spectral Line VLBI in *Very Long Baseline Interferometry. Techniques and Applications, NATO ASI Series C*, **283**,Eds. M. Felli and R.E. Spencer, Kluwer Academic Publishers, Dordrecht, p. 231.

Diamond, P.J., Norris, R.P., and Booth, R.S.: 1983, *Astr. Ap. (Letters)* , **124**,L4.

Diamond, P.J., Norris, R.P., Rowland, P.R., Booth, R.S., and Nyman, L-A.: 1985, *M.N.R.A.S.* , **212**, 1.

Dickinson, D.F., Snyder, L.E., Brown, L.W., and Buhl, D.: 1978, *A.J.*, **83**, 36.

Drake, S.A., and Linsky, J.L.: 1989, *A.J.*, **98**, 1831.

Dyck, H.M., Zuckerman, B., Leinert, C.H., and Beckwith, S.: 1984, *Ap. J.*, **287**, 801.

Elgered, G.K.: 1982, *IEEE Trans. Ant. Prop.*, **AP-30**, 502.

Engels, D., and Heske, A.: 1989, *Astr. Ap. Suppl.* , **81**, 323.

Evans, J.V., and Hagfors, T.: 1968, *Radar Astronomy*, McGraw-Hill, New York.

Fix, J.D.: 1981, *Ap. J.*, **248**, 542.

Fix, J.D.: 1987, *A.J.*, **93**, 433.

Fix, J.D., and Cobb, M.L.: 1987, *Ap. J.*, **312**, 290.

Fix, J.D., and Cobb, M.L.: 1988, *Ap. J.*, **329**, 290.

Fomalont, E.B.: 1986, Image Analysis in *Synthesis Imaging*, Eds. R.A. Perley, F.R. Schwab and A.H. Bridle, NRAO, Green Bank, USA, p.215.

Forrest, W.J., McCarthy, J.F., and Houck, J.R.: 1979, *Ap. J.*, **233**, 611.

Freeman, J.J.: 1958, *Principles of Noise*, John Wiley and Sons, New York.

Gabuzda, D.C., Wardle, J.F.C., and Roberts, D.H.: 1989, *Ap. J.*, **338**, 743.

Garcia-Barreto, J.A., Burke, B.F., Reid, M.J., Moran, J.M., Haschick, A.D., and Schilizzi, R.T.: 1988, *Ap. J.*, **326**, 954.

Gaylard, M.J, and West, M.E.: 1991, personal communication.

Genzel, R., Reid, M.J., Moran, J.M., and Downes, D.: 1981, *Ap. J.*, **244**, 884.

Giguere, P.T., Woolf, N.J., and Webber, J.C.: 1976, *Ap. J. (Letters)*, **207**, L195.

Goldreich, P., Keeley, D.A., and Kwan, J.Y.: 1973a, *Ap. J.*, **179**, 111.

Goldreich, P., Keeley, D.A., and Kwan, J.Y.: 1973b, *Ap. J.*, bf 182, 55.

Gottlieb, E.W., and Liller, W.M.: 1978, *Ap. J.*, **225**, 488.

Guilloteau, S., Lucas, R., Nguyen-Q-Rieu, and Omont, A.: 1986, *Astr. Ap. (Letters)* , **165**, L1.

Güsten , R., and Fiebig, D.: 1990, Magnetic Fields in Dark Cloud Cores and H_2O Masers in *Galactic and Intergalactic Magnetic Fields: IAU Symposium 104*, Eds. R.Beck, P.P Kronberg and R.Wielebinski, Kluwer, Dordrecht, p. 305.

Gwinn, C.R.: 1984, Ph.D. thesis, Princeton University.

Habing, H.J.: 1990, in *From Miras to Planetary Nebulae: Which Path for Stellar Evolution ?*, Eds. M.O. Menessier and A. Omont, Publ. Editions Frontieres, p. 16.

Hagfors, T.: 1976, Atmospheric Effects in *Methods of Experimental Physics*, **12B**, 119.

Hamilton, W.C.: 1964, *Statistics in Physical Science*, The Ronald Press Company, New York.

Harvey, P.M., Lester, D.F., Brock, D., and Joy, M.: 1991, *Ap. J.*, **368**, 558.

Hekkert, P.T-L., Chapman, J.M., and Zijlstra, A.A.: 1992, *Ap. J. (Letters)*, **390**, L23.

Herzberg, G.: 1950, *Spectra of Diatomic Molecules*, Van Nostrand Reinhold, New York.

Hjellming, R.M.: 1983, *An Introduction to the NRAO Very Large Array*, NRAO Internal Publication.

Högbom , J.: 1974, *Astr. Ap. Suppl.* , **15**,417.

Hrivnak, B.J., Kwok, S., and Volk, K.M.: 1989, *Ap. J.*, **346**, 265.

Humphreys, R.M, Strecker, D.W., Murdock, T.L., and Low, F.J.: 1973, *Ap. J. (Letters)*, **179**, L49.

IAU: 1973, *Trans. Int. Astron. Union*, **15B**, 166.

Irvine, C.E.: 1986, *IAU Telegram*, 4286.

Jackson, J.D.: 1962, *Classical Electrodynamics*, John Wiley and Sons, New York.

Jewell, P.R., Batrla, W., Walmsley, C.M., and Wilson, T.L.: 1984, *Astr. Ap. (Letters)* , **130**, L1.

Jewell, P.R., Schenewerk, M.S., and Snyder, L.E.: 1985, **295**, 183.

Jewell, P.R., Snyder, L.E., and Schenewerk, M.S.: 1986, *Nature* , **323**, 311.

Jura, M.: 1987, *Ap. J.*, **313**, 743.

Kellermann, K.I., and Thompson, A.R.: 1985, *Science*, **229**,123.

Knapp, G.R., and Bowers. P.F.: 1983, *Ap. J.*, **266**, 701.

Knapp, G.R., and Morris, M.: 1985, *Ap. J.*, **292**, 640.

Knapp, G.R.: 1989, Carbon Stars as Planetary Nebula Progenitors in *IAU 131: Planetary Nebulae*, Ed. S. Torres-Peimbert, p381.

Kwok, S.: 1982, *Ap. J.*, **258**, 280.

LeVan, P.D., and Sloan, G.: 1989, *P.A.S.P.* , **101**, 1140.

Lewis, B.M., Eder, J., and Terzian, Y.: 1985, *IAU Telegrams*, 4072.

Lewis, B.M., Terzian, Y., and Eder, J.: 1986, *Ap. J. (Letters)*, **302**, L23.

Lewis, B.M.: 1989, *Ap. J.*, **338**, 234.

Linfield, R.P.: 1986, *Ap. J.*, **92,**213.

Lis D.C., Goldsmith, P.F., and Predmore, C.R.: 1989, *Ap. J.*, **341**, 823.

Marcaide, J.M., and Shapiro, I.I.: 1983, *A.J.*, **88,**1133.

McIntosh, G.C.: 1987, Ph.D. Thesis, University of Massachusetts.

McLaren, R.A., and Betz, A.L.: 1980, *Ap. J.*, **240**, 159.

Millar, T.J., Ellder, J., Hjalmarson, A., and Olofsson, H.: 1987, *Astr. Ap.*, **182**, 143.

Miller, K.S.: 1973, *Siam Review*, **15**, 706.

Moran, J.M.: 1973, *Proc. IEEE*, **61**, 1236.

Moran, J.M.: 1989, The Effects of Propagation on VLBI Observations in *Very Long Baseline Interferometry: Techniques and Applications*, Eds. M. Felli and R.E. Spencer, NATO ASI Series C, **283,**Kluwer Academic Publishers, Dordrecht.

Morris, D., Radhakrishnan, V., Seielstad, G.A.: 1964, *Ap. J.*, **139**, 551.

Mutel, R.L., Fix, J.D., Benson, J.M., and Webber, J.C.: 1979, *Ap. J.*, **228**, 771.

Napier, P.J.: 1989, The Primary Antenna Elements in *Synthesis Imaging in Radio Astronomy, PASP Series*, **6**, Eds. R.A. Perley, F.R. Schwab and A.H. Bridle, p.39.

Narayan, R., and Nityananda, R.: 1986, *Ann. Rev. Astr. Ap.*, **24**,127.

Nedoluha, G.E., and Watson, W.D.: 1990, *Ap. J.*, **361**, 653.

Nedoluha, G.E., and Bowers, P.F.: 1992, *Ap. J.*, **392**, 249.

Nercessian, E., Guilloteau, S., Omont, A., and Benayoun, J.J.: 1989, **210**, 225.

Neugebauer, G.N., and Leighton, R.B.: 1969, *Two-Micron Sky Survey*, NASA SP-3047, Washington DC, USA.

NGDC: 1987, *Solar-Geophysical Data Prompt Reports*, **514**,Part 1, National Geophysical Data Center, Boulder, Colorado.

Norris, R.P., Booth, R.S., Diamond, P.J., Nyman, L.-A., Graham, D.A., and Matveyenko, L.I.: 1984, *M.N.R.A.S.* , **208**,435.

Nyman, L-A., Johansson, L.E.B. and Booth, R.S.: 1986, *Astr. Ap.*, **160**, 352.

Olnon, F.M., Raimond, E., and IRAS Science Team: 1986, *Astr. Ap. Suppl.* , **65**, 607.

Olofsson, H., Johansson, L.E.B., Hjalmarson, A., and Rieu, N.Q.: 1982, *Astr. Ap.*, **107**, 128.

Parthasarathy, M., and Pottasch, S.R.: 1986, *Astr. Ap. (Letters)* , **154**, L16.

Pascoli, G.: 1992, *P.A.S.P.* , **104**, 350.

Pearson, T.J., and Readhead, A.C.S.: 1984, *Ann. Rev. Astr. Ap.*, **22**,97.

Pottasch, S.R., and Parthasarathy, M.: 1988, *Astr. Ap.*, **192**, 182.

Reid, M.J.: 1990, Masers and Stellar Magnetic Fields in *Galactic and Intergalactic Magnetic Fields*, Eds. R. Beck *et al.* , IAU, Netherlands, p 21.

Reid, M.J., Haschick, A.D., Burke, B.F., Moran, J.M., Johnston, K.J., and Swenson Jr., G.W.: 1980, *Ap. J.*, **239**,89.

Reid, M.J., Moran, J.M., Leach, R.W., Ball, J.A., Johnston, K.J., Spencer, J.H., and Swenson, G.W.: 1979, *Ap. J. (Letters)*, **227**, 89.

Reid, M.J., and Moran, J.M., Eds.: 1988, *The Impact of VLBI on Astrophysics and Geophysics IAU 129*, Eds. M. Felli and R.E. Spencer, Kluwer Academic Publishers, Dordrecht.

Reid, M.J., Muhleman, D.O., Moran, J.M., Johnston, K.J., and Schwartz, P.R.: 1977, *Ap. J.*, **214**, 60.

Renzini, A.: 1981, in *Physical Processes in Red Giants*, Eds. I. Iben Jr. and A. Renzini, Dordrecht: Reidel, p. 165.

Ridgway, S.T., Joyce, R.R., Connors, D., Pipher, J.L., and Dainty, C.: 1986, *Ap. J.*, **302**, 662.

Roberts, J.A. ed.: 1984, *Indirect Imaging*, Cambridge University Press, Cambridge.

Roberts, D.H., Brown, L.F., and Wardle, J.F.C.: 1991, Linear Ppolarization Sensitive VLBI in *Radio Interferometry: Theory, Techniques and Applications, IAU Coll. 131, ASP Conference Series*, Eds. T.J. Cornwell and R.A. Perley, **19**, p. 281.

Robertson, D.S.: 1975, Ph.D. thesis, Massachusetts Institute of Technology.

Rodriguez, L.F.: 1987, Protoplanetary Nebular in *Planetary and Proto-Planetary Nebulae: From IRAS to ISO*, Ed. A. Preite Martinez, D. Reidel, p. 55.

Rogers, A.E.E., Hinteregger, H.F., Whitney, A.R., Counselmann, C.C., Shapiro, I.I., Wittels, J.J., Klemperer, W.K., Warnock, W.W., Clark, T.A., Hutton,

L.K., Marandino, G.E., Ronnang, B.O., Rydbeck, O.E.H., and Niell, A.E.: 1974, *Ap. J.*, **193**,293.

Rogers, A.E.E.: 1976, Theory of Two-Element Interferometers in *Methods of Experimental Physics*, **12C**,Academic Press Inc., New York, p. 139.

Rogers, A.E.E.: 1983, Haystack Observatory Memorandum to VLBI Group, 7 March 1983.

Rogers, A.E.E.: 1990, personal communication.

Sahai, R., Claussen, M.J., and Masson, C.R.: 1989, *Astr. Ap.*, **220**, 92.

Sault, R.J., Killeen, N.E.B., Zmuidzinas, J., and Loushin, R.: 1990, *Ap. J. Suppl.*, **74**, 437.

Schwab, F.R., and Cotton, W.D.: 1983, *A.J.*, **88**,688.

Sramek, R.A., and Schwab, F.R.: 1986, Imaging in *Synthesis Imaging*, Eds. R.A. Perley, F.R. Schwab and A.H. Bridle, NRAO, Green Bank, USA, p.67.

Taff, L.G.: 1981, *Computational Spherical Astronomy*, John Wiley and Sons, New York.

Thompson, R.I., and Boroson, T.A.: 1977, *Ap. J. (Letters)*, **216**, 75.

Thompson, A.R., Moran, J.M., and Swenson, G.W.: 1986, *Interferometry and Synthesis in Radio Astronomy*, John Wiley & Sons, New York.

Troland, T.H., and Heiles, C.: 1982, *Ap. J.*, **252**, 179.

UAG: 1981, Report UAG-82, International Reference Ionosphere IRI-79.

Valley, S.L. (ed.): 1965, *Handbook of Geophysics and Space Environments*, Air Force Cambridge Research Laboratories.

Van Vleck, J.H., and Middleton, D.: 1966, *Proc. IEEE*, **54**,2.

Vessot, R.F.C: 1976, Frequency and Time Standards in *Methods of Experimental Physics*, **12C**, 198.

Volk, K.M., and Kwok, S.: 1989, *Ap. J.*, **342**, 345.

Walker, R.C.: 1977, Ph.D. Thesis, Massachusetts Institute of Technology.

Walker, R.C.: 1986, Very Long Baseline Interferometry in *Synthesis Imaging*, Eds. R.A. Perley, F.R. Schwab and A.H. Bridle, NRAO, Green Bank, USA.

Wardle, J.F.C., and Kronberg, P.P.: 1974, *Ap. J.*, **194**, 249.

Wardle, J.F.C., Roberts, D.H., Potash, R.I., and Rogers, A.E.E.: 1986, *Ap. J. (Letters)*, **304**,L1.

Whitney, A.R., Rogers, A.E.E., Hinteregger, H.F., Knight, C.A., Levine, J.L., Lippincott, S., Clark, T.A., Shapiro, I.I., and Robertson, D.S.: 1976, *Radio Sci.* , **11**, 421.

Whitney, A.R.: 1990, personal communication.

Wilkinson, P.N.: 1989, An Introduction to Closure Phase and Self-Calibration in *Very Long Baseline Interferometry. Techniques and Applications, NATO ASI Series C*, **283**,Eds. M.Felli and R.E. Spencer, Kluwer Academic Publishers, Dordrecht, p.69.

Zell, P.J., and Fix, J.D.: 1991, *Ap. J.*, **369**, 506.